Design of a Man-Wearable Control Station for a Robotic Rescue System

Wai K. Fong

MSc (Eng) Dissertation

Supervised by Samuel Ginsberg and Tracy Booysen

September 2015

Department of Mechanical Engineering

University of Cape Town

Robotics and Agents Research Laboratory

The financial assistance of the National Research Foundation (NRF) towards this research is hereby acknowledged. Opinions expressed and conclusions arrived at, are those of the author and are not necessarily to be attributed to the NRF.

PLAGIARISM DECLARATION

This thesis is submitted in complete fulfilment of a M.Sc. (Mechanical Engineering) at the University of Cape Town.

I know the meaning of plagiarism and declare that all of the work in the document, save for that which is properly acknowledged, is my own. Each contribution to, and quotation in, this document from the work(s) of other people has been attributed, and has been cited and referenced according to the style for IEEE Transactions.

I have not allowed, and will not allow anyone to copy my work with the intention of passing it off as their own.

Wai Fong
Wednesday, 3 September 2015

Executive

SUMMARY

Introduction

This report details the design, development, and testing of a man-wearable operator control station for the use of a low-cost robotic system in **U**rban **S**earch and **R**escue (**USAR**). The complete system, dubbed the "Scarab", is the 1st generation developed and built in the **R**obotics and **A**gents **R**esearch **L**aboratory (**RARL**) at the **U**niversity of **C**ape **T**own (**UCT**), and was a joint effort between three MSc students. The complete system is illustrated below in **Figure 0-1**:

Figure 0-1 – Scarab Robotic System Developed at RARL, University of Cape Town

Robots have found a place in USAR as replaceable units which can be deployed into dangerous and confined voids in the place of humans. As such, they have been utilized in a large variety of disaster environments including ground, aerial, and underwater scenarios, and have been gathering research momentum since their first documented deployment in the rescue operations surrounding the 9/11 terrorist attacks. However one issue is their cost as they are not economical solutions, making them less viable for inclusion into a rescue mission as well as negatively affecting the operator's decisions

in order to prioritise the safety of the unit. Another concern is their difficulty of transport, which becomes dependent on the size and portability of the robot.

As such, the Scarab system was conceived to provide a deployable robotic platform which was low-cost, with a budget goal of US $ 500. To address the transportability concerns, it aimed to be portable and light-weight; being able to be thrown through a window by a single hand and withstanding a drop height of 3 m. It includes an internal sensor payload which incorporates an array of sensors and electronics, including temperature monitors and two cameras to provide both a normal and IR video feed. Two LED spotlights are used for navigation, and a microphone and buzzer is included for interaction with any discovered survivors.

Operator Control Station

The operator station acts as the user interface between the operator and the robotic platform. It aimed to be as intuitive as possible, providing quick deployment and minimalizing the training time required for its operation. To further enhance the Scarab system's portability, it was designed to be a man-wearable system, allowing the operator to carry the robotic platform on their back. It also acts as a charging station, supplying power to the robotic platform's on-board charging circuitry.

The control station's mechanical chassis serves as the man-wearable component of the system, with the functionality being achieved by integration onto a tactical vest. This allows the operator to take the complete system on and off as a single unit without assistance, and uses two mounting brackets to dock the robotic platform. Key areas focussed upon during design were the weight and accessibility of the system, as well as providing a rugged housing for the internal electronics. All parts were manufactured in the UCT Mechanical Engineering workshop.

Figure 0-2 - On-Screen Display showing Operator Control Unit Video Feed

The control station includes a complete electronics system for providing a user interface. This includes a primary controller board which was custom-designed and developed to manage the communications and data processing throughout the entire system. A complete video system receives the wireless video and audio transmitted from the robot, and an on-screen display (as shown above in **Figure 0-2**) is used to show the sensor and system data on top of the video feed. For data communications, two 433 MHz wireless transceivers were used to provide robust transmission in the presence of rubble and fallen steel structures. The transceiver firmware was provided by G. Knox, who was part of the Scarab team, and was in charge of developing the Scarab's sensor payload. Data logging was also implemented to allow archiving of mission data for later analysis. On-board sensors were included on the control station to provide further functionality, which includes a GPS sensor as well as temperature monitors.

A custom-made hand-held controller, dubbed the Operator Control Unit, was designed and manufactured to provide an input device for the operator. This aimed to be an ergonomic one-handed

solution which could be operated whilst wearing safety gloves. A LCD screen is included for viewing the video display, as well as an on-board magnetometer to supply a compass heading.

A lithium-ion polymer battery is used as the power supply. This provides power to the control station electronics, as well as a supply rail for the robotic platform's on-board charging circuitry. Monitoring and protection boards were included into the system to ensure safety of the battery, as well as additional charging module to allow recharging of it while the system is off-field and in storage.

Embedded C was used as the primary programming language used to write the firmware for the operator control station, and was also the choice for the robotic platform's controlling circuitry. Additional LabVIEW software was written to create a development interface between the control station and a desktop or laptop computer. This is shown below in **Figure 0-3**.

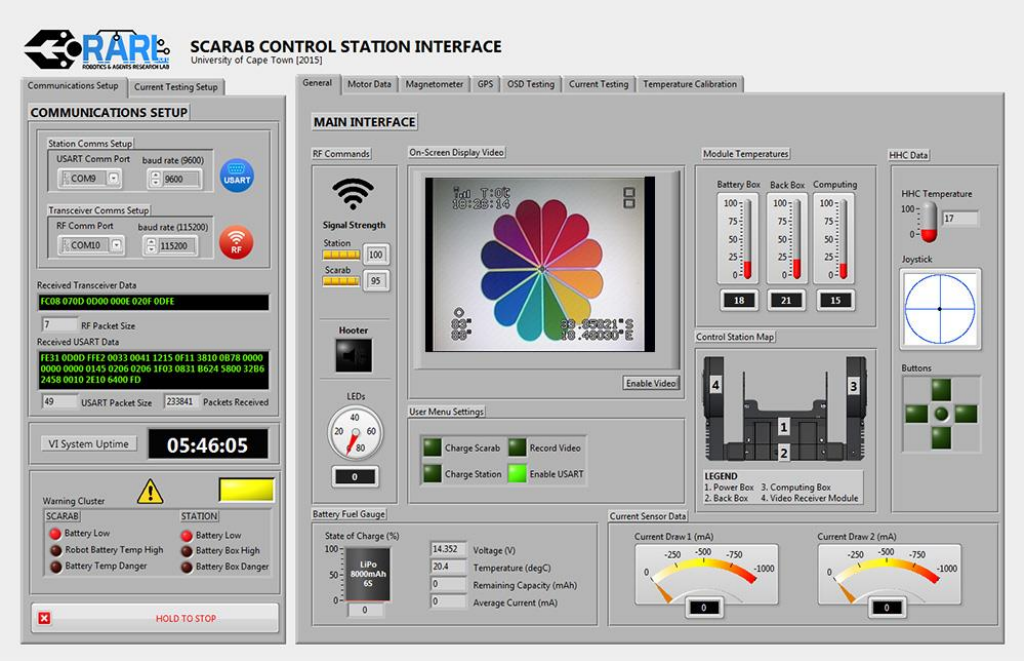

Figure 0-3 – LabVIEW Operator Control Station Interface

Concluding Remarks

The system performed well, with a fully working user interface, and was received positively during user tests. The man-wearable chassis was also found to be a viable solution, able to supply quick deployment times without assistance and supplied an intuitive interface with the external controls. The vast majority of the system's primary specifications were met, with the exception of the feasible charge rate to the robotic platform being at 78.9 % of the specified value.

Suggested improvements include further weight reduction of the system as well as minor changes to the system layout to improve the overall ergonomics. Further refinement to the user interface could also be made to improve the intuitiveness of the system when interacting with the control station's sensors.

ACKNOWLEDGEMENTS

Here are the individuals, to whom I owe great gratitude towards. Without their support and contributions, this project could not have reached its proper completion.

First and foremost I wish to thank my supervisors, Samuel Ginsberg, and Tracy Booysen who have been most tolerant of the never-ending wavering diplomacy between myself and electronics. They both have been greatly inspiring through their leadership and resourcefulness, and making light of many sufferings.

Stephen Marais, for his support and supervision in the first year. Without his contributions, this project would not have initiated.

My fellow team mates, Greig Knox, and Thomas Mathew, who have been a pleasure to work with over all these years for their constant great source of fun and success. And of course, the sharing of many agonies. It has been a great learning experience with you both.

My fellow RARL colleagues, Tim Hope, Max Finbow, and James Dean, who have all provided excellent comradery, and hope.

Dave, for being a constant support and always being there to bear the weight of the operator control station and unforetold lab shenanigans.

My ever supportive family, to whom I would never have come this far without.

Thank you all!

TABLE OF CONTENTS

LIST OF FIGURES

LIST OF TABLES

GLOSSARY OF TERMS

ADC	Analogue to Digital Converter
FPV	First-Person View
GPIO	General Purpose Input Output
GPS	Global Positioning System
I^2C	Inter-Integrated Circuit
IED	Improvised Explosive Device
Li-Po	Lithium-ion Polymer
LOS	Line Of Sight
OCU	Operator Control Unit
OSD	On-Screen Display
PCB	Printed Circuit Board
RARL	Robotics and Agents Research Laboratory
RS-232	Recommended Standard number 232
SPI	Serial Peripheral Interface
UCT	University of Cape Town
USAR	Urban Search and Rescue
USART	Universal Asynchronous Receiver / Transmitter
USB	Universal Serial Bus

1. INTRODUCTION

Figure 1-1 - Northrop Grumman Wheelbarrow UGW [1]

Robots are a polarizing topic in the world of **U**rban **S**earch and **R**escue (**USAR**). On the one hand, they make for invaluable inspection units into dangerous voids in the place of other sentient life, such as dogs, and people [2]. They can also be used to handle hazardous IEDS from a safe distance, as shown above in **Figure 1-1.** On the other hand, reality has shown that robots still have a ways to go before they are robust enough to surmount the challenges presented by the outside world. The first documented use of rescue robots in a disaster zone was in the rescue operations surrounding the September 11 terrorist attacks on the World Trade Centre in New York [3]. The robots were unable to locate any survivors, as they arrived four and a half days after the actual event, where most trapped survivors die within the first two days [4]. Importantly, it was observed that the challenges did were necessarily associated with the robots' mobility, but rather the sensors. This was due to a variety of issues including communication loss, as well as poor camera visibility whilst traversing through dirty, muddy areas which would coat the sensors.

Rescue robots come in the form of ground, aerial or marine based units depending on the task required. Ground rescue robots are typically teleoperated vehicles which use tracks or wheels for movement, and come with an array of sensors to acquire data about the immediate environment. Due to the small size of voids, portable and small solutions are sought after. Modern examples include iRobot's 510 Packbot, and 110 FirstLook, both of which are tracked vehicles with flippers. Similarly, the Recon Scout Throwbot is a miniature "throwable" two-wheeled robot tailored more for reconnaissance missions and can be used for inspection into confined spaces. These robots are very costly, however, and illustrate one of the stumbling blocks of using robots in the USAR environment: they are not economically appealing solutions. The systems range in thousands to hundreds of thousands of US dollars for a single unit, and the Throwbot for example costs US $ 7500 [5] for the entire system. This becomes detrimental to their inclusion in a rescue operation, and also negatively affects the rescue operator's decisions as it adds extra pressure to not lose or damage the unit. Both the Throwbot and 110 FirstLook are shown in **Figure 1-2** below:

Figure 1-2 - Recon Scout Throwbot [6] (left), iRobot 110 FirstLook [7] (right)

CHAPTER 1: Introduction

In spite of all this, rescue robots are still highly relevant. Since 2001, there have been at least 29 uses of robots in disaster zones worldwide [8]. They do however still suffer from a slow deployment time with an average of 6.5 days into the area after the disaster [9]. This is expected to become faster as robots are more widely accepted into rescue communities. The **C**enter for **R**obot-**A**ssisted **S**earch and **R**escue (**CRASAR**) at Texas A&M University specialise in disaster robots, and have participated in 15 of the 35 total documented uses of them in disaster zones. They list the biggest technical barrier being the human-to-robot interaction, and over 50% of failures in 13 incidents have been due to human error [10]. Autonomous control is undesirable [11] in USAR as operators do not trust robots to do tasks without being dictated to, and even less so when subjected to fatigue and sleep deprivation. Therefore it becomes desirable for intuitive user interface systems which require minimal training and are responsive in real time to the operator's actions.

Figure 1-3 - The RATEL USAR Platform [12]

The **R**obotics and **A**gents **R**esearch **L**aboratory (**RARL**) at the University of Cape Town has been developing robots for the use of rescue and inspection. Of relevant note is the RATEL – a **M**obile **R**obotic **P**latform (**MRP**) designed for use in USAR, and is currently the fifth generation in a line of rescue robots from the laboratory. This is shown above in **Figure 1-3**. Its primary features include traversing over uneven terrain using its tracked flippers as well as interacting with the environment using an inverse-kinematic controlled arm with a gripper.

The Scarab is a new robotic system from RARL conceived to tackle the cost issue and desire for small, portable robots. It is of its first generation and serves as a general purpose first-response inspection-class robot for use in USAR. The robotic platform is shown below in **Figure 1-4**. Its two primary attributes are that it can be dropped from a 3 metre height, and is low-cost, with each robotic platform aiming to cost below US $ 500. The complete system was split into three separate concurrent projects done by three MSc students in the same laboratory: T. Mathew, G.Knox, and W.K. Fong, each focussing on the mechanical robotic platform, the internal sensor payload, and the operator control station respectively.

Figure 1-4 - The Scarab USAR Robotic Platform

CHAPTER 1: Introduction

This report therefore describes the design and development of the operator control station for the Scarab low-cost robotic rescue system.

It becomes inherently vital to understand the complete Scarab system for the context of this project. The three main subsystems are briefly described and illustrated below in **Figure 1-5.**

Figure 1-5 - Complete Scarab Robotic System

Robotic Platform	This is the actual Scarab, and includes the mechanical shell body, the driving motors, motor control circuitry, and the wheels.
Sensor Payload	This is located inside the **robotic platform** and acquires and processes data about the environment using its integrated sensor array. It also includes the power supply and charging circuitry for the platform's internal battery.
Operator Control Station	This is remote from the **robotic platform** and provides a wireless operator control interface for the Scarab system.

The main role of the operator control station is to provide a user interface for the robotic platform, allowing the operator to manoeuvre it as well as receiving and logging sensor and camera data back from its sensor payload. To further enhance the Scarab's portability, it is also intended to be a man-wearable system, and act as a charging dock station for the robotic platform. This allows the operator to charge the robotic platform while transporting it on their back. Additional functionality is provided through sensors which help determine the operator's location in the disaster zone. It is important to note that the operator station is not considered as part of the platform, and was therefore not a constituent of the US $ 500 goal.

This report will begin with background research to evaluate existing applicable technologies and solutions for use in the control station. Specifications will be then derived from the findings. A conceptualisation section will then explore possible options before choosing one to develop into the detailed design. Each subsystem will be approached, listing both the mechanical and electronic aspects. A thorough testing section will follow to demonstrate the system's capabilities and the results gained will be used to draw conclusions. Finally, recommendations will be made from the conclusions to provide insight for any future works or derivatives made from the system.

2. BACKGROUND RESEARCH

To develop an effective and functional man-wearable operator control station, it was important to form an understanding behind each of the subsystems and topics required. Background research therefore was done to investigate past and current solutions available both in the market as well as in published research papers.

The complete Scarab robotic system was originally conceived to be used for **U**rban **S**earch **a**nd **R**escue (**USAR**). As such, areas of investigation were focussed upon the use of man-wearable and mobile robotic systems within military, rescue, and security environments.

This research investigated the following topics, and aimed to answer the following questions:

- **Man-Wearable Systems**
  - What are man-wearable systems, and why are they relevant?
  - How are these systems incorporated into current fields?
  - What are the advantages and disadvantages of these systems?

- **Man-Portable Robotic Systems**
  - What robots exist that can be used in USAR?
  - What human interfaces are used to control these robots?
  - What are the advantages and disadvantages of each?
  - How are these systems powered?

- **Batteries and Charging**
  - What types of rechargeable batteries are there?
  - Which are best for use in a mobile system?
  - How should these batteries be safely treated and used?
  - What are the methods used for charging a battery?

- **Wireless Technologies**
  - What frequency bands are ideal for wireless transmission?
  - What technologies are suitable to provide relaying communications?

- **Sensors**
  - What is a GPS sensor and how are they used?
  - What is a magnetometer sensor and how do they work?
  - What should be focussed on when selecting which one to use?

Concluding remarks were drawn from the findings in the topics above, and then compiled into a final conclusions section at the end of this chapter. The conclusions were then used to approach the system specifications, concepts, and design. On each concluding section, a graphical system progression is illustrated using the Hypothetical Operator (shown to the right in **Figure 2-1**).

Figure 2-1 - Hypothetical Operator

CHAPTER 2: Background Research

2.1. MAN-WEARABLE SYSTEMS

2.1.1. INTRODUCTION

Man-wearable devices are sought after in the USAR environment where rapid deployment and mobility are highly advantageous. These systems are typically embedded into the operator's clothing in the form of stitched-in wiring and electronics, or worn as detachable accessorised modules [13]. A prominent feature is their portability; allowing the operator to move around seamlessly and work without hindrance, and the embedded electronics can continue to operate without the user's attention.

Wearable computing is by no means a new concept, and the first documented device [14] was built in 1955 by M.I.T. mathematics professor Edward Thorp: a cigarette pack sized unit designed to beat roulette by predicting the numbers using computed algorithms, and was hidden in a shoe. Further enthusiasm in the mass market for wearable computers has been spurred by the reveal of the more recent Google Glass [15], as well as a range of virtual reality headsets, such as the Oculus Rift [16] (pictured below in **Figure 2-2**). However, both these systems are yet to reach full maturity and are reliant on user input for development.

Figure 2-2 – Edward Thorp's Wearable Computer [17] (left), Oculus Rift Virtual Reality Headset [18] (right)

Man-wearable systems are not isolated to humans, but can also be used on animals. This is seen with examples such as the **Cyber-Enhanced Working Dog** system [19], shown below in **Figure 2-3**. It features a 4 pound dog harness that includes cameras, GPS, gas sensors, microphones and also an automated dog-treat dispenser. The system aims to improve communication between dogs and their handlers, and can be applied from search and rescue to everyday training.

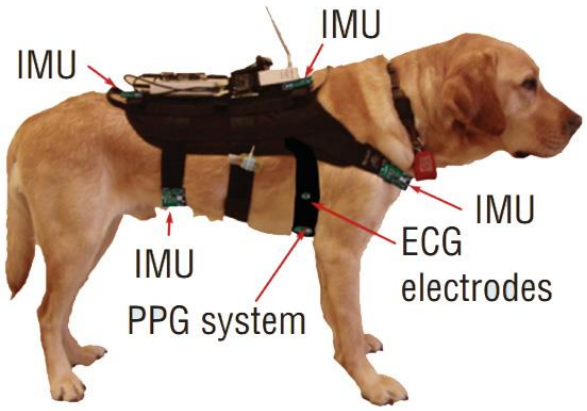

Figure 2-3 - Cyber-Enhanced Working Dog System [19]

CHAPTER 2: Background Research

In the more extreme cases, man-wearable systems can come in the form of entire exoskeletons. One such example is the **XOS 2 Exoskeleton** [20] robotics suit developed by DARPA. It was developed for the US Army, and augments the human wearer's physical capabilities, allowing them to lift 200 lb of weight for long periods of time without strain. Another example is the gas-powered **BLEEX Exoskeleton** [21], which allows the wearer to support 75 extra pounds with ease. Both are shown below in **Figure 2-4**:

Figure 2-4 - XOS 2 Exoskeleton [22] (left), BLEEX Exoskeleton [23] (right)

It is important to consider that in disaster zones, conditions are far from ideal, and devices are often exposed to large forces and environmental hazards. Rain and dust are common concerns, being particularly disadvantageous to electronics. Additionally, the equipment and operator may have to be decontaminated post-operation. Rugged design therefore becomes an inherent requirement. A man-wearable system for use in military applications is commonly allocated a rating of IP67 [13]. This rating indicates complete protection against dust and able to be immersed in water between 15cm and 1m for 30 minutes [24].

When designing a man-wearable system for use in USAR, it is also important to consider the system operator not only as an individual, but as a member of the complete rescue team [25]. As such, the human-to-robot interaction should not compromise the operator's situational awareness, and endanger the safety and cohesiveness of the team. The system should also be quick and intuitive, minimizing distraction during operation, as well as reducing the training time required. Since rescue operators are required to use safety gloves [26], it should be expected that the human interface can be comfortably used whilst wearing them.

Ideally in any given environment, a man-wearable system should be as small and light as possible, while still providing enough power and computational ability to perform the system's functional requirements. This may provide conflicts with the control station's requirements to be able to carry the mobile robotic platform on the person, as the size of the operator control station scales with the size of the robotic platform. The robotic platform's battery requirements also become paramount, as the control station's battery must have enough power and capacity to provide adequate charge to it.

The following sections will provide more in-depth analysis of existing man-wearable systems, and a subsequent section will collate them together in order to draw conclusions from each.

2.1.2. EXISTING MAN-WEARABLE SYSTEMS

A selection of relevant man-wearable systems will be investigated in this section.

2.1.2.1. Land Warrior

The Land Warrior Integrated Soldier System [27], [28] was developed by General Electric for use in the U.S. Armed Forces. It aimed to increase the effectiveness of soldiers by integrating control and communication devices into their armaments. The modules are located around the person's body, and wires are routed along the body. It includes five main subsystems, shown below in **Figure 2-5**:

Figure 2-5 - Land Warrior System [29]

1. **Vest** – Fitted with sensors, the central computing unit, and batteries.
2. **Helmet** – Installed with a **H**ead-**M**ounted-**D**isplay (**HMD**), and a WLAN antenna, providing up to 1km line-of-sight radio transmission.
3. **User interface** – Joystick and mouse buttons for menu selection on the HMD, and a SIM card reader for access control.
4. **Weapon system** – Attached daylight video weapon scope and thermal weapon sight passes video feed into HMD, and has buttons on-weapon to talk, take pictures or switch scope modes.
5. **Power supply** – Lithium-ion rechargeable batteries, and $LiMnO_2$ [30] disposable batteries, which provide 10, and 12 hours of operating time respectively.

The system was criticized for its weight – approximately 7.7 kg. This was deemed unsuitable when taking into account that the average load a ground soldier already carries is 29 – 59 kg [31]. There was also a significant lag in the map's update rate. It was therefore not in real time, and only ideal for periodic position monitoring.

2.1.2.2. Nett Warrior

Figure 2-6 - Nett Warrior End User Device [32]

Nett Warrior [33] was the replacement to Land Warrior. Like its predecessor, it was a situational awareness system designed for use in combat situations by soldiers in the U.S. army. The complete system included a hands-free display, a computing unit, radio transceiver, a power supply, and recharging equipment [34].

The interface device, dubbed the **E**nd **U**ser **D**evice (**EDU**), was based on a rugged touchscreen smartphone which ran an Android operating system. It is shown above in **Figure 2-6**. The EDU displayed the soldier's and leader's location on a geo-map in real time, and set up a communications relay system using each soldier's modules. It operated over a classified network connection exclusive for military use, and provided data encryption for secure transmission and storage.

Figure 2-7 - Nett Warrior End User Device Placement: Wrist [35] (left), Chest [36] (right)

This was better received than Land Warrior, due to being lighter and more compact. However, the system was criticized for excessive light emission from the phone's screen, which was problematic for night time recon operations. The EDU was also initially strapped to the soldiers' wrist area, but was later transferred to the chest due to feedback about discomfort and inconvenience caused by cables routed along the arm. The setups are illustrated above in **Figure 2-7**.

2.1.2.3. Modular Tactical System

Figure 2-8 - Modular Tactical System Carry Configurations [37]

The **M**odular **T**actical **S**ystem **(MTS)** [37] is a man-wearable tactical system developed by Black Diamond Extended Technologies for use in the military. The system was designed to be compatible with tactical vest carriers such as MOLLE. Without the batteries, the entire system weighs approximately 0.8 - 1.1 kg. There are also alternative configurations provided in the form of the MTS Carry Pack and Assault Pack, which allows the system to be transported as a carry pack, or rucksack respectively. These are shown above in **Figure 2-8**.

Figure 2-9 - MTS Universal Tactical Display [37]

The **U**niversal **T**actical **D**isplay (**UTD**) utilizes a 6.5'' sunlight-readable resistive touchscreen display with a 1024 x 768 pixel resolution. It features an on-screen keyboard, five user buttons and an optical mouse. Using it, soldiers can perform essential tasks such as to pinpoint and call in airstrikes. This is shown to the left in **Figure 2-9**.

Processing is handled by the central computing unit which also controls the radio interface and power management electronics. It incorporates an Intel Atom 1.6Hz processor with 2GB RAM, an embedded SSD drive, and a removable SD card [38]. The computer can run a Windows XP/7 or Linux operating system, which comes complete with system configuration software.

A SiRFstarIII GPS module is worn on the shoulder using a small pouch. Included is also an I/O hub which provides RS-232 and USB ports, and is MOLLE-compatible. The electronics' cables are routed through the vest and cummerbund.

The system as a whole was well received for its lightweight and unobtrusive form, but concerns have been raised with regard to the additional complexity and higher potential of failure due to the modular nature of the system. These have however not outweighed the advantages of the working system.

2.1.3. Q-Belt Integrated Computer (QBIC)

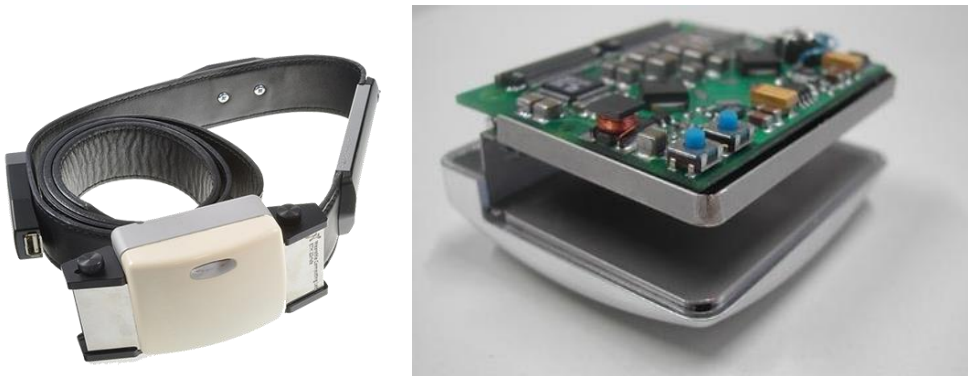

Figure 2-10 - Q-BIC System (left), Q-BIC Buckle Board (right) [39]

The **Q**-**B**elt **I**ntegrated **C**omputer (**QBIC**) [39] (shown above in Figure 2-10) is a miniature wearable-computing system developed by ETH Zurich. It is incorporated into a belt and the buckle contains the circuitry which serves as the core processor, which can then interface with connected peripheral devices. It is intended for use in the fields of medical aid, supervisory systems, as well as security and rescue applications.

The device utilizes an ARM processor, running a Linux operating system. The system can be seen below in **Figure 2-11**.

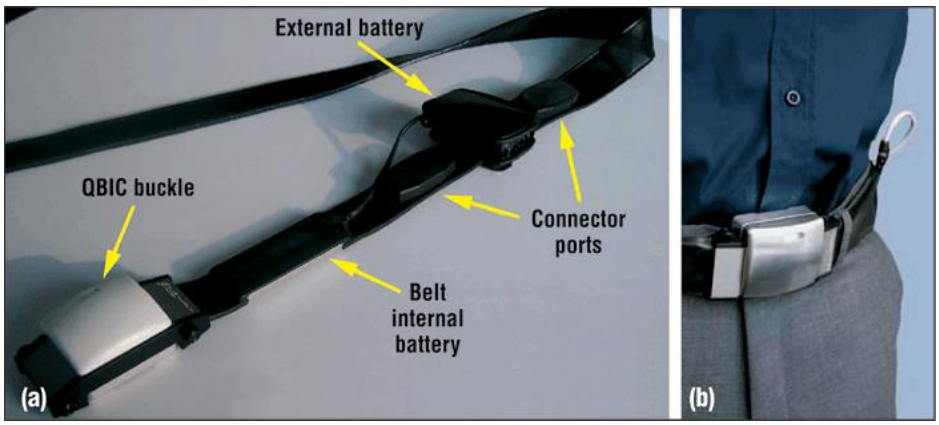

Figure 2-11 - Q-BIC Components (left), Q-BIC Worn as Belt (right) [39]

The core circuitry is located in the buckle, and wires are routed along the belt, which are connected to ports for peripherals which are shown above in **Figure 2-11**. These are described below**:**

Table 2-1 - Available Ports of Q-BIC system and Functions

Port	Function	Maximum Speed	Power [mW]
2 X RS-232	Wired sensors interface	460 kbit/s	1.5
Bluetooth	Wireless sensor interface	921.3 kbit/s	160 (active)
2 X USB Host	Wired multi-function interface	12 Mbit/s	110 (excl. devices)
USB Client	Wired base station interface	12 Mbit/s	Integrated into CPU
VGA	Video displays (640 x 480)		

The QBIC system comes with an internal battery as well as a port to plug in an external battery or mains adapter. The internal lithium-polymer battery provides 2 hours of operating time and an external one provides over 11 hours.

2.1.4. CONCLUDING REMARKS

Based on the findings from the systems described in the previous sections, the following conclusions were drawn for use in a man-wearable system:

- Attachment of human-interface devices to the person's limbs is undesired, and the chest and torso area is preferable for their location.
- Wiring along the body should be limited and avoided as it distracts and causes inconvenience to the operator.
- An IP67 rating is recommended, or at least the ability to be resistant to water and dust.
- A MOLLE-vest type of clothing is best for allowing flexible use of man-wearable devices.
- The weight of the system should take into account the rest of the operator's load.
- While a modular approach is effective, it should be easy to diagnose any problems should any of the modules fail.
- A singular computing control unit should be used to handle all of the system's data processing.
- Should the control station's battery run out, a connector to allow an external backup power supply should be made available

These findings are summarized graphically on the Hypothetical Operator below in **Figure 2-12**.

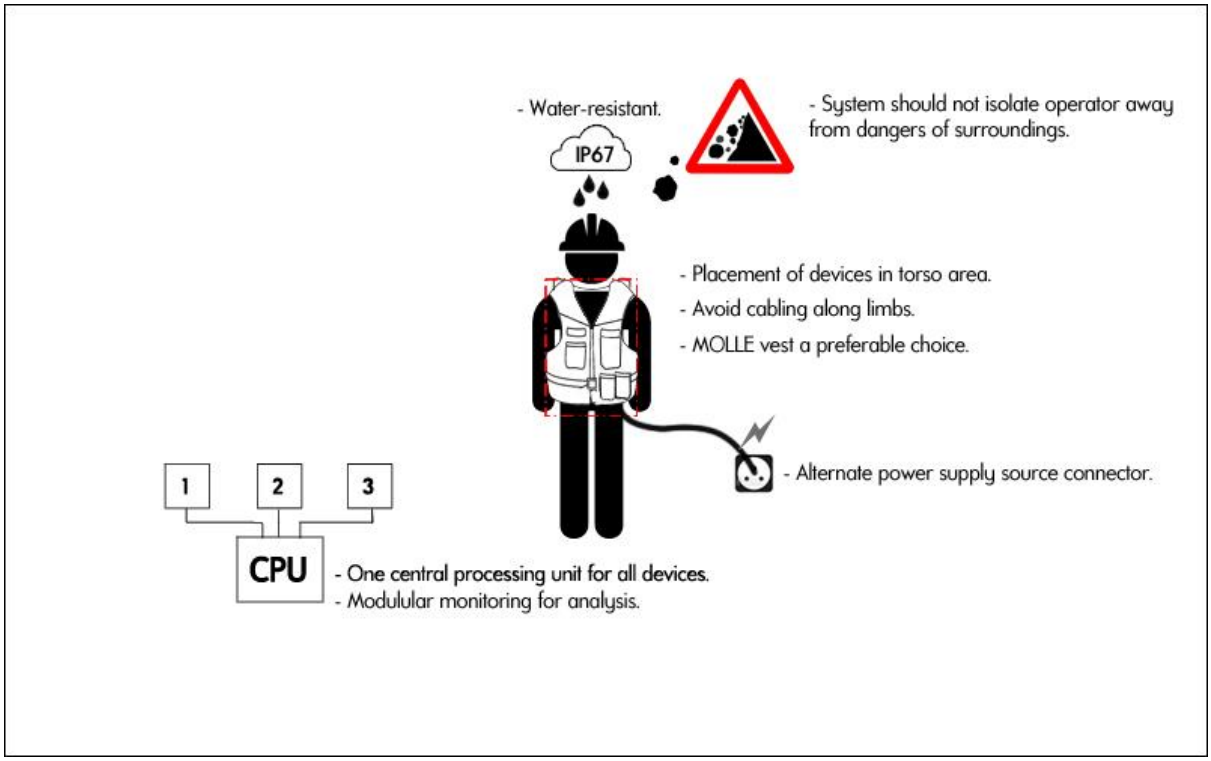

Figure 2-12 - Hypothetical Operator Station System at Man-Wearable Level

2.2. MAN-PORTABLE ROBOTIC SYSTEMS

2.2.1. INTRODUCTION

"Man-portable" refers to the quality of being able to be carried by a single person, with an upper weight limit of 14kg [40]. This becomes relevant to this project as it is intended for the operator to transport the mobile robotic platform on the control station. Possible methods of carrying the robotic platform include:

- Transporting it within a secure storage area on the person (i.e. a rucksack).
- Detaching and reattaching it directly onto the person's clothing.

An example is shown below in **Figure 2-13** of a soldier carrying the iRobot Packbot using a rucksack.

Figure 2-13 - Soldier Carrying iRobot Packbot [41]

This section will explore and investigate robotic man-portable systems which are relevant to the field of **USAR**, giving a brief overview of the robotic system, while also providing focus on the operator interface for each system.

2.2.2. EXISTING MAN-PORTABLE SYSTEMS

A selection of relevant man-portable systems will be investigated in this section.

2.2.2.1. Recon Scout Throwbot XT

Figure 2-14 - Recon Throwbot XT [42]

Robot Overview

The **Recon Scout Throwbot XT**, shown above in **Figure 2-14**, is a light-weight, and compact rugged robot designed for the use in military tactical operations [43]. The robot's primary purpose is to provide video and audio to the operator stealthily, and operates at a quiet 22 dBA. It can also perform tasks such as under-vehicle inspection, quick reconnaissance, and investigation of suspected IEDs. It weighs 540 g, and is small enough to be thrown through a window using one hand. The unit can withstand a 9 m drop.

Operator Control Unit

The **O**perator **C**ontrol **U**nit **II** (**OCU II**) consists of a hand-held controller which features a 3.5'' LCD screen and a thumb-controlled joystick for manoeuvring the robot wirelessly. It was designed to be operated with one hand. An audio jack and a video output port are also available. A separate **C**ommand **M**onitoring **S**tation (**CMS**) allows monitoring of camera transmissions from any Recon Scout robot up to 300m away. It provides three separate video frequency channels (A, B, C), allowing for up to three robots to be monitored.

Figure 2-15 - Recon Throwbot XT OCU II [43]

Batteries

Lithium-ion polymer batteries are used to power the robot and OCU II. At full charge, the robot's batteries offer 60 minutes of operating time. Similarly, The OCU II's batteries provide 120 minutes of operating time.

2.2.2.2. iRobot 110 FirstLook

Figure 2-16 - iRobot 110 FirstLook [44]

Robot Overview

The **iRobot 110 FirstLook** [7], shown above in **Figure 2-16**, is a compact, light-weight robot designed to perform rapid reconnaissance and investigation of confined spaces. Like the Throwbot, it is throwable and can survive a direct 5 m drop onto concrete. It is a compact unit, weighing at 2.45 kg. The robot uses tracks for movement, with a maximum speed of 1.52 m/s, and is capable of climbing stairs using its flippers. The robot was designed for multi-mission capability, and can be fitted with different sensor payload configurations depending on the task required. This includes an arm for manipulating and lifting objects up to 1.6 kg, and a thermal camera for night time operations.

Operator Control Unit

The **OCU** is modelled after a rugged game-style controller and requires both hands to operate. It features a 5'' LCD screen to view the camera feed from the robot. This includes a GUI which displays information about the robot's state and settings. The OCU communicates wirelessly with the robot, and provides integrated radio transmission with a line-of-sight range of up to 200 m.

Figure 2-17 – iRobot 110 FirstLook OCU [44]

Batteries

Both the robot and OCU use rechargeable lithium-ion batteries, which provide more than 6 hours of run time on average. The system includes an AC charger for both units, which comes with an adapter for a BB-2950/U lithium-ion battery.

2.2.2.3. iRobot® 510 PackBot®

Figure 2-18 - iRobot 510 Packbot [89]

Robot Overview

The **iRobot 510 PackBot** [45], shown above in **Figure 2-18**, is an **U**nmanned **G**round **V**ehicle (**UGV**) designed to perform tasks including being a surveillance/reconnaissance unit, disposal of IEDs , and building clearance. The robot is capable of climbing up stairs and moving over rubble using its flippers, and has a maximum speed of 9.3 km/h. It weighs 10.89 kg, and can be carried by a single person, as seen previously in **Figure 2-13**.

Operator Control Unit

The first generation controller was the **P**ackbot **C**ontrol **C**onsole (**PCC**). This used two arcade-based puck controls which were found difficult to use by the younger operators [46]. A later **O**perator **C**ontrol **U**nit (**OCU**) was conceived, which included a 15'' screen AMREL laptop and two hand-held controllers. These controllers were modelled after video game controllers, which were better received by the younger operators, who had greater experience with using such devices. The laptop provided a GUI which displayed a video feed as well as 3D graphics to indicate the robot's orientation and sensor data. Both controllers are displayed below in **Figure 2-19**:

Figure 2-19 - Packbot Control Console [46] (left), Packbot Operator Control Unit [47] (right)

Batteries

The robot is powered by two BB-2590/U lithium-ion batteries, which provide up to 4 hours of operating time. The hand-held controllers utilize removable 11.1 V 7200 mAh lithium-ion batteries.

2.2.3. CONCLUDING REMARKS

- A modern video-game style controller would be best for intuitive learning.
- While a laptop may provide the highest form of processing power for the purpose of graphics and overall performance, it is not a man-wearable solution and would be suitable for USAR operators on the move. Also important to consider is the extra cost of including such a device. Similarly, the Firstlook's OCU is too large to be placed into a pocket.
- A video-screen showing the camera feed and sensor data on top would be highly beneficial to the system.
- The Throwbot XT's controller would be best suited for an USAR operator as it is one-handed and compact enough to be unobtrusive. It shows that the system can be used with a single joystick.
- Lithium-ion batteries are clearly the preferred choice for systems specialising in mobile robotics, but further investigation must be done in order to ascertain their inclusion into this system.
- A means of providing a relay communications system would be ideal for the robotic system, particularly in the disaster zone where wireless communications is very difficult. However, such a system is beyond the scope of this project, but a means to allow it in future implementations will be included.

These findings are added to the previous section's remarks below in **Figure 2-20**.

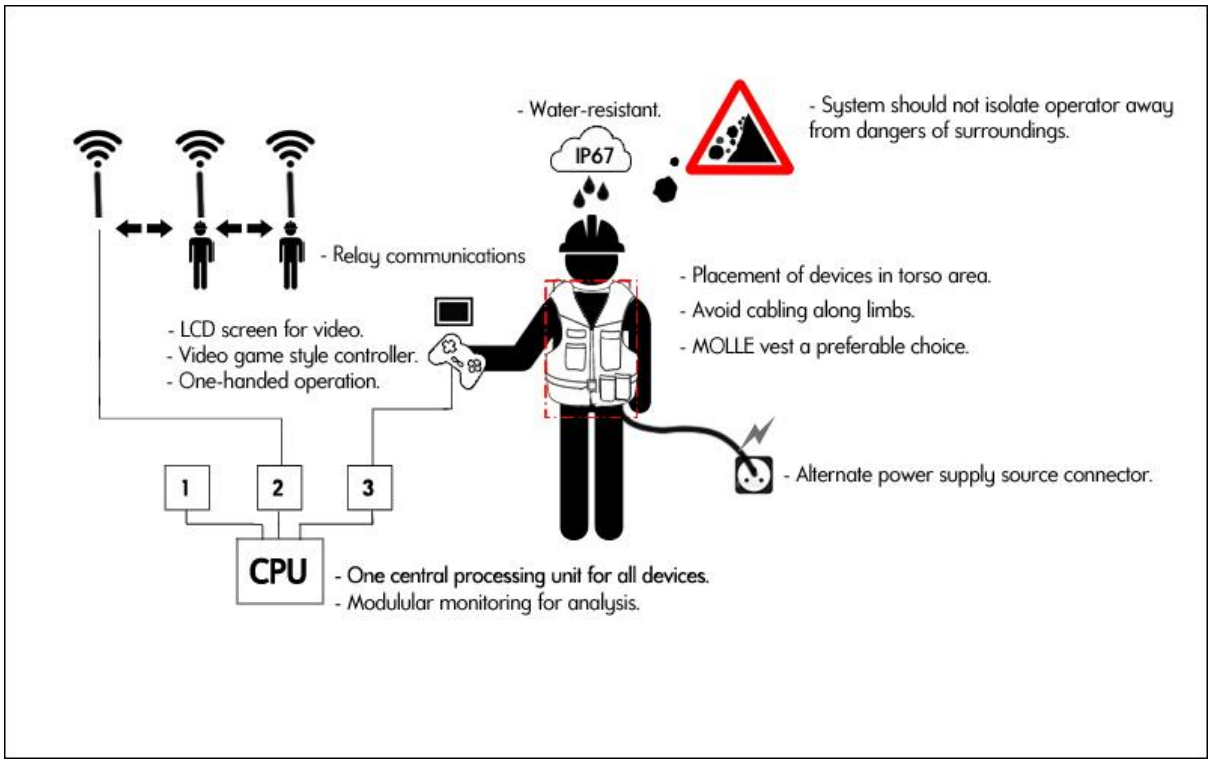

Figure 2-20 - Hypothetical Operator Station System at Man-Portable Level

2.3. BATTERIES AND CHARGING

2.3.1. INTRODUCTION

It was envisioned that while the control station was not busy being used out in the field, and in storage, it can be recharged using an external power supply. Therefore, for the purpose of this chapter, rechargeable batteries were investigated.

Current consumer rechargeable battery solutions come in three main chemistries: lithium-ion (**Li-ion**), nickel-cadmium (**NiCad**), and nickel-metal hydride (**NiMH**). Lead acid batteries have been excluded from this survey due to their low energy density, making them unsuitable for the use on a man-wearable system.

A table compares the qualities of the three battery types below [48], [49]:

Table 2-2 - Comparison of Li-ion, NiCad and NiMH batteries

	Lithium-ion	NiCad	NiMH
Relative Capacity	3	1	1.4
Nominal Cell Voltage (V)	3.7	1.25	1.25
Specific Energy (W.h/kg)	100 - 265	45 - 80	60 - 120
Charge/Discharge Cycle Life(cycles)	300+	500+	300+
Memory Effect	No effect	Noticeable effect	Little effect
Self-discharge rate (%per month)	5-10	15-20	20-30

From the data shown above, it can be seen that **Li-ion** batteries are an ideal candidate for a mobile rechargeable control station. The reasons are listed below:

Advantages

Li-ion batteries have over double the capacity of their counterparts, as well as having the highest specific energy. They also have a low self-discharge rate (5 - 10 % per month) and no memory effect, which helps significantly in decreasing the maintenance required during charging and increasing its lifetime. Li-ion batteries are also more environmentally safe than NiCad batteries, which contain cadmium [50], which is toxic upon ingestion. They are also physically smaller in both weight and size, and have a higher specific power [51].

Disadvantages

Li-ion batteries do however have a lower charge/discharge cycle life when compared to NiCad batteries, but this is not a significant disadvantage when taking into account that the control station is not expected to be used frequently. They are also significantly higher in cost in comparison with NiCad and NiMH batteries; approximately 40% higher than NiCad batteries. These batteries are also prone to damage under excessive conditions, and as such, require protection circuitry to monitor and ensure their safety [52].

In conclusion, it was determined that the advantages in Li-ion batteries' performance and ease of use still outweighed the disadvantages of lower recharge lifetime and cost, and therefore were further investigated.

2.3.2. LITHIUM-ION POLYMER BATTERIES

Lithium-ion **Po**lymer (**Li-Po**) rechargeable batteries provide high power within a small-form package. Effectively, they are the same as Li-ion batteries, but have a slightly lower energy density, and a higher manufacturing cost by approximately 10-30% [53]. They are advantageous in that they are safer to use, and provide significantly higher discharge rates.

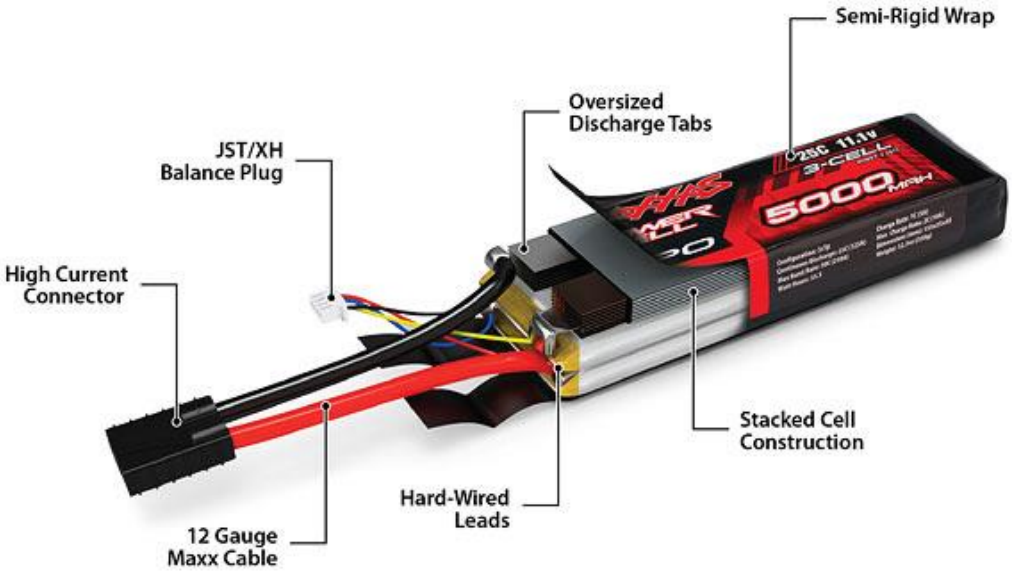

Figure 2-21 - Breakdown of a 3 Cell Lithium-Polymer Battery's Components [54]

These batteries typically come in a pouch with multiple cells contained within a flexible rectangular casing, as shown above in **Figure 2-21**, and can be shaped to fit their application. This makes them appealing for use in small, thin mobile devices, and can be found in many notebook computers, cell phones, and radio-controlled systems of today. These batteries include an integrated balance plug, which allows connection to each individual cell. This is used for functions such as cell voltage measurement as well as cell-balancing.

Fully charged Li-Po batteries have a cell voltage of 4.2 V, and 3.0 V when discharged. Cells must always be kept above approximately 3.0 V, or else they will become unable to accept a full charge again, and incapable of sustaining their voltage under load. Li-Po batteries must also never be overcharged above 4.2 V and failure to do so may lead to the extreme hazard of the battery exploding and catching fire [55]. Upon combustion, the battery cells release hydrogen fluoride gas [56], which when in contact with moisture, produces corrosive hydrofluoric acid. Defective Li-Po batteries can be identified by a swollen appearance, and should never be used if found in this state. These batteries are not immediately disposable and must be fully discharged before they are safe to be sent to a landfill [57]. Inherently, the batteries are also subject to strict transportation regulations when packaged in bulk.

While Li-Po batteries are safer than their Li-ion counterparts, a battery protection circuit should still be employed to maintain safe operation as well as preserving the battery health.

Just like Li-ion batteries, they have no memory effect, meaning they can be safely recharged without having to first be fully discharged and thus minimizing maintenance required.

2.3.3. BATTERY CHARGING

A battery charger restores energy into a rechargeable battery by forcing current through it.

The charge rate is denoted by C or C-rate [58]. This is measured in relation to the capacity of a battery for one hour. A C/2 rate indicates the battery will be fully recharged within 2 hours, whereas a 4 C rate means it will be recharged within 15 minutes.

Charge rates can be segregated into **slow** or **fast** charging:

- A **slow charge** [59] utilizes a charging current that is safe enough to be applied to a battery without the need for monitoring or charge termination methods. This is also known as trickle charging, and can continue to top up the battery even after being fully charged. Slow charging requires extensive amounts of time, and for NiMH batteries, can take up to 36 hours for a full recharge.
- Conversely, **fast charging** is defined as being approximately a 1 hour recharge. This comes with the drawback of requiring complex charging circuitry, which adds to higher component costs. This is however often offset by the significant advantage of being able to offer faster charging times, depending on the system's requirements.

For devices which require frequent and rapid recharging such as cordless tools, fast charging becomes very attractive for a competitive design in the market. Otherwise, a slow charge would become more favourable for its simplicity and lower costs.

2.3.3.1. Lithium-ion Battery Charging

The charging challenges related to Li-ion batteries are not only isolated to overcharging, but undercharging as well. Undercharging 1.2 percent below the battery's full charge voltage can result up to a 9 percent decrease in overall capacity [60]. Therefore designs should aim to charge to within 1 percent of the full capacity. Each cell can be charged to 4.20 V with a tolerance of ± 50 mV.

The charge cycle for a Li-ion battery can be split into four phases [61]:

1. A small **preconditioning charge** is performed when the battery is deeply discharged, applying approximately 10 % of the full current to the cell. This prevents overheating and damaging to the battery. This continues until the cells can safely receive the full current.
2. The charger switches to the **constant current (C-C)** phase, charging the battery until each cell reaches 4.1V.
3. A slow **constant voltage (C-V)** phase is then used to prevent overcharging the battery. During this phase, the current continues dropping until the battery is fully charged.
4. Finally, the charger enters a **standby mode** and continues to top up the battery each time it drops below a set threshold.

A graph of these four phases, with their respective current rates, and voltages over time, is shown on the following page in **Figure 2-22**.

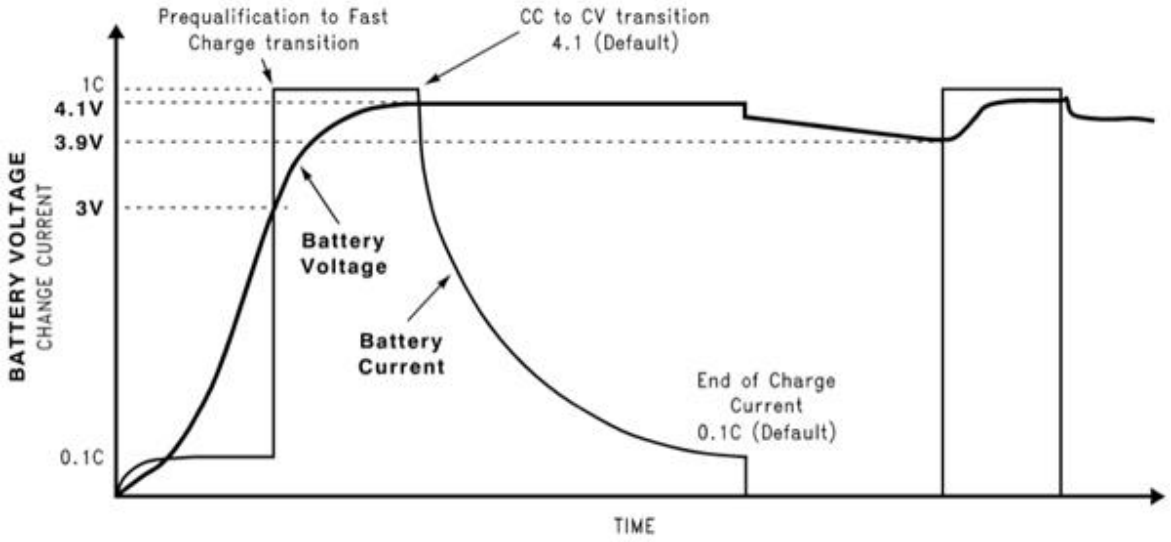

Figure 2-22 - Li-ion battery charging profile [60]

2.3.4. CONCLUDING REMARKS

The following conclusions were drawn from the findings in the battery section:

- Lithium-ion polymer batteries are a suitable candidate for use in the control station due to their high power to weight ratio, and being relatively smaller than their other battery counterparts. They are also simple to maintain with the lack of memory effects and low self-discharge over time, and are therefore more sustainable for use after long periods of storage. This is important to consider as it is expected that this system will not always be constantly used because disasters are generally not a daily occurrence.

- The aforementioned batteries are highly dangerous if not handled properly, and therefore battery protection circuitry must be employed to protect both the operator and the system.

- A combination of both slow charging and fast charging would be preferable for the control station's battery. Fast charging can recharge the battery to a suitable level before converting to a slow charge to top-up the battery. This process therefore becomes very similar to the charging profile described for the charging of lithium-ion batteries.

2.4. WIRELESS TECHNOLOGIES

The project requirements determined that the Scarab system must be tether-less and rely on wireless communications. Because the system was intended for use in USAR, it was vital to consider the interference challenges caused by the fallen structures and metal beams in the disaster zone. This section discusses some basic principles behind radio transmission relevant to this project, as well as technologies which could be used to implement a grid array network.

2.4.1. FREQUENCY BANDS

For the purpose of sending radio waves through a disaster area, where rubble and objects causing signal distortion are present, it becomes essential to identify an effective frequency for signal transmission.

A frequency band is a range, a spectrum, of radio frequencies which are allocated towards different purposes depending on their usefulness. Lower band frequencies transmit through building materials more effectively than higher band frequencies. The disadvantage of using lower band frequencies is a slower data transfer rate [62].

- **U**ltra **H**igh **F**requencies (**UHF**) are the frequencies which fall in between 300 MHz and 3 GHz. A study [62] showed that the advantage of using the UHF band with radio waves is that they travel further into rubble, without the presence of metallic meshes.
- The **L band** (1 to 2 GHz; IEEE) and **S band** (2 to 4 GHz; IEEE) do not penetrate through rubble as effectively as the UHF band system, but perform better in comparison when metallic meshes are present.

A highly generalized diagram comparing building penetration for different frequencies is illustrated below in **Figure 2-23**. This shows how low frequencies which belong in the UHF band are most effective.

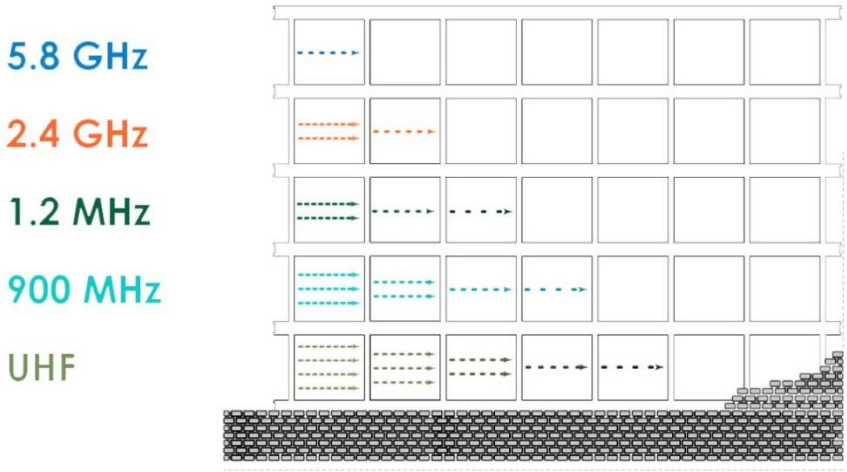

Figure 2-23 - Comparison of building penetration for different signal frequencies [63]

The South African Table of Frequency Allocations [64] lists all the radio frequencies ranging from 9 kHz to 1000 GHz. These frequencies are segregated into separate ranges, stating which radio-communication services are permitted for each one. The 900 MHz range of interest is reserved for cellular networks, and is considered illegal for use in other applications. This serves to prevent interference which results in a higher rate of dropped phone calls. Frequencies below are typically allocated towards amateur radio communications systems as well as for research, such as radio broadcasting for astronomy purposes.

2.4.2. MOBILE NETWORK POINTS

To increase the robustness of a communications network, it would be of benefit to use devices which could serve as mobile network points to in the USAR environment.

2.4.2.1. BreadCrumb

The BreadCrumb line of products [65] are man-wearable modules developed by Rajant Technologies used to create a mobile relay grid network. The project was initiated because of the events of 9/11, when large parts of the wireless infrastructure were crippled due to the terrorist attacks on the World Trade Centre. As implied by their name, these modules each act as a separate network point and collectively form a kinetic VPN mesh network to communicate with one another. This is illustrated below in **Figure 2-24**.

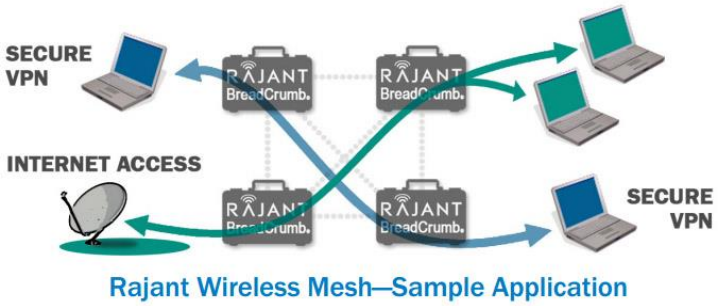

Figure 2-24 – Rajant Wireless Mesh Application [66]

The BreadCrumb ME2 [66] was developed following the events of the London Underground bombings in 2005, and designed with underground environments in mind. As such, they do not rely on cellular or Wi-Fi infrastructures and form their own network hotspots to communicate.

Later revisions have been developed since then. Shown below in **Figure 2-25** is the BreadCrumb ME4 [67]. It supports multiple radio configurations, including 900MHz and 5GHz, and can act as Wi-Fi access point, with data encryption. The module utilizes two transceivers and is battery powered.

Figure 2-25 - BreadCrumb® ME4 [67]

In USAR applications, these devices can be carried by rescue members in the team to not only relay data of one robotic unit, but multiple devices. This also provides the possibility of indicating each member's location on the map.

2.5. SENSORS

For the purpose of extending the capabilities of the operator control station, considerations were made to include low-profile sensors which would benefit the rescue team. It was envisioned that having global location sensors on the control station would be of most use in the disaster zone. Therefore GPS and magnetometer sensors were investigated.

2.5.1. GPS SENSORS

Global **P**ositioning **S**ystem (**GPS**) sensors aid in the USAR scenario where the rescue team can determine their position relative to an object of interest.

Effectiveness of these sensors is based on their tracking accuracy. Most GPS units have an accuracy of 15 m [68]. Influencing factors include the chipset used, the installed antenna, and the update rate. Update rates define how fast the GPS sensor refreshes its position. This becomes significant when measuring the speed and acceleration of a tracked object from the satellite's perspective. The standard update rate is 1 Hz.

GPS satellites transmit in in the UHF frequency band. Original GPS devices utilized two frequencies, dubbed L1 (1575.42 MHz), and L2 (1227.60 MHz). L2 is reserved for military use. These signals travel in a line of sight, and can pass through thin radio transparent objects, including glass and plastic. They will fail to perform when encountering solid objects such as brick walls. GPS cannot operate underwater as the water becomes a conductor which attenuates or reflects the signals. Therefore, GPS can only perform outdoors without the presence of a solid ceiling.

Wide **A**rea **A**ugmentation **S**ystem (**WAAS**) is a system of satellites and ground stations which provide a much higher degree of tracking accuracy [69]. This is achieved by using multiple reference stations which each receive satellite data and then provide corrections back to the master station, as illustrated below in **Figure 2-26**. Devices which use WAAS offer an accuracy of up to 3m. It should however be noted that WAAS satellite coverage is available only in North America.

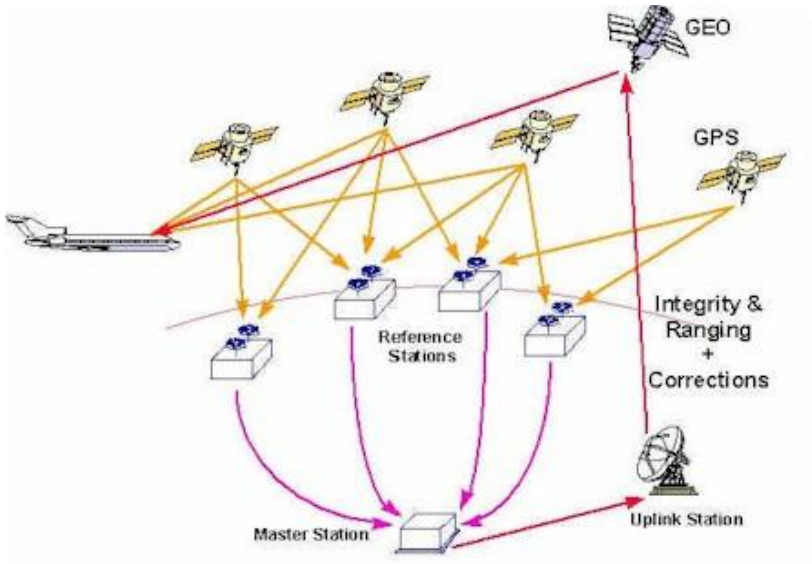

Figure 2-26 - Wide Area Augmentation System Elements and Data Flow [70]

2.5.2. MAGNETOMETER SENSORS

Magnetometer sensors [71] measure magnetic field strengths, and are typically used to measure low fields of less than 1 mT. They can measure both the strength and direction of a magnetic field. These sensors boast a wide array of applications, including searching for ferromagnetic materials underground and underwater, heart beat monitors, guiding systems, as well as electronic compasses. One of the most common methods that magnetometers use is the Hall Effect method. This works on the principle that a Hall Voltage can be detected across a thin metallic element, when the element is placed in a strong magnetic field perpendicular to the element's plane [72]. This is illustrated in **Figure 2-27** below.

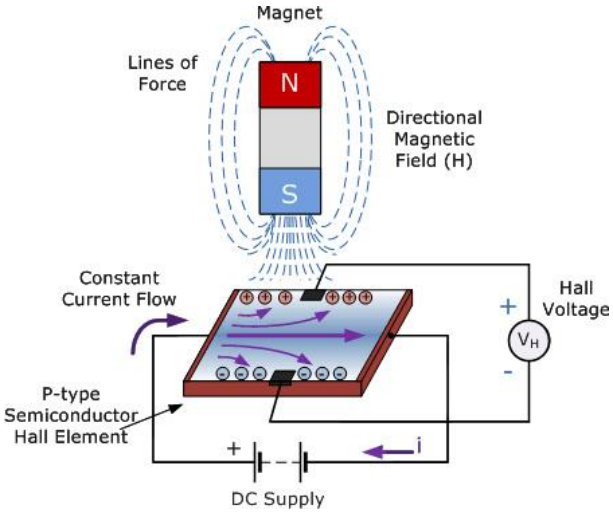

Figure 2-27 - Hall Effect on Element in Presence of Magnetic Field [73]

There are two main types of magnetometers [74]:

1. **Vector magnetometers** – measures the components of the magnetic field.
2. **Total field (scalar) magnetometers** – measures the magnitude of the magnetic field.

Vector magnetometers provide a higher degree of insight, but are highly susceptible to noise. In this regard, total field magnetometers perform better in applications which include the presence of moving ferromagnetic objects, such as a car. Otherwise, in the context of this project, a vector magnetometer would be more desirable for the use as a compass.

Magnetometer calibration is of vital importance, as without it, the data output from the device is essentially useless due to distortions from the immediate environment. In an ideal situation, plotted data from a perfectly calibrated magnetometer will form a spherical scatter plot, centered on the origin axis of the plot [75], as shown in **Figure 2-28**.

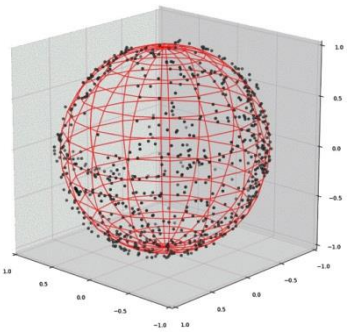

Figure 2-28 - Calibrated Magnetometer Sphere [90]

Data distortions are caused by the earth's magnetic field, and can be classified into **hard-iron** and **soft-iron** distortions.

1. **Hard-iron distortions** offset the ideal magnetometer plot from being centered on the origin. These are caused by objects in the surrounding environment which contribute to the existing magnetic field from the earth, such as magnets in electronic devices.
2. **Soft-iron distortions** cause the ideal magnetometer plot to become elliptical. It is different from hard-iron distortions in that it is not caused by objects which contribute to existing magnetic fields, but rather by objects which distort existing ones. This can be caused by the orientation and placement of metal objects in the environment.

2.6. CONCLUSIONS

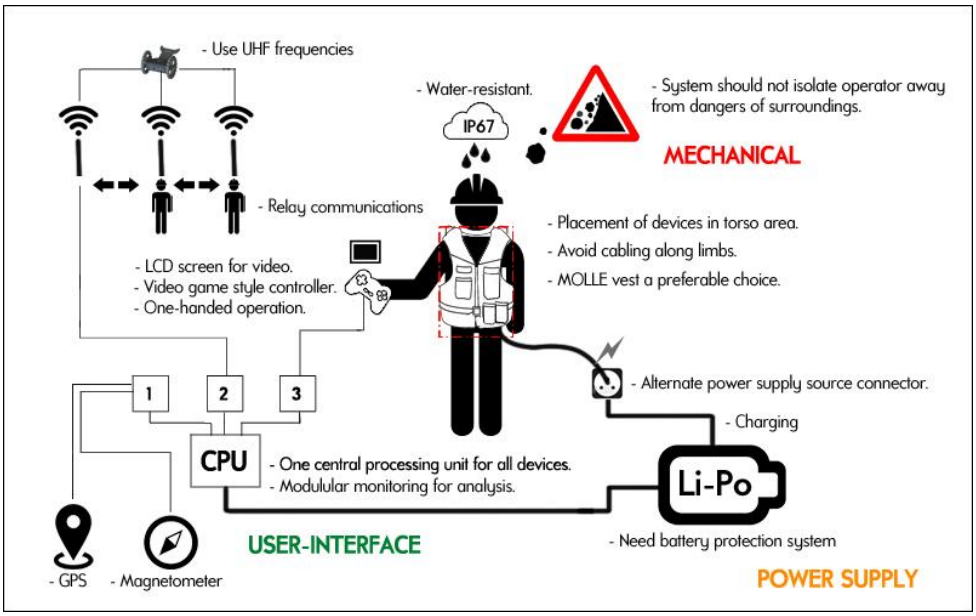

Figure 2-29 - Complete Hypothetical Operator Control Station System

From the findings in the background research, it was concluded that a man-wearable system can be separated into three distinct subsystems: the mechanical carrier, electronic user interface, and power supply. The complete Hypothetical Operator system is illustrated above in **Figure 2-29**.

- It was found that for existing man-wearable systems, there was a singular processing unit, which handled all the data processing as well as peripheral control, including radio transmission and external storage devices. The advantage of using such an approach is superior space economy and centralisation, which is a significant benefit to a man-wearable system. A principal concern is the safety of electronic components being worn on a moving human body. As such, proper circuit protection systems must be employed, and examples from the research have shown that the carrying shell should be designed around an IP67 rating for protection against water and dust.

- Design of the user interface should not make the robotic system's operator a burden to their team. It is therefore imperative to not isolate the operator's senses away from their surroundings, which is crucial for safety when working in hazardous disaster zones.

- A hand held device should be used for user control, as opposed to one that is attached to one of the person's limbs. The device itself should however be light-weight, compact and portable enough to be stored on the person's body and intuitive to use with minimal training.

- Li-Po batteries have a superior capacity and discharge rate compared to their counterparts, but require careful charging and come at a higher cost than NiCad and NiMH batteries. They also require battery protection circuitry which is crucial for their safe usage on a system that is to be worn on the rescue operator's back.

Drawing from these conclusions, the primary system specifications were created, and will be presented in the following chapter.

3. SYSTEM SPECIFICATIONS

Following on from the conclusions derived from the background research, a set of system specifications was created as a design guideline for the operator control station. These also served as benchmark comparison values when testing the final system.

This chapter begins by presenting the **Primary System Specifications** set for the operator control station. It then continues by listing the specification justifications for each value to substantiate their selection. Later subsystem chapters will be preceded with a separate set of specifications tailored specifically for the respective subsystem, and will be referred to as the **Subsystem Specifications**.

Table 3-1 below lists the primary specifications of the operator control station.

Table 3-1 - Primary System Specifications

No	Specification	Desired Value	Achieved Value
Physical Specifications			
1	Maximum control station mass	8 kg	☑ 7.2 kg
2	Transportation	Man-wearable	☑ Man-wearable
3	Water/dust resistant (IP54)	Yes	No
Communications Specifications			
4	Tethered/wireless	Wireless	☑ Wireless
5	Frequency	433 MHz	☑ 433 MHz
6	Range	30 m	☑ 38 m
Power Supply Specifications			
7	System supply voltage	12V, 5V, 3.3V	☑ 12 V, 5 V, 3.3 V
8	Battery protection system	Yes	☑ Yes
User Interface Specifications			
9	Interface	Tactile hand-held controller	☑ Yes
10	Display	LCD Screen	☑ Yes
11	On-screen display	Yes	☑ Yes
12	Audio	Yes	☑ Yes
13	Goggles	Yes	☑ Yes
14	Data logging	Yes	☑ Yes
Sensor Specifications			
15	Magnetic compass	Yes	☑ Yes
16	GPS	Yes	☑ Yes
17	Temperature sensors	Yes	☑ Yes
Robotic Platform Charging Specifications			
18	Minimum charge cycles	2	☑ 2
19	Supply voltage	20 V	☑ 20 V
20	Maximum platform charge rate	8 A	6.3 A
Control Station Charging Specifications			
21	Station battery charger	Yes	No
22	Supply source	Battery (on-field) Wall outlet (storage)	☑Battery (on-field) ☑Power supply (storage)

3.1. SPECIFICATION JUSTIFICATIONS

3.1.1. PHYSICAL SPECIFICATIONS

1. The control station should be as lightweight as possible, but still have enough capacity for the electronics and mechanical parts. There is no legislation which constitutes how much weight is permissible for an individual to carry, and so this must be done through an ergonomics risk assessment. There is however a NIOSH lifting equation [76] which recommends how much weight a person is allowed to lift in the workplace. Using this, a value of approximately 11.43 kg was calculated. Chiropractic doctors [77] recommend for the weight of children's backpacks to not exceed 15 % of their body weight. The average global body mass of an adult human as of this time in writing is 62 kg [78]. 15 % of this translates to 9.3 kg. Therefore, to ensure that the control station would be ergonomically comfortable to carry on an adult operator, 8 kg was used for the maximum total mass. Note that this includes the mass of the robotic platform.
2. As specified by the project requirements, the control station must be able to be worn by a person and transported as a mobile man-wearable system.
3. As stated in the background research, the system should be at least resistant against water and dust. This provides protection against the environmental conditions commonly encountered in the USAR environment. As such, an IP54 rating was assigned.

3.1.2. COMMUNICATIONS SPECIFICATIONS

4. Wireless communications was specified for the Scarab system as per the project requirements. The robotic platform is expected to encounter many obstacles whilst moving inside the void of a collapsed building. A tether becomes undesirable as it has a high likelihood on becoming entangled or caught, as well as bringing additional weight for the robotic platform's motors to handle. It also requires two operators – one to control the robot, and one to handle the tether; increasing the workforce required.
5. The disaster zone presents a very challenging situation for RF communication where interference is present not only from the collapsed structures, but also from the other RF devices which may be in the field. Therefore a UHF band of 433 MHz was specified by G. Knox for the sensor payload's RF transceiver to provide adequate building penetration at a feasible data transfer rate. Accordingly, the control station's matching RF transceiver was specified to match the same frequency to establish communications.
6. It was documented [3] that most of the voids at the Ground Zero rescue sites were 1 m in diameter. For a more extensive use of wireless communications, 30 m was specified for the wireless range. This was convenient for testing within the size of RARL's Duncan McMillan building and is also the specified indoor range of the Recon Scout Throwbot.

3.1.3. POWER SUPPLY SPECIFICATIONS

7. 12 V, 5 V, and 3.3 V are the voltages required by the peripheral devices on the control station. Additional supporting electronics were also specified to be designed by these values.
8. As discovered in the background research, Li-Po batteries are known for their volatile behaviour should they undergo any failure conditions such as overvoltage, or temperature issues, and are prone to explode if handled improperly. The mental picture of this hazard scales considerably when keeping in mind that the control station's battery is stored adjacent to the operator's body. This introduces a scenario where the operator performs the mission knowing they are carrying a potential explosive on their back, which would negatively affect their mental performance. Therefore a battery protection system is critical to protect both the battery, and the operator; body and mind.

3.1.4. USER INTERFACE SPECIFICATIONS

9. From the background research, it was determined that a hand-held controller would be the best portable user interface for a mobile robot.
10. A LCD screen was specified to allow the operator to view the incoming camera feed from the robotic platform's camera.
11. An on-screen-display is highly beneficial for viewing the sensor data from the sensor payload on top of the incoming video feed. This minimises the physical fidelity required from the user interface, and centralises all the appropriate information into one place for the operator. It also adds a high element of customization to the user interface.
12. Because the robotic platform's sensor payload has an in-built microphone, the control station naturally should include the ability to receive and listen to the audio from it.
13. One challenge with using LCD screens in external environments is that they reflect sunlight, rendering them difficult to view. Additionally, dirt and dust becomes an issue when working in disaster zones. It was therefore decided that using an optional pair of FPV goggles would provide the best form of visibility as it provides vision without being obstructed by the environment.
14. Data logging is essential on the control station as it provides a means for the mission data to be recorded and logged for future analysis.

3.1.5. SENSOR SPECIFICATIONS

15. A magnetometer was specified for the control station to provide compass functionality. This helps the operator to find their location relative to the robotic platform's and allows faster location of any discovered survivors/bodies, as well as recovering the robotic platform.
16. For similar reasons to the magnetometer, a GPS was specified for the system. This provides coordinate data which becomes of significant use in the event the operator becomes lost or requires additional aid to be deployed at their specific location.
17. Temperature sensors were specified to provide any over-temperature warnings, as well as a general temperature monitor for each of the control station's modules.

3.1.6. ROBOTIC PLATFORM CHARGING SPECIFICATIONS

18. It was envisioned that the control station and robotic platform would be fully charged by the time they arrived at the disaster zone. Specifying two charge cycles allows for three deployments in total of the robotic platform into the void.
19. To effectively charge the robotic platform's battery, G. Knox's on-board charging circuitry requires at least an 18 V supply, but preferably 19 V - 20 V for sustainable performance. Therefore a 20 V power rail was specified to satisfy this requirement.
20. The maximum charge rate for the robotic platform's charging circuit board was specified to be 8 A at the time of design. Therefore the control station was specified to include a power rail which could satisfy this requirement.

3.1.7. CONTROL STATION CHARGING SPECIFICATIONS

21. Because the control station is to be powered off a battery, it would be highly useful to include charging circuitry for it inside to allow charging off an external power supply during storage.
22. Whilst not in the disaster zone and in storage, it would be of use for the control station to be powered off an external supply, such as a wall outlet instead of the battery.

4. SYSTEM OVERVIEW

The complete operator control station is shown below. It is a man-wearable system which allows the operator to wirelessly communicate with the Scarab robotic platform.

The operator control station was subdivided into four main subsystems which were allocated their own predefined functions. Each subsystem was designed according to their own set of specifications, and are each illustrated below in **Figure 4-1** according their location in the control station.

Figure 4-1 - System Overview of Operator Control Station

1. MECHANICAL CHASSIS

The mechanical chassis is the housing system for the control station's electronics, and acts as a man-wearable docking station for the robotic platform. It is worn on the operator's by attaching it to a tactical vest by using three support ribs inserted into a grid at the back. The operator can mount the robotic platform using the chassis' mounting brackets, and a charge outlet at the bottom allows a power cable to connect from the station to the robotic platform for charging. Control panels are located externally for user interaction with the system's basic controls.

2. CONTROL STATION ELECTRONICS

The control station electronics provide sensor monitoring and data processing functionality to the control station. It primarily uses a custom designed 168 MHz STM32F407VG embedded microprocessor PCB which includes electronics for the on-screen display (OSD) and a RS-232 transmitter for data communication with the OCU. Included are wireless transceivers and a video

receiver required to establish data and video communication with the robotic platform. GPS sensors are included to provide the operator's co-ordinate data in the field. Temperature monitoring is also incorporated to provide warning systems as well as overall analysis of the internal electronics. A pair of Fat Shark Dominator FPV goggles is included as an alternative means to view the video alongside the OCU's LCD screen.

3. OPERATOR CONTROL UNIT

The **O**perator **C**ontrol **U**nit (**OCU**) serves as the primary interface between the operator and the control station. It is a hand-held controller which features a LCD screen for displaying the video, and joysticks and buttons for tactile user inputs, making the OCU suitable for use with safety gloves. Included also is a magnetometer to allow the unit to act as a compass. The OCU is separate from the control station chassis, and is connected via a 2 m data cable.

4. POWER SUPPLY

The power supply encompasses the control station's battery and its accompanying monitoring and management circuitry. A power distribution board is included supply power to the rest of the system as well as the charging circuitry on the robotic platform. A charger is also made available on the control station for charging the station's battery when off-field and in storage.

SUMMARY

A system overview of each of the primary subsystems was presented. The following four chapters will discuss each of the subsystems described above, starting with the mechanical chassis.

5. MECHANICAL CHASSIS

Figure 5-1 - Control Station Mechanical Chassis

Design of the mechanical chassis prioritised keeping the layout intuitive and easy to maintain. **Figure 5-1** above shows the final mechanical assembly. During development, a mannequin was used to test the man-wearability of the chassis and represent the Hypothetical Operator. It also provided a safer testing platform for the internal electronics. This is illustrated below in **Figure 5-2**.

Figure 5-2 - Mechanical Chassis Worn on Mannequin

This chapter will provide a walkthrough through the complete design process and development of the mechanical chassis, and provide discussion into each separate module. It begins by introducing the subsystem justifications before moving onto the conceptual designs.

CHAPTER 5: Mechanical Design

5.1. SUBSYSTEM SPECIFICATIONS

Subsystem specifications were important for ensuring that the mechanical chassis was designed in accordance to the requirements set by the system specifications.

Presented below are the **Subsystem Specifications** for the control station electronics. Values which are denoted with a " * " can be referred back to in the **Primary System Specifications**.

Followed thereafter are the **Subsystem Specification Justifications** which can be referred to for reviewing each set criteria.

Table 5-1 - Mechanical Chassis Subsystem Specifications

No	Specification	Value
Physical Specifications		
*	Maximum Mass	8 kg
1	Maximum Physical Dimensions	500 x 500 x 500 mm
*	Transportation	Man-Wearable
2	Robotic Platform Mass	3 kg
3	Robotic Platform Wheel Dimensions	200 mm diameter x 50 mm thickness
4	Robotic Platform Size	Determined by CAD model
Functional Specifications		
5	Robotic Platforms Carried	1
*	Water/Dust Resistant	Yes

5.1.1. SUBSYSTEM SPECIFICATION JUSTIFICATIONS

5.1.1.1. Physical Specifications

1. The maximum physical dimensions were chosen to be 500 x 500 x 500 mm. This was to accommodate for the smaller working space of the USAR environment. Because the control station is a man-wearable system, the operator should be able to move around in confined spaces without being hindered. To represent an allowable space, the minimum door space indicated by **S**outh **A**frican **B**ureau of **S**tandards (**SABS**) was used [79] which dictates a minimum door width of 750 mm for a passage width of 1200 mm. The standard width of the human body from the chest to back is approximately 241 mm [80]. Therefore to account for the case of a person standing in a doorway while wearing the system, 500 mm was used.
2. During the time of design, T. Mathew specified the robotic platform's mass to be 3 kg.
3. There was no set wheel size at the start of design, as the size of the final wheels was dependent on the results of T. Mathew's testing of the robotic platform. Therefore a 200 mm diameter and a 50 mm thickness diameter was recommended, with the larger size able to accommodate for larger wheels in the future.

5.1.1.2. Functional Specifications

4. The control station would be designed according to the 3D CAD model of the robotic platform supplied by T. Mathew.
5. It was decided by the Scarab team that the ability to carry one platform at any given time would be sufficient for the first generation of the control station.

5.2. CONCEPTUAL DESIGN

Conceptual designs of the control station were made to provide insight on the system before advancing towards the final design. This phase of the project was an open task as the control station's chassis mounting system was reliant on the robotic platform's body and shape, which was yet to be finalised, but was tending towards one very much like the Recon Throwbot's. Therefore concepts revolved around the idea of a system upon which the operator could store or mount a two-wheeled robot with a hammerhead shape. Of vital importance was the ability to equip it as a man-wearable system. This focussed on being able to be operated by a single person, and prioritised on quick and intuitive deployment of the robotic platform.

The section will explore three concepts, and will compare and evaluate each before concluding by selecting the most suitable candidate which was used for the detailed design.

5.2.1. THE RUCKSACK DESIGN

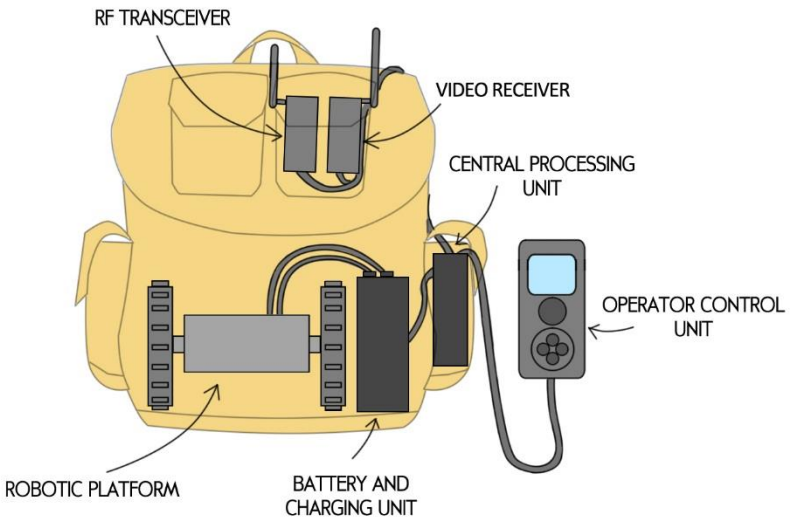

Figure 5-3 - Rucksack Concept Design

By far the most straightforward design is the idea of the operator carrying the robotic platform inside a weatherproof rucksack, as shown above in **Figure 5-3**. This would also contain the battery and necessary charging electronics. A hand-held controller would be used as the OCU, and can be strapped onto a belt.

This system is advantageous for its simplicity and modularity, as each piece of electronics can be treated as an attachable accessory. It does however depend highly on the robotic platform's size, and the rucksack may have to be custom-tailored as a result, which can become problematic due to the weatherproofing required. Another issue is the cumbersome deployment process. The operator must always take off the rucksack, open it, before taking out the platform to be deployed. Additionally, the platform may have to be cleaned before placing it back into the rucksack where the sensitive electronics are located; a task undesirable for efficient retrieval and transport.

5.2.2. THE BELT-STRAP DESIGN

This design minimizes the space required on the operator's body by the robotic platform onto a belt. This makes deployment very simple as all the operator would need to do is route the belt through a slot located on the platform before buckling it back onto their torso or posterior. The control station's battery and electronics would all be located in rugged modules hooked and attached to the belt. A hand-held controller would be used as the OCU. **Figure 5-4** on the following page illustrates this concept.

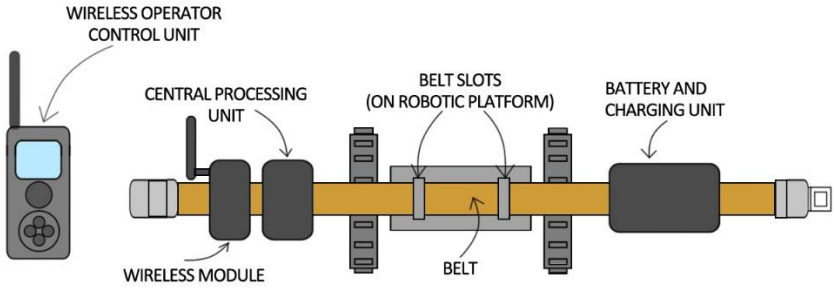

Figure 5-4 - Belt-Strap Concept Design

The primary strength of the system is that it is low-cost and light weight, as well as offering quick and simple deployment without the worries of having to deal with the robotic platform's cleanliness. It does however depend on the robotic platform's body to include a slot for the belt, and may introduce conflicting interests in terms of weight and functional design. Another criticism is that the size of the electronics present may provide hindrance around the operator's torso or waist. The overall weight may also require extra harnesses around the body for support, detracting away from the system simplicity.

5.2.3. THE VEST-DOCK DESIGN

This design revolves around the idea of creating a weatherproof "docking station" for the robotic platform. It centralises the entire system onto the operator's back using a MOLLE-vest. All electronics and the battery would be mounted inside the protective chassis, and the operator can place the robot onto the station using mounting brackets. The robotic platform is docked externally, and is therefore safely isolated away from the electronics. This is shown in **Figure 5-5**.

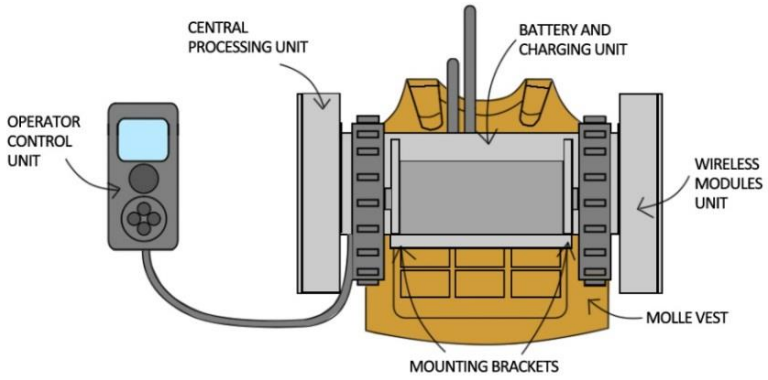

Figure 5-5 - Vest-Docking Station Concept Design

This design is ideal for being an all-in-one solution, as well as not requiring any changes to the robotic platform to function. One significant disadvantage in retrospect is that it becomes dependent on the size and shape of the robotic platform. This may lead it to become substantially large and introduce additional weight. In comparison to the other concepts, it is also the most complex, and requires additional manufacturing and parts.

5.2.4. SELECTED CONCEPT DESIGN

After evaluating all three concepts, the **Vest-Dock Design** was chosen. Functionally, and experimentally, it provided the highest configurability and expandability. It offered the fastest theoretical deployment times as well as being the least obtrusive system concept for being worn on a person's body as it never needed to be removed during operation. Mechanically, it avoided custom-tailoring of third party products like the rucksack and belts to fit on different body physiques and could be designed to fit on a standard MOLLE vest. Electronically, the internal modules could be adapted for use in future generations of the system, making for an ideal development platform.

5.3. DETAILED MECHANICAL OVERVIEW

Following from the concept chosen, a docking station layout was used for the detailed design. The final design's exploded assembly is shown below in **Figure 5-6**. The chassis was designed with four separate "boxes" to segregate the main functions of the control station. This aimed to make assembly and maintenance easier, and also providing an intuitive overview of the complete system flow. SolidWorks 3D CAD design software package was used to design all the parts.

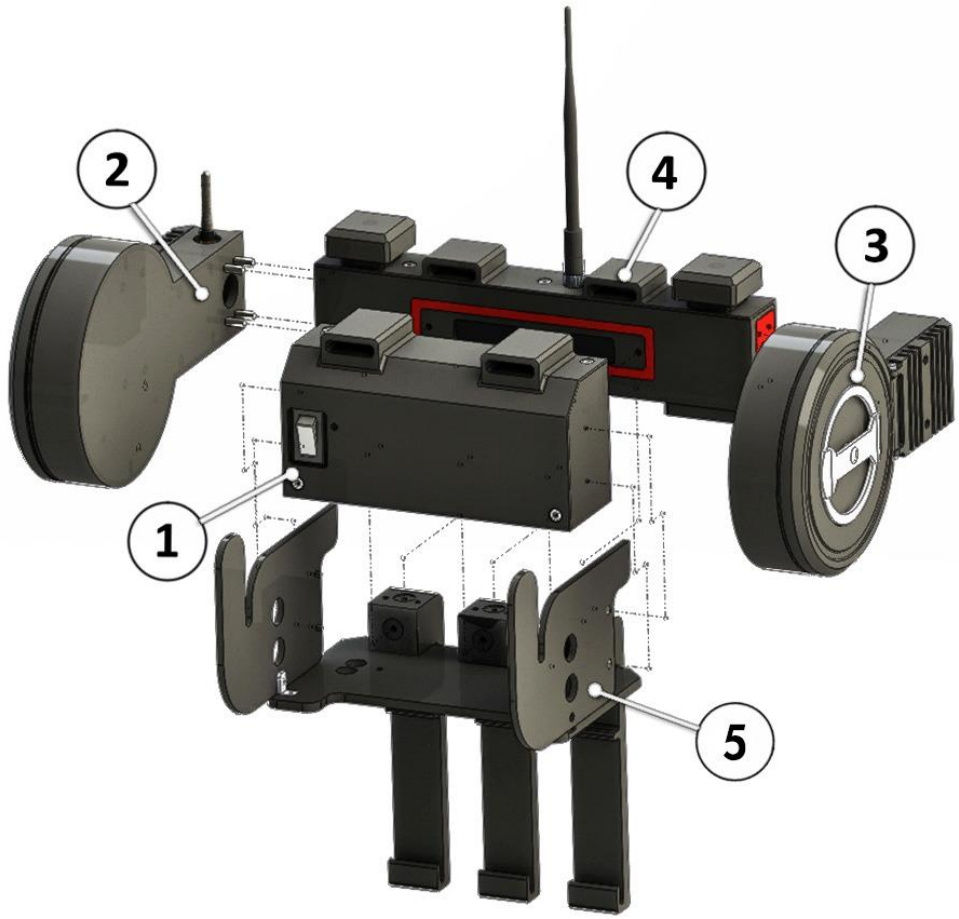

BOX	FUNCTION
1. Power Box	Contains the battery, and all the battery management and charging circuitry.
2. Computing Box	Contains all the electronics required for processing the controls station's data as well as the devices for data logging.
3. Video Receiver Box	Contains the control station's video receiver.
4. Back Box	Contains the power distribution board, and provides a routing channel for all the system's wires from one box to the other.
5. Base and Supports	Supplies the main base and rib mounting supports to the vest. Also includes the mounting brackets for the robotic platform.

Figure 5-6 - Exploded Assembly of Control Station Chassis and Functions Described

Each box is connected to each other using four M5 stainless steel bolts. This was to provide adequate support throughout the entire structure with minimal complexity and ease of assembly. A single opening is made for each box for cable routing between adjacent units. To facilitate waterproofing, 3 mm wide grooves were included along the edges for seating a rubber seal.

Shown below in **Figure 5-7** are the overall dimensions of the mechanical chassis. This illustrates how the chassis can fit within the 500 x 500 x 500 mm space set by the subsystem specifications.

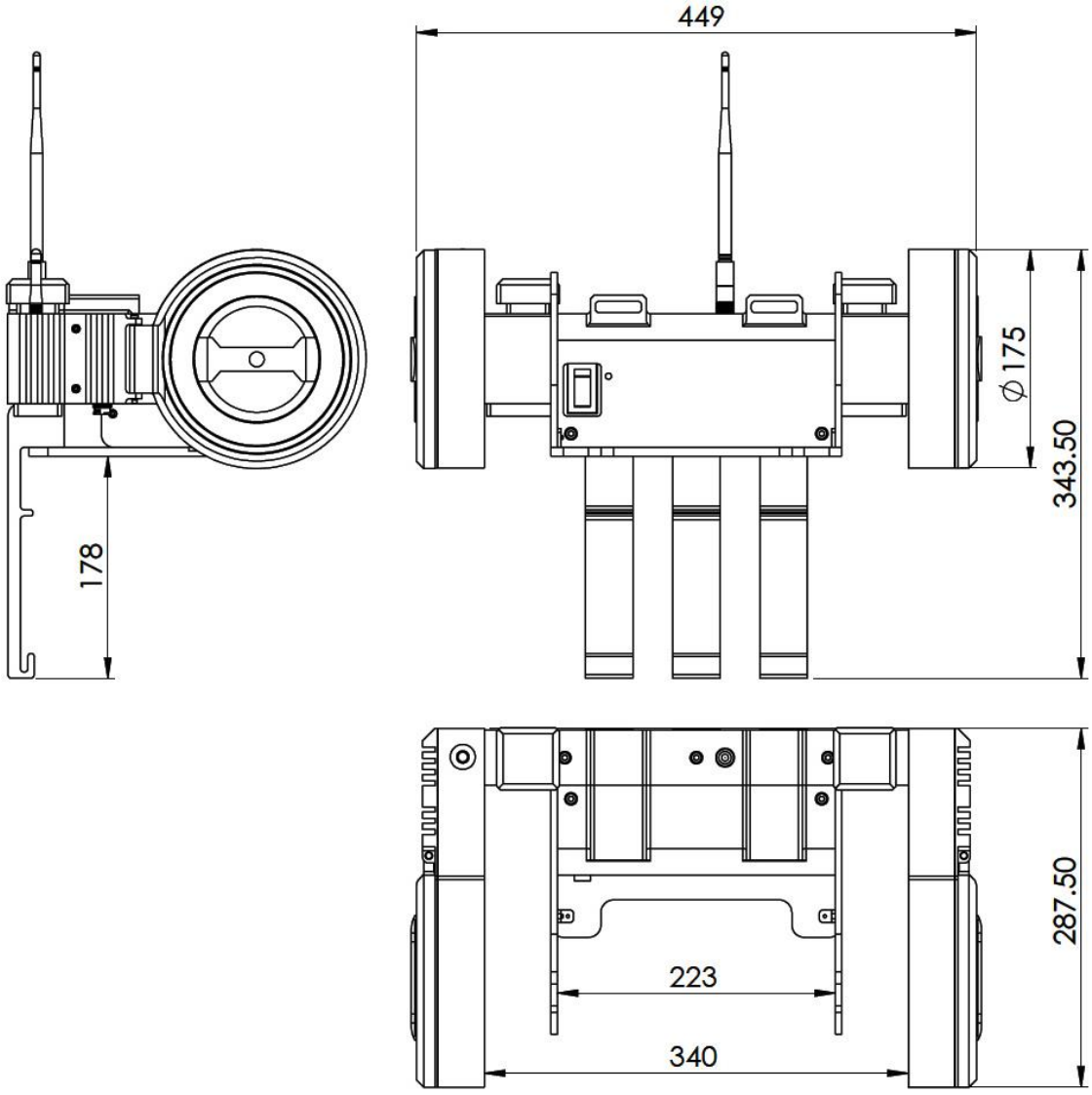

Figure 5-7 - Overall Dimensions of Mechanical Chassis

5.3.1. MATERIAL SELECTION

For a man-wearable system, material selection emphasised on being both lightweight and resistant towards environmental conditions during operation out in the field.

HDPE was therefore selected for the chassis. This material has a high strength to density ratio, introducing good abrasion and impact resistance properties, which made it appealing for a portable rugged system. Importantly, it is also non-conductive, making it ideal for housing electronics.

Aluminium was selected for the metal shafts and the mounting bracket supports. This was chosen for its high strength-to-weight ratio and its ease of machining. Its high corrosion resistance also motivated its inclusion in a weatherproof system for use in USAR.

5.3.2. MANUFACTURE

All parts were manufactured in UCT's Mechanical Engineering Workshop. HDPE parts were made using a CNC mill, and the aluminium parts were made primarily using the available lathes and milling machines. The complete array of manufactured parts is shown below in **Figure 5-8**.

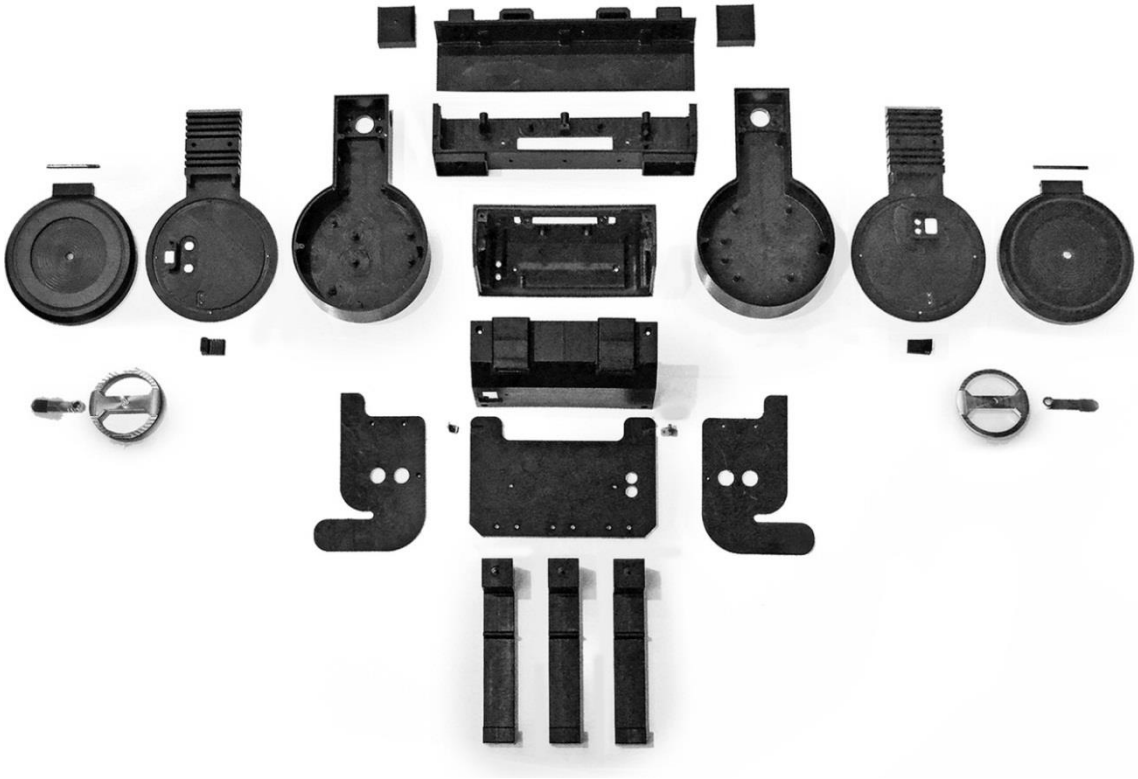

Figure 5-8 - Array of Completed Manufactured Parts

Custom-made Perspex pieces and rubber seals were also included, which were fabricated using the UCT Architecture laser cutter.

The following sections will provide a detailed overview of each box of the chassis, as well as the supporting parts responsible for allowing the mechanical chassis to become a man-wearable system.

5.4. POWER BOX

Design of the Power Box aimed to create an accessible housing which could store the large Li-Po battery along with its battery management and charging circuitry. The exploded assembly diagram is shown below in **Figure 5-9**.

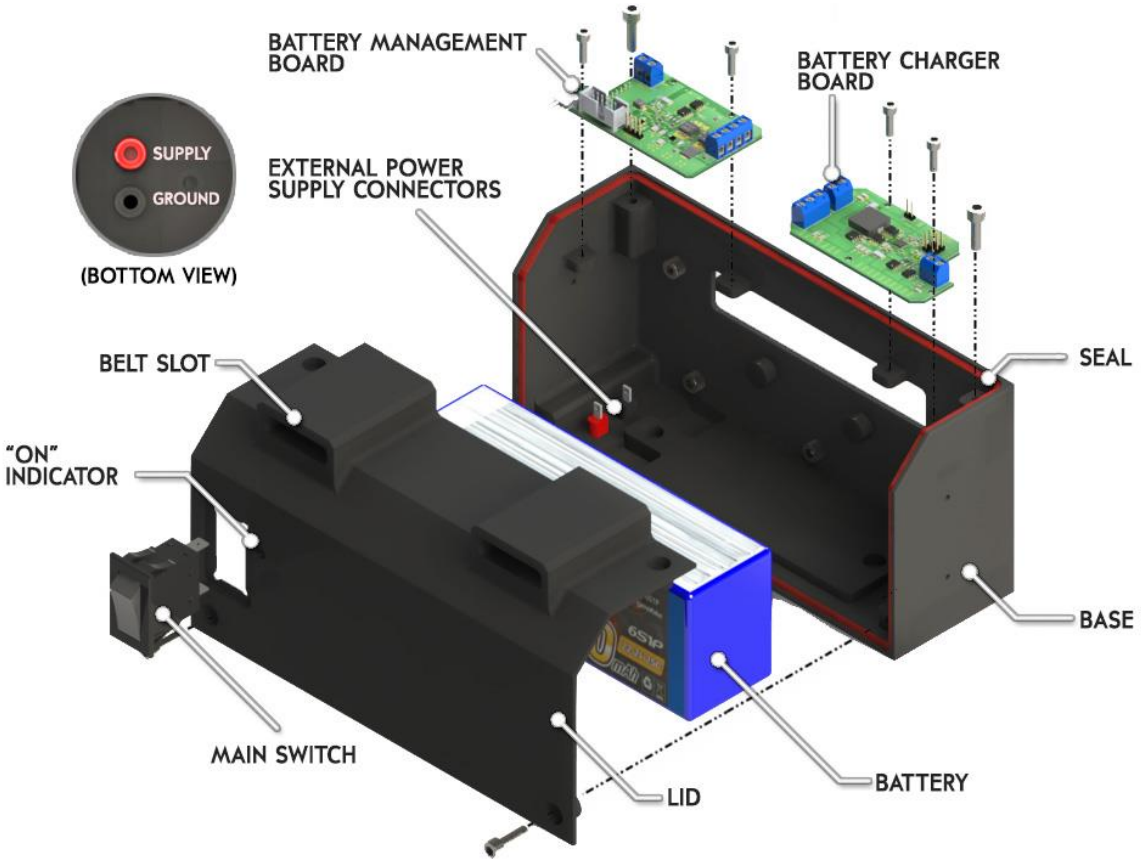

Figure 5-9 - Exploded Assembly of Power Box

5.4.1. ELECTRONIC MOUNTS

To keep the battery fixed in the box, industrial Velcro strips were used, which aimed to allow easy detachment and reattachment during maintenance. Floating M3 mounting supports were provided to locate both the battery management and battery charger board directly above the battery, which was crucial for the thermistor temperature monitoring.

Two banana plug jacks were included on the bottom of the box. These are responsible for connecting to an external power supply during charging. These were chosen to be red for power and black for ground in accordance to standard safety practices. An IP67-rated 15 A switch was also included as the main system switch and an "O" indicator was provided on the outside on the box to indicate the "ON" side of the switch.

5.4.2. MATERIAL CHANGE

During manufacturing of the Power Box, issues were encountered with internal stresses of the HDPE material, which caused shape deformations along the bottom of the structure. This was ultimately remedied by remanufacturing the part using a higher density nylon material, but at the cost of an 18.5% increase in the weight of the part.

5.5. COMPUTING BOX

During design of the chassis, it became apparent that the user should be able to interact with the system's basic controls without having to remove any parts to access the devices. Hence, both the Computing Box and Video Receiver Box were designed to include external control panels for this purpose. A lid cover was also designed to provide additional protection of the control panel from rain and dust.

As such, both boxes utilize three main layers, those being the base to contain the electronics, the interactive control panel, and the protective lid. These are illustrated below in **Figure 5-10** for the Computing Box.

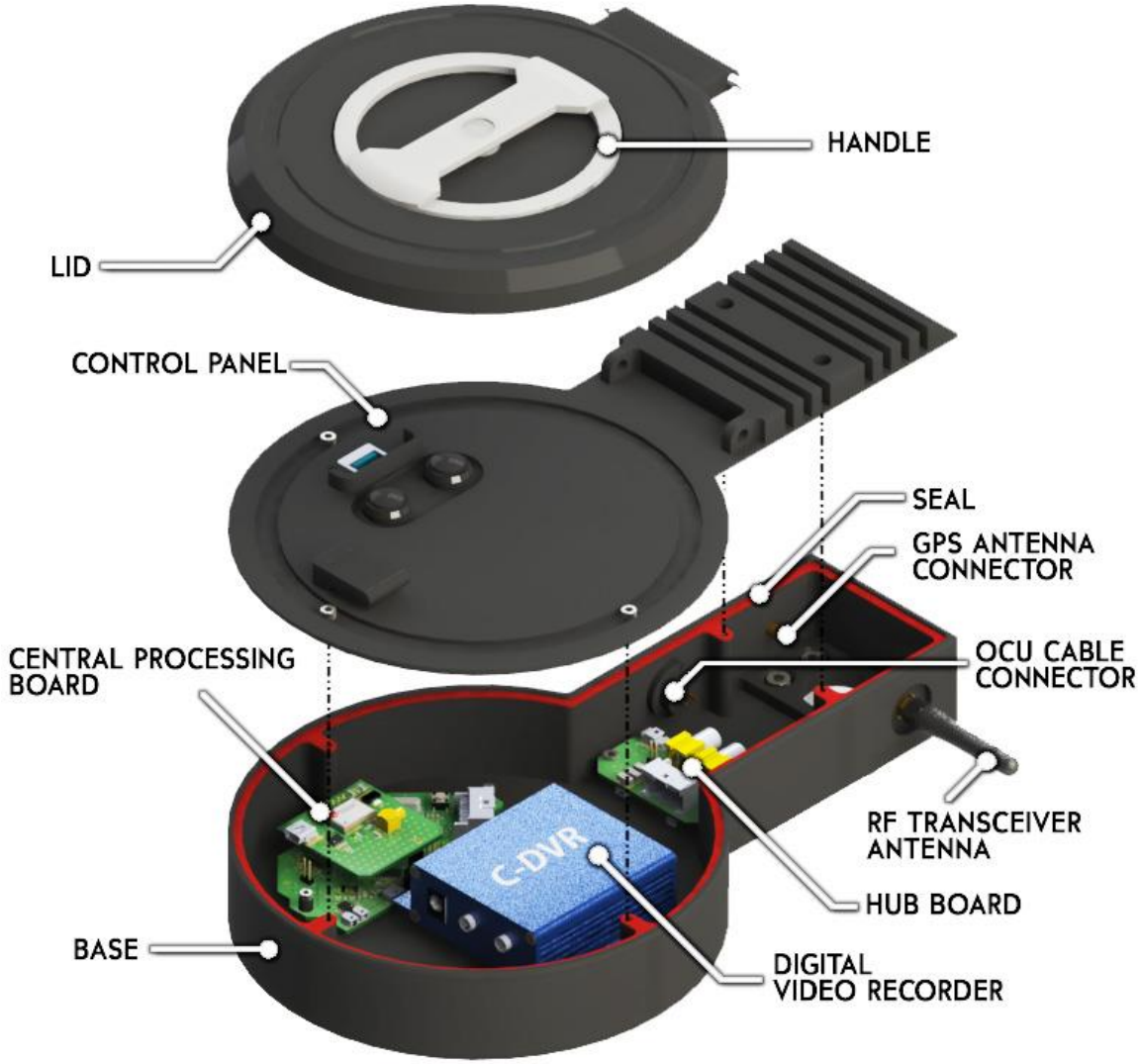

Figure 5-10 - Computing Box Layers

5.5.1. ELECTRONIC MOUNTS

All devices were given M3 mounting supports. On the bottom of the box, a MCX connector was provided for the GPS antenna. An IP67 6-core female connector is also provided for the OCU cable. On top a SMA connector was located for connecting the RF transceiver's antenna.

5.5.2. CONTROL PANEL

The Computing Box's control panel includes two IP67-rated buttons for the following functions:

- **Hardware-Reset:** In the event that the provided software reset function was not adequate for the Central Processing Board's STM32F407VG microprocessor, this button could be used to perform a direct hardware reset.
- **Low-Power Mode:** The operator can set the operator station to be in low-power mode to conserve energy and battery life. In this mode, only the 3.3 V supply rail is left online. This leaves the main microprocessor, the temperature sensors, and the battery monitoring and protection systems online.

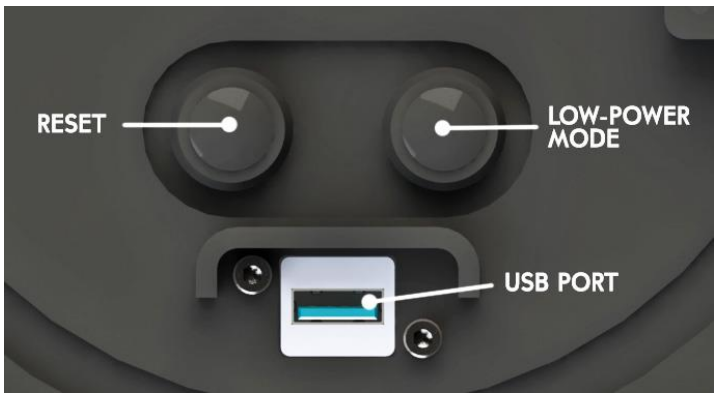

Figure 5-11 - Computing Box Control Panel

An IP67-rated USB port was made available for the purpose of inserting a mini USB flash drive. This was to provide additional data logging alongside the digital video recorder. More information on this module can be found in **Chapter 6. Control Station Electronics**.

A small overhead cover was provided above the USB port for extra protection against any liquids escaping past the cover lid.

5.5.3. LID

The lid was based on a simple hinge system which uses a 4 mm diameter shaft and circlips to be secured. To lock the lid in a closed position a pivoting latch system was used which is controlled by rotating an aluminium handle on the outside. This is illustrated below in **Figure 5-12**.

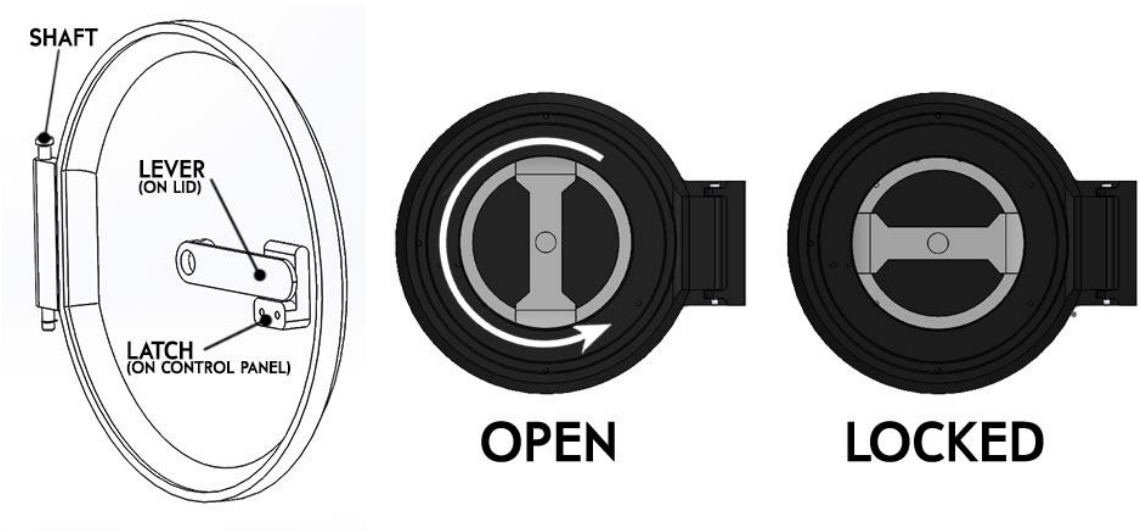

Figure 5-12 - Lid and Latch Mechanism

5.6. VIDEO RECEIVER BOX

This box was designed to be the same shape as the Computing Box to keep the chassis layout symmetrical as well as providing enough space for the video receiver. The same lid and latching system was used to provide additional weatherproofing. The complete assembly diagram is shown below in **Figure 5-13**:

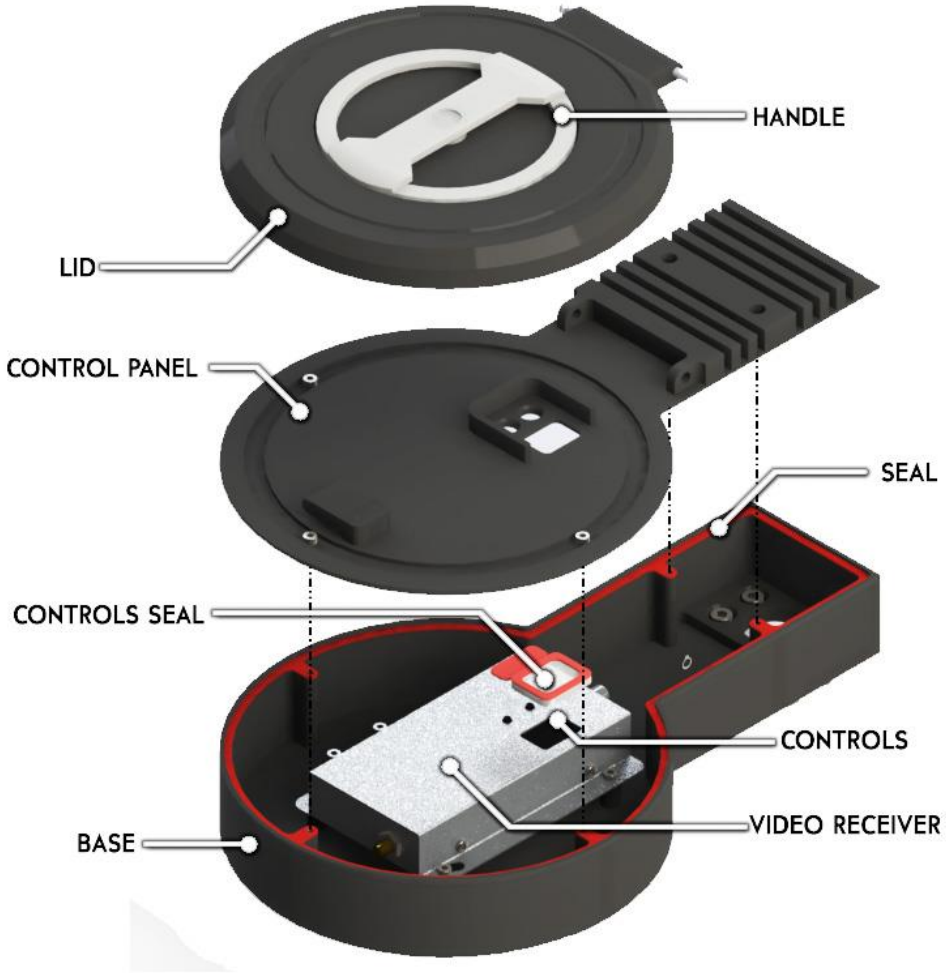

Figure 5-13 - Exploded Assembly of Video Receiver Box

5.6.1. ELECTRONIC MOUNTS

M3 mounting supports were provided for the video receiver and a 5 mm clearance gap was located underneath for routing the antenna's extension cable. During design it was decided to locate the antenna externally on the Back Box. This was to prevent collisions of it with any hanging obstacles, or the robotic platform itself during the docking process. For similar reasons, the original 1.3 GHz antenna was also replaced with a more flexible unit of the same frequency.

5.6.2. CONTROL PANEL

The video receiver's channel LED display can be viewed through a protective 3 mm Perspex screen. Two holes were made to allow access to the channel selector buttons. For protection against ingress, a rubber seal was placed between the holes and the buttons.

5.7. BACK BOX

The Back Box initially began as a simple hub part to interconnect all the other boxes together. It later developed into a holder for electronics which could not fit elsewhere, and also acted as the chassis' ventilation outlet. The exploded assembly is shown below:

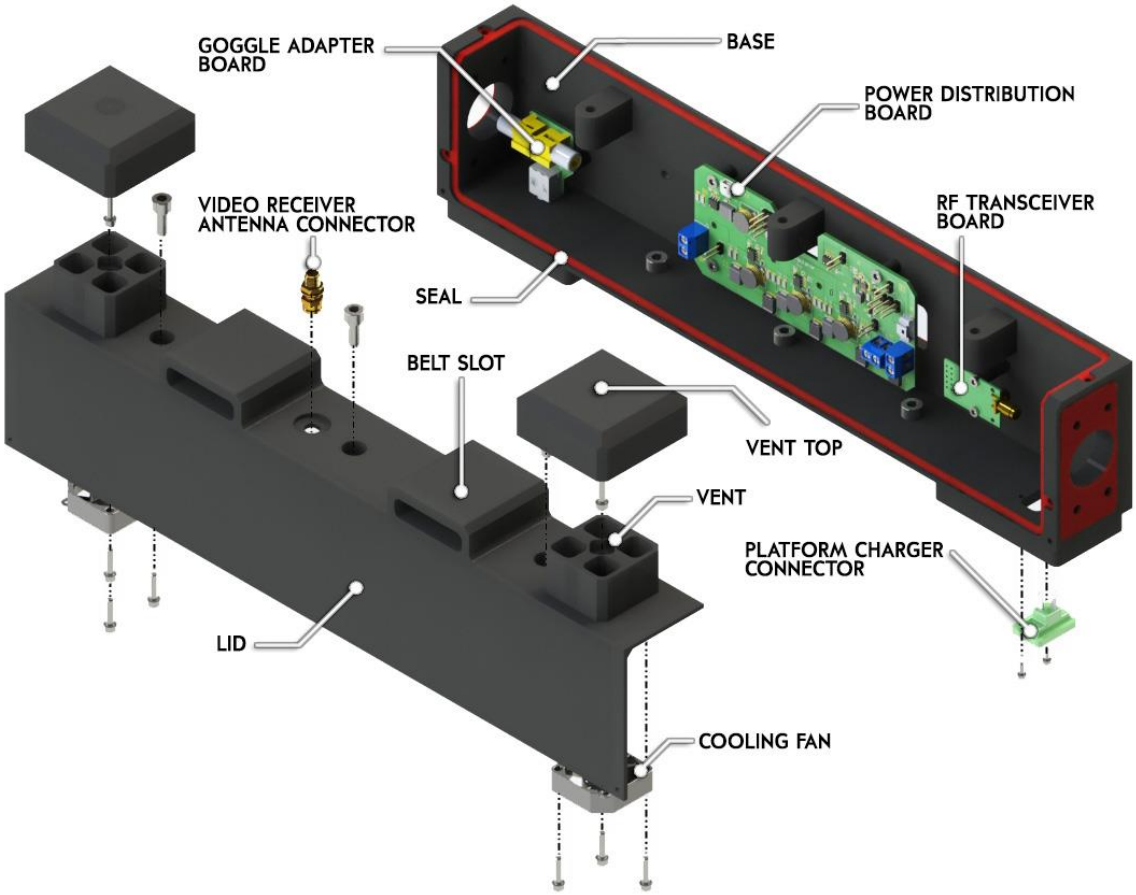

Figure 5-14 - Back Box Exploded Assembly Diagram

5.7.1. ELECTRONIC MOUNTS

M3 and M2 mounting supports were provided for mounting the various PCBs in the box. 8 mm clearances between the PCBs and the back wall allow for cable routing and management. The video receiver's antenna is located on top is connected using a SMA female connector on top.

The control station's robotic platform charging connector is located at the bottom right of the box. This allows the operator to connect to the robotic platform using a two-wire power cable before initiating charging via the user interface. Similarly, the adapter board for the FPV goggles is located on the bottom right of the box. Both the charger and goggle connectors were given protective rims to prevent contact with any liquids or dust coming from above or the sides.

5.7.2. VENTILATION AND COOLING

To provide ventilation to the control station, vents on each of side the box allows airflow between the internal system and the external environment. These were designed with a removable cap system to weatherproof the air vents. A cross section of the system and the resulting air flow can be seen below in **Figure 5-15**.

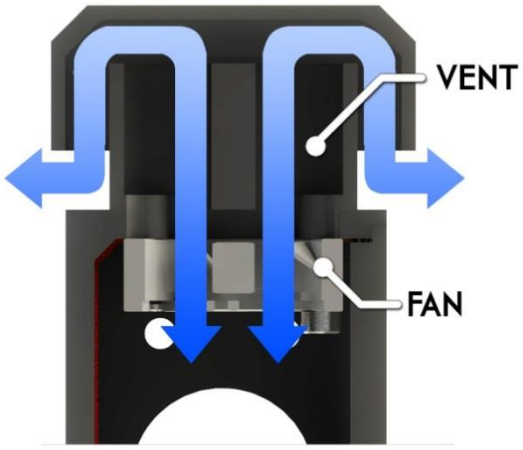

Figure 5-15 - Cross-section of Back Box Vent Showing Allowed Airflow Path

Two Sunon 3.5 CFM 30 mm diameter fans were incorporated for increasing the amount of air flow through the vents. They were configured in a push-pull setup – with one fan pulling air from the external environment, and the other pushing the heated air back out. This is illustrated below in **Figure 5-16:**

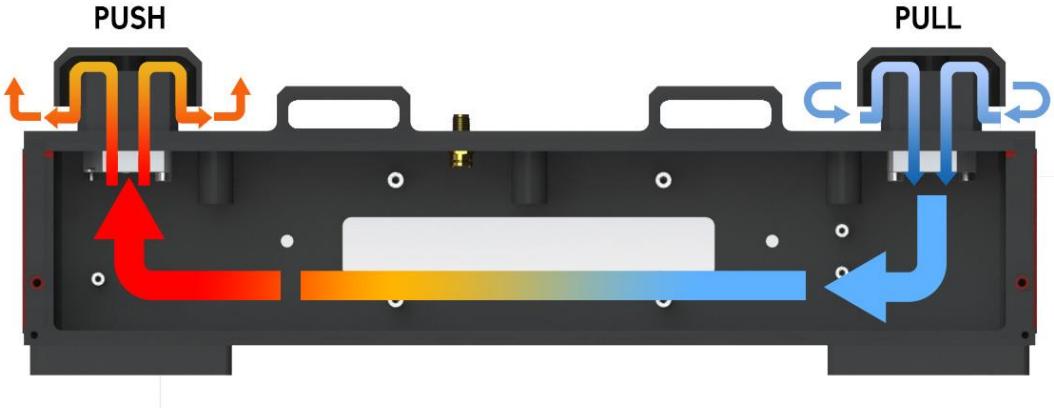

Figure 5-16 - Back Box Push-Pull Fan Setup

Both these fans have a nominal supply voltage of 12 V and draw approximately 70 mA in total.

5.8. DOCKING SYSTEM

Docking of the robotic platform onto the control station was achieved by using two mounting brackets on the Power Box. Two wheel gaps are used to locate the robotic platform's wheels for easy storage. This is illustrated below in **Figure 5-17**:

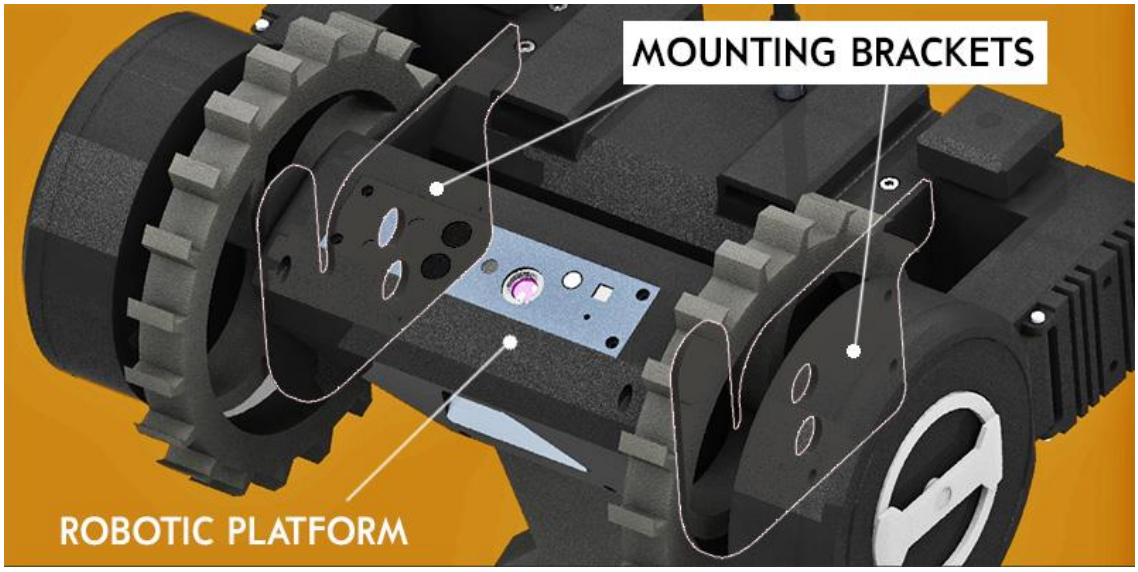

Figure 5-17 - Mounting Brackets

5.8.1. PHYSICAL INDICATORS

One of the main challenges envisioned during docking of the platform onto the control station was that the operator cannot see behind them during the process. Using electronic sensors such as a rear-view camera would have been unnecessarily complex and costly for this purpose. Therefore a simpler approach was to shape the mechanical chassis such that the operator could intuitively sense the robotic platform's location by using physical indicators, as shown below in **Figure 5-18**:

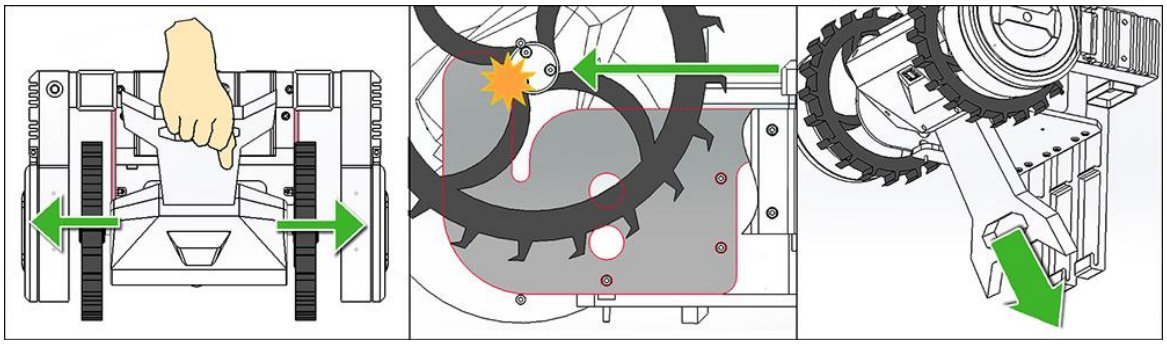

Figure 5-18 - Physical Indicators for Docking

1. The chassis' wheel gaps provide recognisable slots for the robot to locate and begin inserting into.
2. The mounting bracket acts a guide rail for the wheel axel to slide along. A raised column "nose" on the mounting bracket indicates a physical threshold for where the robot wheel axels should begin descent. The curvature of the bracket then guides the wheel axels into the provided slot.
3. The robot can then finally be strapped down to the vest using the tail's hole at the bottom.

5.8.2. WHEEL SIZE ADJUSTMENT

The maximum wheel width of the robotic platform storable in the control station was determined by the size of the wheel slots. This is illustrated below in **Figure 5-19,** which represents the robotic platform's docking space using the coloured shaded area: blue for the wheels, and red for the body.

To comply with the size required by T. Mathew's robotic platform, a 53.5 mm wheel gap was provided. This limit can be increased by adding spacers between the Back Box and the two adjacent side boxes.

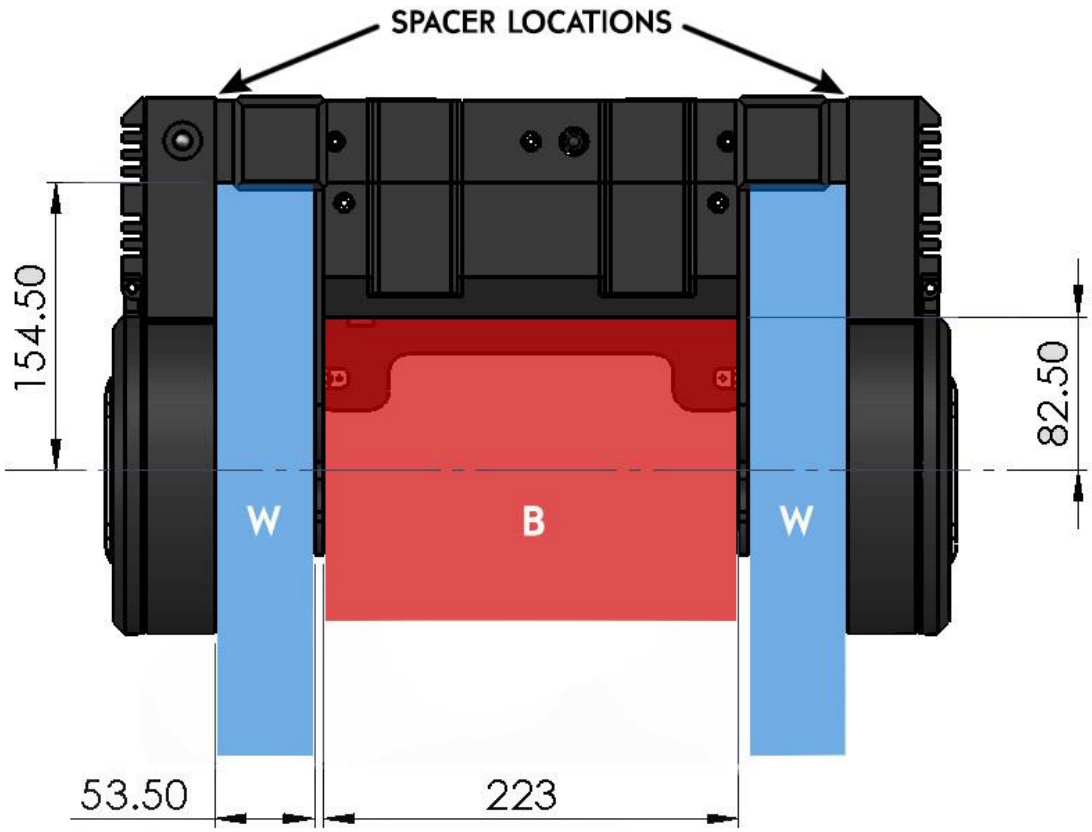

Figure 5-19 - Control Station Scarab Size Allowance

The maximum diameter of the wheel supported is 309 mm, which was substantially higher than the 200 mm originally specified. This was due to the size of the final robotic platform's body, which was larger than expected, and thus increased the distance of the wheel's centre away from the operator's back. This currently accommodates a cylindrical body with a maximum radius of 82.5 mm and a height of 223 mm.

5.9. VEST AND SUPPORT RIBS

To make the mechanical chassis into a man-wearable system, a tactical vest was used to integrate it onto the operator's body. This allowed the operator to simply pick up the vest with the control station attached, and place it on as a single unit.

5.9.1. TACTICAL VEST

To satisfy this requirement, a Condor Cross Draw Vest was selected. This was chosen to give the operator enough utility in the clothing for additional needs such as carrying rescue tools and expandability for attaching additional modules.

The vest includes:

- 7 pouches
- MOLLE Velcro attachment pads
- 2 x D rings on the shoulders, and a carry handle
- A removable weapon holster

Figure 5-21 below shows the **P**ouch **A**ttachment **L**adder **S**ystem (**PALS)** located on the back. This is a grid of webbing used for attaching equipment and contains Velcro inside to provide extra fastening ability.

Figure 5-20 – Cross Draw Tactical Vest

Figure 5-21 - PALs Grid and Shoulder Ring on Vest

On top of the vest shoulder rings are located for attaching rescue hooks.

The weapons holster was used as the OCU holster, which proved effective, as it could fit in comfortably, as well as having a slot at the bottom for the cable to route through. This is shown in **Figure 5-22**.

Figure 5-22 - OCU in Vest Holster

5.9.2. SUPPORT RIBS

During preliminary design, a 4.5 kg weight was strapped to the top, mid, and lower region of the author's back to test which area provided the most comfort. It was determined that the top region was significantly more comfortable, and therefore design of the control station aimed for it to be placed there. It should be noted the design still allowed the chassis to be relocated to other regions of the back, but would affect how the operator docks the robotic platform.

Three support ribs were used to carry the majority of the weight of the system and were located at the bottom of the chassis and adjacent to the operator's back. The ribs were shaped such that they could fit in the PALS grid slots of the tactical vest, and hook onto each strap, as shown below in **Figure 5-23**. This eliminated the need for an additional latching mechanism to prevent the chassis from coming loose from the vest. Testing revealed that these performed very well and were extremely difficult to remove unless specifically intended to.

Figure 5-23 - Mechanical Chassis on Upper Back (left), Support Ribs in PALS Grid (right)

5.9.3. SHOULDER BELTS

Custom-tailored backpack belts were used to provide additional weight support, and prevent the chassis from tilting away from the operator's back. These are routed through the top slots of the Power and Back Box and can be adjusted to suit the user's form, as shown below in **Figure 5-24**. These use a standard plastic clip-buckle system to detach from the vest, and were hand-sewn by the author to the vest's shoulder rings.

Figure 5-24 - Custom-tailored Belts and Buckles

5.10. SUMMARY

A man-wearable mechanical chassis was designed to fulfil the requirements set by the subsystem specifications. This prioritised on keeping it a one-manned unit, without the requirement for additional team members, and also ensuring an easy interface whilst maintaining quick deployment. The chassis was made man-wearable by integrating it with a Condor Cross Draw tactical vest, and using three ribs for attachment. Its layout was designed with keeping in mind ease of assembly of maintenance, allowing enough space to house all the control station electronics.

Chapter 6. Control Station Electronics, which follows, describes all the electronics which are housed within the mechanical chassis and their integration with the Scarab system.

6. CONTROL STATION ELECTRONICS

Following the background research, design of the control station electronics subsystem focussed on the use of a single processing unit. This acted as a nexus; gathering data from both the control station and the sensor payload and compiling it for use by the operator. The advantage of this was increased potential for modularity, as well as scalability of the system for future additions and development.

For the context of this chapter, it is vital to understand what the Scarab sensor payload includes. This is illustrated below in **Figure 6-1**, which shows a combination of both environmental sensors and cameras. Electronics on the control station were selected and designed to process data transmitted from the sensor payload, including a communications and video-processing module. Sensors were also incorporated on the control station, introducing temperature monitoring and GPS functionality.

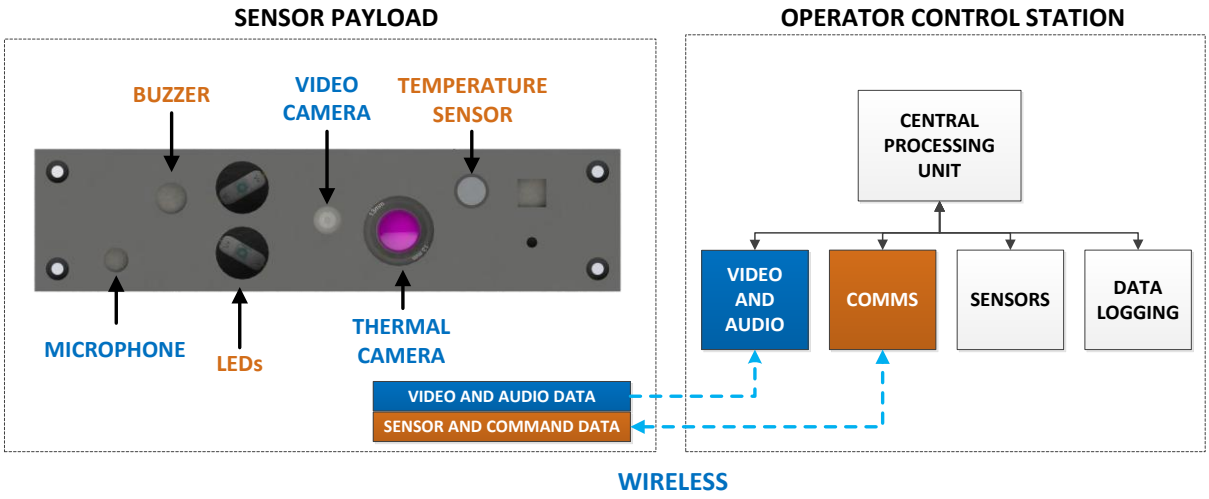

Figure 6-1 - Sensor Payload Diagram and Control Station Electronics Subsystem Breakdown (Sensor Payload Render courtesy of G. Knox)

During development, a variety of custom PCBs were made to facilitate the subsystem requirements. These were all designed using Altium Designer and the generated Gerber files were outsourced to BETA-Layout for manufacture. The completed boards were then hand-assembled and soldered in RARL by the author.

This chapter focuses on the selection and design of the electronics and their integration with the complete Scarab system. As such, the following topics will be discussed:

- **Specifications and Criteria Justifications**
- **Subsystem Overview**
- **Central Processing Unit**
- **Video and Audio Modules**
- **Communications Modules**
- **Sensor Modules**
- **Data Logging Modules**

This chapter begins by listing the subsystem specifications before presenting the subsystem overview.

CHAPTER 6: Control Station Electronics

6.1. SUBSYSTEM SPECIFICATIONS

Subsystem specifications were vital in ensuring that the control station electronics were designed in accordance with the system requirements.

Presented below are the **Subsystem Specifications** for the control station electronics. Values which are denoted with a " * " can be referred back to in the **Primary System Specifications**.

The motivation behind each criteria can be viewed in the **Subsystem Specification Justifications** which follows thereafter.

Table 6-1 - Control Station Electronics Subsystem Specifications

No	Specification	Value
Controller Specifications		
1	Central Processor	Yes
2	OCU Communication Protocol	RS-232
Video and Audio Specifications		
3	Video Receiver	Range Video 1.3 GHz receiver
4	Video format	PAL
5	Colour Video	Yes
*****	On-screen display	Yes
7	Goggles	Fatshark Dominator
8	Audio	Earphones/Headphones
Wireless Communications Specifications		
*****	Frequency	433 MHz
10	RF Transceiver	RF1101SE
*****	Indoor Range	30 m
Sensor Specifications		
12	GPS Accuracy	5 m radius
13	Temperature sensors	Yes
Data Logging Specifications		
14	Video Recording	Yes
15	USB Flash Drive Recording	Yes
Performance Specifications		
16	Maximum Power Consumption	18 W
Coding Specifications		
17	Programming language	C

6.1.1. SPECIFICATION JUSTIFICATIONS

6.1.1.1. Controller Specifications

1. As determined by the background research and proposed design layout of the control station, a single central processing unit was specified for handling all the electronics throughout the system.
2. RS-232 was chosen as the serial communications protocol to the tethered OCU. This was selected for its robustness against noise over long distances, as well as being simple to implement – needing only one wire to transmit data from one side to the other.

6.1.1.2. Video and Audio Specifications

3. The Range Video 1.3 GHz video transmitter and receiver pair were pre-selected for the project by S. Marais. Accordingly, the video transmitter was included on G. Knox's sensor payload, and the partnering receiver was located on the control station.
4. As stated in the primary system specifications, FPV goggles were to be included into the system. During the early stages of the project, a pair of Fat Shark Dominator FPV goggles were available in RARL. These were found suitable due to their small-form and portability, and therefore included into the system.
5. Both the sensor payload's cameras output a PAL video format. Therefore the control station video electronics were specified to be able to receive and process this format.
6. On a rescue inspection system, the ability to display colour video is crucial. This allows the operator to differentiate between hazard signs, as well as identify between different kinds of objects; such as blood from water. In more specific context of the Scarab system, it is vital for the sensor payload's thermal camera, which relies on multi-colour thermographs to indicate temperature levels.
7. Portable headphones or earphones should be able to be connected to the control station to listen to the audio received from the sensor payload's microphone.

6.1.1.3. Wireless Communication Specifications

8. The RF1101SE was selected by G. Knox for the Scarab system's transceivers to satisfy the requirement for the 433 MHz UHF band at a low cost.

6.1.1.4. Sensor Specifications

9. It was determined that a 5 m radius GPS accuracy was adequate for a system to be used outside a building. This allows the rescue team to search the zone within their field of view, without being in the wrong block in the immediate area.

6.1.1.5. Data Logging Specifications

10. Video recording is critical for a system to be used in USAR, as it allows the team to analyse the findings in the void before sending the appropriate equipment down to retrieve any survivors or objects. It also provides a quick means of reviewing the mission data, with the OSD able to overlay the recorded sensor data directly on top of the video.
11. USB logging was specified for the system to allow sensor data to be recorded in text file form. This was not necessary for the on-site purposes like video reviewing, but was still included for the purpose of providing a more empirical means of analysing the data after the rescue mission.

6.1.1.6. Performance Specifications

12. The power supply's 12 V rail was specified to provide a total of 26 W to supply the control station system. Of this, 18 W was allocated to the control station electronics.

6.1.1.7. Coding Specifications

13. The firmware libraries for the RF1101SE were designed and written in C by G. Knox. As such, the control station firmware was specified to use the same programming language to ensure compatibility, as well as making cross-development easier between the control station and sensor payload, which both used the same STM32F407VG microprocessor.

6.2. SUBSYSTEM OVERVIEW

A summary of the connections of the devices in the control station can be found below in **Figure 6-2**. This shows the data flow relative to the Computing Box, and illustrates how all modules are handled by the central node; dubbed the **Central Processing Board**. This uses a **STMicroelectronics STM32F407VG** embedded microprocessor to handle all the data throughout the control station. For a more detailed overview, please refer to the circuit schematics on the accompanying DVD.

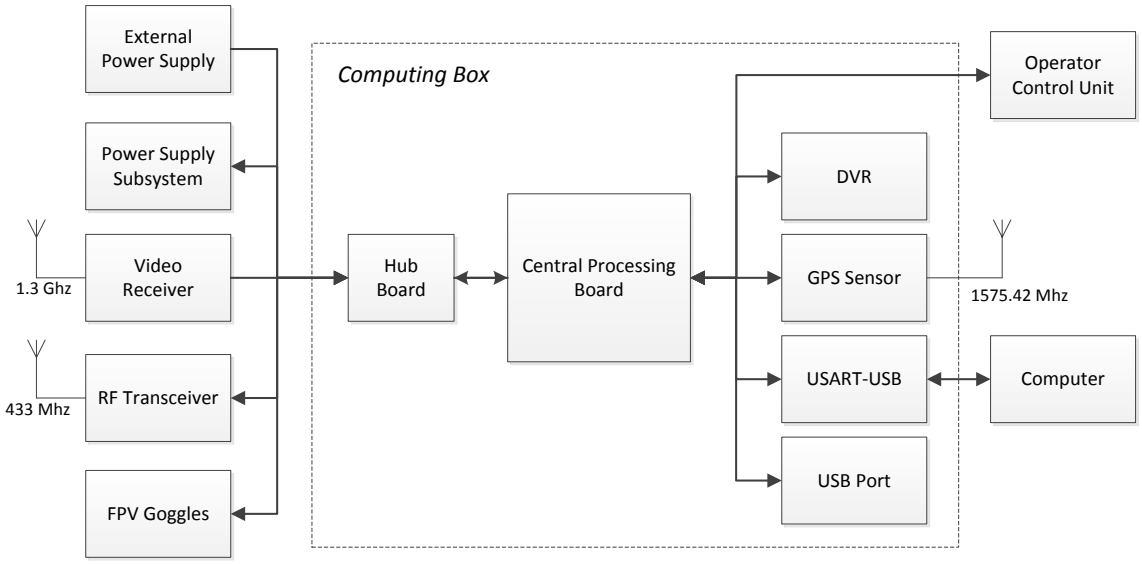

Figure 6-2- Control Station Electronics Subsystem Overview

Tabulated below is a summary of each of the functions required between the modules and the Central Processing Board. Note this can be referred to the final board shown later in **Figure 6-7** for the specific pins allocated from the STM32F40VG.

Table 6-2 - Inputs and Outputs to Central Processing Board

PERIPHERAL	INPUTS (To Central Processing Board)	OUTPUTS (From Central Processing Board)
External Power Supply	External Supply Connected (GPIO)	
Power Supply Subsystem	12 V, 5 V, 3.3 V Supply 2 x Temperature Sensors (ADC) Fuel Gauge I^2C (SDA)	Regulator Switches (GPIO) Charge Enable Switches (GPIO) Fuel Gauge I^2C (SDA, SCLK)
Video Receiver	PAL Video	
RF Transceiver	SPI (MISO)	SPI (MOSI,SCLK,CS) GPIO
FPV Goggles		OSD PAL Video
Operator Control Unit	RS-232 (RX)	12 V Supply OSD PAL Video RS-232 (TX)
DVR		12 V Supply OSD PAL Video
USB Port	USB Data (D-, D+, ID)	5 V Supply USB Data (D+, D-, ID)
GPS	USART (RX)	5 V Supply USART (TX)
USART-USB	USART (RX)	USART (TX)

6.3. CENTRAL PROCESSING BOARD

Design of the Central Processing Board focussed on incorporating all the control station's processing circuitry. As such, this included the following main modules:

- STMicroelectronics **STM32F407VG** ARM Cortex-M4 168MHz 32-bit microprocessor
- Maxim **MAX7456** On-Screen Display generator
- Texas Instruments **MAX3232** RS-232 transmitter

Each of these modules serve as core components of the control station interface, and will be covered later this chapter. The final PCB, with its modules indicated is shown below in **Figure 6-3**.

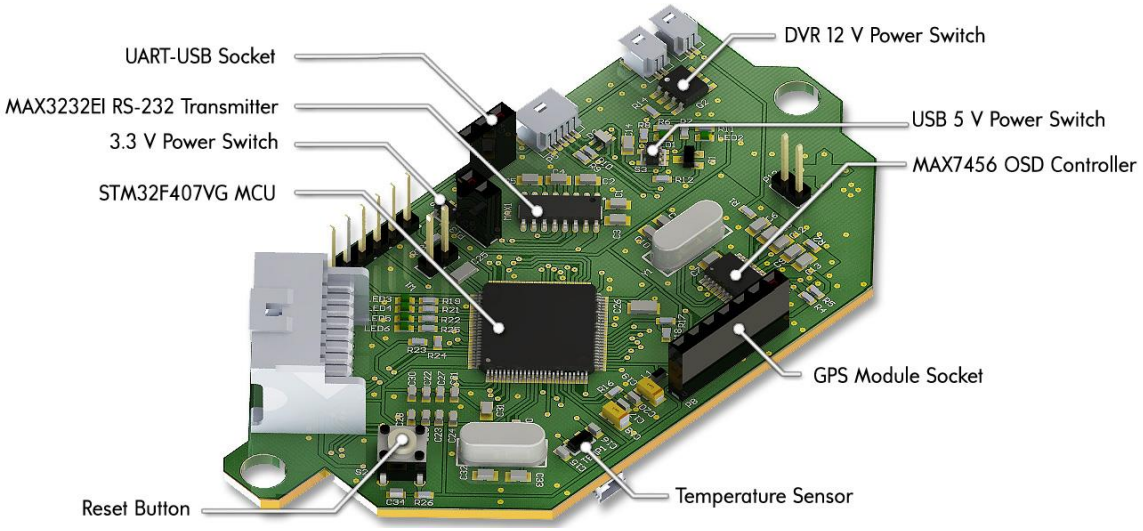

Figure 6-3 - Render of Central Processing Board

6.3.1. BOARD DEVELOPMENT

During the early stages of the project, the STM32F407VG embedded microprocessor was recommended by the UCT Electrical Engineering Department for the project. This was deemed suitable for the Scarab system as it featured high processing power at 168 MHz, with a large multitude of functionality at a relatively low cost. They have been benchmarked [81] to achieve a score of 2.79 CoreMark/Hz, making them one of the highest performance Cortex-M solutions available on the market. It was thus chosen for the operator control station for use as the primary processing unit. The same microprocessor was also included in the high-cost version of G. Knox's sensor payload, which proved highly beneficial during the cross-development and integration of firmware code.

Selection of each additional module on the board was performed on the basis of their function, performance and compatibility with the microprocessor.

The STM32F407VG has an evaluation module in the form of the low-cost STM32F4 Discovery boards. These were used for initiating the coding development of the system, as well as programming the Central Processing Board. One is shown to the right in **Figure 6-4.**

The microprocessor has a nominal supply voltage of 3.3 V, and can draw up to 150 mA of current.

Figure 6-4 - STM32F4 Discovery Board [91]

Over the course of development, two generations of the board were designed and manufactured. The second iteration focussed on correcting design errors from the first prototype as well as making the board more user-friendly for both development and maintenance. Both are shown below in **Figure 6-5**. A more thorough overview of the final PCB can be viewed on the next page.

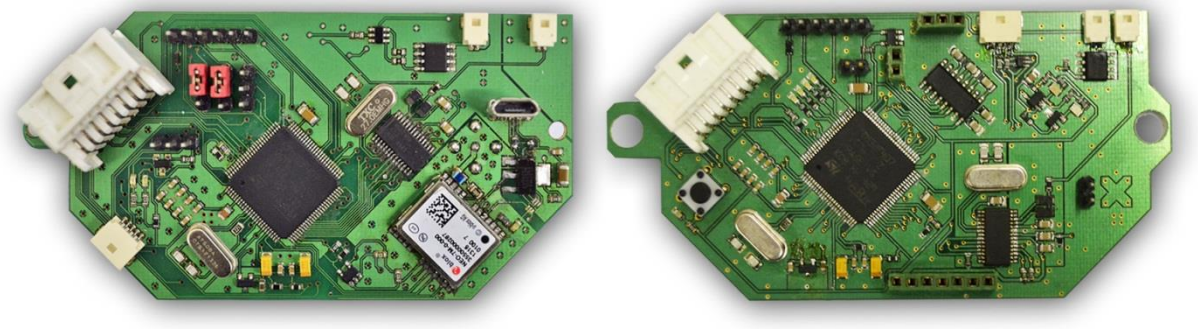

Figure 6-5 - Central Processing Board: Prototype (left), Final (right)

Prototype: The first prototype PCB aimed to test the circuitry design and allow code development to be initiated for the user interface. This was intended to be an all-in-one solution and included all modules on-board, including the GPS sensor and USB-UART convertor.

Final: On the final PCB, a more modular design was approached. This prioritised on making it more accessible for testing as well as addition of future modules. As a result, both the GPS sensor and USB-UART convertor were removed and replaced by breakout-board designs. This allowed all the electronics to be moved to the top side of the PCB, leaving the bottom exclusively for connectors and routing. More vias were also included on the routing, which proved to be invaluable test points for debugging purposes.

6.3.2. PROGRAMMING INTERFACE

To program and debug the STM32F407VG, a ST-LINK/V2 in-circuit debugger was used. This communicates with the microprocessor using a two-wire **S**erial **W**ire **D**ebugging (**SWD**) protocol. A programming header is included on the PCB to connect between the board and the programming interface. During development, the ST-LINK/V2 tool on the STM32F4 Discovery board was used for programming the board. The setup, and pin connections are illustrated below in **Figure 6-6**:

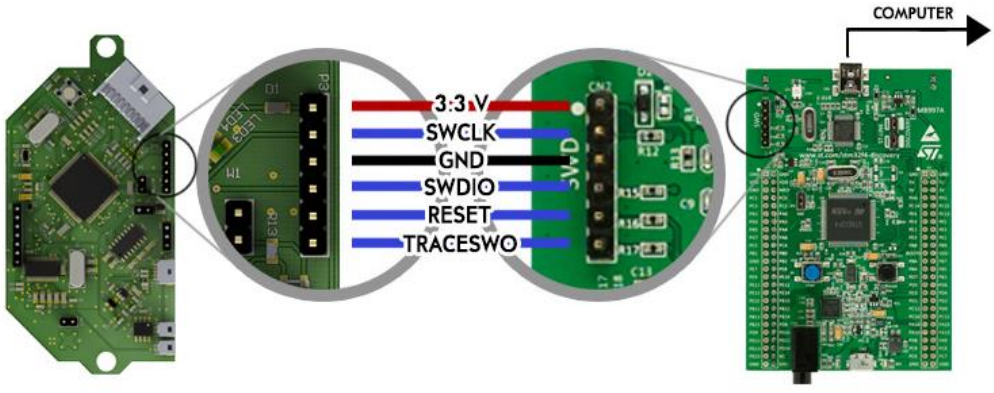

Figure 6-6 - Programming Connections between Central Processing Board and STM32F4 Discovery

6.3.3. FINAL BOARD

The final PCB and each of the connector's pin-out allocations are illustrated in

Figure 6-7 below. For more information on the board and schematic design, please refer to the accompanying DVD.

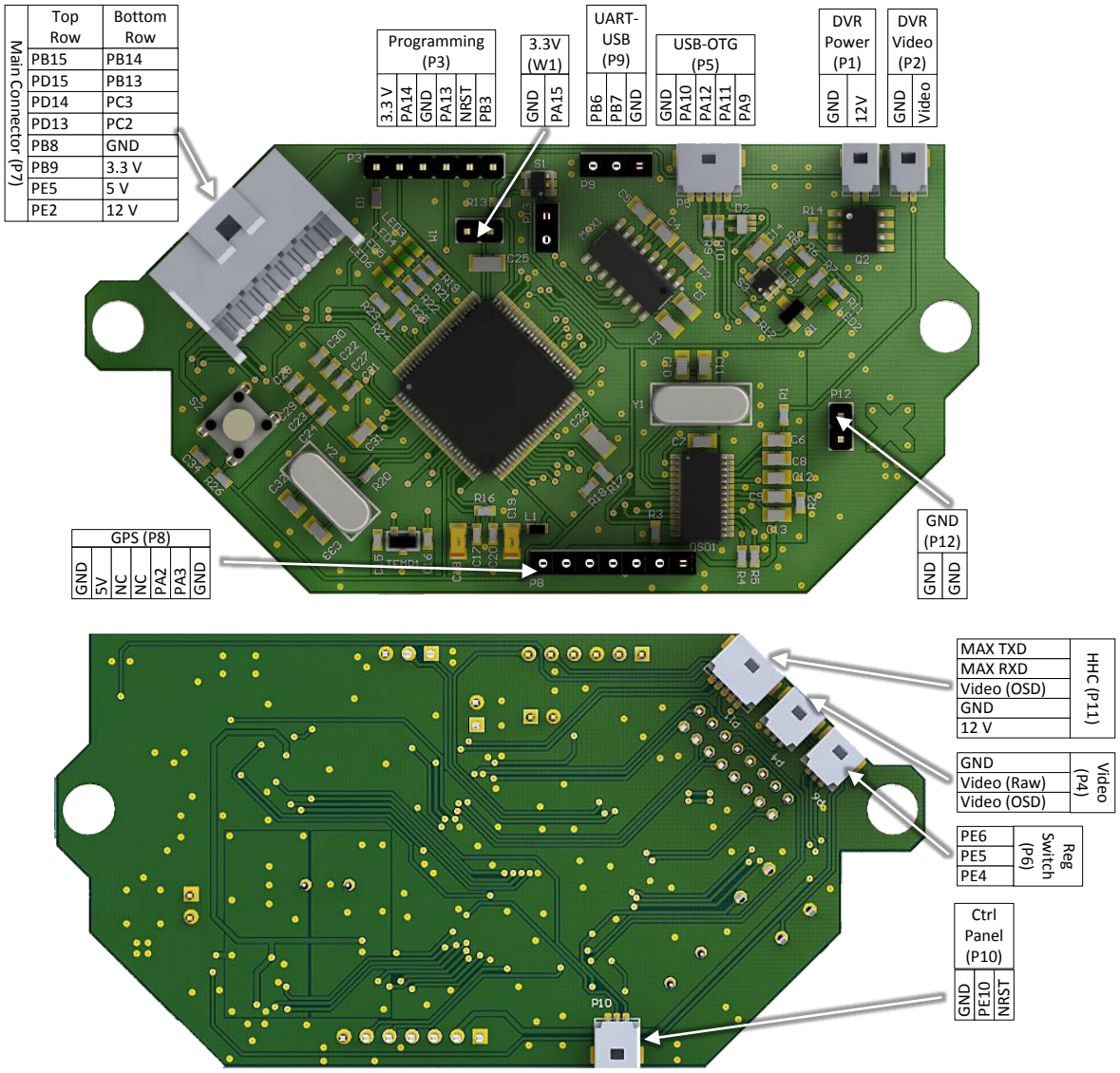

Main Connector (P7)			
PB15	RF MOSI	PB14	RF MISO
PD15	RF GDDO2	PB13	RF SCLK
PD14	RF GDDO0	PC3	Back Box Temp
PD13	RF CS	PC2	Pwr Box Temp
PB8	Fuel Gauge SCL	GND	Board GND
PB9	Fuel Gauge SDA	3.3 V	3.3 V Supply
PE5	20 V Enable	5 V	5 V Supply
PE2	Power Supply Detect	12 V	12 V Supply

HHC Connector	
MAX TXD	HHC RXD
MAX RXD	HHC TXD
Video	Video (OSD)
GND	HHC GND
12 V	12 V Supply

3.3 V (W1)	
GND	Board GND
PA15	3.3 V Switch

USB-OTG (P5)	
GND	USB GND
PA10	USB ID
PA12	USB D+
PA11	USB D-
PA9	USB VBUS
GPS (P8)	
GND	GPS GND
5V	5 V Supply
PA2	GPS RX
PA3	GPS TX
Regulator Switches (P6)	
PE6	12 V Switch
PE5	5 V Switch
PE4	Charge Enable

Programming (P3)	
3.3V	3.3 V Supply
PA14	SWCLK
GND	Board GND
PA13	SWDIO
NRST	Reset
PB3	TRACESWO
USART-USB (P9)	
PB6	USART TX
PB7	USART RX
GND	UART-USB GND
Control Panel (P10)	
GND	Button GND
PE10	Low-Power Mode
NRST	Reset

Figure 6-7 - Central Processing Board: Top Side (Top), Bottom Side (Bottom)

6.4. VIDEO AND AUDIO

The video electronics are responsible for receiving and processing the camera video data from the sensor payload. The wireless receiver intercepts the transmitted video signal which is then processed through the Central Processing Board to apply the OSD. The final processed signal is then transmitted to each of the display and recording devices throughout the system. The received audio from the sensor payload's microphone can also be listened to using a pair of portable stereo earphones or headphones. **Figure 6-8** below illustrates this data flow:

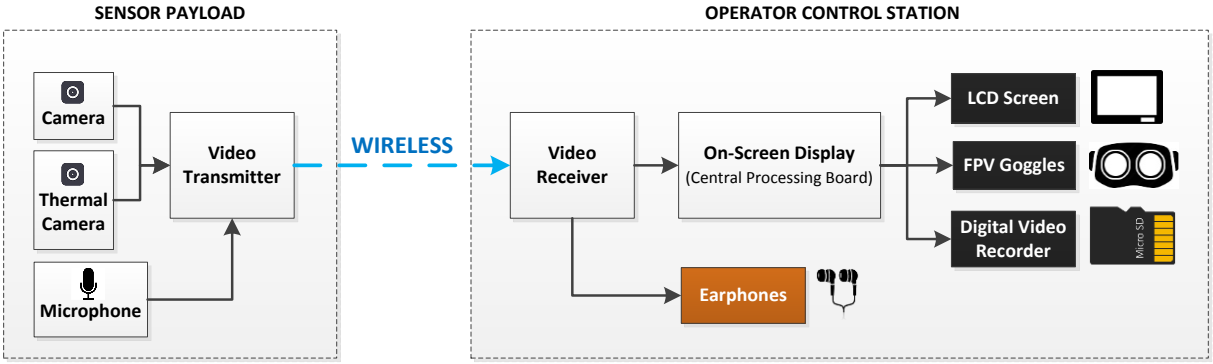

Figure 6-8 - Video and Audio Data Flow in Scarab System

Each of the control station modules shown above will be covered in this chapter. Excluded is the LCD screen, which is covered in the **Operator Control Unit** chapter.

6.4.1. VIDEO RECEIVER

The **Range Video 1.3 GHz 12-channel** video receiver was selected for receiving the camera video feed from the sensor payload's wireless video transmitter. This pair was chosen for their relatively low cost of $ 60 USD, as well as being commercially targeted for use in long-range RC systems. The receiver and transmitter pair is shown to the right in **Figure 6-9**. The receiver has a nominal supply voltage of 12 V and draws 270 mA. It outputs both analogue PAL video signal and stereo audio.

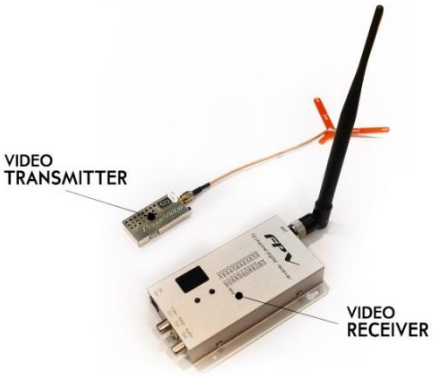

Figure 6-9 – 1.3 GHz Video Transmitter, Receiver

6.4.2. ON-SCREEN-DISPLAY

OSD functionality was achieved using the **MAXIM MAX7456** IC. This incorporates EEPROM, which can store up to 256 pictographs for overlaying on top of a colour or grayscale video image. It has a nominal supply voltage of 5 V, with a specified maximum current draw of 145 mA. The device can process both analogue PAL and NTSC video signals, and SPI serial commands are sent from the STM32F407VG to control how the pictograph overlays are processed. An example output is shown to the right in **Figure 6-10**.

Preliminary software development was performed using breakout boards supplied by Sparkfun Electronics before the IC was included on the final Central Processing Board.

Figure 6-10 - Example OSD Output using MAX7456 IC

6.4.3. FPV GOGGLES

Initial design of the system revolved around the idea of having two means to view the video from the camera: using a LCD screen, or a pair of FPV goggles. On the final control station, a LCD screen was included on the OCU as the main display. An optional pair of **Fat Shark Dominator** FPV goggles provided a more immersive method of viewing the video. These were intended to be used while the operator is outside in a safe area, where sunlight glare would become a prominent issue if using the LCD screen. The goggles are shown below in **Figure 6-11**:

Figure 6-11 – Fat Shark Dominator Goggles: Front View (left), Back View (right)

The goggles features a 640 x 480 pixel resolution stereoscopic display with LED backlighting, and supports both PAL and NTSC video formats. A carry pouch is provided for protection, and can be clipped onto the system's tactical vest for transportation. During the project's development, the goggles were tested to be compatible with the OSD video output from the Central Processing Board. For audio, earphones can be connected to the goggles using its 3.5 mm stereo audio jack. The unit has a nominal supply voltage of 12 V, and was measured to draw 370 mA.

An adapter PCB with a 4-pole stereo connector was made to allow the goggles to connect to the control station's Back Box. This is shown below in **Figure 6-12**:

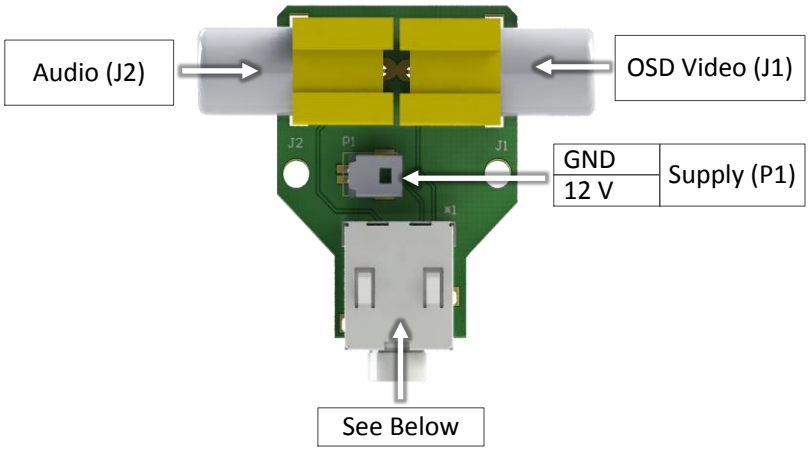

Pin	Function	4-pole stereo connector
4	12 V Supply	2-Pin Pico-Clasp (P1)
1	Ground	
3	Audio	RCA Jack (J2)
2	OSD Video	RCA Jack (J1)

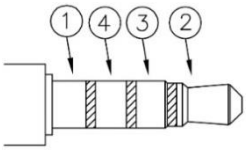

Figure 6-12 - Render of Goggle Adapter Board

6.5. COMMUNICATIONS

The communication electronics in the control station are responsible for establishing a link to the systems separate from the main control station. This includes the wireless connection to the sensor payload on the robotic platform, as well as the tethered connection to the OCU.

6.5.1. WIRELESS SCARAB COMMUNICATION

Two 433 MHz **RF1101SE** wireless transceivers were used to establish communication between the control station and the sensor payload. These were chosen by G. Knox for use in the Scarab system for their low cost and their UHF operation, making them suitable for high building penetration and more resistant to signal interference and jamming in the disaster zone. The transceivers specify a maximum transfer rate of 500 kbps, a maximum signal power of +10 dBm at all frequencies, and a transmission distance of up to 200 m. Despite their name, these boards actually employ the Texas Instruments CC110L IC, and not the CC1101. The transceiver pair is pictured below in **Figure 6-13.**

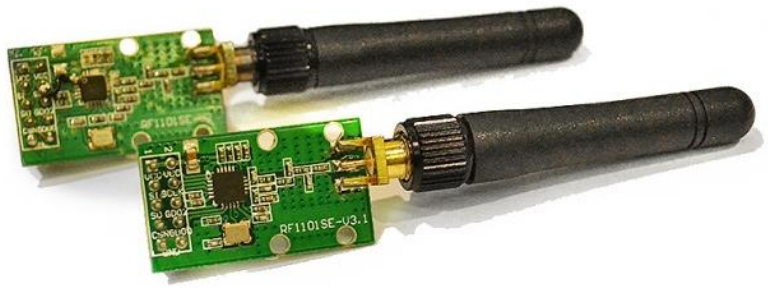

Figure 6-13 - RF1101SE Transceiver Pair

On the control station, the transceiver communicates with the Central Processing Board using SPI serial communications. USART versions of these boards are available for easier and faster adaptability, but at the expense of lacking transceiver configurability, such as being able to change the operating frequency and signal power.

The transceivers have a nominal supply voltage of 3.3 V, and were measured to draw approximately 31 mA of current.

An adapter was made to convert the PCB header pins of the transceiver breakout board into a single Pico-Clasp header. The pin-outs are described below in **Figure 6-14**:

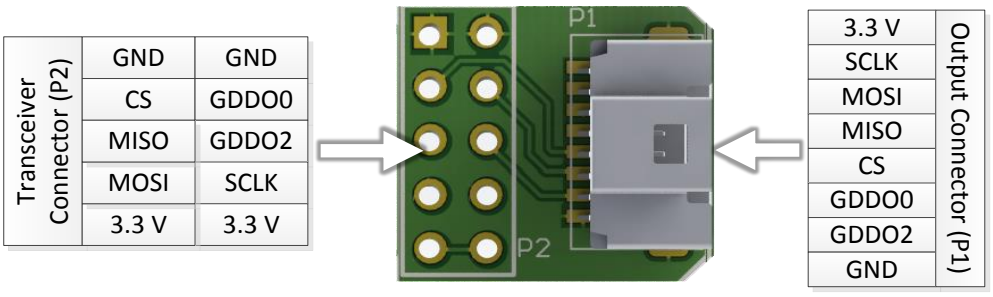

Figure 6-14 - Render of Transceiver Adapter Board

During testing it was discovered that the SPI lines were suffering from signal ringing, which caused intermittent hanging of the transceiver. This was due to the longer nature of the connecting wires, which were just below 300 mm in length. The ringing was eliminated by soldering a 1 K damping resistor in series on each wire between the Central Processing Board and the transceiver to match impedances. The value of this resistor was determined experimentally.

6.5.2. TETHERED OCU COMMUNICATION

The OCU and control station communicate using a 2 m long data cable. More detail on the cable and connections can be found in **Chapter 7. Operator Control Unit**. During design, it was envisioned that when transmitting serial data across the cable, voltage degradation, interference and noise could become an issue. Therefore to mitigate this, a **Texas Instruments MAX3232EI** RS-232 transmitter was incorporated on the Central Processing Board.

The device takes in a 3.3 V USART signal from the STM32F407VG and converts it to a bipolar 10 V RS-232 signal to be transmitted down the cable. A second MAX3232EI on the OCU board converts it back to 3.3 V USART level for the receiving microprocessor. This is illustrated below in **Figure 6-15.** The higher voltage of RS-232 helps increase the signal's robustness, ensuring the accuracy of the transmitted data. The device is full-duplex, meaning it can transmit and receive simultaneously. The devices have a nominal supply voltage of 3.3 V and have a maximum current draw of 1 mA.

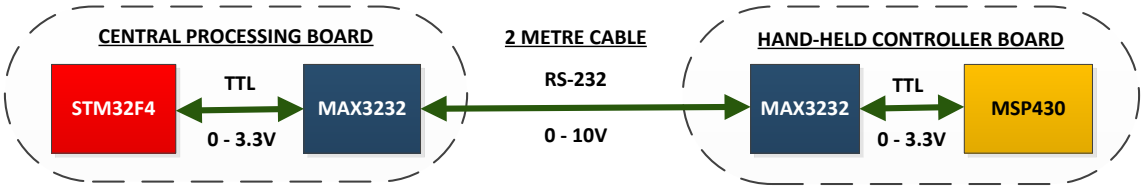

Figure 6-15 - MAX3232 USART communication conversion

6.6. SENSORS

Sensors were included on the control station. This included both temperature monitoring sensors and a GPS sensor for coordinate data.

6.6.1. TEMPERATURE SENSORS

To monitor the temperatures of the control chassis, a single temperature sensor was allocated for each of the boxes. As such, one was included on the Battery Management, Power Distribution, and Central Processing Board; each representing the temperature of their respective boxes. The Video Receiver Box was excluded from monitoring, as it contained only the video receiver, and therefore not seen as a problematic area.

For this purpose, **Texas Instruments LM60** temperature sensors were used. These have a rated temperature range of -40 °C to +125 °C, and have a nominal supply voltage of 2.7 V -10 V and a typical quiescent current of 82 µA. The temperature of the LM60 sensors is calculated using the following linear equation:

V_o is the voltage output from the sensor, and V_{OFFSET} is 424mV according the device's datasheet.

To ensure accurate readings from the temperature sensors, a calibration process was performed using a FLIR A320 IR camera as a reference. Using the data gathered from the calibration, V_{OFFSET} was adjusted accordingly for each sensor in the firmware code. More information on the process can be found in **Appendix C**. **Sensor Calibration**.

6.6.2. GPS SENSOR

uBlox GPS modules have historically been implemented in a number of projects in RARL for their reliability and ease of use. However, the only evaluation boards that were available were not suitable for fitting in the control station due to their size and layout. A new PCB therefore had to be designed and assembled.

The **uBlox NEO-7M** GPS sensor was therefore selected for this purpose. It comes from uBlox's NEO-7 range of GNSS modules, where the M is the lower cost version. The chip is powered by a 56-channel ublox 7 engine, and specifies accuracies up to 2.5 m with a 29 second cold start. It is also backwards compatible with the earlier NEO-6M and NEO-5M. The module uses the **D**ifferential **G**lobal **P**ositioning **S**ystem (**DGPS**), which provides higher accuracy than conventional GPS. Accuracy of these modules decreases with distance away from the broadcasting reference station; a 2004 paper from the University of Nottingham indicated an error increase of 0.22 m for every 100 km [ ].

The PCB was designed to be mounted on the Central Processing Board, following the decision to make it a modular breakout board. These communicate using USART serial communications via the connectors provided. The board and its connections are displayed below in **Figure 6-16**.

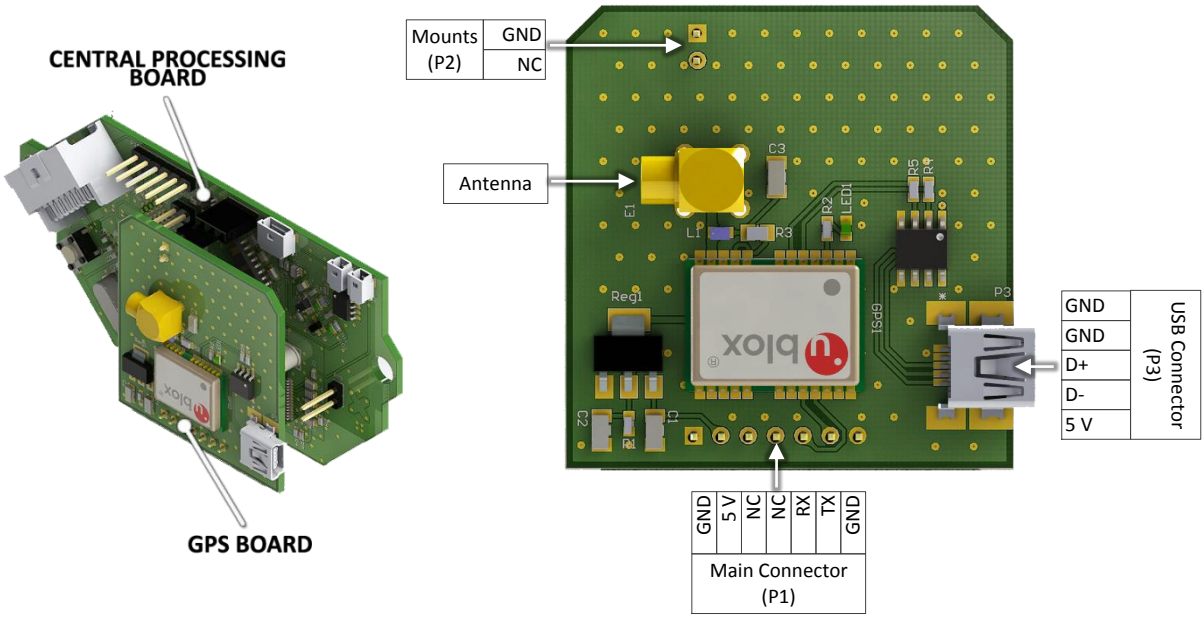

Figure 6-16 - GPS Board Mounted on Central Processing Board (left), GPS Board Connections (right)

A mini-USB connector was included on the board. This allowed connecting of the PCB to a laptop or desktop computer, independent of the control station, and take advantage of the provided uBlox u-centre evaluation software. This lets the user view and log the GPS data using a detailed GUI interface. Included are also sensor configuration options as well as the ability to directly plot the GPS data using Google Maps in real time, which proved invaluable during testing of the board.

The sensor has a nominal voltage of 3.3 V and is specified to draw no more than 67 mA. As such, a 3.3 V regulator was included on the board was used to convert the standard USB supply voltage of 5 V down into a suitable value for the sensor.

On the board, an orange LED was included to indicate a GPS fix. This LED will also flash once upon the sensor's start-up. The sensor was configured to use a 1575.42 MHz active external antenna, which is connected using the gold MCX socket. Note the metal shield cover of the sensor is directly connected to ground and therefore should never come into contact with any other electrical components.

6.7. DATA LOGGING

As required by the subsystem specifications, data logging was approached using two methods. The primary one was video recording, which would log the OSD video, which included all the time and sensor data overlaid on top of the camera video feed. The secondary was to allow text file logging onto a mini USB flash drive. This would be connected via the port available on the Computing Box's control panel.

6.7.1. VIDEO RECORDING

Video recording was achieved using a **Dozen Mini Digital Video Recorder** (**DVR**). This is a low-cost device which takes in a video input and records to it to a Micro SD card, supported up to 32 GB. It also includes a video output port for playback, and an embedded OSD menu interface is used for navigation and setting configuration. The device is compact, and can fit in the palm of a hand, as shown in **Figure 6-17**.

Figure 6-17 - Mini DVR on Person's Palm

To begin recording video, the device must simply be switched on. Therefore an N-MOSFET was included on the Central Processing Board to switch the 12 V supply to the DVR. This is toggled by the STM32F407VG microprocessor via the user interface. This device draws approximately 300 mA, depending on the operation.

Video recording modes include VGA (640 x 480 pixels), and QVGA (320 x 240 pixels). VGA records 2 GB of video data for each hour, while QVGA records at 800 MB per hour. For a 32 GB SD card, this results in 16 hours, and 40 hours of saved video data respectively. The video is recorded in 30-minute segment files, and if the SD card becomes full, the oldest file will be overwritten by the newest one.

6.7.2. USB LOGGING

USB writing functionality was included into the Central Processing Board using the STM32F407VG's included USB **O**n-**T**he-**G**o (**OTG**) module and third party open source FatFS firmware libraries. During development, functionality of the hardware was tested to work using firmware dedicated to writing and saving text files onto a USB flash drive.

However, due to the time and project scope constraints, the firmware was not expanded upon and implemented onto the main system. This was also due to the USB file-opening and writing processes adding a large amount of processing overhead which compromised the working state of the control station firmware. The hardware was still retained on the system as a working proof of concept to be improved on in future development.

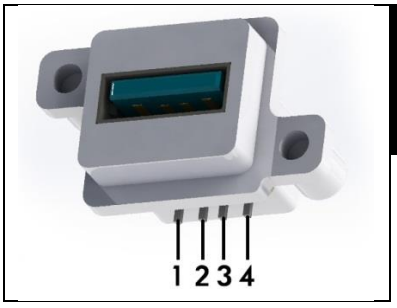

1	5 V
2	D -
3	D +
4	GND

Figure 6-18 - IP67 USB Connector Pin-Outs

The Central Processing Board connects to the USB Type-A IP67 connector on the Computing Box's control panel using a Pico-Clasp connector. The pins for the USB connector are described in **Figure 6-18**.

6.8. PC INTERFACE

A USART to USB converter PCB was designed and assembled to establish a communications bridge between the control station and a desktop or laptop computer. This provided a means to extract the data onto a more interactive software environment, such as National Instruments' LabVIEW, for logging and analysis. The flow of data is illustrated below in **Figure 6-19**.

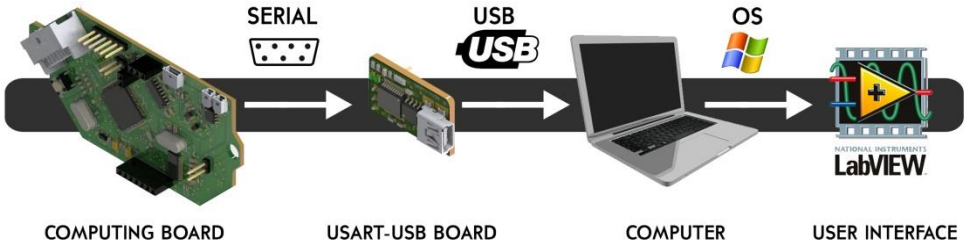

Figure 6-19 - Flow of Information from Central Processing Board to Computer Interface

To achieve this, a **Microchip MCP2200** was used. This is a USB-to-USART serial converter, and includes 256 bytes of EEPROM for storing user settings. It draws 15 mA at a nominal supply voltage of 3 – 5.5 V.

The PCB includes the convertor, as well as an additional ESD protection diode. Like the GPS board, it can be mounted directly on the Central Processing Board using the provided sockets, and communicates using USART. To connect to a computer, a mini-USB connector was provided. Two green LEDs indicate whether data is busy being transmitted. The connections are illustrated below in **Figure 6-20**:

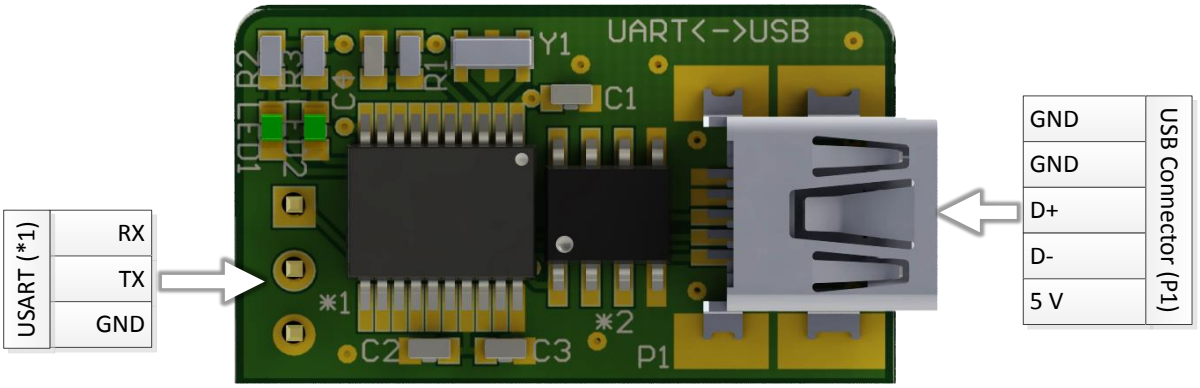

Figure 6-20 - Render of USB-USART Converter Board

Power to the board is supplied exclusively from the computer through the 5 V USB connection. Only ground and the USART pins are required from the Central Processing Board.

Note that driver software for the MCP2200 must be downloaded and installed from the manufacturer's website before the device can be used on a computer.

This board was used to establish communications between the control station and the accompanying LabVIEW interfaces. This is discussed later in **Chapter 9. Firmware Design**.

6.9. HUB AND CONNECTORS

To minimize the number of connectors required on the Central Processing Board, the hub board was used. This is a custom designed PCB which also contains 500 mA fuses to protect the 3.3 V, 5 V, and 12 V power rails to the Central Processing Board, OCU, and RF1101SE transceivers. Each of the connectors was wired symmetrically with the corresponding board's connectors, and can be referred to in their respective sections. The board is shown below in **Figure 6-21**.

A voltage divider was included on the board to convert the 28 V input from an external power supply to a 3.3 V level for safe use for the STM32F407VG microprocessor. This was to indicate to the system whether an external power supply was connected.

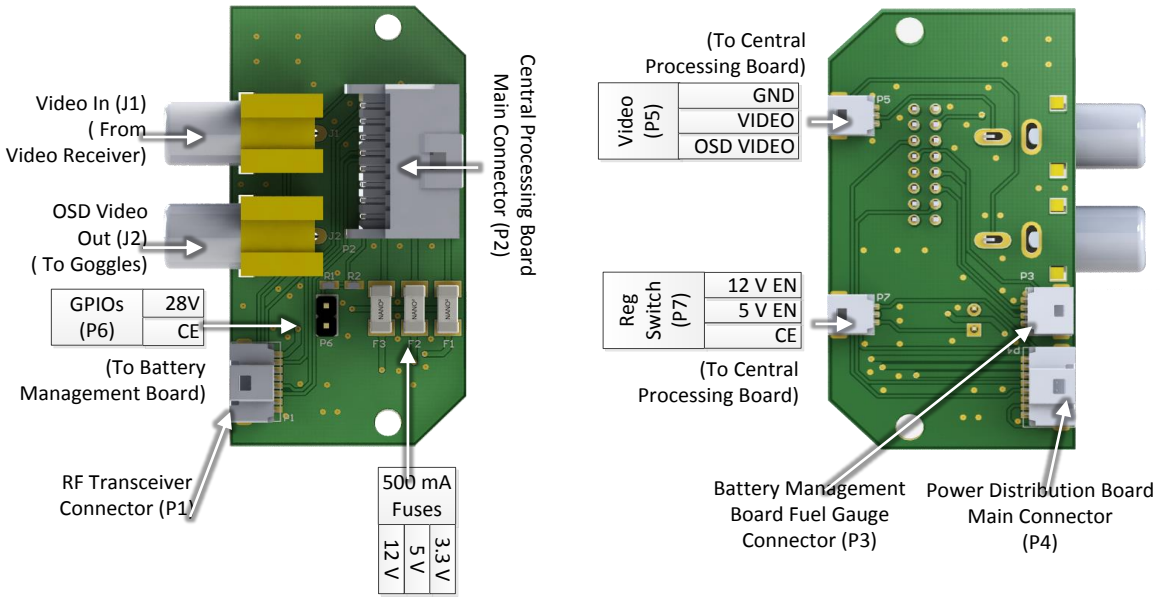

Figure 6-21 - Render of Hub Board: Top (left), Bottom (right)

RCA connectors were used for the video signals to ensure compatibility with the video receiver and other media devices. Throughout the system, Pico-Clasp connectors were used for their small size and ease of use. The main exception was the Central Processing Board's main connector, which uses a MicroClasp 16-pole header. This was chosen to make debugging easier as well as making the wires easier to maintain. Every wire in the system was colour coded according the function allocated:

Red	Black	Yellow	Blue	Orange	Green
Power	Ground	Digital Clock	Digital Data	Analogue Data	GPIO

6.10. SUMMARY

A complete electronics interface was designed to fulfil the requirements set by the subsystem specifications. Included were a central processing unit using the STM32F407VG microprocessor, a video and audio module, communications module, on-station sensors, a PC-interface, as well as a data logging unit. This aimed to create a platform which could interface with the sensor payload.

Chapter 7. Operator Control Unit, which follows, details the design process of the hand-held controller, which provides the means for the operator to interface with the control station's electronics.

7. OPERATOR CONTROL UNIT

Figure 7-1 - Operator Control Unit Held in Safety Glove

Design of the OCU was motivated by the need for a controller which was one-handed, and provided a LCD screen for viewing the OSD video. In the system, it is treated as a standalone module from the mechanical chassis, and is connected using a 2 m long cable, as shown below in **Figure 7-2**:

Figure 7-2 - Cable Connection between Computing Box and OCU

This chapter discusses the development and design of the OCU, focussing on both the mechanical and electronic aspects of the subsystem. It begins by introducing the subsystem specifications which defined the criteria for the OCU's design.

CHAPTER 7: Operator Control Unit

7.1. SUBSYSTEM SPECIFICATIONS

Because the OCU was designed for use of the control station as a standalone subsystem, specifications were drawn to ensure that it could be integrated with control station electronics.

Presented below are the **Subsystem Specifications** for the OCU. Values which are denoted with a " * " can be referred back to in the **Primary System Specifications**.

The motivation behind each criteria can be viewed in the **Subsystem Specification Justifications** which follows thereafter.

Table 7-1 – Operator Control Unit Subsystem Specifications

Part	Specification	Desired Value
Physical Specifications		
1	Maximum Weight	300 g
2	One Hand Operation	Yes
Functional Specifications		
*	Colour LCD Screen	Yes
3	Minimum screen resolution	320 X 240 pixels
*	Magnetometer	Yes
4	Tethered	Yes
5	Primary communications protocol	RS-232
*	Tactile inputs	Yes
*	Water resistant	Yes
6	System Supply Voltage	12 V
Performance Specifications		
7	Maximum Power Consumption	6 W
8	Ergonomic	Yes
Coding Specifications		
*	Programming language	C

7.1.1. SUBSYSTEM SPECIFICATION JUSTIFICATIONS

7.1.1.1. Physical Specifications

1. The weight of a standard PlayStation 2 video game controller was measured to be 200 g. 300 g was therefore specified to account for the additional weight of a LCD screen.

2. As stated in the background research, a one-handed solution would be more viable in a USAR environment.

7.1.1.2. Functional Specifications

3. The OSD's characters each take 12 x 18 pixels. To give enough space for all the sensor data without cluttering the LCD screen, a minimum standard resolution of 320 x 240 pixels was therefore specified. This permitted 13 rows of 26 characters.

4. A tether connection was specified to negate the need for a battery on the OCU. It also limits the number of wireless devices on the control station and saves the space which would be required for extra electronics.

5. Please see **Chapter 5. Control Station Electronics** for more information on this specification.

6. 12 V is provided from the system's power supply to be used for the OCU.

7.1.1.3. Performance Specifications

7. To comply with the specifications listed for the 12 V power rail in Chapter 8. Power Supply, the OCU subsystem was specified to draw no more than 500 mA to stay below the total system draw of 2 A. This translates to 6 W.

8. As with any hand-held device, it should be ergonomic and comfortable to use. Because it is a one-handed device, ambidextrous operation should be possible with different sized hands.

7.2. MECHANICAL DESIGN

7.2.1. CONCEPTUAL SHAPE DESIGN

To ensure that the controller was an ergonomic solution which could be used by a single hand, concept models were produced to determine the shape and layout required. A flat pseudo-hourglass shape was used as it provided an obvious gripping area with ample space for housing electronics. To test this, iterative variations were printed out on paper and then crafted to determine whether the form factor would be comfortable to hold. To simulate the thickness of the controller, a 30 mm thick block was placed between the hand and the printed shape. This proved to be a cheap and efficient method which mitigated the need to manufacture multiple shell prototypes to test the controller's shape.

It was envisioned that the 'hips' of the controller allow space for the operator's fingers to locate and grip onto while also allowing the thumb to locate the joystick with ease. The first iterations used a curvier and smoother appearance in the expectation this would provide more comfort. However, this proved harder to maintain a grip due to the fingers slipping along the said curves and having no defined crevice to squeeze onto. The final iteration therefore used straight surfaces, with defined corners. This was found to be much easier and comfortable to hold onto, as well as introducing an aesthetically pleasing rugged appearance. It was therefore used for the final mechanical design.

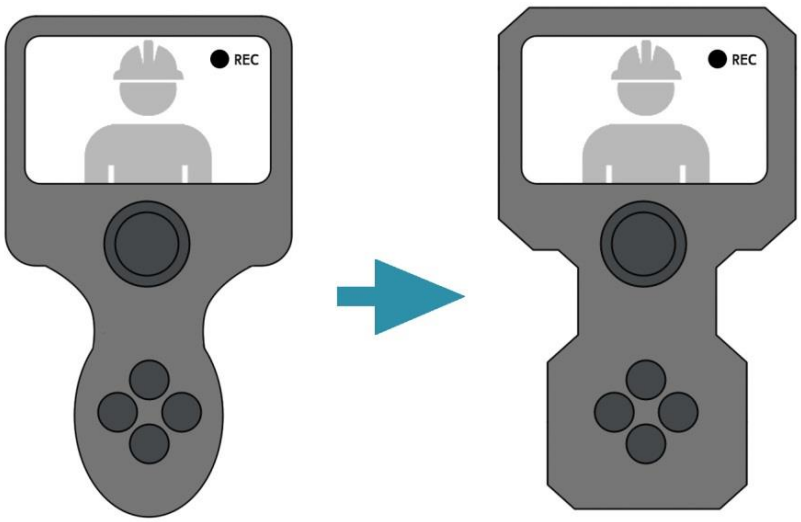

Figure 7-3 - Transition of OCU from Curve-Based Design to Straight-Based Design

7.2.2. FINAL MECHANICAL DESIGN

Following on from the shape chosen in the concept process, detailed mechanical design was done on the OCU to produce a working prototype. The final assembly is shown below in **Figure 7-4**:

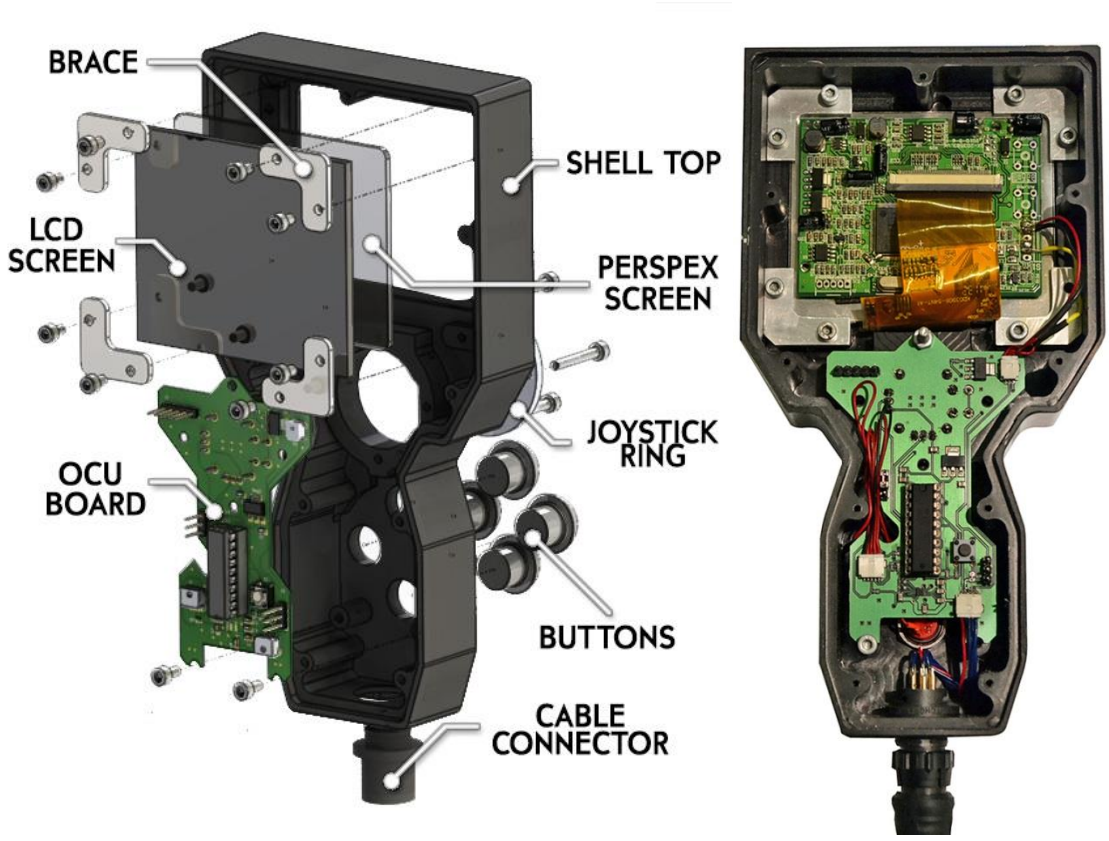

Figure 7-4 - Exploded Assembly of OCU (left), OCU Internal Components Assembled (right)

The OCU uses two main shells for assembly, which are mounted together using M3 screws. This was intended to keep the process simple while minimizing the number parts required. Included were also 1 mm thick rubber gasket seals to provide waterproofing of the unit. **Figure 7-5** below illustrates this layout as well as the OCU's overall dimensions.

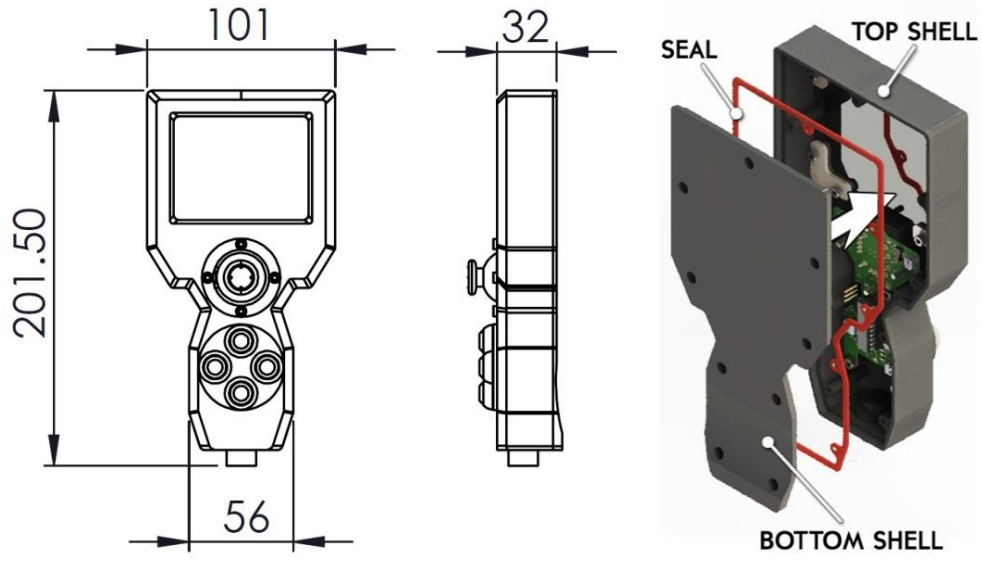

Figure 7-5 - Overall Dimensions of OCU (left), Top, Bottom Shell and Seal Assembly (right)

CHAPTER 7: Operator Control Unit

Similarly to the mechanical chassis, HDPE was used for the OCU's shell material for its high strength-to-weight ratio, and non-conductive properties. Aluminium was also selected for the LCD screen braces, and the sealing ring for the joystick. This was for its high strength-to-weight ratio and corrosion resistance. During assembly, it was discovered it also provided a complementing aesthetic to the OCU's black HDPE shell.

M3 mounts were provided inside for mounting the OCU PCB as well as for the aluminium braces to secure the LCD screen in place. A transparent Perspex layer in front was provided for protection of the screen, and a seal was provided to protect against any ingress escaping past the screen.

Four IP-67 rated tactile momentary buttons were chosen for use in the OCU, and are shown below in **Figure 7-6**. These were located below the joystick, and within reach of the operator's thumb. The joystick chosen was a standard mini-joystick commonly found in standard hand-held game controllers. At the time of design, these were not available from local suppliers, and therefore had to be salvaged from available game controllers in the laboratory.

Figure 7-6 - Figure 7 4 - IP67 Buttons (left), PS2 Joystick (right)

A design challenge of using the mini-joystick was waterproofing it. Waterproof joysticks were available, but the commercial solutions found were either much too large or costly to motivate their inclusion. A sealing system was therefore designed by utilizing a flexible rubber material to cover the joystick gap. This is secured at the top by compressing it between the threaded shaft and the top HDPE cap, as illustrated in **Figure 7-7** below:

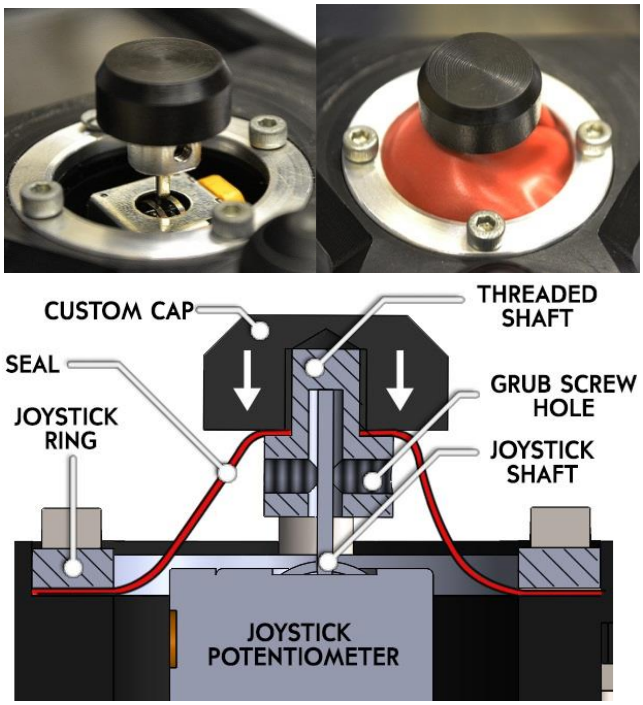

Figure 7-7 - Joystick Sealing System: Cap and Threaded Shaft Assembly (top left), Cap with Seal Assembled (top right), Cross-Sectional Diagram of Sealing System (bottom)

7.3. ELECTRONICS DESIGN

The electronics of the OCU included the main board, which was designed with the primary purpose of providing a simple means of collating the data from the sensors and tactile inputs and sending it to the control station using RS-232. Included was also the LCD screen to display the OSD video.

7.3.1. OCU BOARD

The OCU board utilizes a **Texas Instruments MSP430G2553** 16 MHz 16-bit embedded microprocessor to compile data to be transmitted via RS-232 using a MAX3232EI transmitter. This microprocessor was selected for its low power consumption; drawing 230 µA in Active Mode, and 0.5 µA in Standby. It was also a very cheap solution for the functionality required, and was easily accessible during development via the manufacturer's free sample programme.

During development, two generations of the board were designed and assembled. The initial prototype tested the microprocessor and the magnetometer. The final PCB incorporated all the same circuitry, but included a new transistor switch for turning off the LCD screen, as well as replacing the original 3.3 V regulator with a unit less susceptible to ESD damage. The board shape was also modified to become more compact, and made more user-friendly for maintenance and assembly. The final board is shown below in **Figure 7-8**:

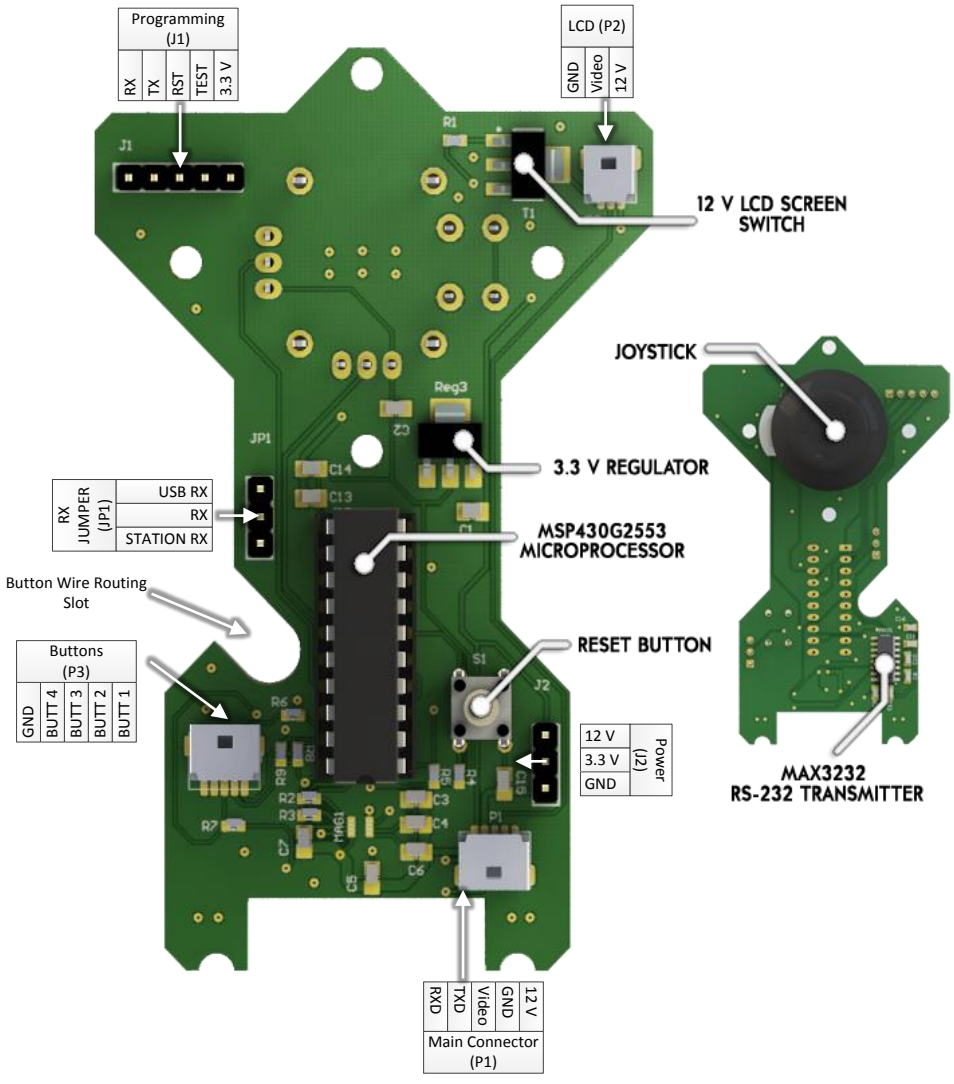

Figure 7-8 - Render of OCU Board: Top Side (left), Bottom Side (right)

7.3.2. LCD SCREEN

Figure 7-9 - OCU LCD Screen Output Showing OCU

As shown above in **Figure 7-9**, a 3.5'' 320 x 240 resolution TFT LCD screen was selected to display the video feed coming from the system. It has 4:3 aspect ratio, and can display either a PAL or NTSC video format in RGB colour. It has a nominal supply voltage of 12 V and draws approximately 80 mA.

7.3.3. MAGNETOMETER SENSOR

At the time of design, the **ST Electronics MAG3110** digital magnetometer was one of the few cost-effective choices available from local suppliers. This has a sensing range of approximately 1000 µT and was deemed suitable for the purpose of a simple compass. It uses a nominal supply voltage of 3.3 V at 900 µA and communicates with the MSP430G2553 via I^2C.

During the layout of the OCU board's components, it became imperative to locate and orient the magnetometer correctly. This was to ensure the origin point was centralized on the operators palm area, and that the axes were aligned perpendicularly to each of the shell's sides. **Figure 7-10** below illustrates both the location of the magnetometer and the axes from the origin point.

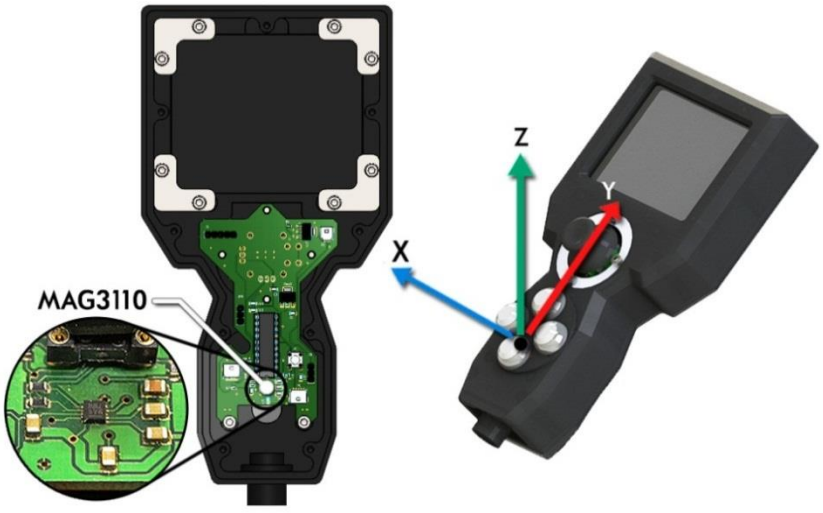

Figure 7-10 - Alignment and Placement of Magnetometer Origin and Axes in OCU

Currently, the compass can only work when the OCU is placed on a horizontal flat surface. Tilt compensation can be introduced by adding an accelerometer to the system.

As discovered in the background research, magnetometers require calibration before their data can be used. A calibration sequence was therefore implemented, and this is covered later in **Chapter 9. Firmware Design**.

7.3.4. OCU CABLE

The OCU cable was made to be approximately 2 meters long to provide enough slack for ease of operation and movement whilst routed along the vest. The extra length also accommodated for fellow team members standing next to the operator to use it. IP-67 rated Switchcraft EN3 female and male connector pairs was used on each end, as shown below in **Figure 7-11**:

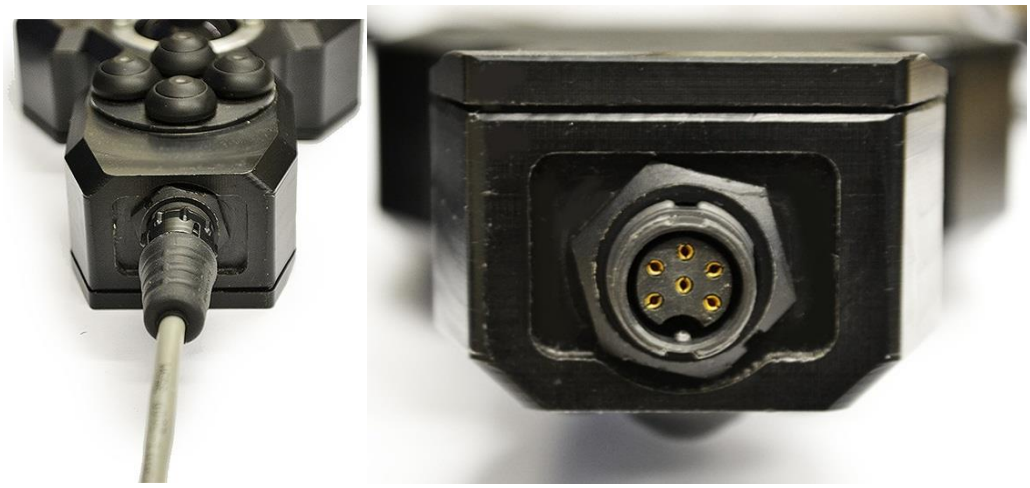

Figure 7-11 - OCU Male Connector (left), OCU Female Connector (right)

The cable itself is a 6-core foil-shielded data cable. The wiring for the connectors is illustrated below, and applies identically to both ends of the cable:

Table 7-2 - OCU Cable Wire Functions

Pin	Wire Colour	Function
1	Black	Ground/Shielding
2	Red	12 V Supply
3	White	TX (to OCU)
4	Blue	RX (from OCU)
5	Green	Not Used
6	Yellow	OSD Video Signal

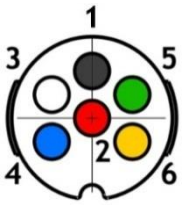

7.3.5. PROGRAMMING

To program the MSP430G2553, a MSP430 LaunchPad was used. This is the device's evaluation board which provides both a programming interface as well as a virtual serial communications port for transmitting data to a computer via USART. The connection layout is illustrated below in **Figure 7-12**:

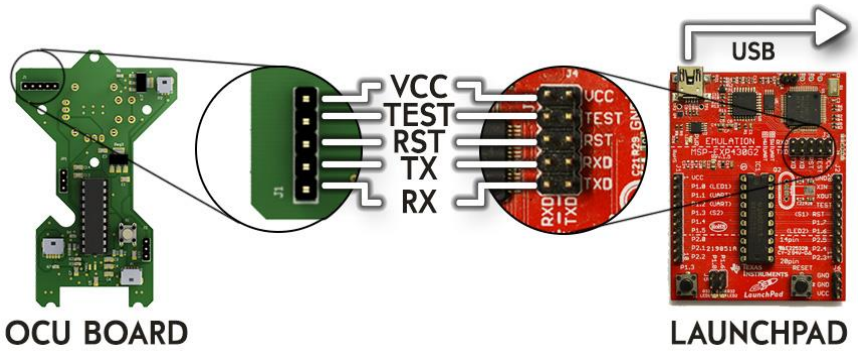

Figure 7-12 - Programming and USART Connections between OCU Board and MSP430 LaunchPad

CHAPTER 7: Operator Control Unit

7.1. SUMMARY

A one-handed hand-held controller was designed to fulfil the specifications required by the subsystem. This included both a complete mechanical and electronic design to encompass a complete stand-alone interface unit. Emphasis was given on the shape of the controller to ensure that it would fit comfortably on a person's hand and being easy to hold.

Chapter 8. Power Supply, which follows, details the design and development of the control station's power supply, which is responsible for all the electronics for maintaining the system's battery, and distributing power throughout the entire Scarab system.

8. POWER SUPPLY

Design of the power supply was critical to the system as it essentially represented the heart of the control station. It emphasised on providing protection and monitoring circuitry to keep system's battery safe as well as providing a window for the operator to see the state of the internal electronics. Also of crucial importance was the power distribution system, which provided the bridge between the battery circuitry and the control station electronics. A charging system was also included to allow recharging of the battery while the system was not in use. **Figure 8-1** below illustrates the subsystem's four main modules. As implied by its name, the majority of the electronics is located primarily in the Power Box, except for the power distribution board, which is mounted in the Back Box.

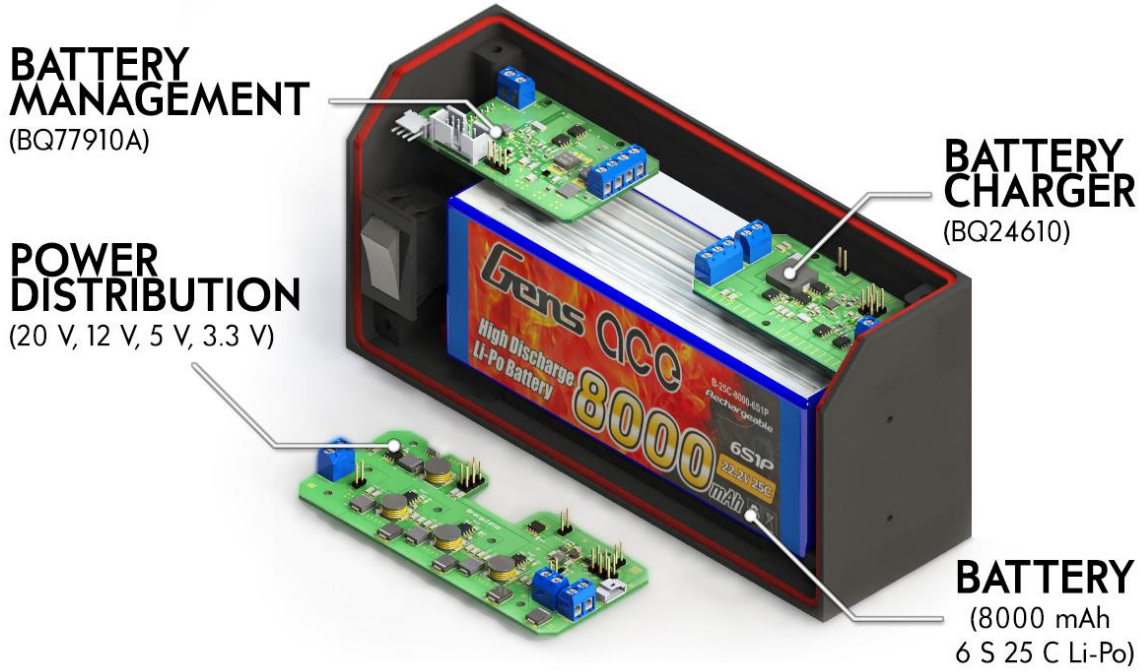

Figure 8-1 - Power Supply Subsystem Components

Similarly to the control station electronics, all the PCBs were custom-designed in Altium Designer and outsourced to be manufactured by BETA-Layout, and the assembly was done in-house within RARL by the author. Each PCB was designed from the ground-up, using the ICs' evaluation modules as the reference schematic designs. To comply with the current track temperature requirements, A 70 µm copper thickness was used for all boards in the subsystem.

This chapter discusses the selection and design of the subsystem's electronics, as well as the integration with the rest of the system. As such, the following topics are covered:

- **Subsystem Specifications and Criteria Justifications**
- **Subsystem Overview**
- **Battery Selection**
- **Battery Management Module**
- **Battery Charging Module**
- **Power Distribution Module**

This chapter begins by listing the subsystem specifications before presenting the subsystem overview.

CHAPTER 8: Power Supply

8.1. SUBSYSTEM SPECIFICATIONS

Subsystem specifications were vital in ensuring that the power supply's modules were designed in accordance with the system requirements.

Presented below are the **Subsystem Specifications** for the power supply. Values which are denoted with a " * " can be referred back to in the **Primary System Specifications**.

The motivation behind each criteria can be viewed in the **Subsystem Specification Justifications** which follows thereafter.

Table 8-1 - Power Supply Subsystem Specifications

Part	Specification	Desired Value
Battery Specifications		
1	Battery type	Lithium-ion polymer
2	Minimum battery nominal voltage	19 V
3	Minimum discharge rate	15 A
*	Platform battery charge cycles	2
4	System uptime (including charging)	3 hours
*	Battery Management System	Yes
Charger Specifications		
5	Minimum charge rate	1 A
6	Charge rate	5 A
7	Power supply selector	Yes
Power Distribution Specifications		
*	Power rails	3.3 V, 5 V, 12 V, 20 V
8	Current output (20 V)	8 A
9	Current output (3.3 V, 5 V)	1 A
10	Current output (12 V)	2 A

8.1.1. SUBSYSTEM SPECIFICATION JUSTIFICATIONS

8.1.1.1. Battery Specifications

1. Li-Po batteries were selected for use of the control station, following the conclusions derived in the background research.
2. A 19 V minimum battery nominal voltage was specified to comply with the requirements for G. Knox's battery charger, as previously discussed in the system specifications.
3. The maximum combined current output of the system was calculated as follows:
4.

   Therefore 15 A was specified for the maximum discharge current required. The extra 5 A was added to account for future additions and providing a safety factor.

8.1.1.2. Charger Specifications

5. The robotic platform's battery was specified for 20 minutes of uptime for one deployment. Because 2 charge cycles were specified for the system, a total of three deployments should be supplied for, which amounts to a total of 1 hour system uptime required. 3 hours was therefore specified to give the operator control station enough system uptime for 3 consecutive missions. It also provides ample time for it to be transported from storage to the disaster zone, and a large preparation window.
6. While it is not critical for the control station to be charged quickly, a full charge should be achieved within a single day. Therefore 1 A was specified as the minimum charging rate.
7. The charge rate was specified after the battery was selected for the system. For the 8000 mAh battery, it was determined that a 5 A charging rate would allow the battery to be fully charged within 1 hour and 36 minutes. This allowed it to be ready for rescue operations on demand within a 2 hour time frame.

8.1.1.3. Power Distribution Specifications

8. During charging, the control station should use the charger's external supply instead of the battery. It should also be able to select to be powered off an external supply instead of the battery, when at storage. This introduces an **U**ninterruptible **P**ower **S**upply (**UPS**) aspect to the system.
9. As previously discussed in the system specifications, G. Knox's battery charger was specified to draw a maximum of 8 A at 20 V.
10. The 3.3 V and 5 V supply rails are responsible for powering the low power devices throughout the control station, which when combined, draw approximately 200 mA. Therefore 500 mA was specified to provide space for future additions and a safety factor.
11. The 12 V supply rail is responsible for powering all of the control station's electronics, including the OCU. Preliminary testing of the current consumption of the peripherals provided for the project showed a total of approximately 1 A. Therefore 2 A was specified to provide extra design space as well as a safety factor. Note that this value includes the 200 mA specified for the 3.3 V and 5 V supply rails.

8.2. SYSTEM OVERVIEW

Layout of the power supply subsystem was highly dependent on the reference schematics supplied by the ICs' manufacturers. Therefore it was crucial to select parts which were compatible from one module to the other. As a result, all the battery circuitry incorporated parts from Texas Instruments, which provided a wide array of battery management and charging solutions. This included the battery protection and fuel gauge, as well as the charger.

A simplified wiring diagram of the complete power supply system is shown below in **Figure 8-2**. This shows the main connections from the battery to its management and charging boards to the power distribution board. In the context of the design schematics and this chapter, the following terms are used to describe the main connections to the boards:

- **BATT** - Battery connections (BATT+ / BATT-).
- **PACK** - External power supply connections (PACK+ / PACK-).
- **VSYS+** - Positive supply rail to power distribution board.
- **DSG-** - Negative supply rail to power distribution board.
- **CHG-** - Negative supply rail to battery charger board.

Note that the positive supply rail (VSYS+) to the power distribution board is controlled by the battery charger board. This was due to the charger's included system power selection feature, which allowed the system to choose between the battery and external power supply as the system supply. This is covered more extensively later in this chapter. It should also be noted that the power distribution board is responsible not only for powering the system, but also provides a 20 V rail for the robotic platform's charging circuitry. It therefore acts as the bridge between the two Scarab subsystems.

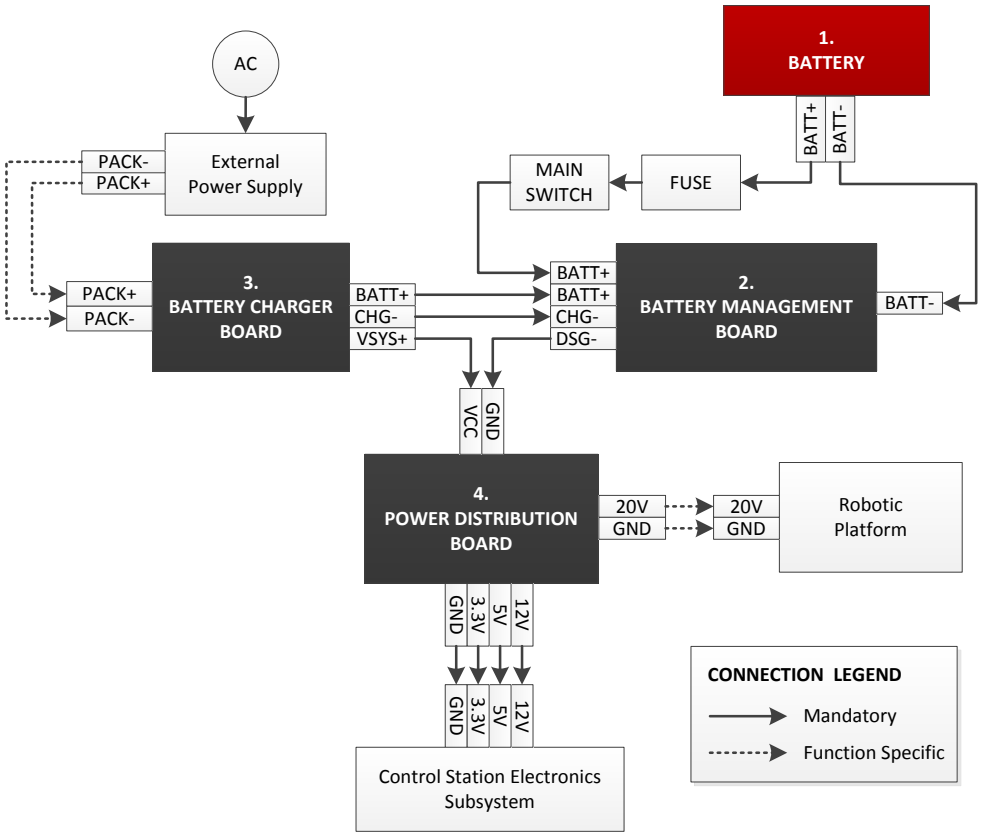

Figure 8-2 - Power Supply Subsystem Main Connection Diagram

8.3. BATTERY

As determined by the subsystem specifications, a Li-Po battery was chosen for use in the control station. To choose a suitable battery, criteria including the nominal voltage, capacity, and discharge rate were investigated Also taken into consideration was the safety and viability of the battery for use on a mobile system. These will all be covered in this section before presenting the final solution.

8.3.1. NOMINAL VOLTAGE

The specified nominal voltage required was 19 V. A **6 S** battery therefore satisfied the criteria, with a nominal battery voltage of 19.2 V (3.7 V each cell). This provided a supply voltage range between 18 - 25.2 V.

8.3.2. CAPACITY

To determine the capacity required for the battery, the power required to charge the robotic platform's battery, as well as supplying power to the control station's system was calculated.

This started with calculating the required charging power. The battery on the robotic platform is a **4 S 3000 mAh** Li-Po battery, with the voltage of a fully charged cell being 4.2 V.

Charging efficiencies were also taken into account. For the calculations, an efficiency of **80 %** was used. This was to include both the robotic platform's charger efficiency of 96 % for 4-cell charging, as well as the 85 % efficiency of the power distribution board's 20 V regulators' when outputting 8 A. The extra 5 % was used to account for additional electronic and line transmission losses.

Therefore **63 Wh** was required for one charge at 80% charging efficiency. For two charges this translated to **126 Wh**.

Next was the system uptime. The subsystem specifications listed a minimum of 3 hours required. Additionally, the control station electronics were specified to draw a maximum of 2 A at 12 V.

Therefore a battery capable of providing **198 Wh** was required. The required battery capacity could then be finally calculated using this value, with the above selection of a 6S battery with a full cell voltage of 4.2 V:

A **7860 mAh** battery was therefore required. **8000 mAh** was selected as this was the closest value in the available range of commercial Li-Po batteries.

8.3.3. DISCHARGE RATE

For an 8000 mAh battery, a minimum discharge rate of **0.53 C** was required to achieve the 15 A current output.

8.3.4. FINAL SELECTION

The battery selected for use of the system was a **Gens Ace 6 S 8000 mAh 25 C Li-Po Battery**. This satisfied all the criteria required. The unit is shown below in **Figure 8-3**.

Gens Ace batteries are commonly used for quad copters, UAVs, and multi-rotor helicopters and the like, being designed to be sent flying around the sky at high velocities. Comparatively, for the purpose of being carried on an ambling operator person, this was deemed suitable.

Figure 8-3 - Gens ace Li-Po 8000 mAh 6S 25 C Battery

8.3.5. FUSE AND POWER SWITCH

A 15 A blade fuse was provided to provide a hard cut-off of the battery from the system in the event of any overcurrent or short-circuit conditions. This was housed using an in-line fuse holder, as shown in **Figure 8-4**. To turn on the control station, a 15 A switch was used to connect the battery to the system.

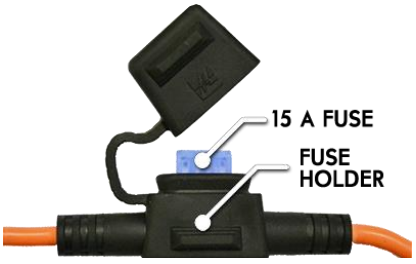

Figure 8-4 - Fuse Holder

During testing it was discovered that current inrush issues were had with the charger board upon system start-up. A 5 Ω NTC inrush-limiting thermistor was therefore implemented on the line, which mitigated the problem. Two connectors were used to bypass the thermistor once the system has completed its start-up sequence, and is done manually by the user. The connection diagram is shown below in **Figure 8-5**.

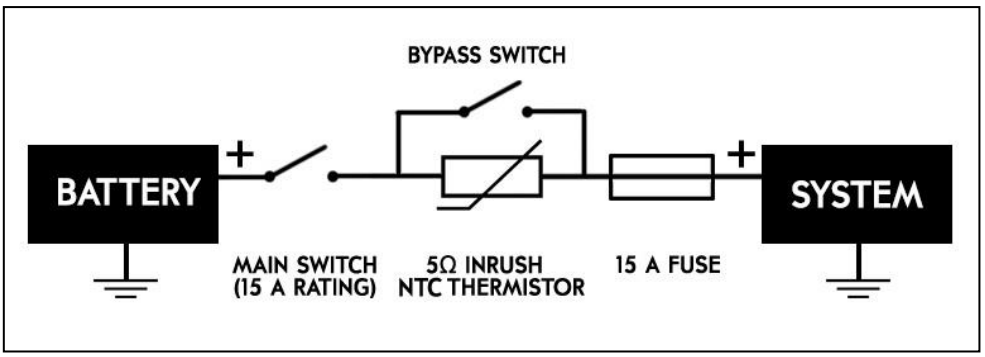

Figure 8-5 - Battery Connection to System

8.4. BATTERY MANAGEMENT

Design of the battery management board aimed to include both the functionality of battery protection and battery fuel gauging. The battery protection would serve as a supervisor for the battery, and terminate connections with the rest of the system should any faults occur. The battery fuel gauge would provide the operator a monitor for the battery's state on the user interface. It also allows the system and operator to act accordingly before encountering any extreme thresholds, providing a soft buffer for the battery protection.

These were both implemented on the final board, as shown below in **Figure 8-6**. The following parts were used for each function:

1. **Battery Protection** – Texas Instruments BQ77910A
2. **Battery Fuel Gauge** – Texas Instruments BQ34Z100

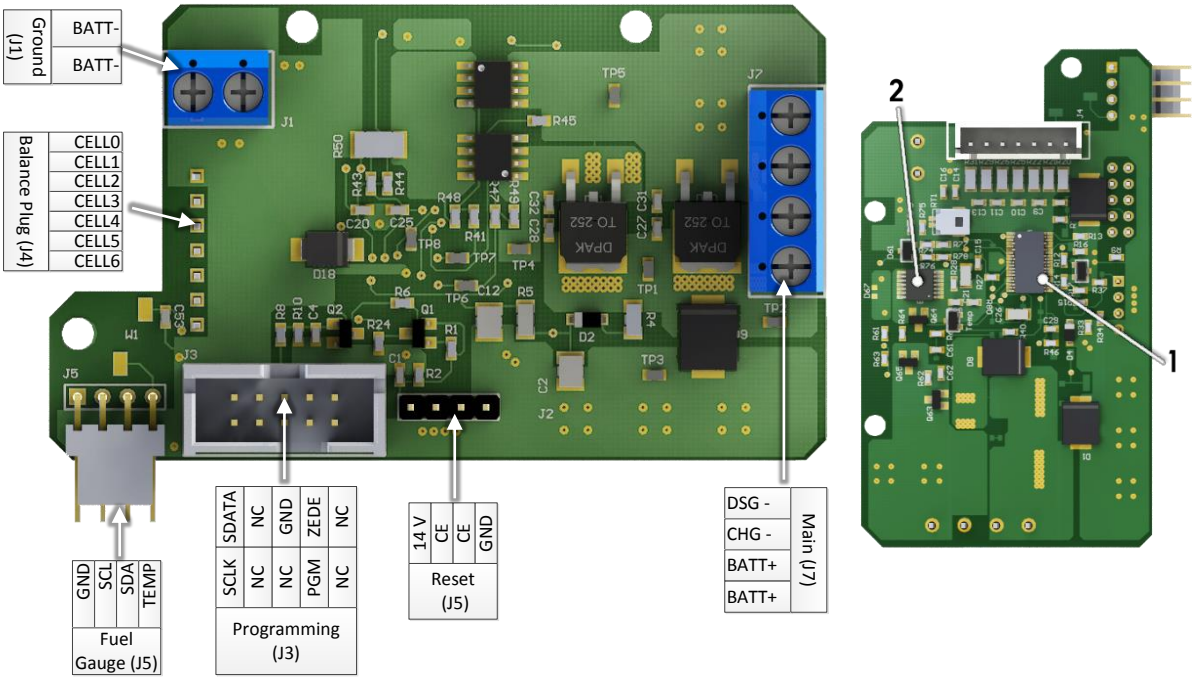

Figure 8-6 - Render of Battery Management Board: Top (left), Bottom (right)

A single generation of the board was manufactured and assembled, and was deemed suitable for use with the system.

This section will explore both devices, providing their functions as well as diagrammatic explanations of the critical areas. It will also provide a brief overview of the user interface required to configure both the devices' settings.

CHAPTER 8: Power Supply

8.4.1. BATTERY PROTECTION

The **Texas Instruments BQ77910A** was chosen as one of the few battery protection solutions available for 6-cell Li-Po batteries during the time of design. It is a stand-alone part, meaning it does not require additional processing circuitry to control it, and includes embedded EEPROM for programmable functions. The basic specifications of the IC are described below:

Table 8-2 - BQ77910 Battery Protection IC Basic Specifications [82]

Company:	Texas Instruments	
Supply Voltage:	5.6 – 50 V	
Supply Current:	50 µA	
Series Cell Protection:	4 - 10	

The IC protects the battery by monitoring it for any fault conditions using the board's included circuitry. A multitude of functions are included, with thresholds which can be set by the user:

Table 8-3 - BQ77910A Battery Protection Functions

No.	Programmable Functions	Fixed Hardware Functions
①	**Cell overvoltage** Preventing overcharging of each cell.	**Over-temperature Protection** Detect if temperature reaches over 60°C.
②	**Cell undervoltage** Preventing further discharging of the battery under low-battery conditions.	**Open-Cell Detection** Close battery from system upon any open cells detected.
③	**Pack Discharge Overcurrent** Prevent further discharge if the load current surpasses a set threshold.	**Open/ Shorted Thermistor Detection** Close battery from system if thermistor is open or shorted.
④	**Pack Discharge/Charge Short-Circuit** Close battery from system upon detection of short-circuit.	**Brownout Detection** Shut off FETs to prevent them overheating under low-battery conditions.

8.4.1.1. Protection MOSFETS

Two low-side 40 V, 20.5 A N-MOSFET switches were used to control the current flow between the battery and the system:

1. **Charge (CHG) FET** – Controls current flow **TO** the battery.
2. **Discharge (DSG) FET** – Controls current flow **FROM** the battery.

When encountering any fault conditions, the **BQ77908A** shuts off the MOSFETS, isolating the battery away from the rest of the system, and protecting both from further damage. These are illustrated and described below in **Figure 8-7**.

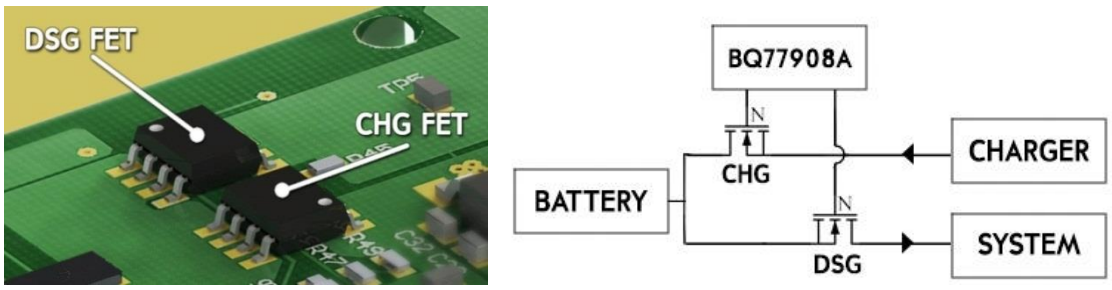

Figure 8-7 - Protection MOSFETs: Location (left), General Implementation (right)

Both MOSFETS were located at the top side of the board to avoid dissipating heat onto the battery below. This also aimed to keep all the high power tracks on the top side, and the low-power control circuitry on the bottom.

8.4.1.2. Current Sensing

Current sensing was required to detect any overcurrent and short-circuit fault conditions. For this purpose, a 1 mΩ sense resistor was used. As prescribed by the BQ77908A's datasheet, a Kelvin contact was used to establish connection between the resistor and the IC. This aimed to minimize the measurement errors caused by wire resistance. The connection is illustrated in **Figure 8-8.**

Note the same resistor is used for current sensing for the **BQ34Z100** fuel gauge on the same PCB.

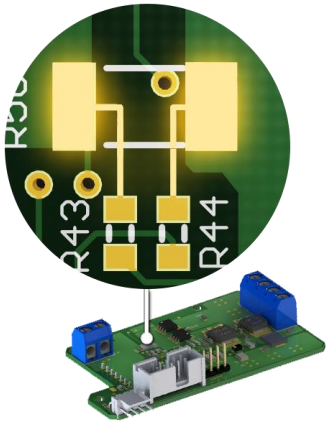

Figure 8-8 - Kelvin Connection for Sense Resistor

8.4.1.3. Thermistor Connection

A 10 KΩ NTC thermistor was used for temperature measurement of the battery. This is connected using a 2-pin Pico-Clasp connector available on the bottom of the board.

8.4.1.4. Cell-Balancing and Voltage Monitoring

Cell balancing ensures that the battery cells are always at the same voltage. This is vital in preventing overcharging of each of the battery's cells and prolonging the battery life. The BQ77908A includes this functionality, and in the IC settings, this was configured to occur only during charging. This was to prevent unnecessary current draw while the system was idle. A 7-pin JST-XH header was located on the bottom of the board for the battery's balancing connector. This also allows for cell voltage monitoring as well as open-cell detection.

8.4.1.5. Battery Error Recovery

On the PCB, a **C**harge-**E**nable (**CE**) header pin was provided. Pulling this high opens the CHG MOSFET, allowing current to flow from the charger board to the battery. Importantly, this pin also acts as a reset to recover from an error condition and reopens the MOSFETs to restore power to the system. To clear the error state, the pin must be toggled from low to high after resolving the fault cause. On the OSD user interface, this can be toggled using the "Charge Operator Station" menu option. If the user interface cannot be accessed, a full power cycle is required.

8.4.1.6. Chip Programming

The BQ77908A's programmable functions are stored in EEPROM which can be accessed using a SPI serial communications interface. Texas Instruments has made available an evaluation software package for use in Microsoft Windows, making it possible to configure the IC settings using a GUI interface. This required a separate Texas Instruments **USB-TO-GPIO** adapter module, which was used to establish communication between the IC and the computer. Note that a separate 14 V supply is also required for programming. The connection configuration is shown in **FIGURE** below:

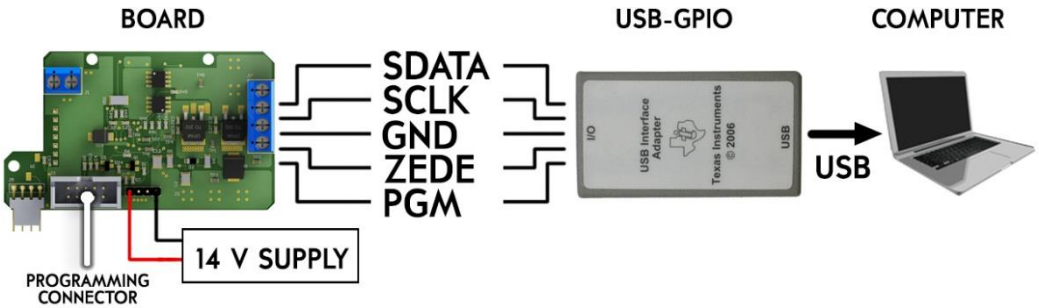

Figure 8-9 - Battery Protection Programming Connections

8.4.2. BATTERY FUEL GUAGE

The **Texas Instruments BQ34Z100** was selected for the system for use as the battery fuel gauge. This was chosen for its large variety of monitoring functions, allowing the user to acquire information about the control station's battery. It also required minimal external components, which further motivated its inclusion. The basic specifications of the IC are listed below:

Table 8-4 - BQ34Z100 Battery Fuel Gauge IC Basic Specifications [83]

Company	Texas Instruments
Supply Voltage	2.7 – 4.5 V
Supply Current	140 µA
Battery Voltage	3 – 65 V
Battery Capacity	Above 65 Ah

Values are extracted from the fuel gauge to the Central Processing Board for application on the user interface. For this purpose, only values which were useful and intuitive to the operator were chosen: the battery voltage, state of charge, and average current draw. In the firmware these were utilized to setup warning indicators if any critical thresholds were met. These are later discussed in **Chapter 9. Firmware Design**. To communicate between the two modules, I^2C serial communications was used, as required by the BQ34Z100.

8.4.2.1. Battery Measurements

To measure the battery current, the same 1 mΩ sense resistor for the BQ77908A was used. The battery voltage is measured using a voltage divider, with the resistor values prescribed by the device datasheet. The voltage value is then calculated internally by the IC.

Battery state of charge is measured using the IC's internal coulomb counter. Coulomb counting is the method of measuring the battery current and then integrating it with time. However, because it is an integral, a known starting point is required.

Since every value required internal calculations and specific component selection, prior configuration and calibration of the device settings was mandatory for operation. Without doing so, the readings from the fuel gauge were essentially meaningless.

8.4.2.2. Calibration and Configuration

To calibrate the fuel gauge, Texas Instruments has made available a **bq Evaluation** GUI software package for Microsoft Windows. This provides a complete step-by-step calibration sequence as well as tools to configure and record the IC's settings and readings.

During development, communication was established between the BQ34Z100 and a computer using a **Texas Instruments EV2400** evaluation module. The connection configuration is shown below in **Figure 8-10**

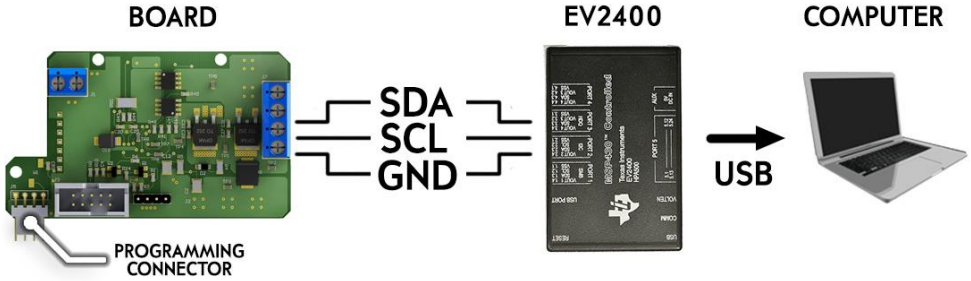

Figure 8-10 - Battery Fuel Gauge Programming Connections

8.5. BATTERY CHARGER

Design of the battery charger was motivated by the need to include a charger to recharge the battery whilst in storage. This would mitigate the requirement for an external third party charger, and also allowed for the possibility for both the Scarab systems' batteries to charged using a single supply. The final board is shown below in **Figure 8-11**.

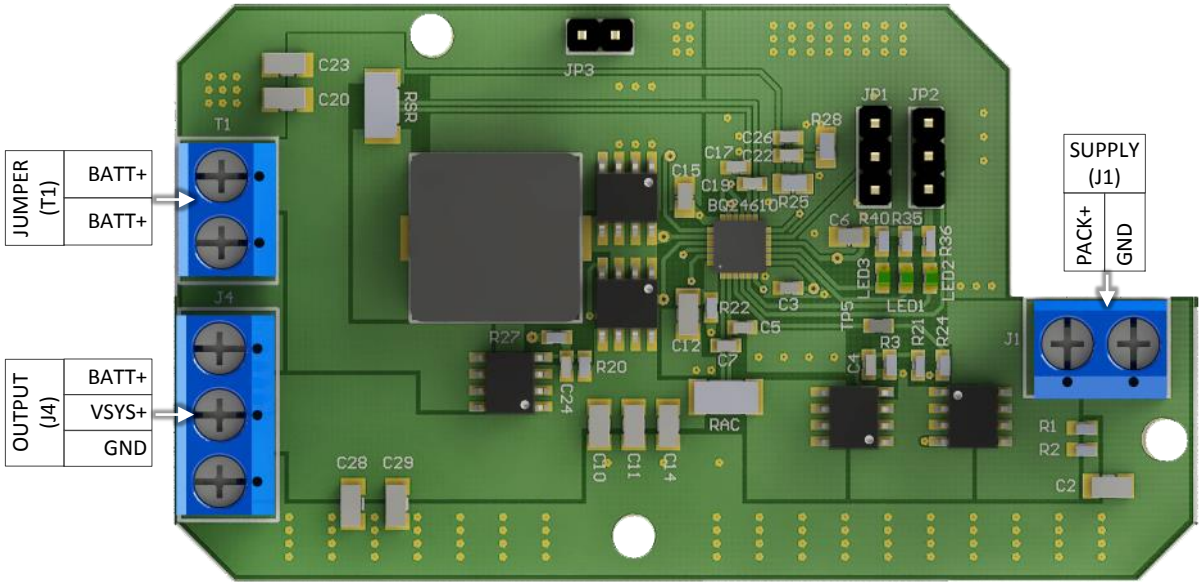

Figure 8-11 - Render of Battery Charger Board

For the complete Scarab system, two charging schemes were envisioned to set different charge rates depending on the situation required. These are listed below:

- **In-Field Charging –** While the Scarab system is out in the field and the robotic platform is docked into the control station for charging its battery.
- **Storage-Mode Charging** – While the Scarab system is in the storage area, and both the control station and robotic platform battery is to be charged and ready for the next mission.

The following charge rates were set for each charging scheme. This aimed to reduce the cost required for an external supply which could supplement the charging of both systems at the same time.

Table 8-5 – Charging Schemes and Rates

Charging Scheme	Charge Rate (A)	
	Robotic Platform	Control Station
In-Field Charging	8	0
Storage-Mode Charging	1	5

This section will cover the selection of the IC used as well as the incorporated features which were implemented for use in the control station.

8.5.1. CHARGER IC SELECTION

The first charger PCB prototype design utilized the **Texas Instruments BQ24600**, a stand-alone synchronous switch-mode charger. This was later replaced by the newer **BQ24610** charger, which offered similar functionality, but with the added benefit of a system power selection feature. The basic specifications of this IC are listed below:

Table 8-6 - BQ24610 Charger IC Basic Specifications [84]

Company:	Texas Instruments
Charger type:	600 kHz NMOS-NMOS Synchronous Buck Converter
Battery support:	Li-ion, Li-Po (1 – 6 S)
Charge current:	Up to 10 A
Voltage Input:	5 – 28 V

8.5.2. CHARGING

Two 40 V, 13.6 A N-MOSFETS were used for the synchronous switching battery charger, with the 6 V gate drivers being internally integrated into the charger IC. To enable charging, the **C**harge **E**nable (**CE**) pin must be set high. This is shown in **Figure 8-12.**

To satisfy the subsystem specification requirements, a 5 A charge rate was set for the charger. This uses the on-board resistor divider network to set the voltage required for this value. This can be changed by removing the jumper on JP1, shown in **Figure 8-12**, and use an external voltage source to determine the rate instead.

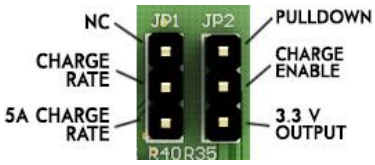

Figure 8-12 - Charger Jumpers

8.5.3. LED INDICATORS

To indicate the state of the charging process, three LEDS were used, as illustrated below in **Figure 8-13**. “Power good” refers to when the charger has a valid supply voltage.

Table 8-7 - Charger Board LED Indicators

LED		Indication
●●●	PG (CE low)	Power good
●●●	PG + STAT1	Charge in progress
●●●	PG + STAT2	Charge completed
●●●	PG (CE high)	Power good, charge suspend, timer fault, overvoltage, sleep mode, battery absent

Figure 8-13 - Charger LEDs

8.5.4. CURRENT MANAGEMENT

The **BQ24610** provides current management using its **D**ynamic **P**ower **M**anagement (**DPM**) system. This automatically reduces the charging current should the overall current to both the battery and system reach over a pre-set threshold. This protects the power supply from overload, and provides extra flexibility to the system’s usage of power from the battery. This threshold was set to 10 A to accommodate the combined system load in storage mode. To monitor the current, a 10 mΩ sense resistor was included on the board.

8.5.5. CHARGER POWER SUPPLY

To supply power to the charger, an external power supply is used. This is connected to the control station using the two banana plug jacks located underneath the Power Box. The setup is illustrated in **Figure 8-14**. The BQ24610's datasheet recommends an input voltage of at least 1.5 V - 2 V above the battery voltage for charging. Therefore a power supply which can output 27.2 V at 8 A was suitable. The 8 A was to account for both the total charging at 6 A, and the system load of 2 A.

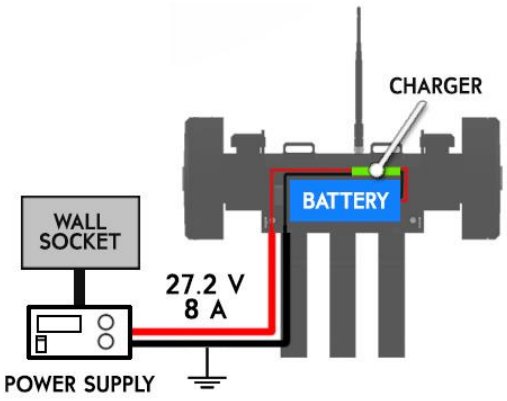

Figure 8-14 - Charger Power Supply Setup

An example would be the **Manson HCS-3302** switch-mode power supply, which was used during testing in the RARL environment. This is displayed below in **Figure 8-15**.

HCS-3302 SPECIFICATIONS	
Output Voltage	1 – 32 V
Output Current	0 – 15 A

Figure 8-15 - Manson HCS-3302 Power Supply

8.5.6. SYSTEM POWER SELECTION

As previously stated, the BQ24610 includes a system power selection feature. This works in that if an external power supply is connected to the charger, and has a higher voltage than the connected battery's voltage, the external power supply is selected to power the control station electronics. This allows the control station to be powered off an external supply while in storage and charging. Importantly, it also isolates the battery from the system during the charging process.

The system supply is determined by using three 40 V, 18 A P-MOSFETS which are controlled by the IC. **Figure 8-16** below illustrates the positive supply rail path to the system (VSYS+) from both possible supply sources:

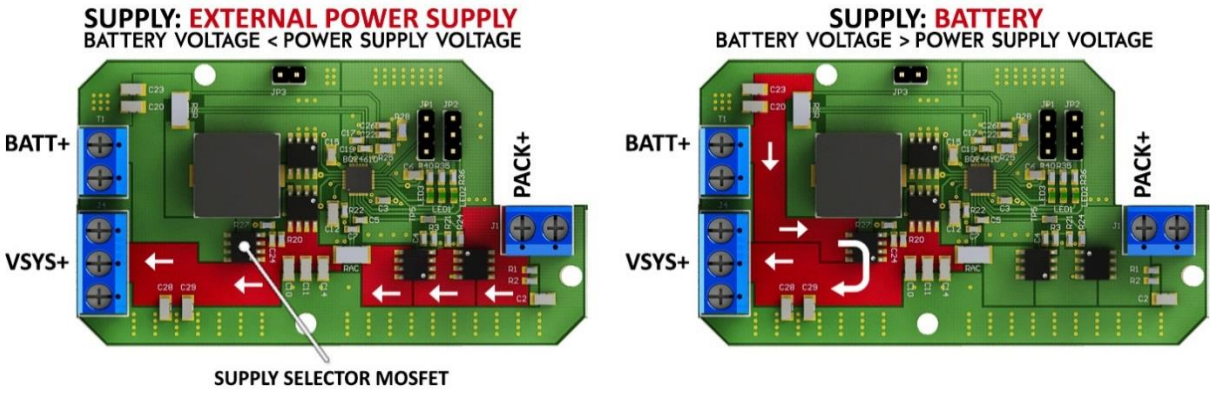

Figure 8-16 - System Power Selection with Supply Path to System

Importantly, if the external power supply were to be disconnected from the system, the battery takes over as the supply without interruption to the system power. This therefore acts as an **U**ninterruptible **P**ower **S**upply (**UPS**) system.

8.6. POWER DISTRIBUTION

The power distribution module incorporates a combination of switching and linear regulators to convert the system supply voltage down into separate supply rails suitable for system use as well as to charge the robotic platform. During design, power efficiency became important as it was essential for keeping the operating station's electronics online as long as possible whilst using the battery as a supply.

The system's power rails, regulators and their connected devices are listed in the table below:

Table 8-8 - Power Distribution Regulator Allocation and Connected Devices

RAIL	CONNECTED DEVICES	REGULATOR	REGULATOR MAX CURRENT
3.3V	1. STM32F407VGT6 MCU 2. MAX3232EI Transmitter 3. LM60 Temperature sensors 4. RF1101SE RF Transceiver board	**Infineon Technologies IFX27001TF** (Linear)	1 A
5V	1. MAX7456 On-Screen Display IC 2. uBlox NEO-7M GPS Board 3. USB Peripheral port	**Richtek RT8258** (Switching)	1.2 A
12V	1. Operator Control Unit 2. Dozen Mini Digital Video Recorder 3. Range Video 1.3Ghz Video Receiver 4. Fatshark Dominator Goggles 5. Cooling Fans	**Richtek RT8289** (Switching)	5 A
20V	Scarab Robotic Platform Charger	**3 x Richtek RT8289** (Switching)	10 A

8.6.1. REGULATION SCHEME

Three cascades of regulation were used, starting from the battery supply voltage. This aimed to minimize the number of voltage regulators required, and reducing the power dissipation losses from high voltage drops. This is illustrated in **Figure 8-17** below.

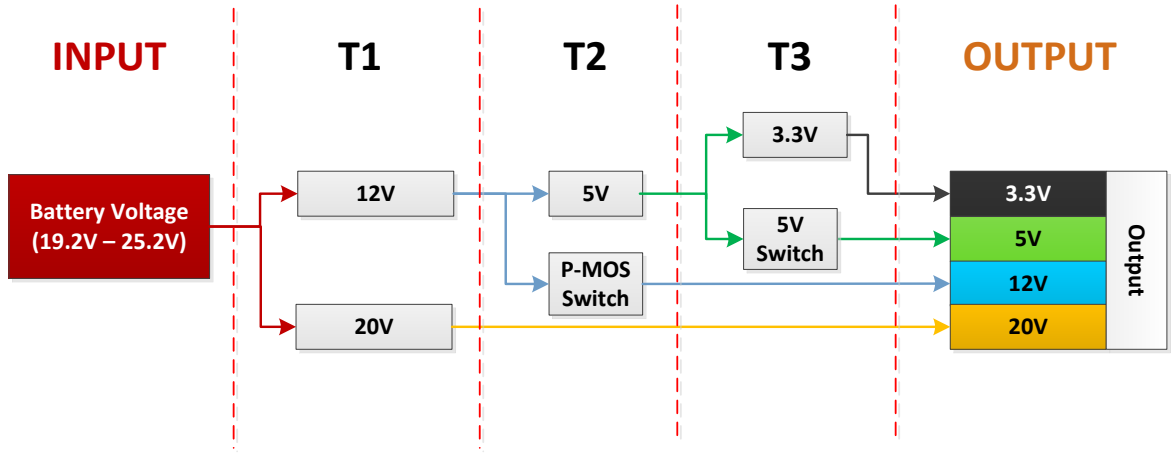

Figure 8-17 – Power Distribution Regulation Cascade

8.6.2. 12 V, 5 V, 3.3 V SUPPLY RAILS

Linear regulators were not suitable on the 12 V and 5 V supply rails due to the high voltage drops at the current required, which resulted in hazardous levels of heat dissipation. Therefore switching regulators were used instead, which had superior power efficiency, but at the cost of requiring more external components. A linear regulator was used for the 3.3 V rail, as this was supplied by the 5 V regulator, and thus had a lower voltage drop.

8.6.3. 20 V SUPPLY RAIL

One of the main design challenges of the board was providing a 20 V supply rail capable of delivering 8 A to the robotic platform for charging. Commercial solutions for regulators were either unavailable, or too expensive and complex for the purpose. DC-DC converters were also investigated, but the available options found were substantially expensive, as well as being physically too large to fit in the control station.

Therefore an alternative solution was to use multiple switching regulators in parallel to produce the combined current output required. Three **Richtek RT8289** 5 A switching regulators were selected for this purpose for their specification and low cost of approximately $ 1 USD per IC. The third regulator was added for a factor of redundancy. A 5 A diode was included on each of the regulator's output lines to prevent feedback current flowing between each of the three regulators. Similarly, a single 15 A diode was located on the combined output to prevent any reverse current flowing back from the robotic platform's battery charger. A simplified schematic is shown below in **Figure 8-18**.

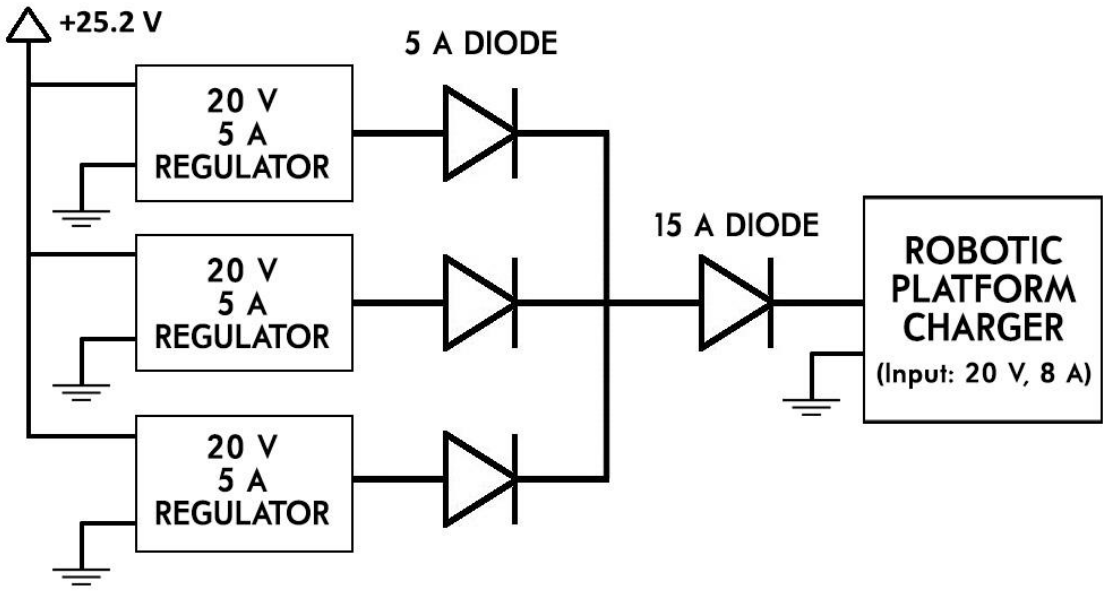

Figure 8-18 - Parallel Setup of 20 V Switching Regulators

8.6.4. REGULATOR OUTPUT SWITCHES

Due to the cascade system, if the 12 V regulator was turned off, the 5 V and 3.3 V regulators would also become offline. Therefore a P-MOSFET switch was used to control the 12 V output instead. Similarly, the 5 V output uses a switch to prevent the 3.3 V rail from going offline upon shutdown.

To turn on these switches, each device has a not-enable pin which must be pulled low. On the system this is done via a logic low signal from the Central Processing Board. There are also jumper-headers on the final PCB to pull the pins low at all times.

The 20 V rail is not affected by the cascade and is therefore controlled by directly switching off the regulators. Unlike the other switches, a logic high signal is required.

The switches were used to control the **Low-Power Mode** set by the Computing Box's control panel button. It was also used for the incremental start-up sequence of the system, which turned on one rail at a time in 1 second intervals. This aimed to prevent any current inrush issues due all the devices turning on at once.

8.6.5. TEMPERATURE SENSOR AND HEAT SINK

To measure the board temperature, a **Texas Instruments LM60** temperature sensor was included on the final PCB. This was located nearby the 5 V regulator and 20 V output as this was foreseen to be the area of highest temperature.

To address any potential heat issues, an aluminium heat sink was designed and manufactured for mounting on the final PCB. Removal of the heat is purely reliant on air-cooling and is aided by the system fans. Heat pad material was used underneath the heat sink to ensure the aluminium part did not come into contact with the conductive components underneath.

8.6.6. PROTOTYPE PCB

A prototype PCB was designed and assembled to provide a testing platform before being developed into the final board. It also served as a backup development power supply without the need for a 20 V supply rail. The board and its connections are shown below in **Figure 8-19**:

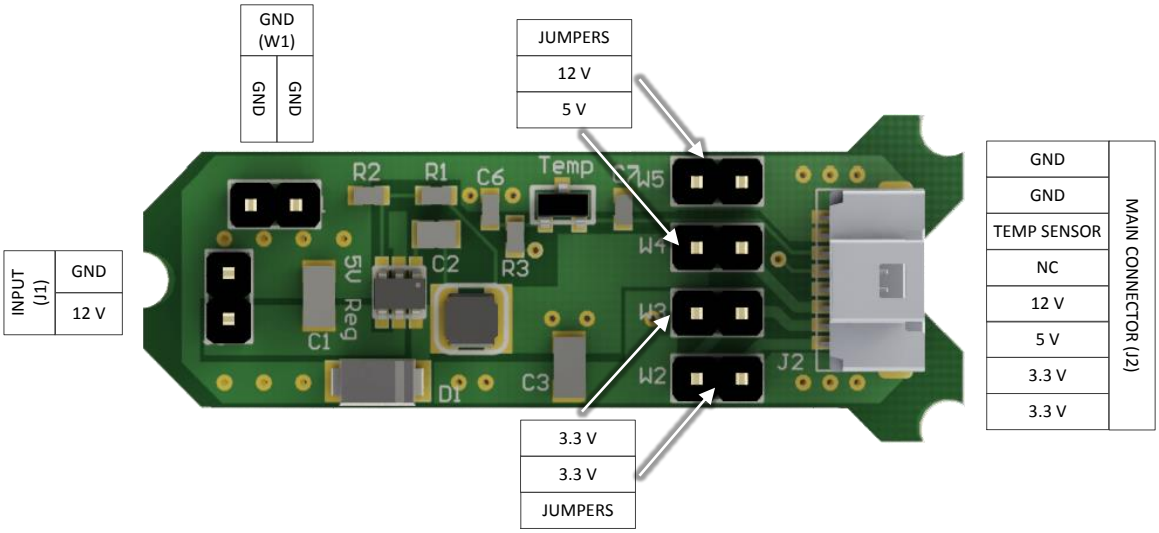

Figure 8-19 - Render of Power Distribution Prototype Board

The board's noise levels were measured to be at a maximum $V_{PEAK\text{-}PEAK}$ of less than 400 mV for all power rails. This stayed consistent with the final board, and was deemed suitable for operation.

CHAPTER 8: Power Supply

8.6.7. FINAL PCB

The final PCB implemented all the regulators used on the prototype, and added the switching regulators used for the 12 V and 20 V rails. Design of the board emphasized on easy maintenance and interconnection with the control station electronics throughout the chassis. The board and its main connections and components are described below in **Figure 8-20**.

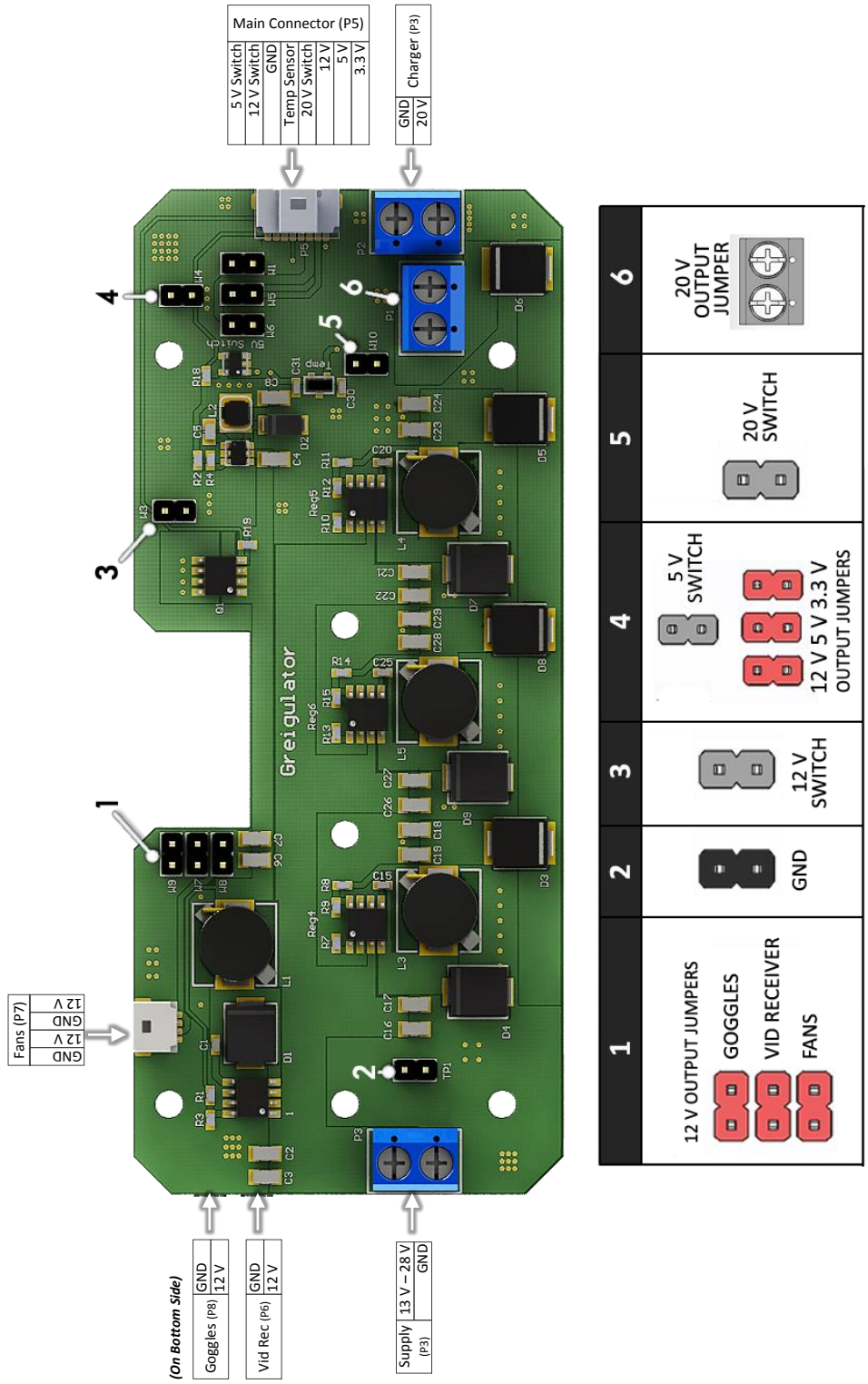

Figure 8-20 - Render of Power Distribution Board and Connections Shown

8.7. SUMMARY

The control station's power supply was designed to fulfil the requirements set by the subsystem specifications. Of vital importance was the included Li-Po battery, which was designed to be supported with protection and monitoring circuitry to ensure its safe and transparent operation whilst being used on a man-wearable system. To recharge the battery during storage, a battery charger was included. A power distribution system was also designed to supply suitable voltages to the control station electronics and the robotic platform for charging.

Chapter 9. Firmware Design, which follows, describes the control and interface firmware that was implemented on the Central Processing Board's STM32F407VG to handle all of the control station's subsystems.

9. FIRMWARE DESIGN

Design of the control station firmware focussed on creating a communications bridge between the operator and the system electronics. This determined the effectiveness and performance of the user interface and thus the appeal of the Scarab system as a whole from a user's point of view.

The system's primary firmware is located exclusively inside the STM32F407VG embedded microprocessor on the Central Processing Board. As required by the control station electronics' specifications, embedded C was used as the coding language. Separate firmware was also written for the MSP430G2553 embedded microcontroller on the OCU board. The CooCox and Energia IDE's were used to develop the C code for each respective microprocessor. Additional software was written in National Instruments' LabVIEW to allow interaction with the control station data on a desktop computer or laptop.

The complete user interface software can be summarized into five stages of the main while loop in the STM32F407VG, as shown below in **Figure 9-1**. This starts at the User Input stage which receives data from the OCU firmware's generated USART serial packet. Data is then collated and processed throughout the proceeding stages before being sent to the sensor payload, or a desktop computer.

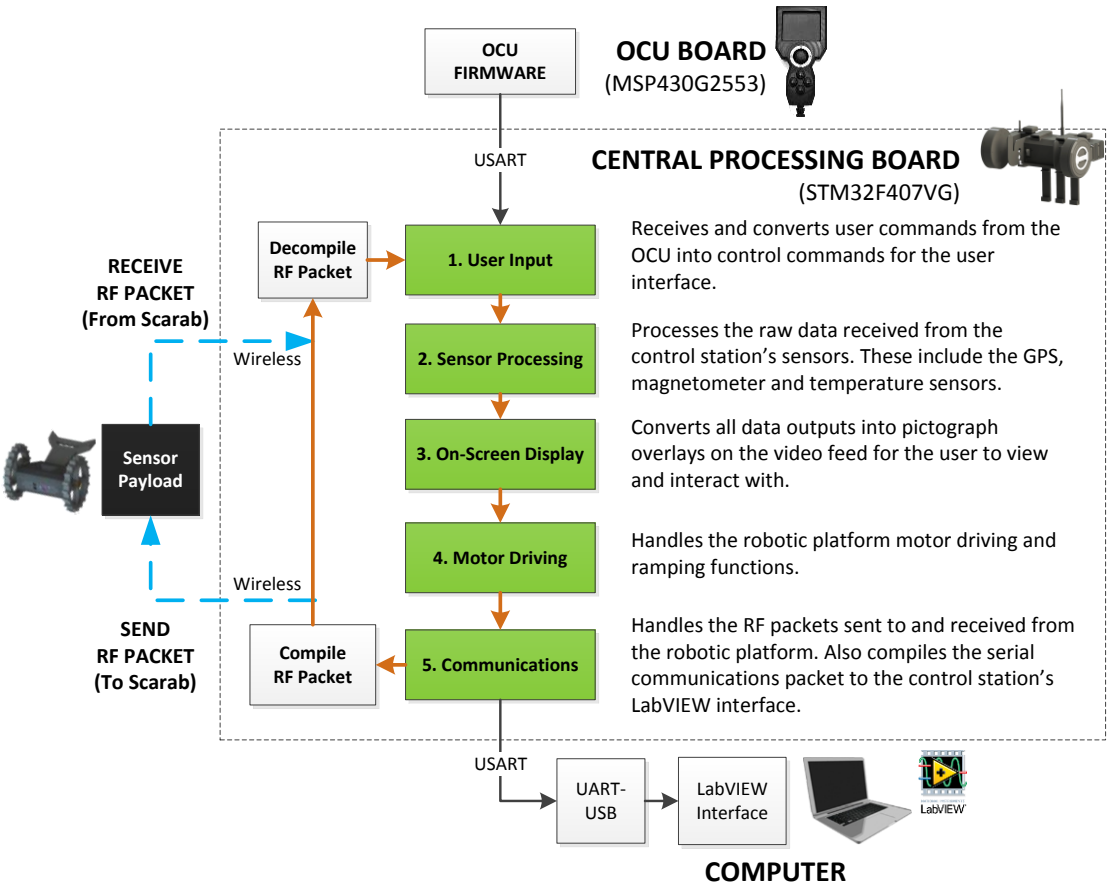

Figure 9-1 - Control Station Firmware Layout

This chapter begins by introducing the OCU firmware, which is responsible for capturing the user input data and compiling it to be sent to the Central Processing Board. It will then proceed to cover each of the five stages of the STM32F407VG code described above. A brief overview of the LabVIEW operator control station software will also be provided at the end.

CHAPTER 9: Firmware Design

9.1. OCU FIRMWARE

The primary purpose of the OCU firmware was to receive data from the controller's tactile user inputs and the magnetometer before compiling it into a single packet sent back to the control station. It includes four main operating modules, including

- The ADC to read in the button and joystick analogue data,
- An I^2C interface with the magnetometer,
- The internal temperature sensor, as well as
- The communications interface to the control station.

This OCU USART serial interface was set to constantly transmit at a baud rate of 9600 bps at 50 millisecond intervals. Using global variables, all of the above mentioned module's data were compiled into a single 14-byte serial USART packet before being transmitted to the Central Processing Board using RS-232. The structure is described in the table below:

Table 9-1 - OCU USART Packet Structure

Byte No.	**0**	**1**	**2-3**	**4-5**	**6-7**
Data	*Header Character*	*Buttons*	*Joystick X Axis*	*Joystick Y Axis*	*Magnetometer X Axis*
Byte No.	**8-9**	**10-11**	**12-13**	**14**	
Data	*Magnetometer Y Axis*	*Magnetometer Z Axis*	*Temperature Sensor*	*Termination Character*	

The five tactile buttons are read as single bit values. A logic low indicates an engaged button. The joystick axis values are read and converted using the 10 bit resolution ADC on the MSP430G2553 with a reference voltage of 3.3 V. As such, the values range from 0 to 1023 for each axis. The joystick boundaries are described below in **Figure 9-2**:

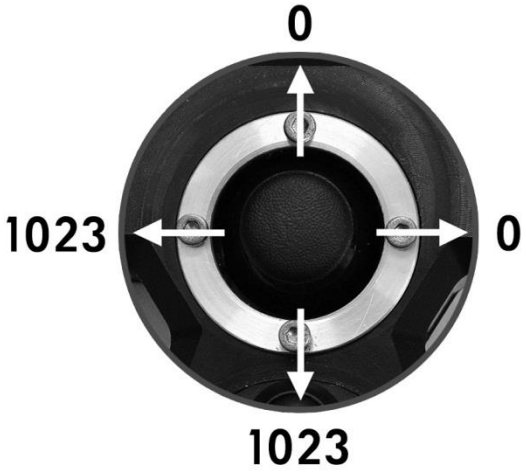

Figure 9-2 - Joystick Boundaries in Bits

The magnetometer was set to output at the device's fastest rate of 80 Hz to ensure that were was an adequate amount of data during the calibration process. The MSP430G2553 has an internal temperature sensor which is read using the 10 bit resolution ADC. As required by the device, a 1.5 V reference voltage was used.

9.2. USER INPUT

This stage handles the 14-byte USART serial data packet coming from the OCU, taking the user input data and converting for it use in the user interface. As such, it was also responsible for the layout of the interface. All USART communications use a serial interrupt routine to receive and process the data on the control interface. This includes both the OCU and GPS sensor data.

To keep the user interface intuitive and organized, it was segregated into two main modes: **Robot Mode**, and **Menu Mode**. This aimed to allocate the data appropriately for viewing on the OSD, minimizing distractions to the operator whilst performing the task at hand. Additionally, it introduced more intelligent handling of the control station's monitoring and calibration functions, preventing unnecessary processing if not immediately required. These are explored below:

1. **Robot Mode** - This mode allows the operator to drive the robotic platform, and view the sensor data from its sensor payload. Commands can also be sent to change the LED brightness, and turn on the buzzer.
2. **Menu Mode** - This mode provides access to the control station settings and system data not required for driving the robotic platform. In this mode, the robotic platform cannot be driven, nor can the sensor payload be interfaced with. Therefore it also serves as a robot safety lock.

On the OSD, each mode was allocated its own HUD, namely the **Robot HUD**, and the **Menu HUD**. These are both explored later in this chapter in the On-Screen Display section.

The OCU's buttons were mapped differently for each mode. This aimed to be as simple and intuitive as possible. The buttons for Robot Mode are illustrated below in **Figure 9-3**. For Menu Mode, each of the four buttons serve only as menu navigation direction buttons, and the joystick button is used to toggle the mode.

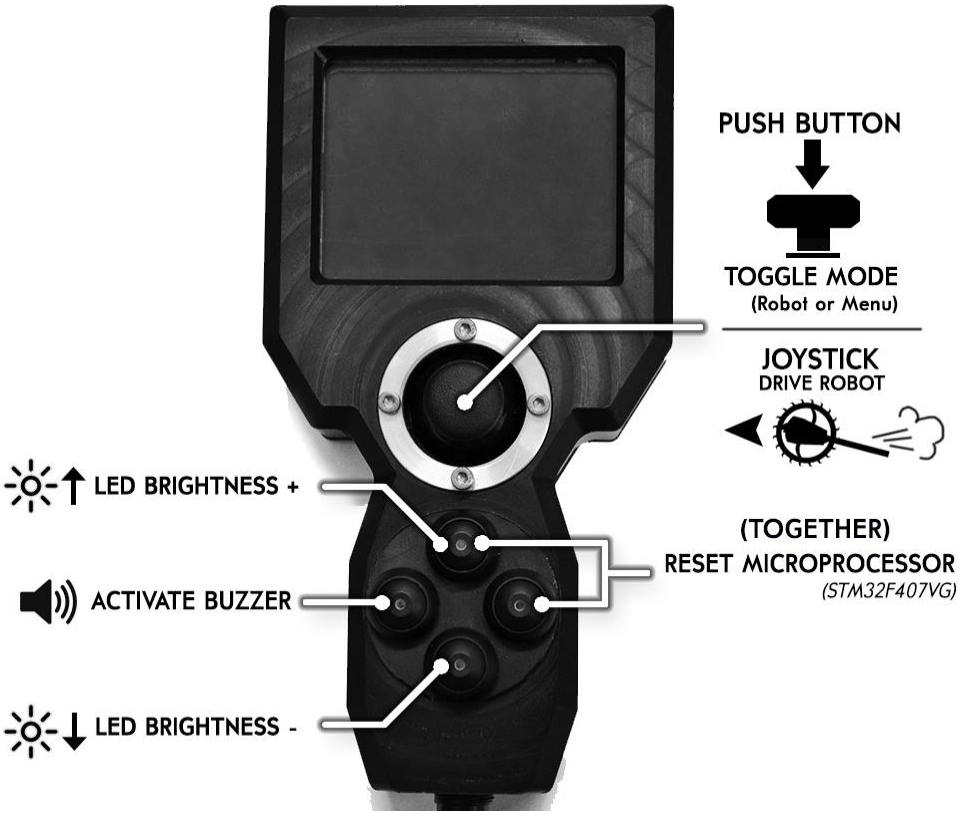

Figure 9-3 - OCU Button Mapping for Robot Mode

9.3. SENSOR DATA PROCESSING

Sensor data processing was required to convert the raw data from the sensors into usable and visible values for use by the operator.

9.3.1. GPS SENSOR

The USART serial data was set to be received at a rate of 9600 bps from the uBlox NEO-7M GPS sensor. The packets come as **NMEA 0183** (**N**ational **M**arine **E**lectronics **A**ssociation) messages, which use an ASCII format and are denoted into separate sentence lines by a "$". Each sentence contains different data from the GPS, and one of the most important is "$GPGGA" which contains the global positioning system fix data. An example of this sentence is shown below:

```
$GPGGA,123519,4807.038,N,01131.000,E,1,08,0.9,545.4,M,46.9,M,,*78
```

For the user interface, only the first four pieces of data were used. These are described below:

Table 9-2 - NMEA 0183 $GGPA Sentence Components

Data	Description	Value
$GPGGA	Header	Global Positioning System Fix
123519	Time	12:35:19 UTC
4807.038,N	Latitude	48° 07.038' N
01131.000,E	Longitude	11° 31.000' E

In the firmware, the latitude and longitude co-ordinate data was converted such that it displayed on the Robot HUD as degrees instead of minutes, making it more accessible for use on mapping applications. By default the GPS clock is set to the UTC time zone. In the firmware, this was set to match RARL's time-zone of UTC+02:00, and use the 24 hour format.

9.3.2. MAGNETOMETER CALIBRATION

To calibrate the magnetometer, the minimum and maximum value of each axis must be recorded in the immediate environment. To do this, the device must be rotated in all possible directions to acquire the values required. On the user interface, the calibration sequence was implemented in the following manner:

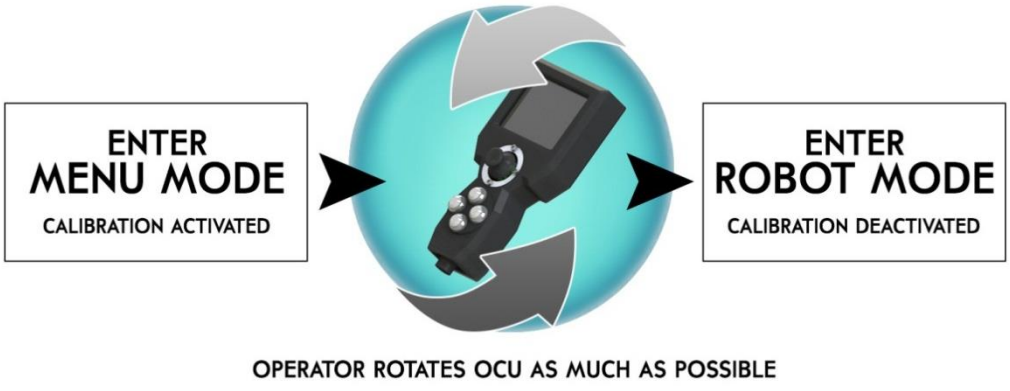

Figure 9-4 - Magnetometer Calibration Sequence

Calibration is only invoked while in the Menu Mode to decrease the processing required when doing more intensive communications operations with the robotic platform in Robot Mode. The calibration process and calculations are explained in **Appendix C. Sensor Calibration**.

9.3.3. WARNING SYSTEM

In the interface, it is of critical importance to alert the operator in case any dangerous conditions are encountered by the Scarab's electronic subsystems. This would mitigate any possible cases where the operator obliviously pushes the subsystems beyond their limit, resulting in system failure and potential bodily harm. Therefore, two critical areas were chosen to monitor the safety of both the control station and robotic platform, each using the subsystems' electronics to provide the data. This included the **battery temperature**, and **battery state of charge**.

On the control station, the battery state of charge is supplied by the battery fuel gauge, and the battery temperature is read using the LM60 sensor located on the battery management board. The raw temperature sensor data is processed using a 10 bit resolution ADC and then converted to degrees Celsius in the firmware. On the robotic platform, both values are read back wirelessly, and are supplied by its on-board fuel gauge.

A warning alert will appear if any of the values' set thresholds are encountered. This comes as a blinking warning message on the Robot HUD. It is removed upon clearing the error condition. An example of the warning message for "Robot Battery Low" is illustrated below in **Figure 9-5**:

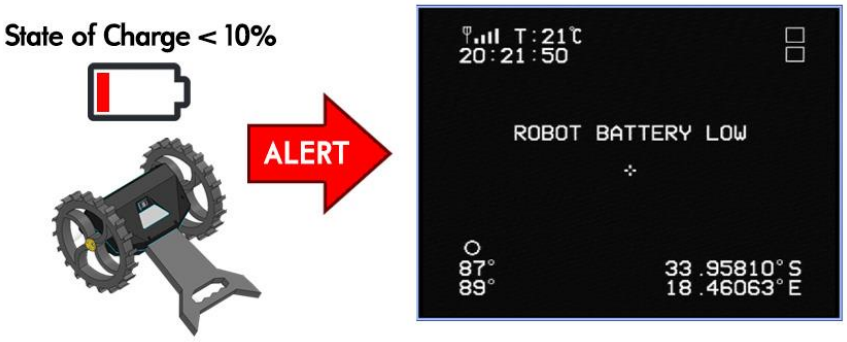

Figure 9-5 - "Robot Battery Low" warning on Robot HUD

The complete list of warnings and their thresholds are listed below. It should be noted that any battery temperatures above 60°C would have been handled by the battery protection circuitry already, and therefore appearance of the warning would indicate failure of the system. Any higher indicates extreme hazard.

Table 9-3 - Warning Thresholds and Messages

Error Condition	OSD Indicator	OSD Indicator *(Both Scarab and System have Errors)*
State of Charge Low (SoC < 10%)		
Station Battery Low	"Station Battery Low"	"System Battery Low"
Scarab Battery Low	"Robot Battery Low"	
Battery Temperatures High (60°C < Temp < 80°C)		
Station Temp High	"Station Temp High"	"System Temp High"
Scarab Temp High	"Robot Temp High"	
Battery Temperatures Extreme High (Temp > 80°C)		
Station Temp Extreme High	"Station Explosion"	"System Explosion Imminent"
Scarab Temp Extreme High	"Robot Explosion"	

For both subsystems, a more complete overview of the battery and temperature data can be viewed on the Menu HUD. This includes information including the battery voltage, average system current, remaining capacity, and the temperature of each vital area.

9.4. ON-SCREEN DISPLAY

The OSD was one of the most critical features of the system as it was the only method, besides using a computer, of viewing the user interface data. As such, a large amount of development was dedicated to providing firmware libraries for the MAX7456 OSD generator. All commands to the device were done using SPI communications at a clock frequency of 1.25 MHz, which was found to be sufficient for stable operation.

The basic OSD system can be described in the following steps:

1. **OSD Configuration** – Configuration of the MAX7456's settings.
2. **HUD Mode** – Which HUD interface must show?
3. **Interface Modules** – Each piece of data was allocated its own module in the interface. These would then be located around the screen according to which HUD was active.
4. **Character Handling** – Finally allocates the character to be assigned for each interface module; generating SPI commands to be sent to the MAX7456.

On the device, it was important to use image settings which would ensure the best visibility of the characters on top of the video feed. For this, white characters were used, with the least amount of sharpness along the edges to prevent any unwanted artefacts.

As previously mentioned in the User Input layer, each operating mode was given its own HUD using the OSD interface. These are described below:

9.4.1. ROBOT HUD

Location of the modules for the Robot HUD was inspired by cell-phones, which commonly display their sensor data around the four corners of the screen.

Feedback and responsiveness is crucial in a user interface system – in that every action from the operator should register back quickly in some visible form. As such, value indicators for all the interactive sensors are shown on the Robot HUD. These include a brightness level indicator for the sensor payload's LEDs, as well as an indicator for when the buzzer is turned on. When battery charging is enabled, it is indicated by showing the charge time remaining next to the state of charge indicator.

Figure 9-6 - Robot HUD OSD Interface

A mini-crosshair in the centre of the screen provides the user a point of reference while driving the robotic platform.

9.4.2. MENU HUD

Because of the OSD, an interactive menu navigation interface was made possible. As shown below in **Figure 9-7**, options were provided for toggling battery charging and video recording, and lists showing the system's battery and temperature data were also made available.

A simple line-by-line text format was used for the menu layout. For navigation, an arrow on the left was used to indicate the current line, and square brackets to indicate option selection. The menu structure was coded to be navigated in multiple tiers. Double arrow indicators appear when additional navigation tiers of the menu are available.

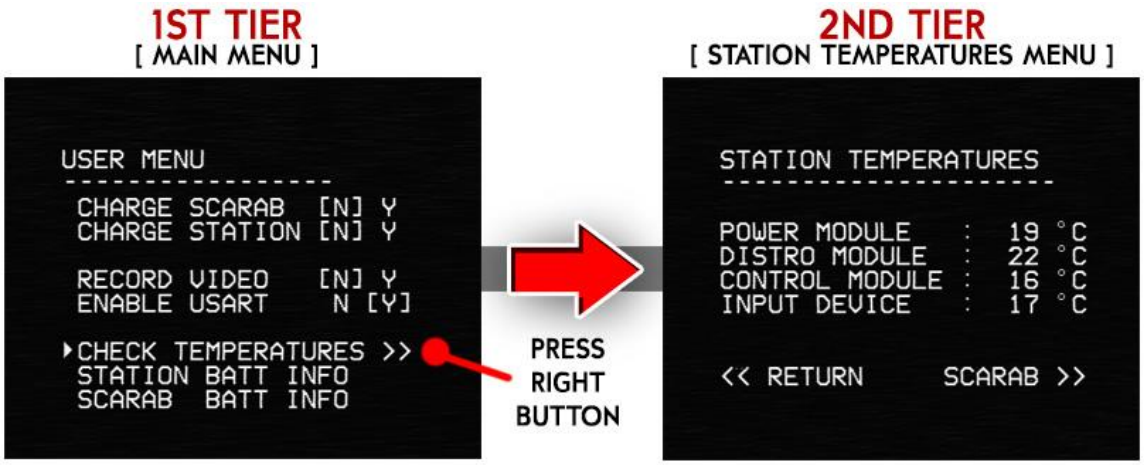

Figure 9-7 - Menu HUD OSD Interface

The complete HUD structure is described in **Figure 9-8** below, which illustrates all the available menu tiers and the navigation between each one. Note that any tier can be instantly exited to the Robot HUD by using the Toggle Mode button on the joystick.

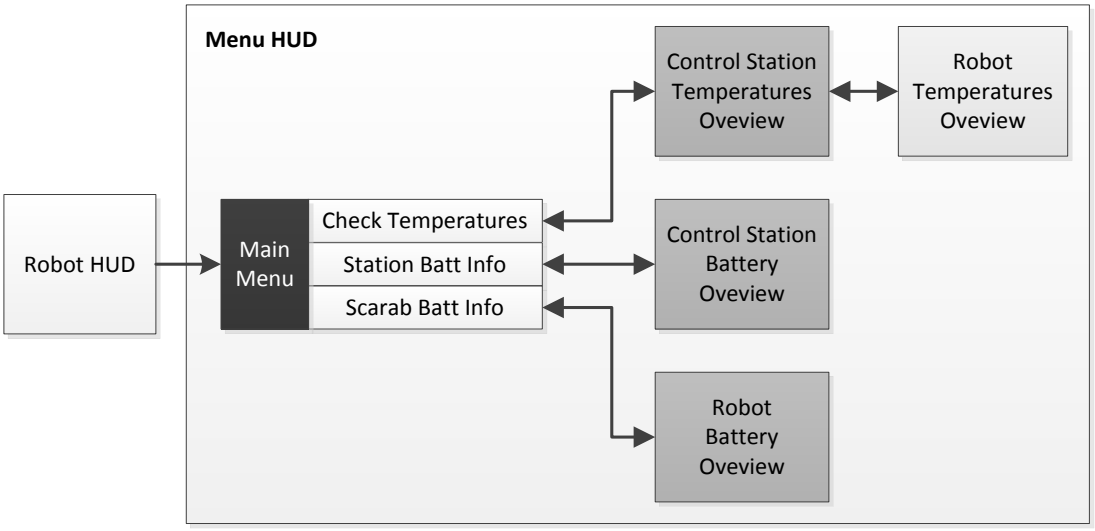

Figure 9-8 - OSD Menu Navigation Layout

A complete video demonstration of the OSD navigation system can be found on the accompanying DVD.

9.4.3. CHARACTER ADDRESS MAP

The MAX7456 is capable of storing 255 characters. These are all indicated within a character address map, and are referenced to starting from 0x00 to 0xFF. A total of 24 new custom characters were created for use in the control station and testing. The complete map is illustrated below in **Figure 9-9**, with the custom characters highlighted:

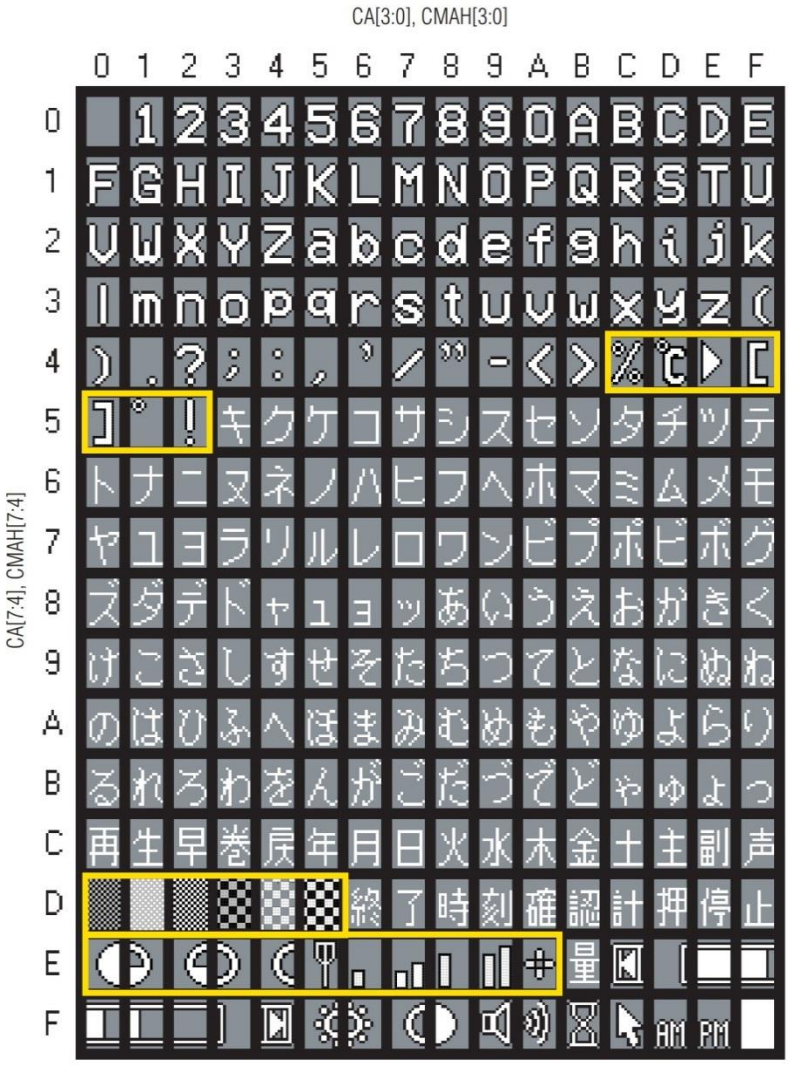

Figure 9-9 - Custom-Modified Character Map for MAX7456 OSD Generator

Creating new characters required separate SPI commands to set values for every single pixel of the 12 x 18 character pixel array.

To streamline this process, QEEWiki's MAX7456 Img Gen software [85] was used to create an image within a GUI. This generated a complete list of commands for uploading onto the STM32F407VG. The interface is shown in **Figure 9-10**.

Characters are processed onto the screen by first sending a SPI command to indicate their position on the screen, and then using the table to allocate the character required.

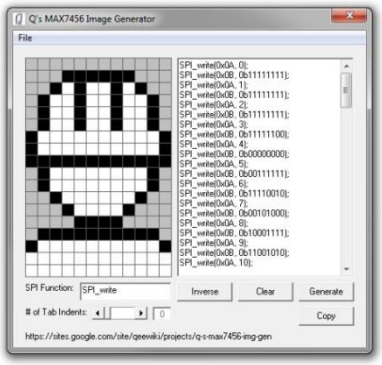

Figure 9-10 - QIMG Software Interface

9.5. ROBOT DRIVING

The robot driving controls aimed to be as intuitive as possible – in that the joystick's movements would directly translate directly to the directions used by the motors. During development, T. Mathew's motor control protocol was used, which dictated that 100% is full speed in the forward direction, and -100% being full speed in the reverse direction.

In the code, the motor profiles were written to include two turning modes:

- **Swing Turning –** The robotic platform turns around a pivot point. This is done by making one motor move faster than the other in the same direction.
- **Pivot Turning** – The robotic platform rotates about a single fixed point. Both motors turn at the same speed, but in opposite directions.

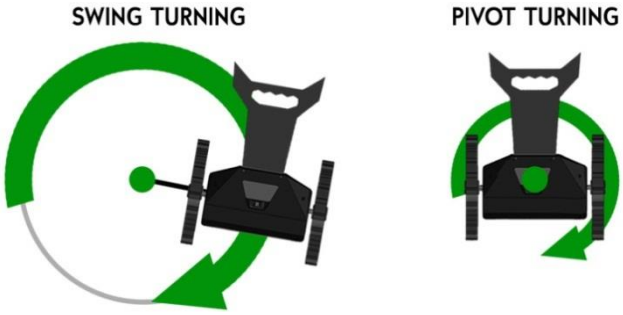

Figure 9-11 - Robot Turning Modes

For the OCU, this was set such that swing turning and pivot turning were invoked according to the Y-axis value of the joystick. This aimed to allow the operator to switch between turning modes on the fly without the need for additional controls. This is illustrated below in **Figure 9-12** which shows how each zone corresponds to an allocated driving profile:

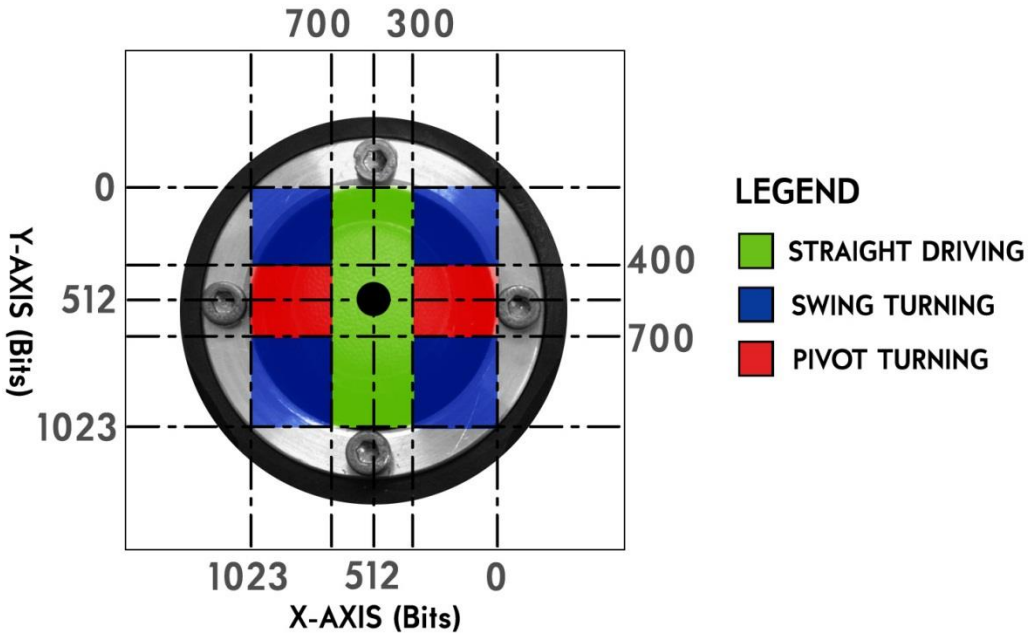

Figure 9-12 – Allocated Driving Behaviour According to Joystick Position, Depicted in Bits (Not to Scale)

9.5.1. ACCELERATION / DECELERATION PROFILES

During T. Mathew's testing of the robotic platform's mobility, issues were had with the platform constantly flipping over due to it decelerating too quickly and being subjected to the inertia of its tail and the body's centre of gravity. Therefore it was determined in the recommendations that an acceleration and deceleration function would be of benefit for better operation. This was coded into the control station firmware, but can be migrated in future developments onto the robotic platform's motor controller board. It should be noted that the primary aim of these functions was to create simple ramping and deceleration speed profiles which reacted appropriately towards the operator's commands. It did not focus on the mechanical testing and closed loop control of the motors as this was not within the scope of the project.

For both acceleration and deceleration, exponential curve profiles were chosen, and would therefore act as illustrated below in **Figure 9-13:**

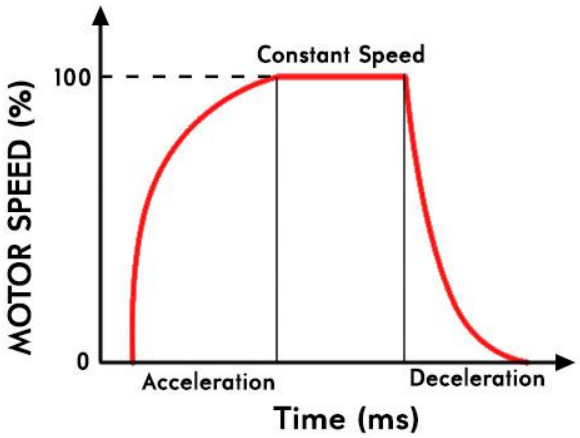

Figure 9-13 - Proposed Motor Speed Profile

It was desired that when accelerating in discrete segments, the motors do not first ramp up, and then perform a hard step-up. Therefore code was written such that each segment would be allocated its own ramp phase. However, if the difference between the initial motor speed and the goal motor speed was small enough this would be bypassed. To view the results of these profiles, please refer to **Chapter 10. Testing and Results**.

9.5.2. ZERO-TOGGLE

When operating the Scarab's motors, it was discovered that the system was short circuiting when toggling between directions at maximum speed. This was a result of the MOSFETs on the H-bridge driver not closing in time before the opening of the partnering MOSFET, creating a short-circuit condition. This proved problematic for the robotic platform's battery system as the short circuit blew the main fuse, and threatened the safety of the electronics.

To address this, the ramping software was made to include a Zero-Toggle function. This ensured the motors would always start at zero speed upon changing direction before ramping up. This gave the MOSFET enough time to close before opening the next, and therefore avoiding the short circuit.

9.6. COMMUNICATIONS

9.6.1. RF SOFTWARE

The firmware code for the RF transceivers was designed and written by G. Knox. Therefore development of the control station's wireless communications software became dependent on the working state of the firmware code, as both projects' systems were being developed concurrently.

On the system, it was found using a SPI clock speed of 5.25 MHz was optimal for stable performance. To provide validation of the transmitted data CRC checks are present in the libraries' protocols.

9.6.1.1. Transmitted Packet

On the control station, the primary packet developed was the one to be transmitted to the sensor payload.

The structure for the transmitted packet is described below:

Table 9-4 - RF Transmitted Packet Structure

Byte No.	0	1	2	3	4
Data	*Packet Length*	*Bit Mask*	*Left Motor Commands*	*Right Motor Commands*	*LED Commands*
Byte No.	5	6	7	8	
Data	*Enable Buzzer*	*Set Charge Rate*	*Enable Charging*	*Shut Down*	

The packet length refers to the number bytes after the packet length byte, including the bit mask byte. This byte was necessary due to the variable packet design used by the libraries.

The bit mask byte is calculated by adding the values allocated for each data byte sent in the packet:

Table 9-5 - RF Transmitted Packet Data Bit Mask Values

Data	*Left Motor Commands*	*Right Motor Commands*	*LED Commands*	*Buzzer Enable*	*Set Charge Rate*	*Enable Charging*	*Shut Down*
Value	1		2	4	8	16	32

Note the left and right motor commands are treated as one single value for the bit mask calculations.

9.6.1.2. Received Packet

The received packet from the sensor payload was handled by G Knox's libraries which provided a packet decompiler. This converted each value to global variables for use throughout the control station.

9.6.2. OPERATOR STATION SOFTWARE

A LabVIEW software interface was developed for the control station. This aimed to provide a development platform upon which the control station's data could be graphically plotted and viewed in an interactive GUI environment.

Importantly, it also provided a visual means to test the RF1101SE transceivers in the system. This was done via G. Knox's provided USB-USART converter modules which converted the SPI communications of the transceivers into USART, and then into USB protocol for use on a desktop computer.

This communicated with the control station using the MCP2200 USB-USART converter board. In the firmware, all the data was collated into a single packet to be sent into LabVIEW.

The software included a main interface which displays the control station data, such as the temperatures and battery fuel gauge information. This also included the RF information coming from the control station's RF transceiver into the one connected to the desktop computer, and thus emulating the sensor payload. Extra modules were included to test and plot the motor driving profiles and the magnetometer sensor data. A GPS mapping module was also made to plot the sensor data using a Google Maps API. These are all illustrated below in **Figure 9-14.**

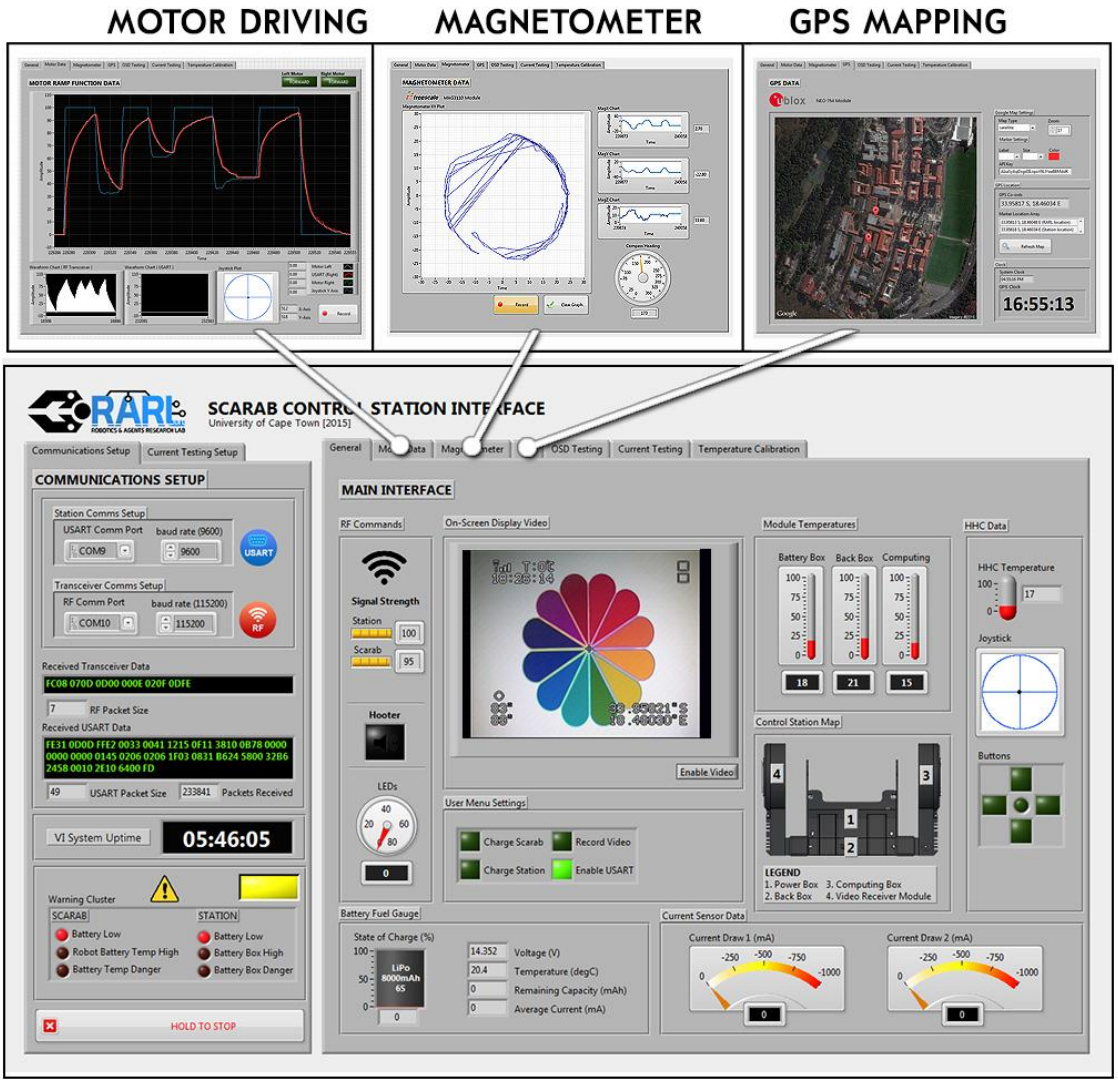

Figure 9-14 - Operator Control Station LabVIEW Software Interface

9.7. SUMMARY

A complete operator user interface was designed and developed for the control station using embedded C on the STM32F407VG and MSP430G2553 microprocessors. The priority was to keep the OSD interface as simple and intuitive and possible to allow communication between the operator and the robotic platform. Included was also a LabVIEW control station interface for viewing the system data on a desktop computer. For more information on all the interfaces described above, please refer to the commented code provided in the accompanying DVD.

Chapter 10. Testing and Results, which follows, details the procedures and results of the testing of the control station's components to verify their compliance with their desired specifications.

10. TESTING AND RESULTS

This chapter describes the testing of the system for its functionality as well as being able to conform to the requirements set by the primary system and subsystem specifications. Tests were performed to evaluate all major aspects of the system, which encompassed the mechanical, software, communications, and electrical components. Results were drawn from each test which were then to be used to draw conclusions in the following chapter.

10.1. MECHANICAL TESTS

These tests aimed to validate the mechanical chassis, and the control station system as a whole as a man-wearable system.

10.1.1. SYSTEM WEIGHT DISSECTION

This test was to validate the complete system weight requirement of not exceeding 8 kg, ensuring it could be worn comfortably on an adult operator's back. To measure the mass of each part, a scale was used with a 1 g resolution. The robotic platform was also measured to provide a complete overview of the system's mass. The vest was excluded from the complete system measurement, as it was not a component which was worn on the back, but rather around the body.

10.1.1.1. Results

The control station and its electronics weighed a total of **4.71 kg**. Illustrated in the figure below are each of the components shown as percentages of the total mass, excluding the robotic platform. As can be seen the battery was found to be the heaviest component, with each of the chassis boxes contributing similar masses of 10-12 %. However, it can be seen the Computing and Video Receiver Box are 2 % heavier, which is a result of the extra control panel and lid configuration.

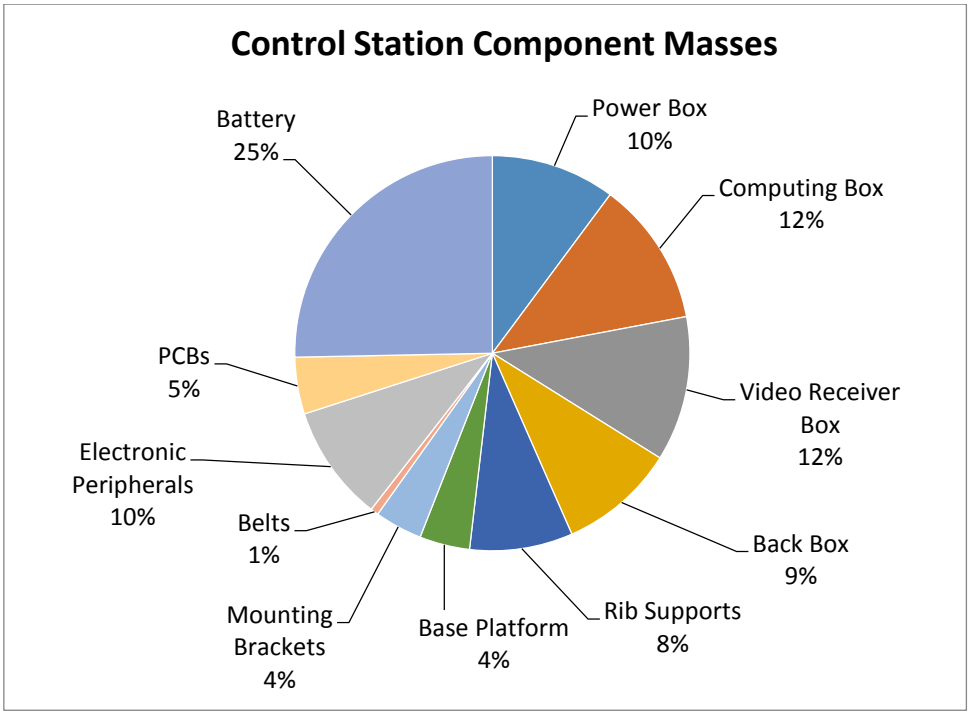

Figure 10-1 - Pie Chart Breakdown of Component Masses Percentage Respective of Total Mass

CHAPTER 10: Testing and Results

The complete list of masses is shown below, which includes the mass of the robotic platform:

Table 10-1- Mass of Components Including Robotic Platform

System Component Masses (g)			
Power Box	**470**	**Base Platform**	**190**
Base Box	270		
Lid	200	**Rib Supports**	**390**
		Rib 1	130
Computing Box	**548**	Rib 2	130
Base Box	220	Rib 3	130
Control Panel Cover	140		
Lid	120	**Mounting Brackets**	**180**
Lever	7	Bracket 1	90
Handle	50	Bracket 2	90
Shaft	7		
Latch	4	**Belts**	**30**
Video Receiver Box	**548**	**Electronic Peripherals**	**440**
Base Box	220	Digital Video Recorder	110
Control Panel Cover	140	Video Receiver	140
Lid	120	RF Transceiver	10
Lever	7	Fans	20
Handle	50	Fat Shark FPV Goggles	160
Shaft	7		
Latch	4	**PCBs and Wiring**	**215**
		Battery	**1170**
Back Box	**440**	**Robot**	**2530**
Base Box	200	**Nuts and Bolts**	**92**
Lid	220		
Vent Cover 1	10	**TOTAL**	**7243**
Vent Cover 2	10		

As can be seen, the complete system weighted **7.24 kg**, which was within the specified weight of 8 kg, being approximately 10.5 % lighter. However, this result should take into account the fact that the final robotic platform was 470 g lighter than the 3 kg originally specified.

10.1.2. SYSTEM INTEGRATION

This test was essential as it tested the core requirement of the mechanical chassis to be able to act as a docking station for the robotic platform. To perform this this, the control station was mounted on the mannequin before the robotic platform was docked on its mounting brackets.

10.1.2.1. Results

As can be seen in the figures below the robotic platform was able to fit on the control station without any issues. It was however noticed that the robotic platform was easier to deploy with the tail situated on the upper side, as opposed to being secured to the bottom of the vest. Future work should therefore consider the means to mount in the robot in this orientation.

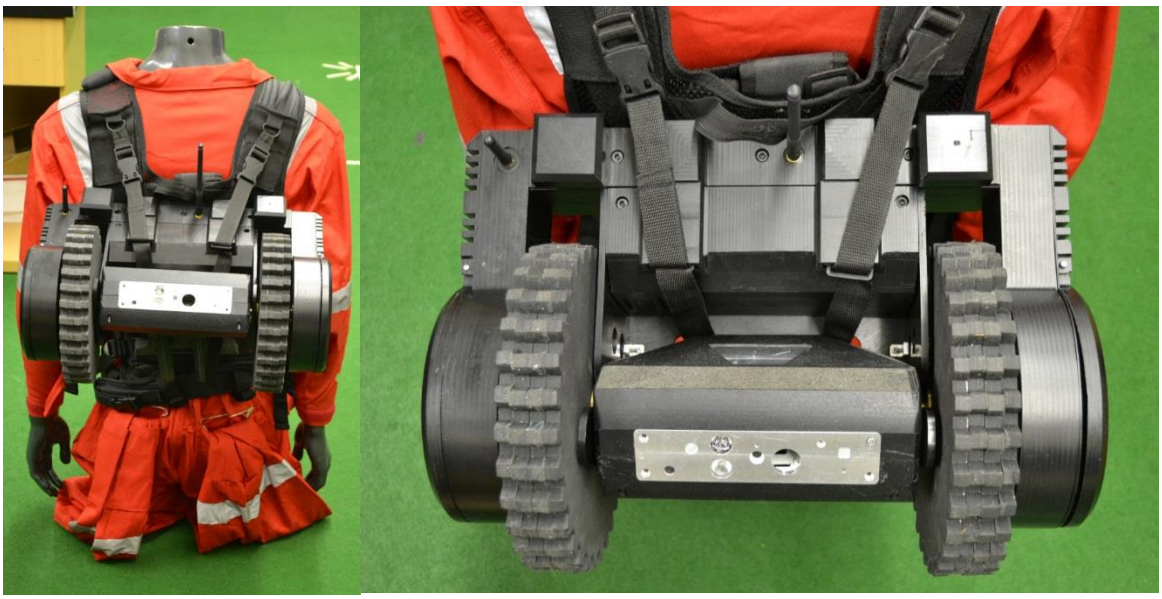

Figure 10-2 - Robotic Platform Mounted on Control Station: Back View (left), Top View (right)

Figure 10-3 - Robotic Platform Mounted On Control Station: Side View

10.1.3. SYSTEM BOUNDARY

This tested the control station's ability to fit within a standard sized door whilst being worn on a person. This was to ensure that the operator control station could be feasibly used in an USAR environment where confined spaces are common. To test this, the control station was mounted onto the mannequin before being placed within a standard sized door frame. Each orientation of the mannequin was measured, with the gap allowance recorded. This included both a frontal orientation, and a side orientation. The centre of the door was marked to place the mannequin. A tape measure was then used to measure the size of each resulting gap from the orientations. The breadth of the mannequin from its back to chest was measured to be 240 mm. The width of the door opening was measured to be 785 mm.

10.1.3.1. Results

Figure 10-4 - Boundary Tests in: Frontal Orientation (left), Side Orientation (right)

As expected, the frontal orientation fitted through the door any without issue, with a gap of at least 170 mm on each side.

While the control station was able to fit in the side orientation, it was only able to do this with the mannequin being situated away from the centre of the door, with a total distance from the mannequin's chest to the edge of the robot being 540 mm. This would become problematic in a narrow corridor and a source of danger was approaching from ahead, which would rapid turning to escape.

To accomplish being able to perform a full pivot turn in the centre of the door, a 27.5 mm reduction would be required of the horizontal size of the chassis. It was also noted that the final wheels mounted on the Scarab during testing were measured to have a total diameter of 240 mm, which exceeded the 200 mm originally anticipated.

10.1.4. ONE-MAN TEST

The quick deployment and detachment of the system without assistance of team members is vital as it validates the appeal of using a man-wearable system design as well as illustrating the system's ease of use. The quick detachment of the system also becomes a safety concern should the internal electronics become a hazard. To perform the test, the control station was worn by the author and the tasks of mounting the system, docking the robotic platform, and taking it off were done. To provide a quantitative approach, the time taken to complete each operation was recorded. The operations were performed at a natural pace without urgency to provide a less biased approach.

10.1.4.1. Results

As expected, the system was able to be placed on without the need for any assistance. Taking off the system was the simple act of unzipping the vest, unbuckling the belt, before taking it off along with the control station attached. It was also noted that the effort of wearing the control station was not uncomfortable and almost unnoticeable without the robotic platform docked. With it docked, the author was able to stay standing and walking with the system for over an hour without discomfort.

Docking and removal of the robotic platform was also possible without assistance, with the physical indicators on the mounting brackets being very helpful. However, the docking process proved to be awkward due to the faraway location of the wheel axle slots, which required unnatural twisting of the shoulder backwards in order for the arm to reach the area required. It was also discovered that the overhead method required to dock the robot resulted in the knocking of the head often. Future work should therefore focus on reducing the distance of these slots away from the operator's back. The following times were recorded for each action:

Table 10-2 - Deployment and Detachment Times for One-Man Test

No.	Putting on System (s)	Taking off System (s)	Docking Scarab (s)
1	13.67	6.52	12.06
2	16.53	5.41	15.06
3	17.33	6.12	10.86
Average	**15.84**	**6.02**	**12.66**

While this was by no means an exhaustive testing process which would have otherwise been best done with multiple subjects, it displayed the system's ability to be reliably worn and taken off within the space of less than half a minute.

10.1.5. WATER AND DUST RESISTANCE

Water and dust resistance testing would ensure the system's ability to withstand the environmental conditions present in the USAR environment.

After manufacture of the parts, it was discovered that the sealing in the walls between the chassis boxes would be inadequate due to the flexibility of the thinner and longer HDPE parts. This introduced air gaps, and thus compromised the flat surface required for compression of the seals between the chassis boxes. Additionally, it was discovered the manufacturing of the seating grooves of the seals was unsatisfactory, in particular reference to the Power Box and Back Box. This was due to the L-shape layout used by the parts' lids, which proved to be problematic for manufacture and ultimately negatively affected the quality of the grooves.

As such, these tests were not performed as even temporary success would have been rendered unlikely with the aforementioned issues. The system was therefore concluded to have failed in this regard. Formal testing of the system otherwise would have made the use of spray and dust testing chambers.

10.2. SOFTWARE TESTS

Software tests were performed to evaluate the control station as a visual user interface. Also included were the on-station sensors and motor driving profiles.

10.2.1. USER INTERFACE RESPONSIVENESS

The responsiveness of the OSD user interface is an important performance factor as any lag between the user input and the response on the screen would discourage use of the system, and indicate poor overall design of the firmware. Ideally any input from the user should result in a near instant response from the OSD. This test was performed by capturing a video of the LabVIEW control station interface to record the amount of time between a button press on the OCU being registered and the response on the OSD video. A button press was indicated by an LED on the GUI interface, as shown below in the figure below.

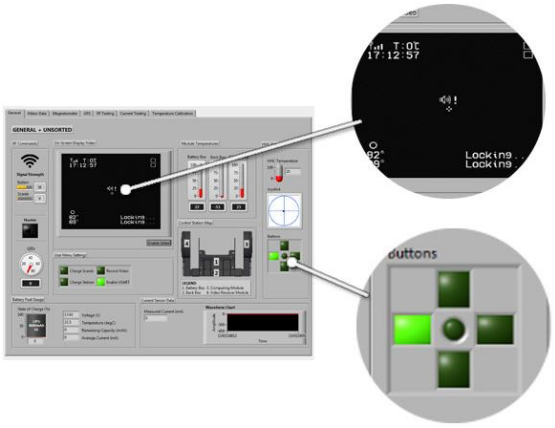

Figure 10-5 - OSD Buzzer Indicator and Left OCU Button LED Indicator

FRAPS video capturing software was used in to record the GUI interface at the software's maximum rate of 60 frames per second, which equated to 16.67 ms for each frame. Media Player Classic was then used to navigate through the video frame by frame. Upon encountering the button reaction LED, the number of frames was counted until the OSD response was seen on the recorded video screen. This was done a total of 5 times, and the results were recorded.

10.2.1.1. Results

The results can be seen below. Latency refers to amount of time it took between the user input being registered, and the resulting OSD output.

Table 10-3 - Amount of Frames Recorded Between Indicators

No.	Number of Frames	Latency (ms)
1	2	33.34
2	0	0
3	4	66.68
4	2	33.34
5	1	16.67
Average	**1.8**	**30.01**

As can be seen, the delay between the user input and the system indicator never exceeded 4 frames and had an average latency of approximately 30 ms. For the system this was deemed more than suitable as this is three-hundredths of a second; a delay which would not be normally noticed by the human eye.

10.2.2. OSD CHARACTER VISIBILITY

Perhaps of obvious importance was the visual quality of the OSD. This determined its readability to the operator as well as overall clarity of text on top of different backgrounds. This was important in the use during USAR, where clutter is prominent in the form of rubble, with harsh lighting present in the external environment. To test this, video feeds which would test the white colours of the characters were chosen. It was determined that two of the most difficult backgrounds to view white characters upon would be a purely white background, as well as a checker pattern made of black and white squares, as shown below.

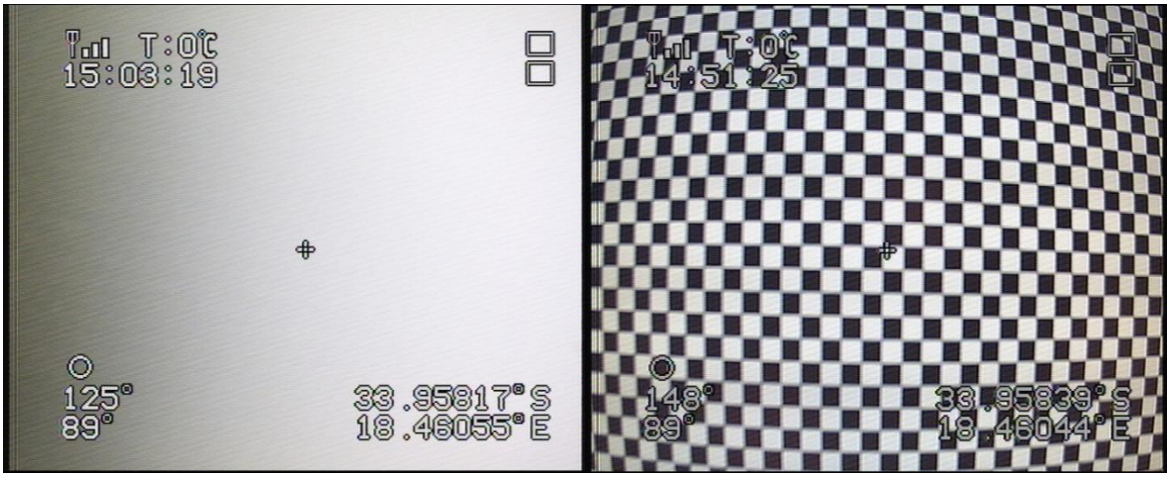

Figure 10-6 - White Background (left), Checker Background (right)

10.2.2.1. Results

It was observed that both cases showed clarity of the characters, with each one being able to be discerned from one another. One concern however was the use of large white shapes, such as the LED and battery state of charge indicators; as there were no means of distinguishing them from the white background. Therefore a recommendation for future work would be to avoid wide shapes for indicators, and rely on the use of narrow, tighter variations, with black borders. It should be noted the fisheye distortion present in the checker pattern video feed was a result of the security camera that was used, and does not reflect on the quality of the OSD itself.

10.2.3. OSD CHARACTER FLOOD

It was important not only for the screen to be able to display all characters stored in the MAX7456's EEPROM, but also the ability to sustain communications with the device over a prolonged period of time. As such, a character flood test routine was coded in the firmware which continuously refilled the entire screen with all the characters stored in the MAX7456. This was continued for over 8 hours before confirming that all 255 characters were still being shown correctly on the screen.

10.2.3.1. Results

The tests were successfully passed, with no apparent change in the character quality after prolonged operation of the device. As shown in **Figure 10-7,** all 255 characters, including the custom-made ones were able to be processed. The highlighted portion illustrates the importance of using an offset function, as it can be seen that some characters are not visible on the screen. This was significant during the testing of the FPV goggles during development, which resulted in the crosshair being off centre due to the different resolution from the LCD screen. Therefore future implementations of the OSD should consider including a horizontal and vertical screen offset adjustment option.

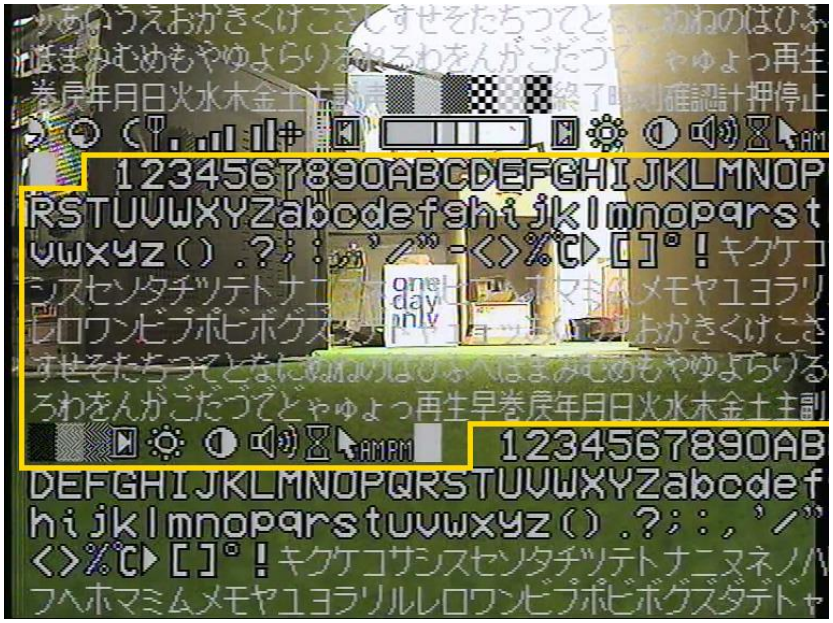

Figure 10-7 - OSD Flood Test with Cut-Off Array Due to Screen Offset Being Shown

10.2.4. OSD COLOUR CONSISTENCY TEST

Colour consistency is crucial particularly for the thermal camera, which relies on specific colours to indicate different temperatures. This therefore ensured that the colour characteristics of the raw video data were not affected by the OSD. This was also to gauge the effect of the system's electrical noise on the image. To perform this, a colour wheel was used, which is shown in **Figure 10-8**. This provided a reliable spectrum of colours to be measured.

Figure 10-8 - Colour Wheel

Two screenshots were taken using the LabVIEW control station interface, one of the video feed using the OSD, and one with the camera directly connected to the computer using the Video2Go module. These are shown below in **Figure 10-9**:

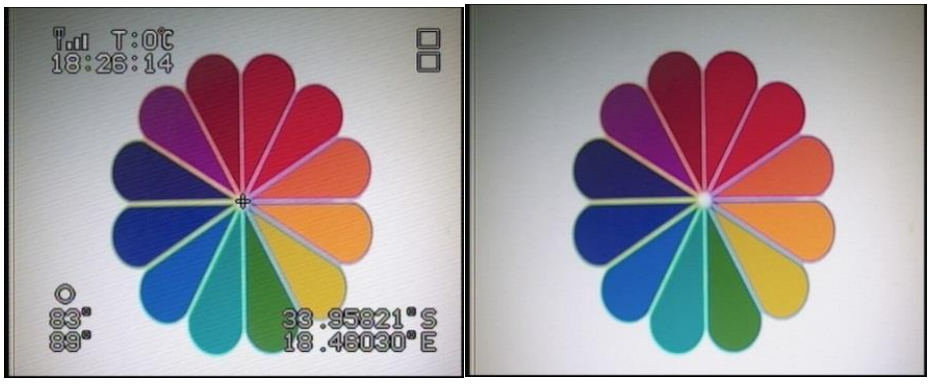

Figure 10-9 - Colour wheel on OSD (left), and colour wheel without OSD (right)

Pixel-perfect crosshairs were drawn onto each colour of the spectrum wheel to isolate a single pixel to be measured. This is illustrated on the following page in **Figure 10-10.** The pixel's hue value for each of the colours on both screenshots was then measured using a colour eyedropper tool, and recorded. Hue is the property of colour which provides its identification. It is represented in degrees, starting from 0 to 360, with each colour being defined cyclically in 30 degree multiples around the colour

wheel. This provided both a quantitative and unbiased approach upon which each colour could be evaluated without relying on the naked human eye.

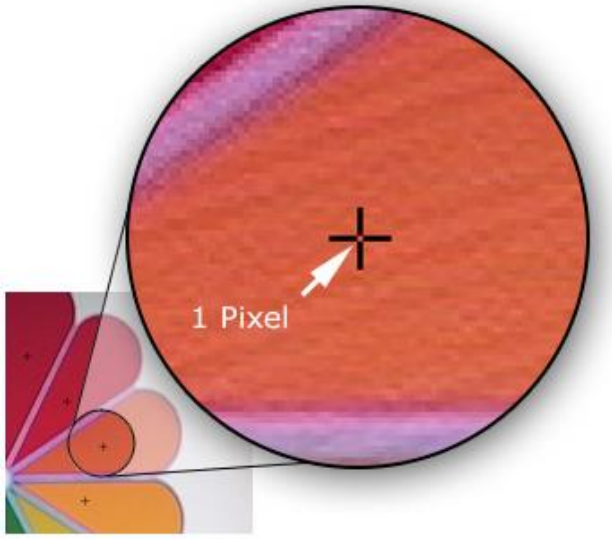

Figure 10-10 - Pixel Crosshair on Orange Colour Plane

10.2.4.1. Results

From the results tabulated below, it can be seen that the hue value differences were minimal, with a hue difference maximum of 2. This therefore validated the MAX7456 OSD generator produced no post-processing colour or brightness effects on the image.

Table 10-4 - Hue Values of Measured Points from OSD and No-OSD Camera Colour Wheel Images

No.	Colour	Hue Value (h)		
		Without OSD	With OSD	Difference (Δh)
1	Red	349	348	1
2	Red-Orange	350	349	1
3	Orange	13	12	1
4	Yellow-Orange	28	29	1
5	Yellow	49	48	1
6	Yellow-Green	112	112	0
7	Green	186	187	1
8	Blue-Green	216	216	0
9	Blue	228	228	0
10	Blue-Violet	241	239	2
11	Violet	301	301	0
12	Red-Violet	346	345	1

10.2.5. THERMAL CAMERA AND HAZARD SIGNS

This validated the OSD's ability to show an output from a thermal camera. For this purpose, a FLIR A320 IR camera was used. Also illustrated was the OSD interface's layout's ability to portray hazard signs without clutter. To do this, various hazard signs were used to provide a mixture of both text and symbols.

CHAPTER 10: Testing and Results

10.2.5.1. Results

Below is a series of images logged using the LabVIEW control station interface. These depict both the functionality and usefulness of thermal camera functionality when identifying a survivor in dark conditions. The body used was the author's.

Figure 10-11 - Thermal Camera Test: Normal Camera Image of Body in Darkness (left), Thermal Camera Image of Body (middle), Thermal Camera Image of Remaining Heat Signature (right)

One of the problems encountered during the testing was the NTSC video format of the FLIR camera, which required rearranging of the OSD modules around the screen. While the sensor payload's thermal camera outputs PAL, it should still be recommended in future work to include an option which allows toggling of the video format layout in the menu interface to accommodate easy adjustment for adding of new viewing peripherals.

Shown below are two examples of the hazard signs used. It could be seen that the signs could be clearly seen without hindrance from the layout caused by the OSD.

Figure 10-12 - Hazard Signs with OSD

10.2.6. MAGNETOMETER CALIBRATION

The MAG3110 magnetometer calibration process was tested to ensure the processed data was suitable for use in the control station. As determined from the background research, an ideally calibrated magnetometer would produce axis values which collate to form a perfect sphere centered at the plot's origin. This would be accomplished by rotating the OCU in all directions. To log the axis values, the LabVIEW control station software was used. This recorded both the magnetometer data pre-calibration and post-calibration. The logged data was then exported to Gnuplot to produce 3D scatter graphs for analysis of the sphere's shape. For a more quantitative approach, a 2D plot was made by turning the magnetometer in the XY plane in a circle, and the logged data was plotted using Microsoft Excel.

10.2.6.1. Results

The magnetometer points pre-calibration and post-calibration are shown in the following page. As can be seen, before calibration, the points were neither centered nor spherical, creating a split elliptical shape. Post-calibration, it was seen the sequence successfully produced a spherical scatter plot centered on the origin of the plot. However, it was observed there were points which were not within the sphere's range, and can be attributed to the serial communications used to link to LabVIEW from the control station, as well as electronic noise on the magnetometer sensor.

Perhaps as expected, the 2D XY graph after calibration revealed that plot was also circular, with a minor offset of approximately 4 µT. This is shown below in **Figure 10-13**. However it should be noted that the acquiring process of all the points for calibration was a lengthy process, requiring over a minute of rotating the device. This was due to there being no visual indicator on whether each direction was already complete, resulting in redundant rotations.

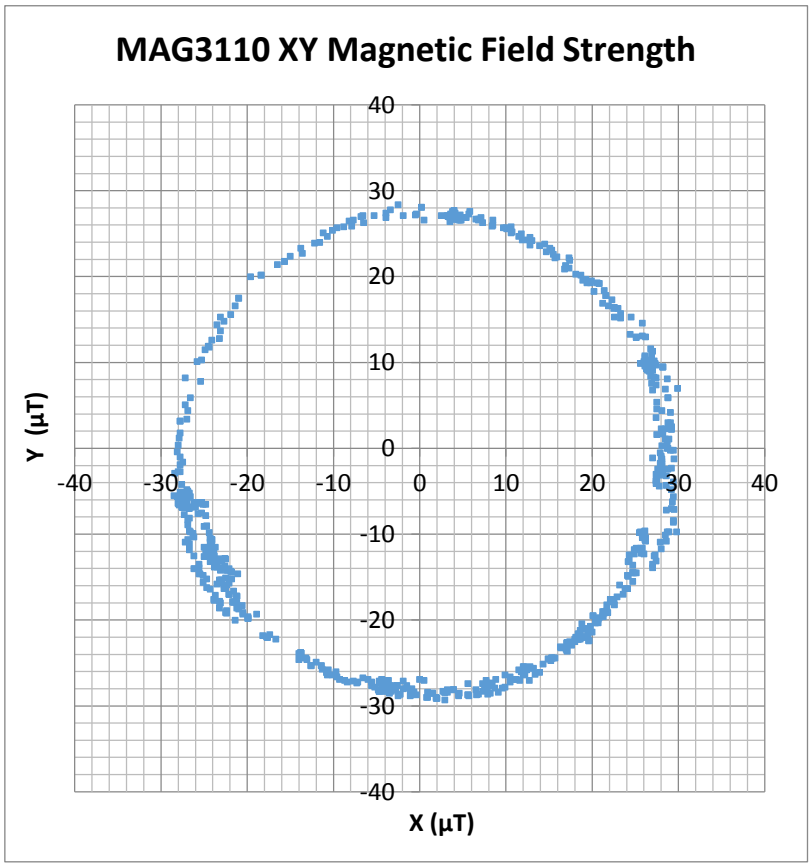

Figure 10-13 - XY Plot of Magnetometer Magnetic Field Strength Values Post-Calibration

CHAPTER 10: Testing and Results

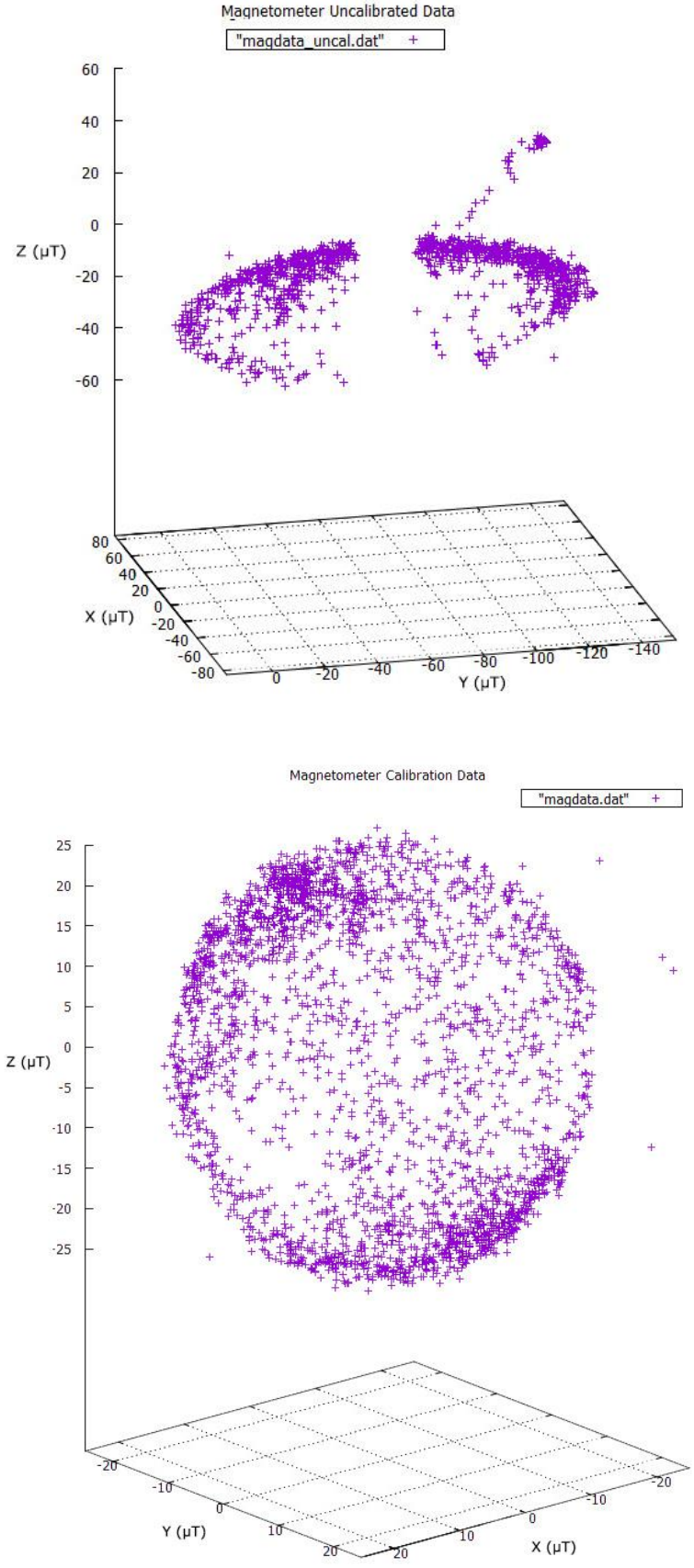

Figure 10-14 - Magnetometer Axis Values in Scatter Plot: Pre-Calibration (top), Post-Calibration (bottom)

10.2.7. GPS LONGETIVITY TESTS

This was a test done to ensure that the control station's uBlox NEO-7M GPS sensor was capable of tracking the operator control station's location over long distances over a prolonged period of time.

To do this, the GPS module was installed into a car which was then driven between two pre-determined locations. Using Google Maps, this was measured to be a 28.1 km route with an estimated total drive time of 36 minutes. A separate test was performed by walking around with the sensor in UCT Upper Campus. This allowed a more clear view of whether the logged routes had any overlaps with buildings when plotted. The data was recorded using uBlox's provided u-center GNSS evaluation software with the sensor connected to and powered by a laptop. The logged kml files were then parsed onto Google Maps using the GPS Visualizer website [86].

10.2.7.1. Results

It could be seen that full route was recorded in both tests. During the long distance test, it was observed there were some areas where the signal was lost, but this was prominent only in busy commercial sectors where many high-rise buildings were present.

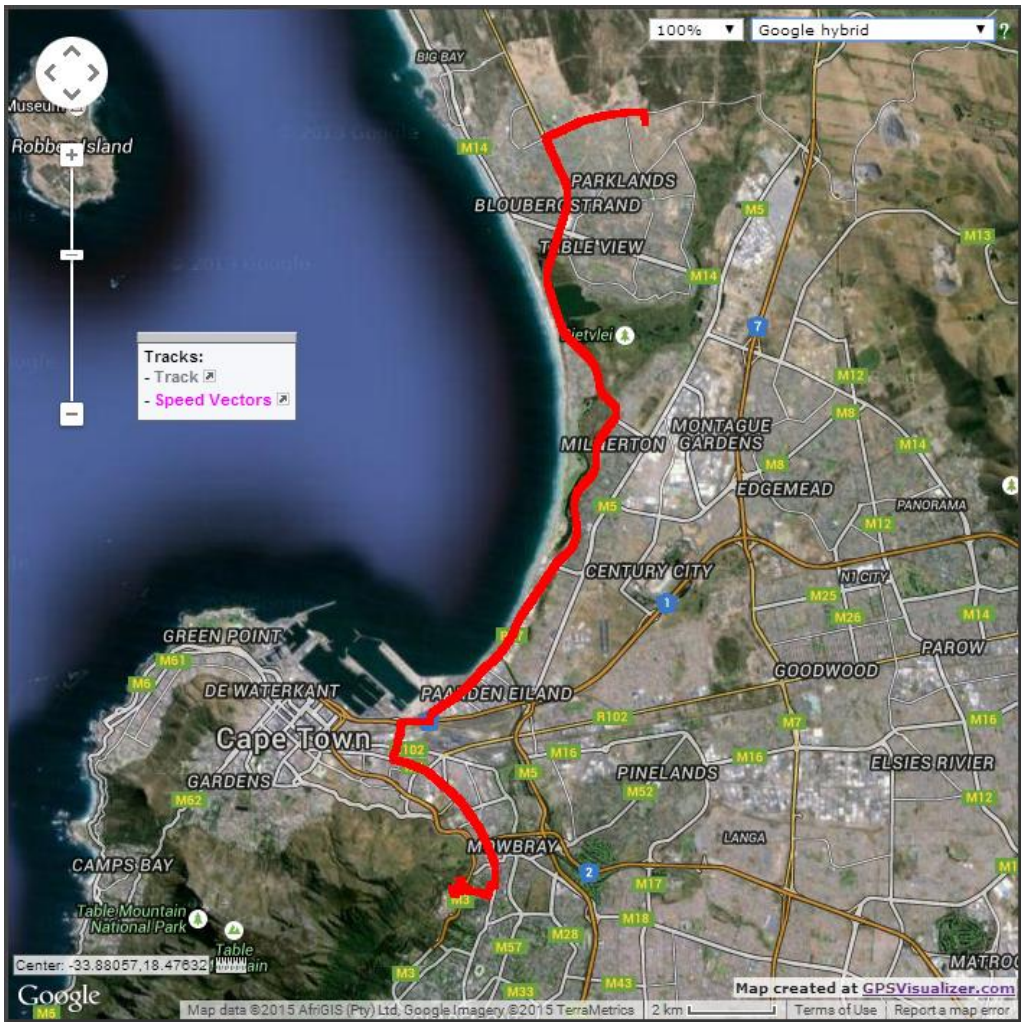

Figure 10-15 - Recorded Long-Distance GPS Data Plotted Onto Map Using GPS Visualizer

CHAPTER 10: Testing and Results

Figure 10-16 - Recorded Short-Distance GPS Data Plotted onto Map Using GPS Visualizer

As can be seen above, the route logged in the university showed little to no signs of overlapping into buildings.

10.2.8. GPS ACCURACY TEST

These tests were performed to measure the accuracy of the GPS board. This was not an exhaustive test, but was done to prove that the module was capable of providing accuracies within 5 m. To perform this, the author walked with the GPS board connected to a laptop, and followed a circle located in front of UCT's Jameson Hall, shown in **Figure 10-17**. This was measured to be a 6.75 m radius circle, and thus the path was adjusted to be 5 m within it using the 450 x 450 mm square tiles on the surface as a reference.

Figure 10-17 - Jameson Hall Circle

Google Maps and the uBlox NEO-7M GPS module both use the same **WGS84** (**W**orld **G**eodetic **S**ystem of **1984**) datum reference for their coordinate system. This ensured that the coordinate data from both systems correlated accurately with each other during analysis.

10.2.8.1. Results

The plotted points are shown below, with the actual circle's size and position illustrated using a solid green line. Using the scale provided on the map, the largest offsets were determined to be approximately 10 m in the horizontal direction. Vertical offsets illustrated less than 2 m of offset. It should be emphasized that the offsets may largely be due to how Google Maps is not completely accurate due to the 3D terrains being stretched at an angle. Additionally, while the accuracy was not within 5 m according the mapping system used, it could be clearly seen that the plotted points were well within the intended area's field of view, making it viable for use in an open area in USAR.

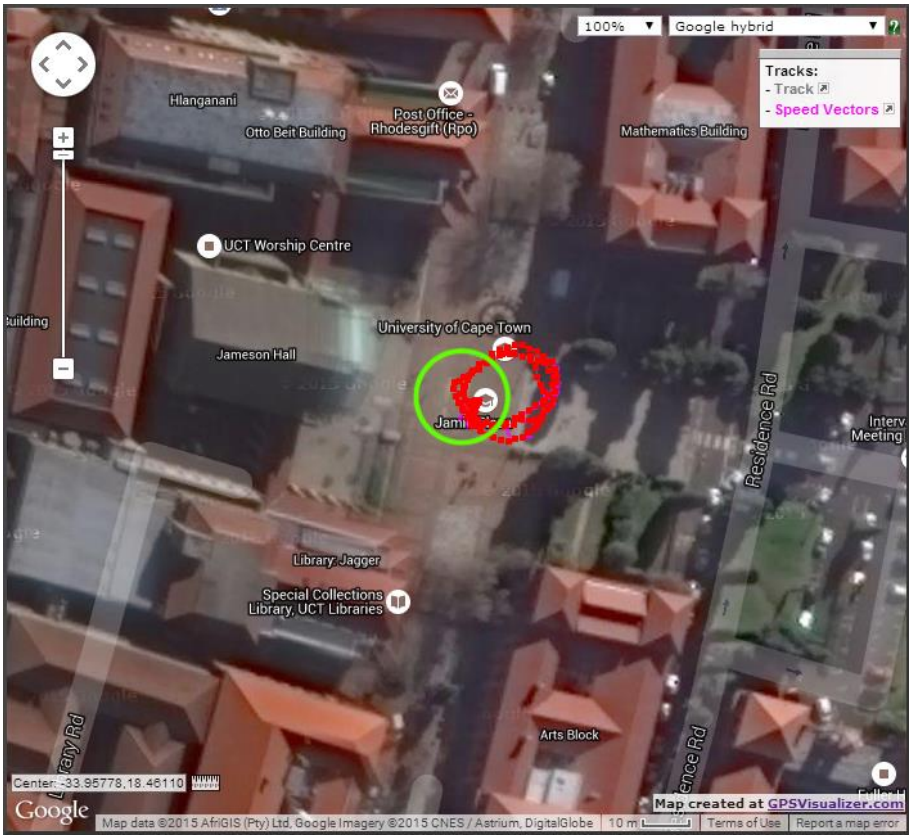

Figure 10-18 - Plotted GPS Path Shown Next to Actual Path

10.2.9. MOTOR PROFILE TESTS

This test was performed to validate the acceleration and deceleration motor speed profiles which were coded for use in the robotic platform. This was important in determining that the profiles reacted correctly according to the OCU's joystick position, as well as accounting for incremental acceleration and deceleration. Ideally these profiles would have been formally tested on the robotic platform itself. However this was not possible due to the motors having been damaged during T. Mathew's testing of the platform which required replacing, and did not fit within the time constraints and scope of the project.

In order to monitor the generated motor speed profiles, the LabVIEW operator control interface was used. This logged the speed of motors on a real-time waveform chart, allowing the user to graphically view the data during the process. The following profiles were performed:

- Incremental Acceleration
- Decremented Deceleration

Included was also a test to demonstrate the Zero Toggle function which was used to protect the H-bridge MOSFETS from short-circuiting.

Each test also plotted the joystick's position, converted using a linear function to 0-100 to represent the motor speed prior to being processed through the profile functions. This was to illustrate the nature of the profiles according to user input as well as the timing.

A video demonstration of each of the profiles can be found on the accompanying DVD.

10.2.9.1. Results

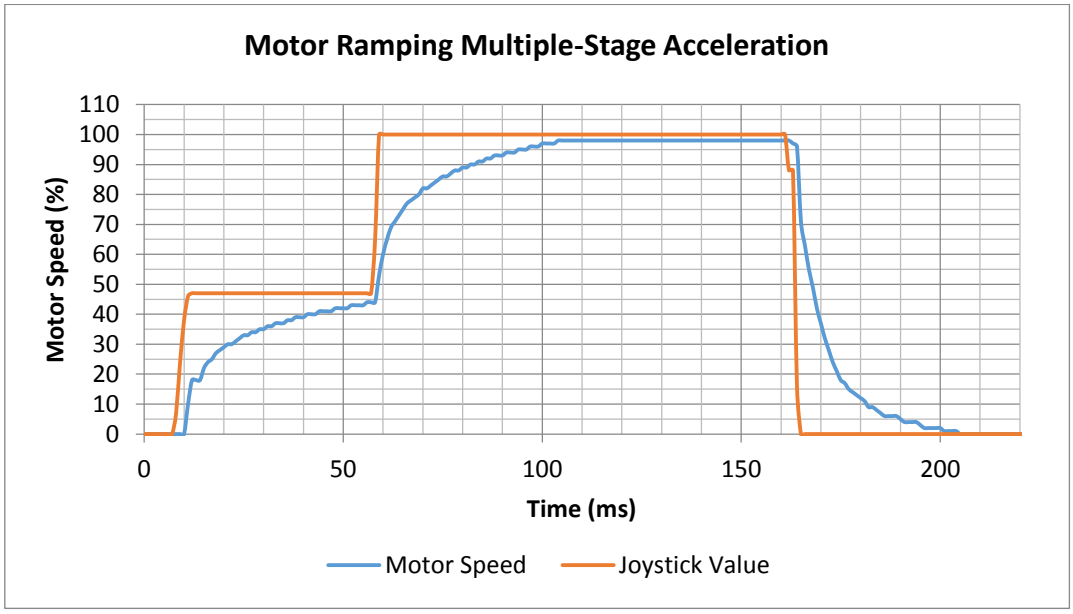

Figure 10-19 - Graph of Motor Speed Profile Over Time for Multi-Stage Acceleration

The above graph shows the motor profiles incremental acceleration, where the motors accelerate to an initial goal speed of 44 %, before following a new acceleration curve for a new, higher goal speed of 100 %. Currently, this profile produces an acceleration from the starting speed to goal speed within approximately 50 ms. It was observed that a slight lag was present between the user input and the initiation of the curve, but was deemed to be negligible at less than 5 ms.

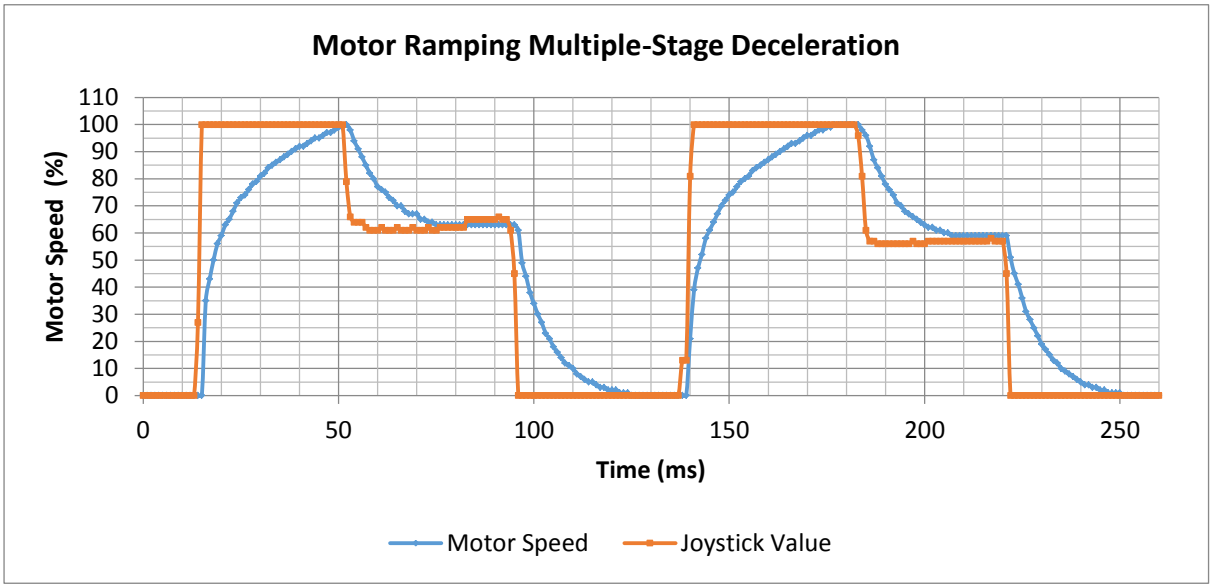

Figure 10-20 - Graph of Motor Speed Profile Over Time for Multi-Stage Deceleration

The multi-stage deceleration tests were similar to the previous ones. Both captured cycles show an acceleration to 100 % motor speed before decelerating to 60 %, and then again to 0 %. The time taken for acceleration and deceleration was always approximately 45 ms independent of the difference in speed. From this observation of both acceleration and deceleration, it should be noted that future iterations of the code should include a setting to scale the amount of time required depending on the starting and end speed. This would account for what would be most likely perceived as a driving lag due to too many acceleration/deceleration times being used.

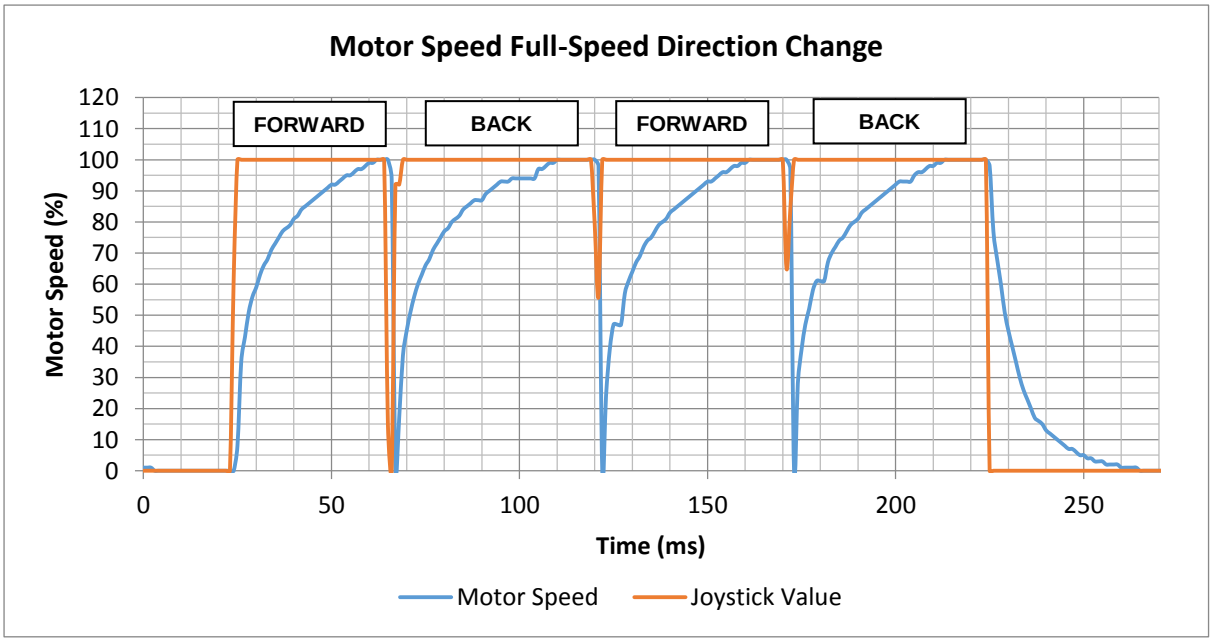

Figure 10-21 - Graph of Zero Toggle Motor Speed Profile Over Time

The Zero Toggle function is illustrated above, where the motor speeds always start from zero upon changing direction at 100 % motor speed. These worked well for the most part, but sometimes suffered due to the code not able to register the transition during quick flicking of the joystick, which resulted in a constant 100 % of the user input value, as opposed to a dip required to indicate the direction change. This was due to the OCU sending data only every 50 ms, which resulted in a slower sampling rate.

10.2.10. OVERALL SYSTEM USABILITY TEST

It was important to test the user interface with different people, as this would validate the system's ability to be used by people of different experiences as well as different physiques.

Therefore this test was performed to evaluate the intuitiveness of the user interface, and the ergonomics of the OCU whilst wearing a pair of safety gloves. Importantly, it also validated the visual and layout clarity of the OSD. For this purpose, 12 candidates, with no prior experience of using the system were invited for the test.

In order to log the data from the candidates, a questionnaire was used. This included the questions regarding the comfort of the OCU, the interface's ease of use, and the readability of the OSD on top of a real time video feed. Each question was allocated with a rating of 1 – 5, where 5 was the most satisfactory, and 1 the worst. The questionnaire can be found in **Appendix B. User Test Documentation**. To remove the need to measure the size of the user's hands, two sets of Securetech safety gloves were used to represent a small size, and a medium-large size. These are shown below in **Figure 10-22**. This also accommodated for both left and right-handed people, which was important for testing the ambidexterity of the one-handed design of the OCU.

Figure 10-22 – OCU Shown Next to Two Differently Sized Leather Safety Gloves

Each person was asked to select a pair of gloves depending on their hand size. They were then guided on how to operate the system before allowing them to perform the tasks required by the questionnaire. This included interfacing with the LabVIEW operator interface, as well as navigating through the menu structure on the OSD. They were also questioned about the clarity of the OSD feed on the video, and whether the navigation structure as well as the sensor indicators were intuitive.

10.2.10.1. Results

The following data was recorded, and the averages of all the user responses are shown on the following page for each hand size. Throughout the 12 candidates, 6 were categorized as small handed, and 6 were categorised as medium-large.

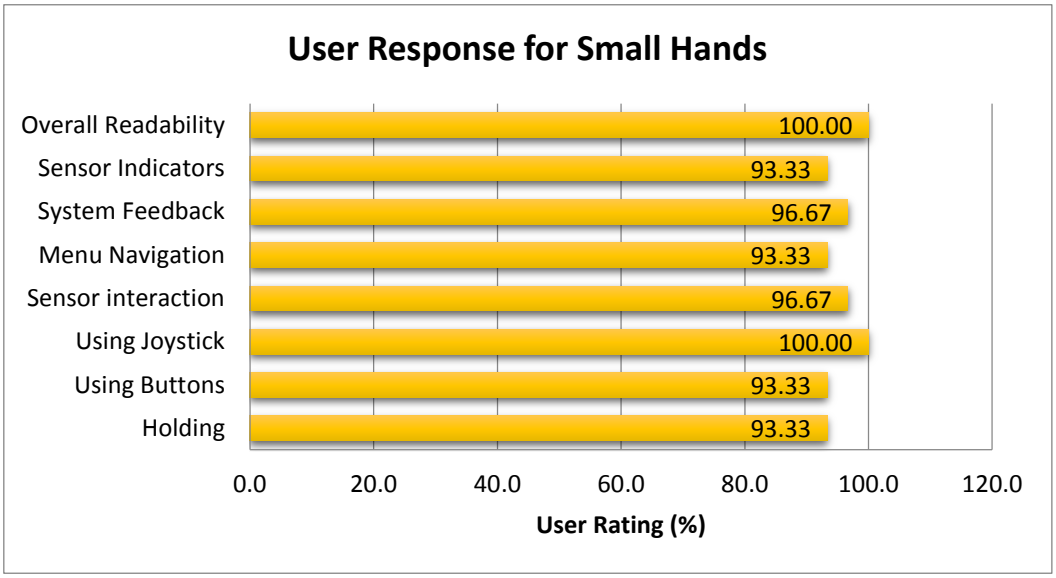

Figure 10-23 - Graph of User Response for Small Hands

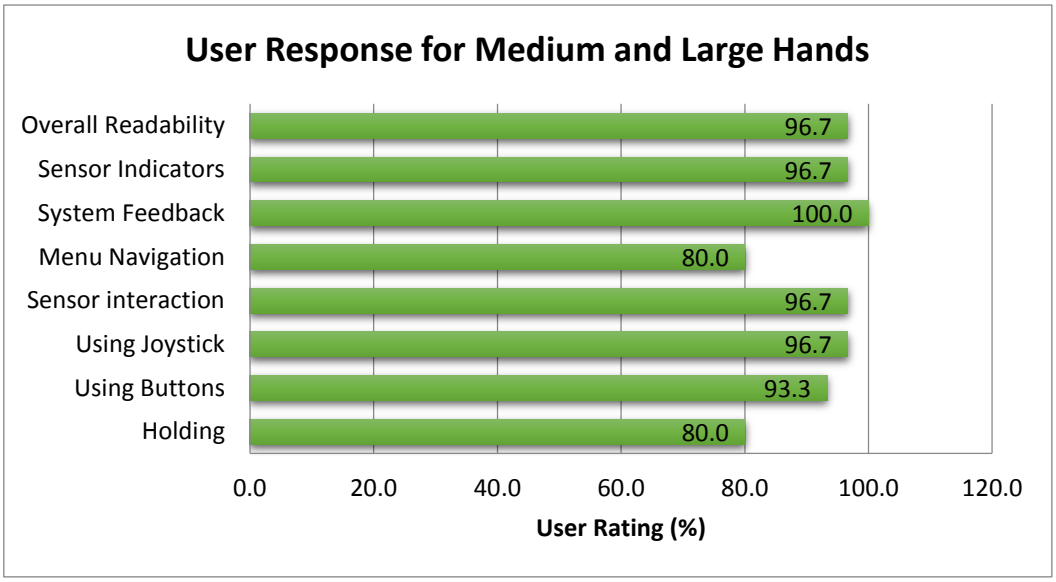

Figure 10-24 - Graph of User Response for Medium-Large Sized Hands

As can be seen in the graphs above, the feedback was mostly positive for the interface and the OSD. However, it was discovered that the OCU was less comfortable to hold for medium to larger sized hands. More critical comments in this regard made referral to the bottom being blocky to hold, and should rather use a curved shape. It was also discovered that some snagging was present while the fingers were trying to reach from one button to the other.

In regards to the navigation, a prominent comment made by almost all the candidates was the wish to use the joystick as the menu navigation directions, as opposed to using the buttons. This was however prior to being informed about the reason being that Menu Mode acted as robot lock whilst the OCU was placed in the vest holster, which changed the opinion. A sound suggestion made by one of the candidates was to include a small, but obvious button dedicated to locking in the middle of the four buttons, as opposed to relying on Menu Mode.

Comments in regards to the OSD were mostly those of personal preference. A suggestion was made to move the LED indicator to the top as it was not immediately obvious, as well as being easily confused with the compass heading indicators in the same area.

10.3. RF COMMUNICATIONS TESTS

Testing of the RF communications was imperative to evaluate how G. Knox's transceiver firmware integrated with the control station firmware and electronics. To perform these tests, a virtual sensor payload was written in LabVIEW using G. Knox's provided code used for his testing of the RF transceivers. This allowed viewing of the data sent to the interface, as well as being able to code testing routines for both communication nodes of the system without having to interact with the actual sensor payload which was still under development at the time of testing.

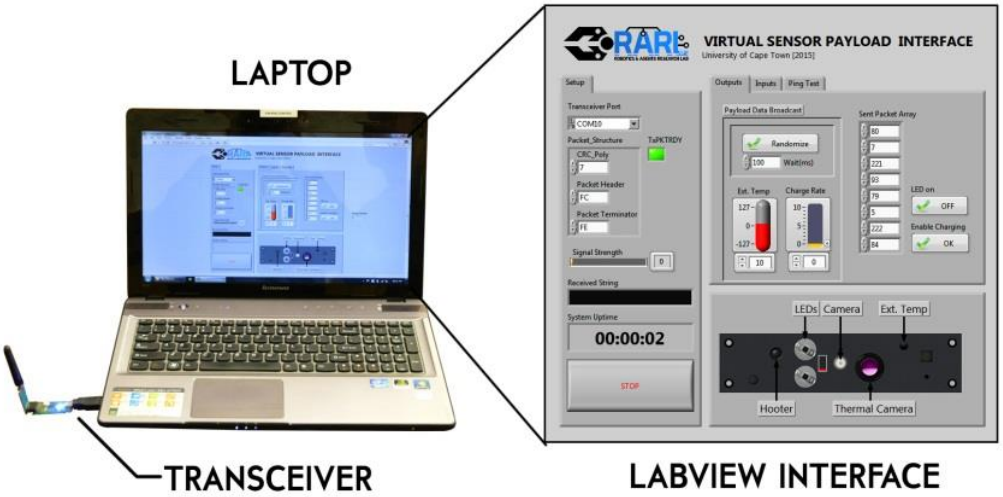

Figure 10-25 - Virtual Sensor Payload Interface Platform

To establish a means to view the virtual sensor payload's LabVIEW GUI while away from it, a remote desktop connection was used, which used the university's internet Wi-Fi services. This allowed viewing of both LabVIEW interfaces on the same computer, and proved to be very useful in determining whether any commands were registered promptly on the GUI interface's indicators.

10.3.1. RF RANGE TEST

The purpose of this test was to quantitatively evaluate the radio communications of the RF systems between the control station and the sensor payload. The main metric was the maximum distance between the two stations. The Duncan McMillan building was used for the range tests, and the virtual sensor payload was set at 3 m intervals away from the control station. The building's progression is shown on the following page in **Figure 10-26**, which illustrates a mixture of clear LOS locations as well as metal and concrete barriers. It should be noted that just before the 9 m mark is a solid concrete wall.

To provide a quantitative approach of evaluating the ideal distance, the packets lost during communications were counted. This would serve as a measure of the communication's reliability as any lost packets would equate to data not received and CRC failure. To determine the number of lost packets, a linear function was transmitted from the control station to provide constantly varying data to the virtual sensor payload. This was coded to increment in set intervals. On the virtual sensor payload, if the expected next incremented value was not received, it would be recognised as a packet that had been lost.

For each 3 m range interval, 10000 packets were sent to the virtual sensor payload. The lost packets were then logged and calculated as a percentage of the total packets been sent. The amount of time required for the complete process each interval was also logged. This allowed the average time for each packet transmission to be calculated.

Figure 10-26 - Duncan McMillan Building Beyond 9 m Testing Point

10.3.1.1. Results

It was found that after 38 m the communications showed a noticeable deterioration, with the transmitted linear function displaying a lot of missing values. This was attributed to the additional metal structures present at that point. As can be seen in the graphs below, the packet loss percentage remained consistently at approximately 21 %, until the 45 m range mark, which introduced an additional concrete wall. Beyond there, communications were found to be still usable, with one-value commands being able to be sent from the OCU without trouble, but the linear function was illegible with a lot of delays. Observing using the remote desktop connection, a button press from the OCU registered almost immediately on the virtual sensor payload even at the 57 m mark. Further tests were not performed beyond that mark as it was well beyond the 30 m originally specified, and would have extended beyond the building.

The average time per packet transmission was found to follow the same behaviour, experiencing a high spike after the 45 m mark. Before then, it showed a maximum time of 38.9 ms.

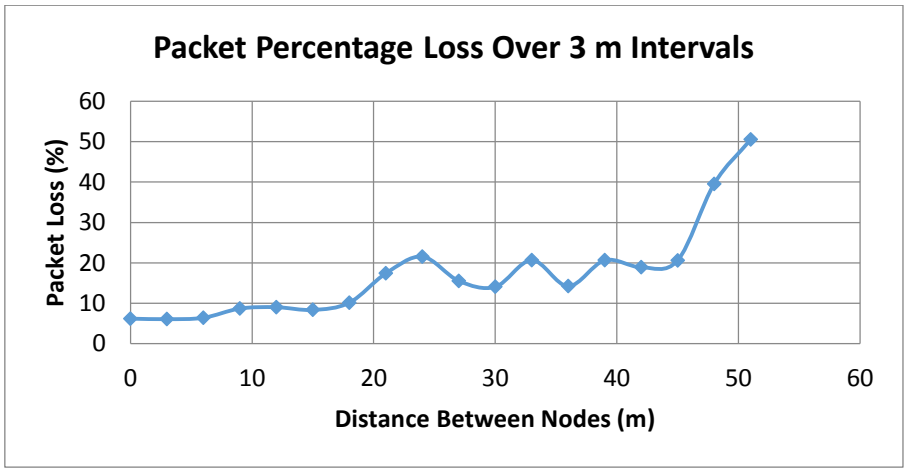

Figure 10-27 - Graph of Packet Percentage Loss over 3 m Intervals

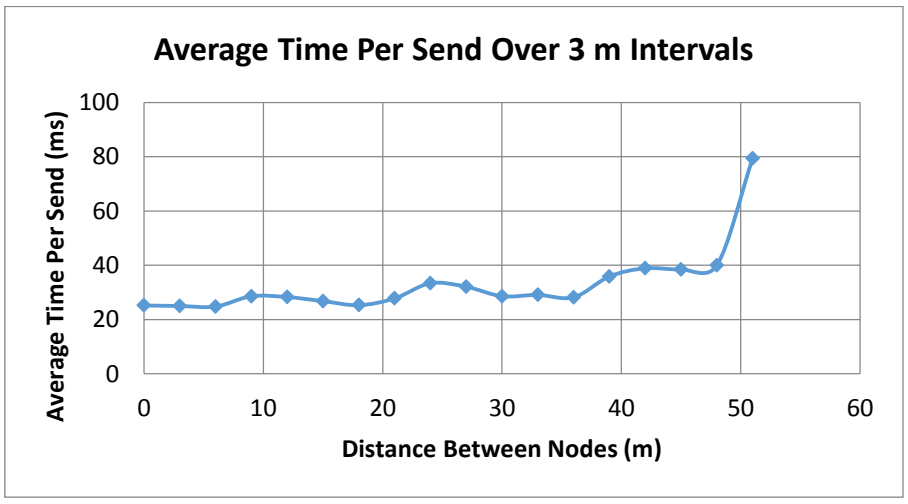

Figure 10-28 - Graph of Average Time Per Send Over 3 m Intervals

From these tests it was determined that the use of time-dependent functions over the transceivers was highly discouraged, and simple movement commands should be used; with the functions being processed on-board the robotic platform as originally envisioned.

10.3.2. LATENCY PING PONG TEST

The latency of the RF communications was essential as it determined the response time between the control station and the sensor payload. A ping pong test was therefore coded into the virtual sensor payload interface and the control station firmware to evaluate the relative latency at varying distances between the two systems. The basic algorithm is illustrated below in **Figure 10-29**. The virtual sensor payload sends a value which the control station registers as a “ping”. Upon receiving this value, the control station transmits a “pong” value which is then registered on the virtual sensor payload and shown as an indicator. On the virtual sensor payload interface, an event structure is used to determine the amount of time between the sending of the ping and the receiving back of the pong.

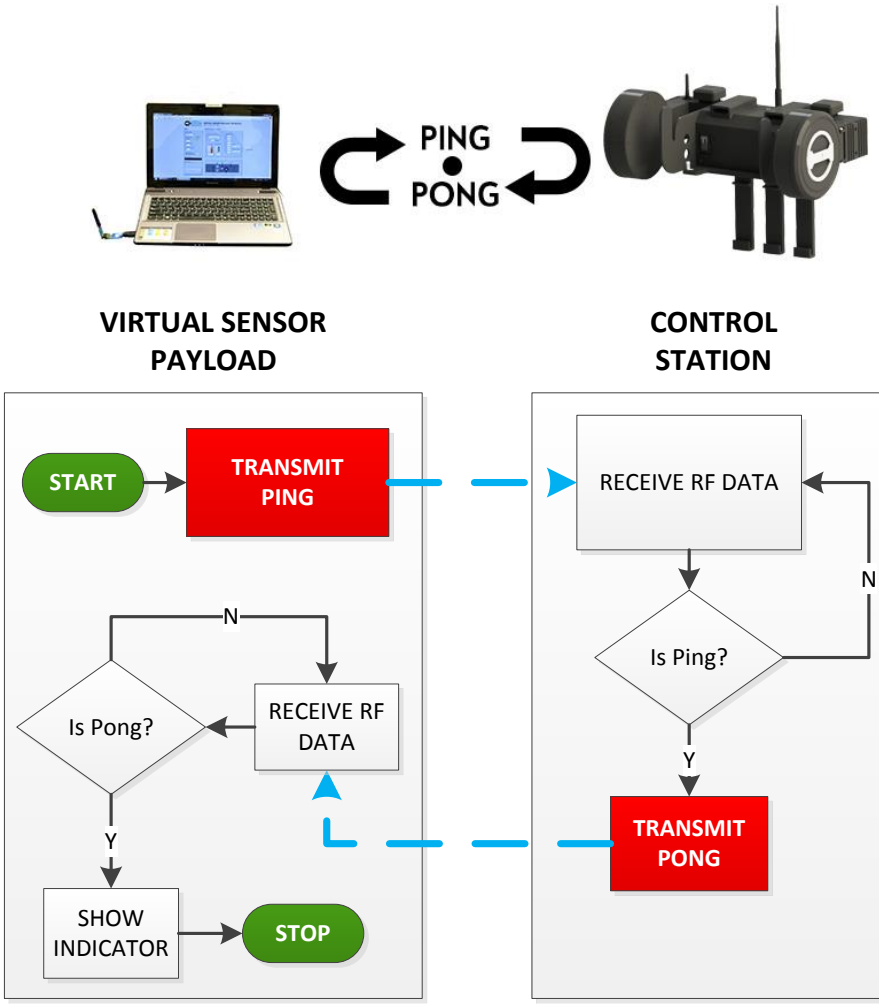

Figure 10-29 - Algorithm for Ping Pong Test

Following from this, the ping pong routine was coded to occur repeatedly in a loop, with a moving averaging function used for smoothing the recorded array of values. Similarly to the range test, the virtual sensor payload was then located at 3 m intervals away from the control station to determine the relative difference between the latency values at different distances.

10.3.2.1. Results

It was observed during testing that the latency values measured were very sporadic, but had a clear trend of displaying higher values with further distance of the virtual sensor payload away from the control station. **Figure 10-30** below displays this trend, which showed a maximum of 81 ms at the 51 m mark. Using the graph's trend line, a 1.25 % increase in latency was calculated for every 1 m.

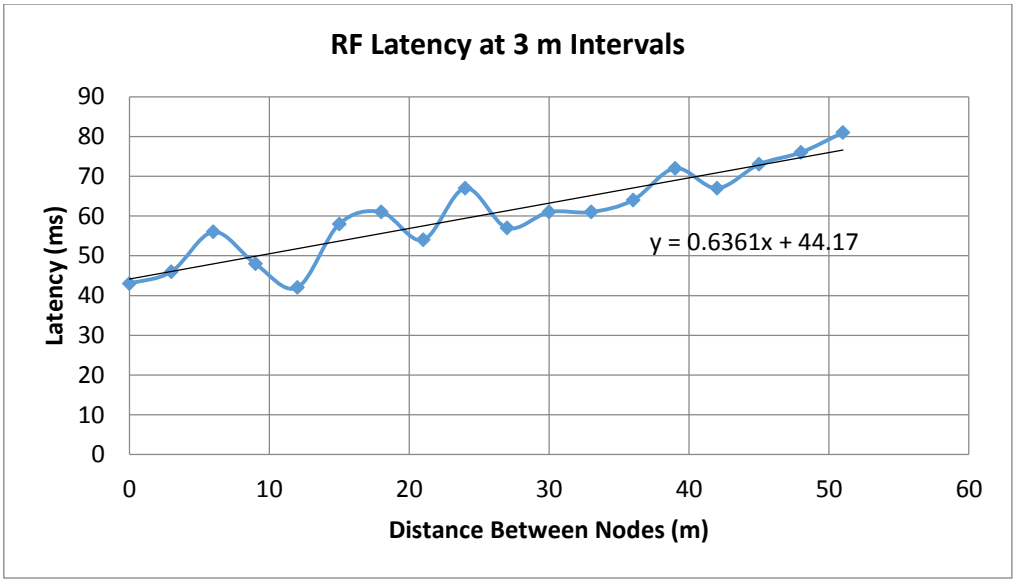

Figure 10-30 - Graph of RF Latency Times at 3 m Intervals

10.3.3. RF COMMUNICATIONS SURVIVABILITY TEST

Survivability of the RF communications is essential to maintain a link between the two nodes over a prolonged period of time. Ideally, at least 20 minutes of communications should be achieved, as this was the specified deployment time of the robotic platform into the void. To test this, the two wireless nodes were set 10 m apart, and the same repeating linear function used for the range test was used to constantly transmit data from the control station to the virtual sensor payload. The amount of time was recorded as well as the number of lost packets in the duration.

10.3.3.1. Results

It was discovered that communications were able to sustain themselves well above the 20 minutes required. The longest time recorded was 5 hours 17 minutes and 46 seconds before its termination was done manually by the author. During this period, a total number of 737274 packets were transmitted, averaging at 38.67 ms for each transmission. It should be noted that this is higher than the average time per send value found in the range tests at the 10 m range, and is most likely a result of the extra processing time compounded over time for the much larger number of transmissions.

The relationship amount of lost packets relative to the amount of packets sent was found to be linear, as can be seen in the graph on the following page.

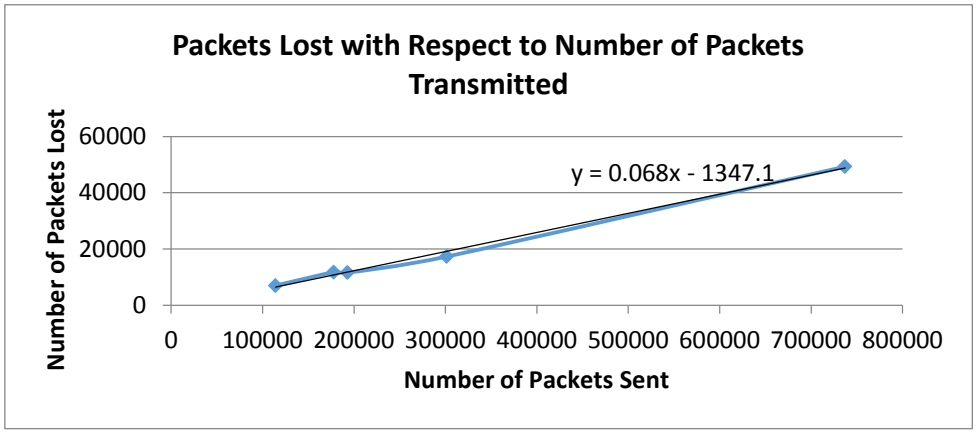

Figure 10-31 - Graph of Packets Lost Relative to Packets Transmitted

The number of lost packets did not exceed 6.7 % of the total number of packets transmitted. The shortest time was recorded to be 47 minutes and 14 seconds, which displayed a 6.1 % packet loss. This therefore illustrated that while the amount of transmissions did increase the packet loss percentage, it did not do so at a rate which would severely affect the communications.

10.4. ELECTRICAL TESTS

Electrical tests were performed to evaluate the performance of the modules in the power supply subsystem. Throughout the tests INA220 current sensor boards were used. These were provided by G. Knox, and communicated using I^2C with a MSP430 LaunchPad. These were calibrated to provide a 1 mA resolution. The advantage of using I^2C communications was that the boards could all communicate on a single bus, making them ideal for multiple testing points. The below figure illustrates the general setup, which made use of the power distribution board's current sensor connection points:

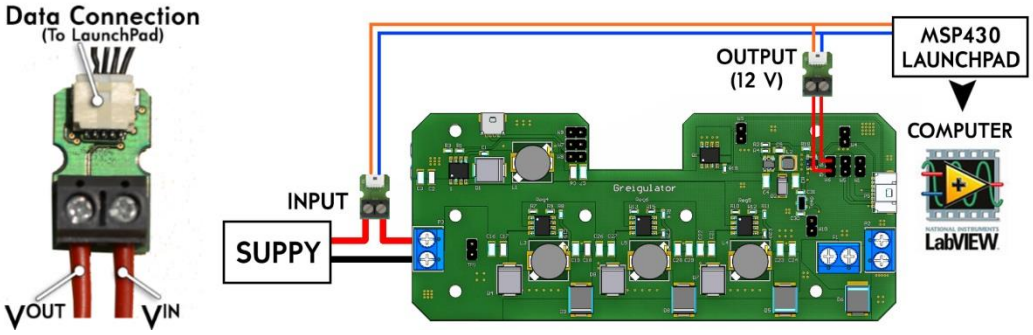

Figure 10-32 - Connection Layout of INA220 Current Sensors

Throughout the tests, different power modes were used to illustrate different possible configurations during usage of the control station:

- **Low-Power** – Only the 3.3 V supply rail is online.
- **Normal-Power** – Everything, except for the DVR, and FPV Goggles is online.
- **Full-Power** – Everything is online.

Normal power mode was therefore representative of all the peripherals required for a working control station. Note the 20 V rail used for charging the robotic platform is not included in any of the modes and has a dedicated testing section, as it was considered separate from the control station electronics.

10.4.1. POWER CONSUMPTION

This test aimed to measure the power consumption of the control station electronics during each of the power modes, as well as the separate components. This served to provide a basis of how much power was being used relative to the entire system. To perform this, the current through each supply rail was measured using the INA220 sensors, and the devices were then turned on depending on the mode required. The voltage of each supply rail was measured using a multi-meter, and the power was then calculated using the two values acquired.

10.4.1.1. Results

As can be seen below, the system together combined was found to draw less than 10 W. In Full Power mode, the system draws 48.8 % more power than when in Normal Power, with the video receiver being the highest power component. While Low Power mode draws only 4.0 % of normal operating conditions, it was still noted that 257 mW was still high for what is considered to be a standby state. This was due to the STM32F407VG embedded microprocessor, and as such, future work should consider incorporating turning off of its unneeded peripherals, such as the SPI communications to the OSD, during Low Power mode.

Table 10-5 - Power Consumption for 3.3 V, 5 V, 12 V Supply Rails in Different Power Modes

Supply Rail	Power (mW)		
	Low Power	Normal Power	Full Power
3.3 V	257.4	283.8	283.8
5 V	0	584.3	584.3
12 V	0	5539.1	8666.3
TOTAL	**257.4**	**6407.2**	**9534.4**

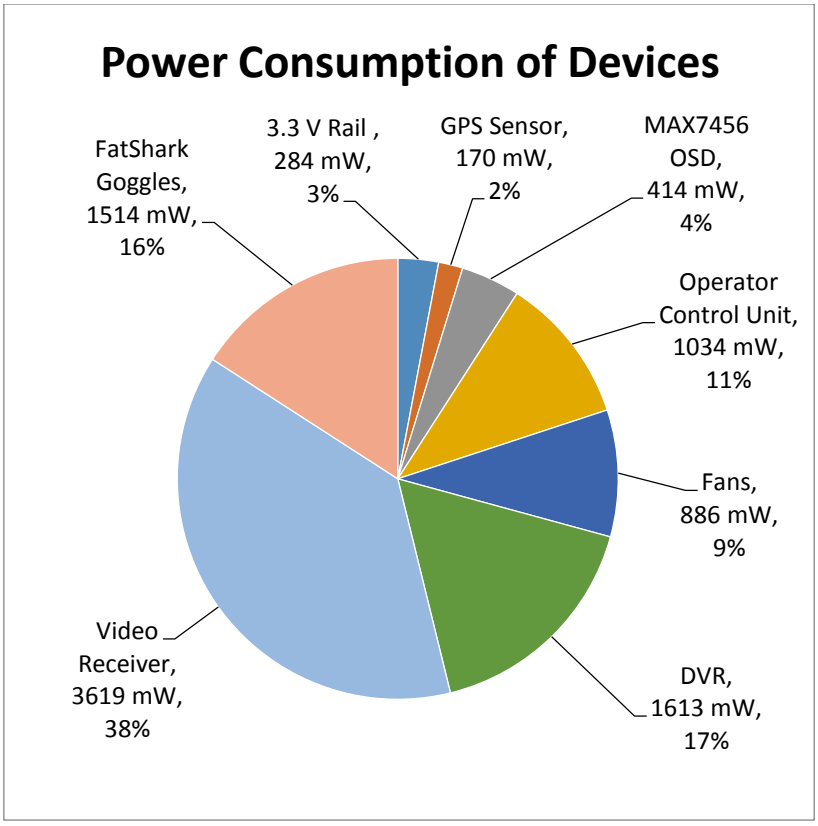

Figure 10-33 - Power Consumption of Control Station Electronics

It was observed that the majority of the consumption was due to the peripherals connected to the system, as opposed to the controlling electronics, and constituted a total of 71 %. The highest power consumption was due to the video receiver which constituted 38 % of the total consumption.

10.4.2. SYSTEM POWER EFFICIENCY

Power efficiency is vital in the control station to ensure the most running time from the battery. To test this, the main supply current to the power distribution board was measured using a INA220 current sensor board, and additional sensor boards were used to measure the current to each of the supply rails. The voltage of both the input supply and the power rails were also measured using a multi-meter. These were then collated together to calculate the power efficiency by using the calculated input power and the output power totals:

This was done at 0.5 V intervals from the input supply to determine the system's power efficiency at different supply voltage levels from the battery.

10.4.2.1. Results

The total power efficiency for the control station electronics is shown below. It was seen that the power efficiency for all rails decreased with increasing voltage, which agreed with the data found in the regulators' datasheets. A minimum of approximately 86 % power efficiency was determined for Full Power and Normal Power mode when using a 25.5 V input supply.

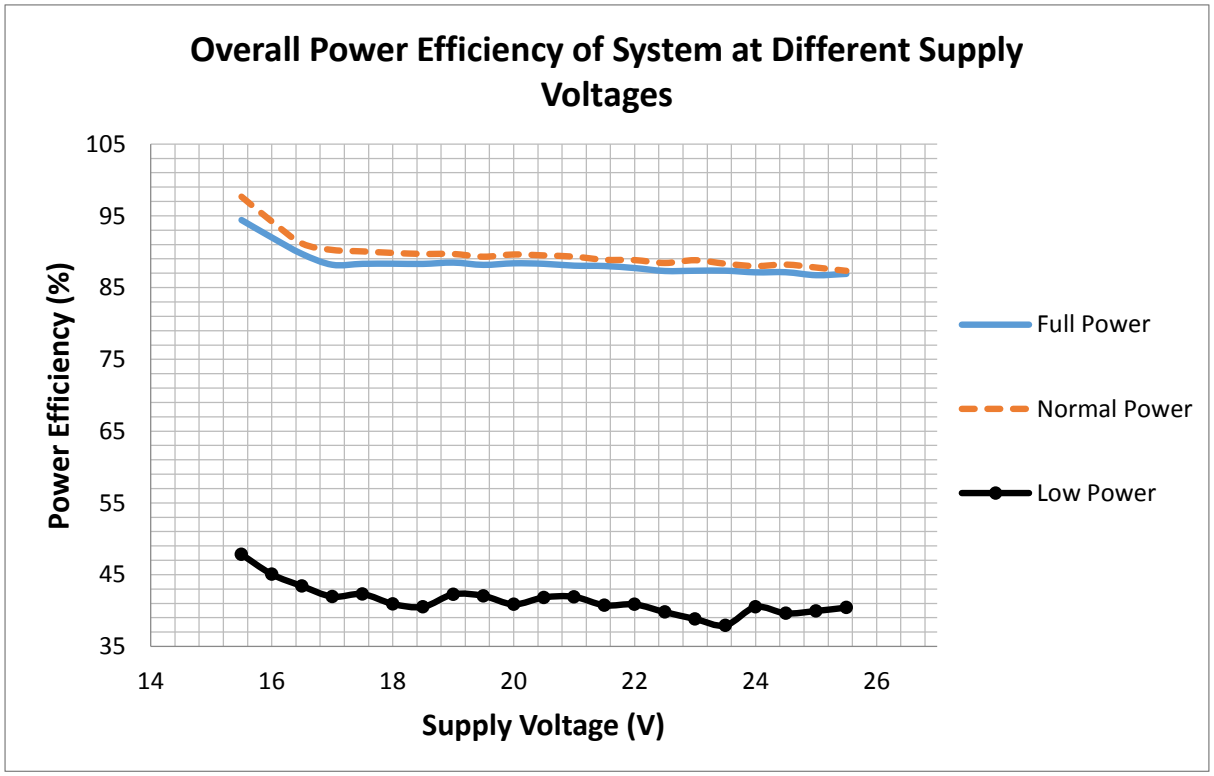

Figure 10-34 - Graph of System Power Efficiencies at Different Supply Voltages

While it could be seen that in Low Power mode, the power efficiency was particularly low, being 37.9 % at 25.5 V, this was due to regulators being used which typically display very low levels of power efficiency at minimal current consumption. This was also deemed to be negligible due to the overall amount of power being consumed in this mode, which can be further improved upon by the suggestions made in the previous test.

10.4.3. 20 V SUPPLY RAIL TESTING

The 20 V supply rail was a crucial area of testing as it determined the control station's ability to supply enough power to fulfil the robotic platform's charging requirements. This was tested in isolation as it was the highest power rail in the system, with a total of 160 W. This was also to test the behaviour of the three switching regulators used in parallel. To perform the test, a variable resistor was connected to the 20 V rail to produce different current outputs. The temperatures of each regulator and the power efficiency the rail were also measured. The temperature of each regulator was monitored using a FLIR A320 IR camera. This was to provide an idea of whether each regulator was handling the load without the need for individual current sensors. Like the previous tests power efficiency was calculated by using INA220 current sensors at both the input supply and the 20 V output and measuring the voltage using a multi-meter. A supply voltage of 25.2 V was used.

10.4.3.1. Results

The voltage outputs of each regulator were measured to be 20.96, 20.96, and 20.97 V with a combined parallel voltage of 20.84 V.

The 20 V rail was tested to be able to supply over 8 A of current. However, sporadic behaviour began at the 6.5 A mark where the regulators would begin to periodically change in current output value. An example is shown below for the 8 A testing, which illustrates how the current continuously changed in large intervals over a 110 ms period. A maximum of 6.3 A was found suitable for stable operation.

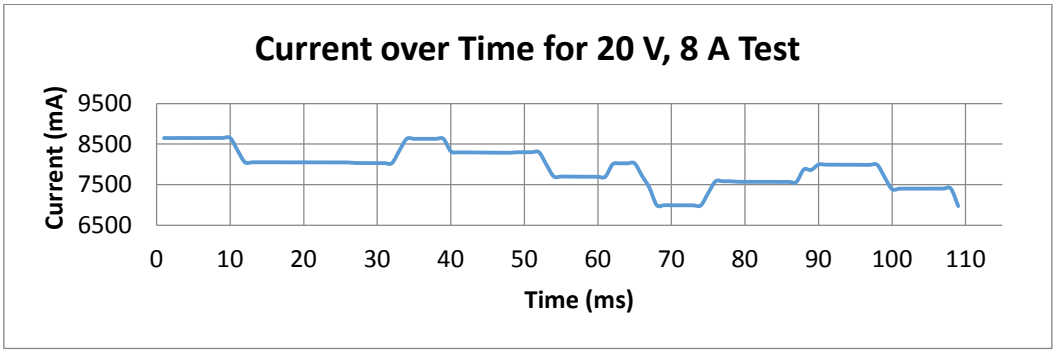

Figure 10-35 - Graph of Current Over Time for 20 V, 8 A Discharge Test

The power efficiency of the 20 V supply rail was found to be above 80 % for all current outputs tested. At the recommended 6.3 A output, a power efficiency of 87.1 % was recorded.

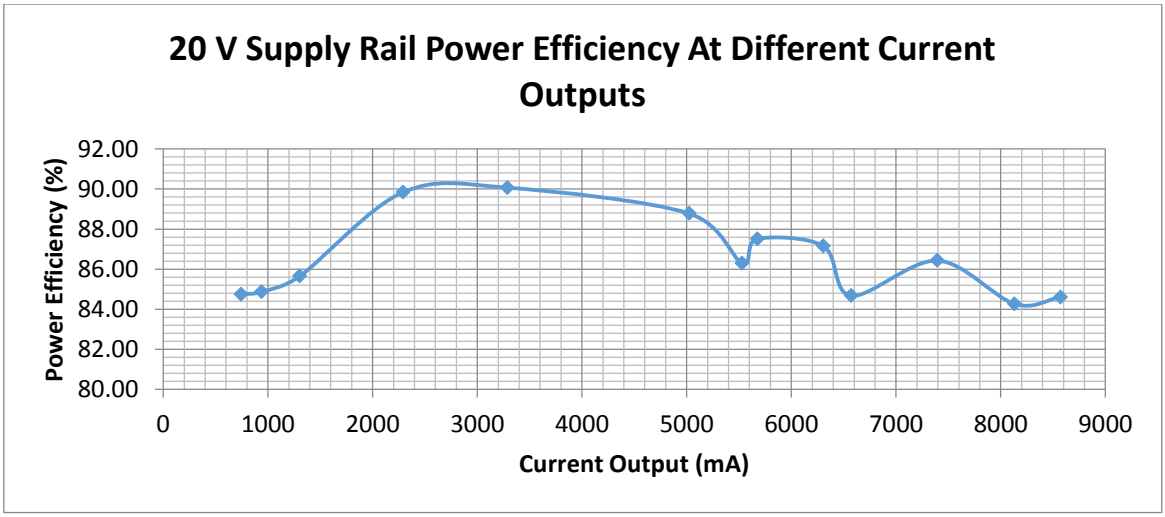

Figure 10-36 - Graph of 20 V Supply Rail Power Efficiency at Different Current Outputs

CHAPTER 10: Testing and Results

Temperatures were measured to be up to 86.3 °C without a heat sink during the 5.3 A tests. The heat sink was mounted onto the board afterwards to protect the components from failure. Because the thermal camera could not measure the temperature of reflective surfaces, a digital thermometer with a thermocouple was used instead, as shown in **Figure 10-37**. The heat sink was then measured to show temperatures no higher than 60.1 °C during the 8.3 A test.

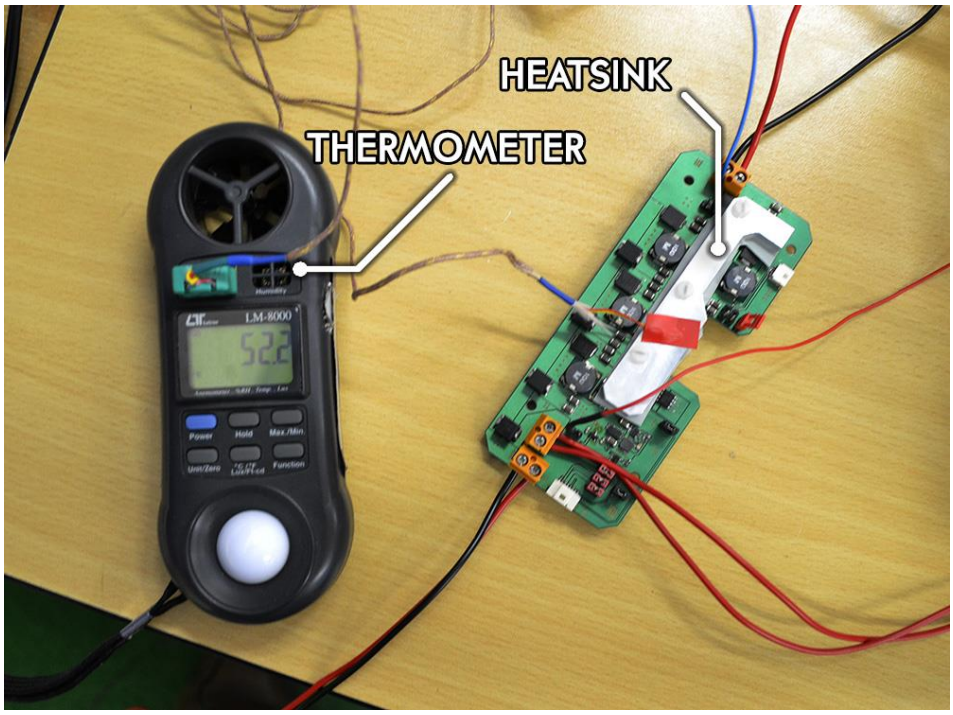

Figure 10-37 - Digital Thermometer and Power Distribution Board Heat Sink Mounted

Before the heat sink was mounted, it was noticed that while the regulators' temperatures were within a 10 °C range to each other, the middle regulator was consistently the hottest. It was also discovered that sometimes only two of the regulators would be active, as shown below in **Figure 10-38**, which served as a reason to explain the sporadic behaviour encountered.

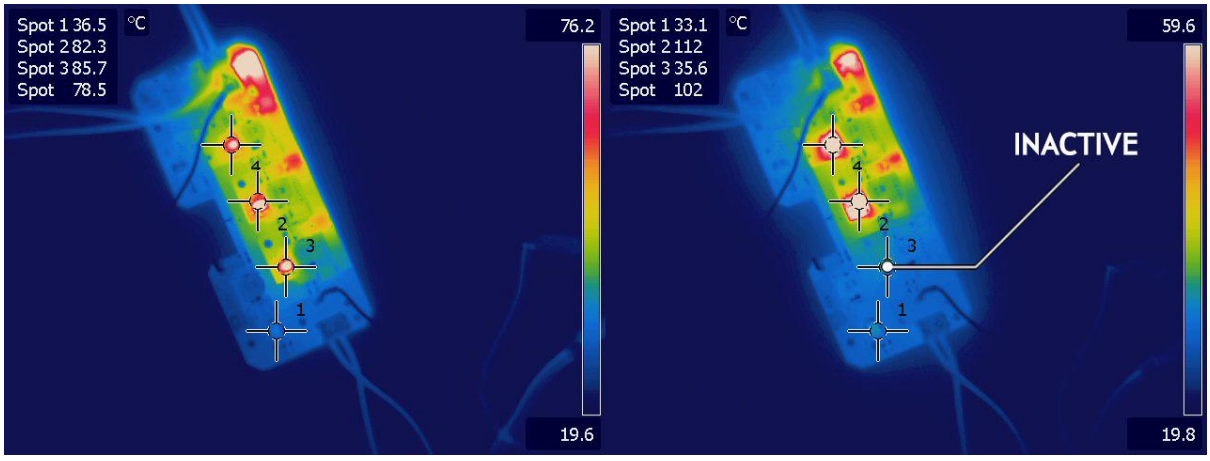

Figure 10-38 – Highest Recorded 20 V Regulator Temperature (left), Inactive Third Regulator (right)

This therefore suggested that while the voltage outputs of the regulators were very close to each other, the amount of heat generated caused intermittent failures of the regulators, forcing the other two to take the load. Further testing would be best performed by including current sensors on each of the 5 A outputs in the future.

10.4.4. OPERATING TEMPERATURE

This test aimed to determine the temperatures of each chassis box and the OCU. This test was important especially to account for the Back Box, which had the highest surface area in contact with the person's back.

In the event that chassis box may accidentally come loose and lodge itself onto the person's bare back, it must be ensured that it does not cause any harm. The temperature at which a person begins to perceive pain is known as the Threshold of Pain. A study by A.M. Stoll et al [87] showed that being in contact with steel at a temperature of 54.4°C for three seconds was enough to invoke bodily pain.

The tests were done in the laboratory with all of the control station's electronics, including the power supply inside of the chassis. The ambient room temperature measured was 19.3 °C. The system was then allowed to run for approximately one hour.

The LabVIEW control station interface was used to log all of the temperature data throughout the system onto a 2D array. This was then exported onto Microsoft Excel to plot a graph.

10.4.4.1. Results

The highest recorded temperatures for each component were as follows:

Table 10-6 - Highest Recorded Temperatures in Each Chassis Box

Component	Temperature (°C)
Back Box	26
Computing Box	22
Power Box	23
OCU	20

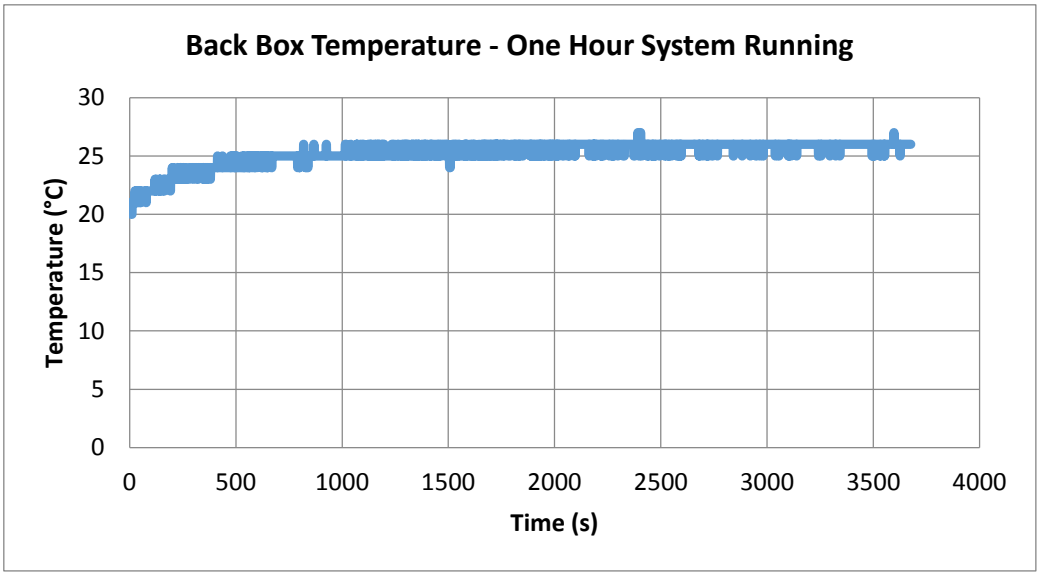

Figure 10-39 – Graph of Back Box Temperature after One Hour with System Running

It was observed that the operational temperatures were well within safe levels, with maximum temperature being recorded in the Back Box, displaying a maximum value of 26 °C. This was therefore deemed to be at safe levels to be against the operator's back.

10.4.5. BATTERY PROTECTION

Ensuring the working state of the battery protection was critical as this was a vital indicator of whether the battery would be safe for use in the control station. Tests were therefore performed to determine whether the circuitry reacted appropriately towards each of the battery error conditions. To do this, each of the battery error conditions were produced in the system, and the resulting effects were recorded. To monitor the battery errors, the BQ77910 Evaluation Software was used. Importantly, the means to recover the system from the error was also noted.

For this test, **DSG** refers to the discharge MOSFET, and **CHG** refers to the charge MOSFET.

10.4.5.1. Results

Charge/Discharge Short Circuit

This was tested by connecting a wire between the CHG-, DSG- outputs, and the BAT+ input in order to apply a short circuit condition.

MOSFETS open: DSG, CHG
Recovery: Remove short circuit, toggle CE pin low, then high

Over Temperature

Thermistor functionality was tested by applying a heat air gun on the thermistor.

MOSFETS open: DSG, CHG
Recovery: Allow cool down of the thermistor.

For the cell under-voltage and over-voltage tests, a fixed resistor voltage divider circuit was used to provide varying voltages into each of the cell monitoring inputs into the IC.

Cell Under-Voltage

The voltage of the cell was set to be below 3.0 V from the adjacent cell:

MOSFETS open: DSG
Recovery: Cell set above 3.0 V.

Cell Over-Voltage

The voltage of the cell was set to be above 4.2 V from the adjacent cell:

MOSFETS open: CHG
Recovery: Cell set below 4.2 V.

It was determined the battery protection functions were working as expected, with the majority of the functions requiring passive methods to recover from the error which did not require interaction from the author.

It was noted during both development and testing that the CE toggle required to clear the short-circuit errors could not be performed via the user interface due to the fact the DSG FET becomes open. A future addition to the system should therefore include a manual reset button on the Power Box.

Included were also concerns about the fact the MOSFETS will always stay open if there is a battery error – meaning that if an external power supply were to be used in its stead, it would not work unless the battery protection was bypassed.

10.4.6. BATTERY CAPACITY

This test was performed to determine whether the 8000 mAh Li-Po battery could supply the two charges required for the robotic platform.

Ideally the test would have been performed by attempting to charge the sensor payload's battery two times using G. Knox's charging circuitry. Unfortunately the charger was unavailable due to failure of the board after its testing, and required reassembly and reordering of components which did not fit within the time and scope constraints. Therefore the charger's recorded test data was used to determine the time required to complete a single charge. G. Knox documented that 51 minutes was required in order to achieve a full recharge using the charger's maximum charge rate of 6 A.

Using this data, the battery was then used to supply power to the power distribution board's 20 V supply rail, and used a variable resistor to produce a 6 A discharge rate. This was allowed to run for 100 minutes, and the battery management board's fuel gauge was used to log the battery voltage for this duration. The logging software used was TI's bq Evaluation package. Please see **Chapter 8. Power Supply** for more information on this setup.

10.4.6.1. Results

It was discovered that the battery successfully supplied two charges worth of discharge over a 100 minute time period.

The battery voltage was measured to be 24.8 V before the discharge, and was 21.4 V at the end of the process. This was found favourable as the safest lowest voltage of the battery is 18 V.

Below shows the graph plotted using the battery fuel gauge's data. The periodic spikes seen are not attributed to the actual battery voltage, but are a result of communication errors between the device and the EV2300 used to communicate to the computer.

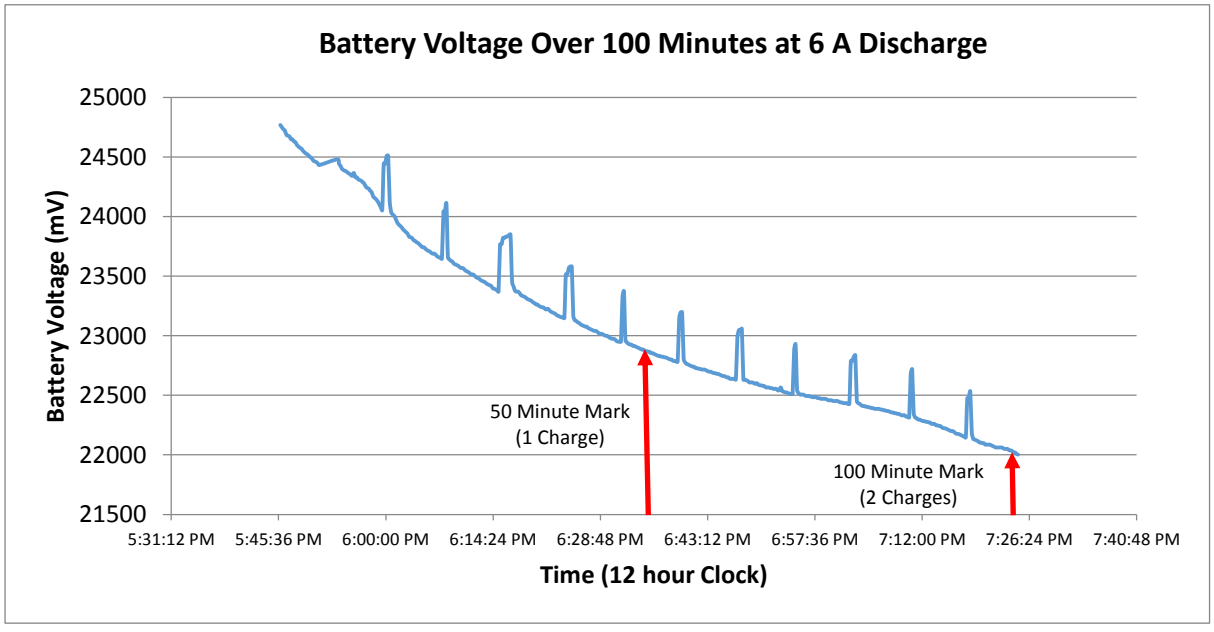

Figure 10-40 – Graph of Battery Voltage at 6 A Discharge Over 100 Minutes

10.4.7. CHARGER TESTS

10.4.7.1. System Power Selection Test

This tested the system power selection feature of the charger, ensuring that it was able to select the correct power supply, switching between the battery and an external power supply depending on which one had the higher voltage. Importantly, it was also observed whether there was any interruption to the input supply to the control station electronics during the transition between supplies. To test this, the battery and external power supply were connected to the system, and used different voltage levels to indicate which supply was used.

This was tested successfully, with the battery voltage being read as the system supply instead of the external power supply upon disconnection of the external power supply. Upon connecting the higher voltage external power supply to the system, it was discovered that there was no interruption to the power. This test was therefore deemed to be successful.

10.4.7.2. Charging

Initiation of the charging was found to be unsuccessful. As mentioned previously in **Chapter 8. Power Supply**, inrush current issues were encountered with the charger board upon system start-up, causing multiple failures of the device, and therefore a NTC inrush current-limiting thermistor was implemented to prevent this issue. This solved the start-up inrush issues, but the charge process was still not able to start, with multiple failures of the device upon attempting to do so.

Upon a more aggressive inspection of the boards, it was discovered a matte compound was formed underneath the pads of each of the components which formed a non-conductive barrier between the PCB pads and the component. This suggested a manufacturing error due to contamination of the boards during the storage process, as it was verified that every other board from the same manufacturing run displayed the same issue. The significance of this was reflected by the fact the charger IC uses a QFN footprint package, which uses connecting pads located directly underneath the IC, and therefore could not be reliably tested for continuity due to them being inaccessible from the outside. Reassembly of the boards would have required the reordering of shipped components and ideally, remanufactured and properly treated boards, which did not fit within the time constraints of the project. As such, this component was deemed to have unfortunately failed in this respect.

10.5. SUMMARY

The tests presented in this chapter served to display the working state of the system as well as to benchmark its performance against the required system specifications. Overall, it was found that the specifications were met, with a working control station able to communicate with a virtual version of the robotic platform's sensor payload, and providing a complete operator user interface with working sensors. **Chapter 11. Conclusions and Recommendations**, which follows, collates the results data found from this chapter and forms conclusions to be used for recommendations which can be applied in future developments of the system.

11. CONCLUSIONS AND RECOMMENDATIONS

This chapter details the conclusions and recommendations derived from the results found in **Chapter 10. Testing and Results**. Included are discussions of possible extensions and designs which were realised during testing and development which can be applied in future work of the Scarab system. A summary section at the end collates all the key recommendations which were found to be most critical.

11.1. Mechanical Chassis

The man-wearable chassis proved to be an effective system overall, being tested to provide deployment times within less than half a minute, and being able to taken off as a single unit within less than 6 seconds.

The docking method used was found to be effective, allowing mounting of the robotic platform without assistance within the space of 13 seconds. However, this was not a comfortable procedure due to the long distance of the wheel axel slots away from the back as well as the requirement to bend the shoulder backwards whilst trying to locate the platform into the mounting brackets. It was also discovered that deployment was more intuitive if the tail of the robotic platform was located on the upper side of the chassis as opposed to the bottom. This is a simple adjustment which can be performed by using the vest's top carry handle as the strap down location for the tail slot. To facilitate this however, the video receiver antenna must be relocated away from the centre of the Back Box.

The total mass of the system was measured to be 7.43 kg, including the robotic platform. While this fitted within the specification of 8 kg required, further significant weight reduction can be achieved by reducing the size of the Computing and Video Receiver Box and is expected with smaller iterations from future generations of the robotic platform.

The system boundary tests revealed that an operator can fit within a standard door frame whilst wearing the system, but cannot perform a full 360° turn if standing in the centre. This presents both a safety concern as well as an overall system usability deterrent. To achieve this turn, a minimum of 27.5 mm reduction in length of the system from the operator's back would be required.

The L-shape of the lids for the Back Box and Power Box proved problematic for the system's sealing. While it made maintenance to the internal components very accessible, it came at the cost of higher complexity in manufacturing and being non-ideal for seating a seal around the edges. Future versions of these two boxes should therefore be redesigned to use a flat lid to provide an even surface for the seals. Also due to the flexible nature of HDPE, sealing between the Back Box and Power Box was not ideal as it depended on a flat surface for compression. This illustrated that seating seals between flat walls is not recommendable for longer parts made from HDPE material, and a hub press fit approach should be used instead for interconnection and wire routing. Another consideration is the addition of dust filters for the Back Box's air vents as well as a seal on the side box's lids to introduce compressibility between them and their respective control panels.

11.2. Control Station Electronics

The RF results were found to be suitable, displaying the transceiver's communication ability to exceed the 30 m range specified, at a maximum latency of 81 ms at 51 m. They were also able to sustain communications for over hours at a time, achieving the 20 minutes required. However it was discovered this was only reliable for simple commands, which indicates that keeping the amount of data sent minimal is vital in maintaining stability. This also further motivates the reason to include all the processing on the sensor payload and motor control board, and wireless data communications should be isolated to only single value commands and periodically polled readings. This should all however be taken into account only after further refinement of G. Knox's firmware code for the transceivers, which can potentially lead to an overall increase in RF performance between both systems. As such, a more cohesive and dedicated integration process would also be of great benefit.

As discovered during the integration of the transceivers in the system, signal ringing was present in the SPI data communication lines due to the wire length, and was resolved by soldering 1 K signal damping resistors in series on each wire. Therefore future development should include these resistors on the Central Processing Board and transceiver adapter board, located as close to the transmitting pins as possible. Another recommendation is to relocate the RF transceiver into the Computing Box to reduce the wire length. This can be done simply by including a new header onto the Hub Board for it to be mounted on.

The uBlox NEO-7M GPS sensor selected was found to perform very well, being able to reliably supply coordinate data over prolonged periods of time, as well as being able to serve as a unit which could help locate the control station in an external environment. Additionally, the decision to make it into a module breakout board to allow it to become independent of the control station proved very helpful, allowing it to be connected with other devices.

The MAX7456 OSD generator selected was tested to be a suitable and robust solution, allowing ease of development, and characters to be overlaid on a camera feed correctly without distortion or change to the raw video image. The custom characters generated were correctly processed, but notes should be taken to avoid the use of large white shapes in the future, as these were found difficult to differentiate from brighter backgrounds, even with black borders.

One safety concern is that the only means for an operator to know whether the battery protection has failed, and the battery is at hazardous temperature levels is by noticing a warning message on the OSD. This can go easily unnoticed if the operator is not looking at the video feed, and it is therefore highly recommended to include a buzzer in the future to serve as an audible alarm.

11.3. Operator Control Unit

Through the user tests, the OCU was concluded to be suitable for the use of different sized hands, as well as offering ambidextrous operation while wearing safety gloves. There were concerns in regards to the thick blocky shape of the holding area, which was a result of the conceptual design phase which migrated away from a curvier approach in favour of more holdable areas. The specification of a smaller main cable connector would therefore be of great benefit as it was the part which defined the thickness of the body.

It was also discovered that the controller was better received by smaller handed people. This illustrated the importance of the distance between the joystick and buttons, as it determined how easy it was to move between controls with minimal adjustment of the hand. It would therefore be recommended to change the LED brightness settings to use only the top button on the array. This would allow all essential driving controls to be within the thumb's reach.

Considerations should also be made to include a small button dedicated to act as a robot lock. This would provide an obvious control which keeps the system intuitive and usable even without any training.

11.4. Firmware

Overall the user interface performed very well, providing a basic platform upon which further modifications and developments can be made with ease. The user tests revealed that the system was intuitive and could be learned within minutes after being guided through. However this was only for the menu interface and further validation is required for driving the actual robot.

One issue encountered during the OSD testing was the requirement for basic user settings to adjust the screen offset for different screen resolutions as well as layout adjustments when switching between PAL and NTSC video formats. It is believed that with future development of the camera in the sensor payload, which provides options to directly change the image settings, such as brightness and contrast, a full image and screen adjustment menu interface is possible and would be of significant benefit to the Scarab system overall.

As determined in magnetometer calibration testing, the calibration managed to produce a spherical shape centered on the origin as required. This however suffered from requiring a lengthy sequence in order to reach the number of data points needed. This was due to there being no actual indication in the user interface to confirm whether the sequence was complete, nor was there any guide to show whether a rotation direction was already performed. Therefore future implementations should consider including a dedicated calibration menu interface which displays the currently recorded maximum axis values, and provide a list of rotation directions which can be followed and completed. To remove the need to always recalibrate the magnetometer in the same immediate area after a system reset, EEPROM should be implemented on the Central Processing Board. This would provide non-volatile memory storage which can be used for other useful functions, such as storing security access data, as well as user configuration settings for the RF1101SE transceiver.

The behaviour of the motor profiles was found to perform correctly as expected, and are deemed ready for actual testing with the robotic platform once it is operational. As shown by the RF transceiver tests, which discourages transmitting of functions wirelessly, the code should be ported to the microprocessor on the motor controller board. This would be a simple and quick process as all the inputs and outputs of the functions would essentially remain the same.

11.5. Power Supply

The power supply was found to be suitable for the use of the control station electronics, with an overall of 86 % power efficiency from the combined cascade of regulators, and provided minimal heat issues when operating under normal conditions.

Testing of the 20 V supply rail demonstrated the ability to supply 8 A which was required for charging the robotic platform, but was not at a stable rate due to the parallel switching regulator setup used. It was discovered that not all three regulators would be active at all times, resulting in the other two regulators having to a handle the larger load. This indicated the need for a control system which can be best implemented by including on-board current sensors for each 5 A output rail to provide feedback. It should also be noted that while the voltage of the three parallel regulators was measured to be within 100 mV of each other, further accuracy can be achieved by using 1 % tolerance resistors for the voltage setting for each regulator over the 5 % tolerance components which were used. The supply rail was determined to be capable of supplying a maximum of 6.3 A at a stable rate, which did not meet the 8 A originally specified, but was still suitable for the robotic platform's charger which was tested by G. Knox to demonstrate a 6 A maximum feasible charge rate.

CHAPTER 11: Conclusions and Recommendations

The battery protection module was tested to perform its functions as required. One issue realised in the tests was that if the battery encountered an error, or was removed, it would be necessary to use an external power supply in its stead. However, this would not be possible due to the discharge MOSFET on the battery management board being open in response to the battery fault. Therefore a MOSFET switch should be implemented on the battery charger board to allow bypassing of the battery management board in this scenario and directly connect the external power supply to the power distribution board.

As discovered in the system supply selection tests, a 5 Ω NTC inrush-limiting thermistor was required to prevent current inrush issues when connecting the battery to the charger board. However, this was implemented as an improvised in-line solution with the fuse holder which required manual bypassing by the operator using physical connectors. As such it was deemed cumbersome for both maintenance and assembly. The thermistor should therefore be included in future versions of the battery management board along with an automated means of bypassing it once the start-up sequence has completed.

Unfortunately the system could not be tested with the charger due to manufacturing defects present with the boards. Future testing of the system should aim to measure the temperature of the battery and system during charging as well as its voltage behaviour during storage charging, which involves both the control station's and robotic platform's batteries being charged concurrently by using the same supply.

11.6. SUMMARY

The first generation of the operator control station for the Scarab robotic rescue system was successfully developed and built. Overall, it met the majority of specifications but requires further development before it can fully integrate with the robotic platform and sensor payload as a robust system for the use in USAR. A summary of the major recommendations derived from the conclusions are listed below:

- Decrease the size of the control station's length from the operator's back by reducing the size of the two side boxes.
- Adjust the docking method to accommodate for being able to fix the robotic platform's tail in an upright position.
- Redesign the Power Box and Back Box to use flat-lid covers.
- Incorporate a current inrush protection system on the battery management board.
- Implement a buzzer to be used as an alarm.
- Incorporate new modules into the user interface to account for a more intuitive calibration process as well as screen adjustment options.
- Avoid sending continuous large packets of data wirelessly to the sensor payload, and focus on the usage of simple commands which rely on single values.

12. REFERENCES

[1] P. Ryan and RAF/MOD, “A Mk 8 Wheelbarrow explosive ordnance disposal (EOD) robot remotly detonates a suspect explosive device,” *Wikimedia Commons*, 2002. [Online]. Available: https://commons.wikimedia.org/wiki/File:A_Mk_8_Wheelbarrow_explosive_ordnance_disposal_(EOD)_robot_remotly_detonates_a_suspect_explosive_device._Afghanistan._13-03-2002_MOD_45141173.jpg. [Accessed: 04-Aug-2015].

[2] M. van Zomeren, “Search Methods in USAR,” *Delft Univ. Technol. Collab. a Distance Proj. Lit. Rev.*, no. September, 2008.

[3] Robin Murphy, “Activities of the Rescue Robots at the World Trade Center from 11–21 September 2001,” *IEEE Robot. Autom. Mag.*, no. September, pp. 50–61, 2005.

[4] R. R. Murphy, J. Casper, and M. Micire, “Potential Tasks and Research Issues for Mobile Robots in RoboCup Rescue,” 2001.

[5] P&R Infrared, “Recon Scout Throwbot.” [Online]. Available: http://pr-infrared.com/shop/recon-scout-throwbot/. [Accessed: 04-Aug-2015].

[6] Robo Phil, “Throwbot XT Product Review,” 2015. [Online]. Available: http://www.robophil.com/2015/05/19/throwbot-xt-product-review/. [Accessed: 05-Aug-2015].

[7] iRobot, “iRobot 110 Firstlook Specifications.”

[8] Center for Robot-Assisted Search and Rescue (CRASAR) at Texas A&M University, “Table of Responses,” 2015. [Online]. Available: http://crasar.org/about/table-of-responses/. [Accessed: 04-Aug-2015].

[9] CRASAR Rescue Robots, “A Decade of Rescue Robots,” 2012. [Online]. Available: https://www.youtube.com/watch?v=QPQrKAYbQUQ. [Accessed: 04-Aug-2015].

[10] CRASAR, “Center for Robot-Assisted Search and Rescue (CRASAR) at Texas A&M University,” 2015. [Online]. Available: http://crasar.org/. [Accessed: 04-Aug-2015].

[11] R. R. Murphy, J. G. Blitch, and J. L. Casper, “AAAI/RoboCup-2001 Urban Search and Rescue Events: reality and competition,” *AI Mag.*, vol. 23, no. 1, pp. 37–42, 2002.

[12] M. Rieger and RARL, “Research and Development of a Rescue Robot End-Effector,” 2013.

[13] P. Dietrich and C. Tech, “Conquering the design challenges of soldier-wearable applications,” *Computer-On-Module*, 2012.

[14] E. O. Thorp, “The Invention of the First Wearable Computer,” *Edward O. Thorp Assoc.*

[15] P. N. Holey and V. T. Galikwad, “Google Glass Technology,” *Int. J. Adv. Res. Comput. Sci. Manag. Stud.*, vol. 2, no. 3, 2014.

[16] P. R. Desai, P. N. Desai, K. D. Ajmera, and K. Mehta, “A Review Paper on Oculus Rift - A Virtual Reality Headset,” *Int. J. Eng. Trends Technol.*, vol. 13, no. 4, 2014.

[17] A. Diaz, “7 methods to predict roulette numbers Roulette Bet,” *Roulette-Bet*, 2015. [Online]. Available: http://www.roulette-bet.com/2015/02/7-methods-to-predict-roulette-numbers.html. [Accessed: 03-Aug-2015].

[18] Oculus VR, “Crescent Bay Prototype,” *Oculus Connect 2014*, 2014. [Online]. Available: https://www.oculus.com/en-us/blog/oculus-connect-2014/. [Accessed: 03-Aug-2015].

[19] A. Bozkurt, D. L. Roberts, B. L. Sherman, and North Carolina State University, “Toward Cyber-Enhanced Working Dogs for Search and Rescue,” *Intell. Syst. IEEE*, pp. 32–39, 2014.

[20] Army Technology, “Raytheon XOS 2 Exoskeleton, Second-Generation Robotics Suit,” 2008. [Online]. Available: http://www.army-technology.com/projects/raytheon-xos-2-exoskeleton-us/. [Accessed: 03-Aug-2015].

[21] A. Zoss, H. Kazerooni, and A. Chu, “On the Mechanical Design of the Berkeley Lower Extremity Exoskeleton (BLEEX),” 2005.

[22] J. B. Carnett, “Building the Real Iron Man,” *Popular Science*, 2008. [Online]. Available: http://www.popsci.com/scitech/article/2008-04/building-real-iron-man. [Accessed: 03-Aug-2015].

[23] UC Berkeley, “Next-Gen Military Man: Wearable Machines,” *Popular Science*, 2004. [Online]. Available: http://www.popsci.com/scitech/article/2004-07/next-gen-military-man-wearable-machines. [Accessed: 03-Aug-2015].

[24] Engineering Toolbox, “IP - Ingress Protection Ratings.” [Online]. Available: http://www.engineeringtoolbox.com/ip-ingress-protection-d_452.html. [Accessed: 21-Jun-2013].

[25] Defense Tech Briefs, “Man-Wearable Control Units for Military Robotics,” 2009. [Online]. Available: http://www.defensetechbriefs.com/component/content/article/4952?start=1. [Accessed: 21-Jun-2013].

[26] J. Bae, A. Larson, R. M. Voyles, R. Godzdanker, and J. Pearce, “Development and User Testing of the Gestural Joystick for Gloves-On Hazardous Environments,” *16th IEEE Int. Conf. Robot Hum. Interact. Commun.*, 2007.

[27] Army Technology, “Land Warrior Integrated Soldier System.” [Online]. Available: http://www.army-technology.com/projects/land_warrior/. [Accessed: 19-Jun-2013].

[28] Map 21, “The Army’s New Land Warrior Gear,” 2013. [Online]. Available: http://yourtactic.com/news/view/7?lang=en. [Accessed: 06-Jul-2013].

[29] C. Broz and R. Curtis, “Land Warrior System,” 2008. [Online]. Available: http://w2.militarytimes.com/land-warrior/multimedia/land-warrior-high-res.jpg. [Accessed: 03-Aug-2015].

[30] M. J. Zieniewicz, C. Douglas, D. C. Wong, and J. D. Flatt, “The Evolution of Army Wearable Systems,” 1989.

[31] Army Times, “Report: Combat soldiers carry too much weight,” 2014. [Online]. Available: http://archive.armytimes.com/article/20110214/NEWS/102140308/Report-Combat-soldiers-carry-too-much-weight. [Accessed: 03-Aug-2015].

[32] DDAWSON, “Equipment Piece of the Week: Nett Warrior,” *PEO Soldier Live*, 2011. [Online]. Available: http://peosoldier.armylive.dodlive.mil/2011/12/19/equipment-piece-of-the-week-nett-warrior-2/. [Accessed: 03-Aug-2015].

[33] B. S. R. Gourley, “Nett Warrior : Mission Command at the Tactical Edge,” 2013.

[34] Army Programs, “Nett Warrior,” 2011.

[35] K. Molinaro and U.S. Army, “Nett Warrior EDU,” 2012.

[36] DDAWSON, “Equipment Piece of the Week: Nett Warrior (NW),” *PEO Soldier Live*, 2013. [Online]. Available: http://peosoldier.armylive.dodlive.mil/2013/07/24/equipment-piece-of-the-week-nett-warrior-nw-3/. [Accessed: 03-Aug-2015].

[37] Black Diamond Technologies, “Modular Tactical System - A Modular Wearable Computing System.” [Online]. Available: http://bdatech.com/mts. [Accessed: 19-Jun-2013].

[38] V. D. Link, “Advancements in Wearable Computing Solutions Aid JTAC Missions,” pp. 1–8, 2009.

[39] ETH Zurich, “Q-Belt Integrated Computer,” 2005.

[40] Military Factory, “Military Dictionary - Definition of the military term man portable.” [Online]. Available: http://www.militaryfactory.com/dictionary/military-terms-defined.asp?term_id=3207. [Accessed: 21-Jun-2013].

[41] Defense Update, “PackBot Tactical Robot,” 2007. [Online]. Available: http://defense-update.com/products/p/pacbot.htm. [Accessed: 07-Jul-2013].

[42] M. Ekern and University of St.Thomas, “The Throwbot XT,” 2013.

[43] Recon Robotics, “Throwbot XT – With Audio,” 2012.

[44] B. Heater, “iRobot 110 FirstLook,” *Endgadget*, 2012. [Online]. Available: http://www.engadget.com/2012/03/09/irobot-110-firstlook-hands-on-video/. [Accessed: 03-Aug-2015].

[45] iRobot, “iRobot 510 PackBot Specifications.”

[46] Latest News Link, “The Military Has Found The Perfect Use For Video Game Controllers In War,” 2013. [Online]. Available: http://latestnewslink.com/2013/09/the-military-has-found-the-perfect-use-for-video-game-controllers-in-war/. [Accessed: 03-Aug-2015].

[47] AMREL, “AMREL Laptop Solutions,” 2015. [Online]. Available: http://computers.amrel.com/custom-solutions/laptop-solutions/. [Accessed: 03-Aug-2015].

[48] Tyco Electronics, “Comparison of NiCd , NiMH , and Li-Ion Batteries.”

[49] “Advantages and limitations of the Different Types of Batteries.” [Online]. Available: http://batteryuniversity.com/learn/article/whats_the_best_battery. [Accessed: 01-Sep-2015].

[50] R. A. Bernhoft, “Cadmium Toxicity and Treatment,” *The Scientific World Journal*, 2013. [Online]. Available: http://www.hindawi.com/journals/tswj/2013/394652/.

[51] M. Oswal, J. Paul, and R. Zhao, “A comparative study of Lithium-Ion Batteries,” *Univ. South. Calif.*, 2010.

[52] C. Simpson and Texas Instruments, “Characteristics of Rechargeable Batteries,” *National Semiconductor*, 2011. [Online]. Available: http://www.ti.com/lit/an/snva533/snva533.pdf. [Accessed: 03-Aug-2015].

[53] Battery University, “Li-polymer Battery: Substance or Hype?,” 2015. [Online]. Available: http://batteryuniversity.com/learn/article/the_li_polymer_battery_substance_or_hype. [Accessed: 03-Aug-2015].

[54] Traxxas, “LiPo Powercell Batteries,” 2015. [Online]. Available: https://traxxas.com/products/parts/batteries/powercellbatteries/lipo. [Accessed: 03-Aug-2015].

[55] Muchmore, “Lithium-Polymer Battery Series - Safety and Handling Instructions,” 2015. [Online]. Available: http://manuals.hobbico.com/mmr/lipo-manual.pdf. [Accessed: 03-Aug-2015].

[56] LRP VTEC, “Material Safety Data Sheet - LRP VTEC Lithium-Polymer Ultra Performance batteries,” 2009.

[57] RC Toys, “Disposal of LiPo Batteries.” [Online]. Available: http://www.rctoys.com/pdf/thunder-power-disposal-of-old-damaged-lipo-batteries.pdf. [Accessed: 03-Aug-2015].

[58] Battery University, “All About Battery Chargers.” [Online]. Available: http://batteryuniversity.com/learn/article/all_about_chargers. [Accessed: 08-Jul-2013].

[59] C. Simpson, “Characteristics of Rechargeable Batteries,” 2011.

[60] National Semiconductor, “A Designers Guide to Lithium Battery Charging,” *Digi-Key Electronics*, 2012. [Online]. Available: http://www.digikey.com/en/articles/techzone/2012/sep/a-designers-guide-to-lithium-battery-charging. [Accessed: 03-Aug-2015].

[61] Battery University, “Charging Lithium-Ion Batteries,” 2015. [Online]. Available: http://batteryuniversity.com/learn/article/charging_lithium_ion_batteries. [Accessed: 03-Aug-2015].

[62] “SYSTEM TO DETECT HUMAN BEINGS BURIED UNDER Embedded Design SYSTEM TO DETECT HUMAN BEINGS BURIED UNDER EARTHQUAKE RUBBLE.”

[63] VideoComm Technologies, “Radio Frequency Penetration Chart.” [Online]. Available: http://www.videotransmitters.com/Radio-Frequency-Penetration-Chart. [Accessed: 07-Jul-2013].

[64] Independent Communicatons Authority of South Africa, “Draft South African Table of Frequency Allocations,” vol. 34, no. 31264, 2008.

[65] Rajant, “Portable High-Speed Mobile Networks,” 2007.

[66] Rajant, “BreadCrumb ® ME 2 Datasheet.”

[67] Rajant Corporation, “ME Series,” 2015. [Online]. Available: http://www.rajant.com/technology/breadcrumb-wireless-nodes/me-series/. [Accessed: 04-Aug-2015].

[68] CMT, “Introduction to GPS.” [Online]. Available: http://www.cmtinc.com/gpsbook/. [Accessed: 21-Jun-2013].

[69] HM Pipeline Services, “XLI GPS Accuracy White Paper,” 2006.

[70] Ross Bowie, “Global Positioning System/Wide Area Augmentation System,” *Aviation Safety Letter*, 20-May-2010. [Online]. Available: https://www.tc.gc.ca/eng/civilaviation/publications/tp185-1-04-535-3026.htm. [Accessed: 04-Aug-2015].

[71] P. Jain, “Magnetometers: Types & Applications,” *Engineers Garage*, 2015. [Online]. Available: http://www.engineersgarage.com/articles/magnetometer. [Accessed: 04-Aug-2015].

[72] D. B. Pengra, J. Stoltenberg, R. Van Dyck, and O. Vilches, “The Hall Effect,” *Science*, 2015.

[73] W. Sageer, “Hall Effect Sensor: Circuit & Working,” *Engineers Garage*, 2015. [Online]. Available: http://www.engineersgarage.com/contribution/hall-effect-sensor. [Accessed: 04-Aug-2015].

[74] J. Včelák and P. Kašpar, “Sensors for vector magnetometers,” *J. Electr. Eng.*, vol. 57, no. 8 SUPPL, pp. 178–180, 2006.

[75] M. Kok, J. Hol, T. Schön, F. Gustafsson, and H. Luinge, “Calibration of a magnetometer in combination with inertial sensors,” *Proc. 15th Int. Conf. Inf. Fusion*, pp. 787–793, 2012.

[76] Canadian Centre for Occupational Health and Safety, “Calculating Recommended Weight Limit (RWL) : OSH Answers,” 2012. [Online]. Available: http://www.ccohs.ca/oshanswers/ergonomics/niosh/calculating_rwl.html. [Accessed: 04-Aug-2015].

[77] V. Lavigne, “Weight limit recommendation in backpack use for school-aged children,” *J. Clin. Chiropr. Pediatr.*, vol. 14, no. 2, pp. 1156 – 1159, 2014.

[78] S. C. Walpole, D. Prieto-Merino, P. Edwards, J. Cleland, G. Stevens, and I. Roberts, “The weight of nations: an estimation of adult human biomass,” *BMC Public Health*, vol. 12, no. 1, p. 439, 2012.

[79] SABS Standards Division, “The application of the National Building Regulations,” *SANS 10400-S*, 2011.

[80] J. M. Griggs, “Human Figure average measurements,” 2001. [Online]. Available: http://www.fas.harvard.edu/~loebinfo/loebinfo/Proportions/humanfigure.html. [Accessed: 17-Aug-2015].

[81] Futurlec, “New Performance Record for ARM Cortex-M Microcontroller.” [Online]. Available: https://www.futurlec.com/News/ST/STM32_F4_Series.shtml. [Accessed: 31-Aug-2015].

[82] Texas Instruments, “BQ77908A | Stand-Alone Multi-Cell Li-Ion/Li-Polymer Precision Protector.” [Online]. Available: http://www.ti.com/product/bq77908A. [Accessed: 31-Aug-2015].

[83] Texas Instruments, “BQ34Z100 | Battery Fuel Gauge.” [Online]. Available: http://www.ti.com/product/bq34z100. [Accessed: 31-Aug-2015].

[84] Texas Instruments, “BQ24610 | Battery Charger IC.” [Online]. Available: http://www.ti.com/product/bq24610. [Accessed: 31-Aug-2015].

[85] QEEWiki, “Q’s MAX7456 Img Gen - QEEWiki.” [Online]. Available: https://sites.google.com/site/qeewiki/projects/q-s-max7456-img-gen. [Accessed: 31-Aug-2015].

[86] GPS Visualizer, “GPS Visualizer,” 2015. [Online]. Available: http://www.gpsvisualizer.com/. [Accessed: 01-Sep-2015].

[87] A. M. Stoll, M. A. Chanta, and J. R. Piergallini, “Prediction of Threshold Pain Skin Temperature from Thermal Properities of Materials in Contact,” 1982.

[88] A. Bozkurt and NC State University, “Cyber Enhanced Working Dog,” 2014.

[89] iRobot, “iRobot 510 PackBot the Multi-mission Robot.” [Online]. Available: http://www.irobot.com/For-Defense-and-Security/Robots/510-PackBot.aspx#PublicSafety. [Accessed: 03-Aug-2015].

[90] Мужиг.ру, “Magnetometer Calibration - HMC5883L IMU.” [Online]. Available: http://muzhig.ru/magnetometer-calibration-hmc5883l-imu/. [Accessed: 01-Sep-2015].

[91] STMicroelectronics, “STM32F4DISCOVERY Discovery kit with STM32F407VG MCU.” [Online]. Available: http://www.st.com/web/catalog/tools/FM116/SC959/SS1532/PF252419. [Accessed: 02-Sep-2015].